*Universiteit Gent*
*Faculteit Wetenschappen*
*Vakgroep voor Subatomaire- en Stralingsfysica*
*2000-2001*

# Experimental Study of the Virtual Compton Scattering Process at $Q^2 = 1.0\,(GeV/c)^2$

*Proefschrift ingediend tot het verkrijgen*
*van de academische graad van*
*Doctor in de wetenschappen : Natuurkunde*

*Promotor : Robert Van de Vyver*

*door*

**Natalie Degrande**

# Contents

# Introduction

At the end of the 19th century, one had reached the point of knowing that atoms are the building blocks of everything around us. A series of experiments in the beginning of the 20th century showed evidence that the atom itself is formed by a nucleus, which represents almost all of the atom's mass, surrounded by a cloud of electrons. With the discovery of the neutron in 1932, it became clear that the atom's nucleus is composed of neutrons and protons, both called nucleons. Later, in the 1970s one observed that the nucleons, from which one thought they were the smallest particles in the atom's nucleus, are in fact composed of quarks. Until now, there is no evidence that quarks have an underlying structure and they are supposed to be the smallest particles in the atom's nucleus.

Today, a fundamental problem of subatomic physics is the characterization of the internal structure of the nucleon. At short distance there is no problem : point-like quarks and gluons act following the laws of Quantum Chromo Dynamics (QCD). But at larger distance (of the order of the nucleon size) things become more difficult to understand. A lot of models exist to describe the electromagnetic structure of nucleons, but experimental data are needed to check the hypotheses that are made and/or fix the values for the parameters that are used in these models.

The electromagnetic interaction is a powerful tool for investigating the nucleon structure since it is well understood and it reveals observables that can be directly interpreted in terms of the current carried by the quarks. Until recently, the electromagnetic structure of nucleons has been studied by elastic electron scattering, Real Compton Scattering (RCS) and deep inelastic scattering. Elastic scattering leads to the form factors that describe the spatial charge and current distributions inside the nucleon in its ground state. RCS provides means to obtain the electric ($\bar{\alpha}_E$) and magnetic ($\bar{\beta}_M$) polarizabilities that describe the nucleon's abilities to deform when it is exposed to an electromagnetic field. Finally, deep inelastic scattering yields structure functions that reveal information on the internal structure of the nucleon.

Virtual Compton Scattering (VCS) is also a fundamental exclusive reaction and it is the natural complement to form factor measurements, RCS and deep inelastic scattering. VCS off the proton refers to the process where a virtual photon, with negative four-momentum squared $Q^2$, is absorbed by a hadronic target and where this target emits a real photon to return to its original state. This process can be accessed through the photon electro-production reaction $e + p \rightarrow e' + p' + \gamma$. Below the pion production threshold, it gives a way to access the generalized polarizabilities of the proton. These polarizabilities, that are functions of $Q^2$, are new nucleon structure observables that describe how the charge and current distributions, to which we have access through elastic scattering, change under the influence of an electromagnetic field perturbation. They are an extension of the electric and magnetic polarizabilities from RCS ($Q^2 = 0\ (GeV/c)^2$).

Although VCS has been proposed many times since the late 1950s by theorists, the experiments had to wait until the advent of the new generation of electron accelerators. Indeed, since the VCS cross section is much smaller than the elastic scattering cross section, experiments need high duty cycle electron beams to achieve acceptable counting rates. Moreover, high resolution spectrometers are indispensable to separate the $\pi^0$ events, which generate a physical disturbing background, from VCS events and to obtain high precision on the cross sections. With the birth of the CEBAF (Continuous Electron Beam Accelerator Facility) research center in the USA that provides high luminosity and high resolution spectrometers, the experimental VCS program finally got started. When organizing the experimental strategy, one realised that part of it could already be performed at the MAMI (Mainz Microtron) accelerator in Germany. So the first dedicated VCS experiment below the pion production threshold, at $Q^2 = 0.33\ (GeV/c)^2$, took place in 1995-1997 and at this moment the analysis reaches a final stage. Two structure functions that are linear combinations of generalized polarizabilities have been extracted. In the spring of 1998 the data taking for the experimental program E93-050 “Nucleon Structure Study by Virtual Compton Scattering” at TJNAF (Thomas Jefferson National Accelerator Facility, formerly known as CEBAF) took place. Data were taken at $Q^2 = 1.0\ (GeV/c)^2$, $Q^2 = 1.9\ (GeV/c)^2$ and in the resonance region. A third VCS experiment below pion production threshold at $Q^2 = 0.05\ (GeV/c)^2$ is planned at Bates.

Besides the VCS threshold region, two other kinematical regimes also look promising to explore. First, the hard scattering regime that can provide tests of perturbative QCD predictions and of the valence quark wave function. But at this moment, no existing accelerator is able to perform experiments in this regime. Second, the Bjorken regime in which Deeply Virtual Compton Scattering (DVCS) gives access to off-forward parton distributions that can give more insight in the nucleon spin. At this moment experiments for DVCS are being prepared.

In the first chapter of this work, the physics framework for VCS will be outlined. Some theoretical aspects of VCS will be summarized, as well as how to extract information on generalized polarizabilities, starting from photon electroproduction experiments. The second chapter discusses the first dedicated VCS experiment at MAMI. The experimental setup for the VCS experiment at TJNAF is described in the third chapter. Chapter 4 gives a detailed description of the Monte Carlo simulation that is used for the analysis of the VCS experiment at TJNAF. The analysis of the data at $Q^2 = 1.0\ (GeV/c)^2$ that were taken during this experiment and preliminary results on cross section values are described in chapters 5, 6 and 7. Finally, chapter 8 describes a first attempt to extract preliminary information on combinations of generalized polarizabilities at $Q^2 = 1.0\ (GeV/c)^2$.

# Chapter 1

# Physics Framework

## 1.1 Overview

Nucleon polarizabilities have long been intriguing quantities and they will remain so for many years to come. This is mainly due to their fundamental importance for the understanding of the internal structure of the nucleon as they are as important as the charge and magnetic radii. Another reason is that only recently appropriate probes have become available to start a (hopefully) fruitful expedition to the sub-hadronic world where quarks and gluons live together, causing the properties of nucleons as we experimentally observe them. The electromagnetic interaction is considered to be a particularly suitable mechanism to explore nuclear matter. Its strength is twofold : it is relatively weak and it can be calculated very accurately in Quantum Electro Dynamics (QED). In this respect, the Compton Scattering process off the nucleon is of great interest since it examines the most elementary nuclear system (the nucleon) by the most elementary probe (the electromagnetic interaction).

Up to now, Real Compton Scattering (RCS) off the nucleon has been studied in terms of the electric $\bar{\alpha}_E$ and magnetic $\bar{\beta}_M$ polarizabilities, which contain global information on the excitation spectrum of the nucleon. Recently, with the advent of a new generation of electron accelerators, Virtual Compton Scattering (VCS) has become accessible. VCS is the process where a virtual photon (e.g. from electron scattering) interacts with the nucleon and a real photon is emitted. This process is likely to provide even more information on the nucleon structure since it promises to yield 6 generalized polarizabilities, depending on the transferred four-momentum ($Q^2$) of the virtual photon.

Before digging into the more theoretical aspects of RCS, VCS and the polarizabilities, a short reminder on electron scattering and nucleon form factors will be given. To conclude this chapter, a state of the art considering the experimental program of VCS below the pion production threshold will be summarized.

## 1.2 Electron Scattering off the Nucleon

### 1.2.1 Some considerations on electron scattering

The process of electron scattering off nucleons is governed by the electromagnetic interaction. As already stated before, this is one of the most powerful tools to investigate the nuclear structure. The interaction of the electron with the nucleon primarily happens by the exchange of a virtual photon, which is the field-quantum of the electromagnetic interaction. It interacts with the charge density and the electromagnetic currents in the nucleon, transferring energy $q^0$ and momentum $\vec{q}$. When performing electron scattering experiments at various kinematics, the response of the nucleon to the electromagnetic probe can be studied, providing information on some of the constituents of the nuclear current.

Since the electromagnetic interaction can be described very accurately by QED, it is possible to investigate in detail the nuclear current and obtain precise information on the nuclear structure. This is to be contrasted with hadron scattering that is dominated by the strong force, yielding more model-dependent interpretations of experimentally obtained results. The electromagnetic interaction is also relatively weak, so for light nuclei it can be described in the one photon exchange approximation. Moreover, this weakness implicates that the virtual photon can penetrate the nuclear surface and interact with the nuclear current throughout the entire nuclear volume, while hadronic probes are only able to scan the nuclear surface. Dealing with virtual photons also has some advantages in comparison to real photons : the momentum and energy of the virtual photon can be varied independently. So one could for example fix the energy transfer and map out the spatial distributions of the nuclear charge and current densities by measuring the nuclear responses at a range of momentum values. Moreover, the virtual photon has both longitudinal and transverse polarisations, giving access to information on the charge density and electromagnetic current density of the nucleon, respectively. The real photon only has a transverse polarisation and thus yields information only on the current density.

Of course, there are also drawbacks and difficulties. Being a weak interaction, the electromagnetic interaction yields small cross sections. Therefore high luminosities and significant more beam time than for hadron scattering is needed. The fact that one deals with light charged particles (electrons) also implies one has to take into account radiation processes, so in this respect the analysis and interpretation of electron scattering experiments is somewhat more involved.

### 1.2.2 The concept of form factors

Since the proton electric and magnetic form factors are important variables for this experiment (see section 1.5), some attention will be paid to them in this and the following subsection.

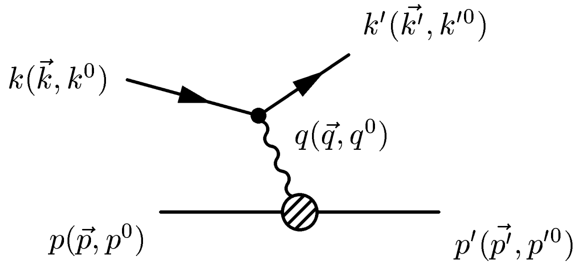

*Figure 1-1: Schematic for electron scattering.*

In figure 1-1 the electron scattering on a single nucleon in the one photon exchange approximation is presented. Note that in this work, all particles will be described by a four-momentum $v$, composed of the energy component $v^0$ and three-momentum $\vec{v}$, the modulus of the momentum $|\vec{v}|$ will be denoted $\mathsf{v}$. In figure 1-1 $k$ and $k'$ are the four-momenta of the incident and scattered electron respectively, $p$ and $p'$ the four-momenta of the target and recoil nucleon and $q$ the four-momentum of the virtual photon :

$$\begin{aligned} q^2 = (k - k')^2 &= (k^0 - k'^0)^2 - (\vec{k} - \vec{k'})^2 \\ &\approx -4k^0 k'^0 sin^2 \frac{\theta}{2} \\ &\leq 0 \end{aligned} \tag{1-1}$$

with $\theta$ the angle between the incoming and scattered electron. In order to deal with positive quantities, the invariant variable $Q^2$ is defined :

$$Q^2 = -q^2 \tag{1-2}$$

The transferred energy $q^0$ is defined as :

$$q^0 = k^0 - k'^0 \tag{1-3}$$

When performing scattering experiments on nucleons, one observes that the experimental cross section only agrees with the Mott cross section (electron scattering where the spin of the electron and recoil of a spinless and structureless target are taken into account) in the limit of $\mathsf{q} \to 0$. This is because of the spatial extent of nucleons : when $\mathsf{q}$ gets larger, the reduced wavelength ($\bar{\lambda} = \hbar/\mathsf{q}$) of the virtual photon and thus the scale of observation becomes smaller, so one does not probe the entire nucleon anymore, but only parts of it. This spatial extension of nucleons is described by form factors [1].

To clarify the concept of form factors, let's consider the simple case of an electron scattering experiment on a spinless particle (charge Ze) with a static, spherical symmetric charge distribution. One can describe the charge distribution $\rho(\vec{r})$ with a function $f(r)$ :

$$\rho(\vec{r}) = Zef(r) \tag{1-4}$$

the radial function is normalized as follows :

$$1 = \int f(r)d^3r = 4\pi \int f(r)r^2dr \tag{1-5}$$

It can be shown [1] that the scattering cross section becomes

$$\left(\frac{d\sigma}{d\Omega}\right) = \left(\frac{d\sigma}{d\Omega}\right)_{Mott} \left|\int e^{i\vec{q}\vec{r}/\hbar} f(r)d^3r\right|^2 \tag{1-6}$$

The integral

$$F(\vec{q}) = \int e^{i\vec{q}\vec{r}/\hbar} f(r)d^3r \tag{1-7}$$

is the Fourier transform of the function $f(r)$, which is the space charge density $\rho(r)$, normalized to the total charge Ze. $F(\vec{q})$ is called the form factor of the charge distribution. It contains all information on the spatial charge distribution of the investigated particle.

### 1.2.3 Nucleon electric and magnetic form factors

Analogous to the example above, the charge and current distributions of nucleons can be described by the electric and magnetic form factors, respectively. The cross section for electron scattering off nucleons can be described by the Rosenbluth formula [1]:

$$\left(\frac{d\sigma}{d\Omega}\right) = \left(\frac{d\sigma}{d\Omega}\right)_{Mott} \cdot \left[\frac{G_E^2(Q^2) + \tau G_M^2(Q^2)}{1+\tau} + 2\tau G_M^2(Q^2) tan^2\frac{\theta}{2}\right] \tag{1-8}$$

where $G_E(Q^2)$ and $G_M(Q^2)$ are the electric and magnetic form factors and $\tau$ is given by :

$$\tau = \frac{Q^2}{4M^2} \tag{1-9}$$

with $M$ the mass of the nucleon.

Measuring the $Q^2$-dependence of these form factors gives information on the spatial extent of the electric charge and magnetisation current in the nucleon. The two form factors can again be interpreted as the Fourier transform of the charge and current distributions of the nucleon. The limit $Q^2 \to 0$ is of particular interest : the reduced wavelength of the virtual photon becomes large and the internal structures can not be resolved anymore, so $G_E(0)$ is equal to the electric charge of the particle, normalized to the elementary charge $e$, and $G_M(0)$ is equal to the total magnetic moment, normalized to the nuclear magneton $\mu_N (= e\hbar/2m_p)$. For the proton and neutron one obtains :

$$G_E^p(Q^2 = 0) = 1 \qquad G_E^n(Q^2 = 0) = 0 \tag{1-10}$$

$$G_M^p(Q^2 = 0) = 2.79 \quad G_M^n(Q^2 = 0) = -1.91 \tag{1-11}$$

From the 1960s on, a lot of experiments have been performed to measure the nucleon electromagnetic form factors. For a short review, see reference [2]. Many theories and models have been developed to fit and/or predict them.

Early experiments have shown that for values of $Q^2 \leq 2\ (GeV/c)^2$ the electric and magnetic form factors of the proton and the magnetic form factor of the neutron can be described to a good approximation (up to the 20 % level) by a so-called dipole fit :

$$G_D(Q^2) = \left(1 + \frac{Q^2}{0.71}\right)^{-2} \approx G_E^p(Q^2) \approx \frac{G_M^p(Q^2)}{2.79} \approx \frac{G_M^n(Q^2)}{-1.91} \tag{1-12}$$

The neutron appears from the outside to be electrically neutral, hence it has a very small electric form factor.

This observed dipole form factor corresponds to an exponentially decreasing charge distribution. So one can conclude that nucleons are neither point-like particles, nor homogeneously charged spheres, but that they are rather diffuse systems. The fact that electric and magnetic form factors of the proton and the magnetic form factor of the neutron suit the same parametrisation indicates that the mean square radii of the charge distribution of the proton and of the magnetic moment distribution in the proton and neutron have about the same size. These radii are determined by the slope of the form factor in the limit $Q^2 = 0$ and yield $\approx 0.86 fm$. Determining the electric form factor for the neutron is quite difficult since no free neutron targets exist. Alternative methods yield a negative value for the slope of the form factor in the limit $Q^2 = 0$, indicating that the negative charge of the neutron is located on the exterior, so it is only from the outside that neutrons seem to be electrically neutral.

Two frequently used parametrisations for the form factors are the Bosted [2] and the Höhler [3] parametrisation. Both are fits to a different compilation of world form factor data covering a range for $Q^2$ from 0 $(GeV/c)^2$ to 30 $(GeV/c)^2$. The analysis of the VCS experiment at MAMI is done using the Höhler parametrisation for the proton form factors. The use of this parametrisation was validated by measuring the elastic scattering cross section for each kinematical setting of the experiment. In the region of interest for this experiment, the two parametrisations for the proton electric form factor are in good agreement, while the values of the magnetic form factor differ by 3% [4]. For the analysis of the VCS experiment at TJNAF one has chosen to use the Bosted parametrisation for the proton magnetic form factor. The error on this parametrisation in the regions of interest (around 1.0 $(GeV/c)^2$ and 1.9 $(GeV/c)^2$) is about 3% [2].

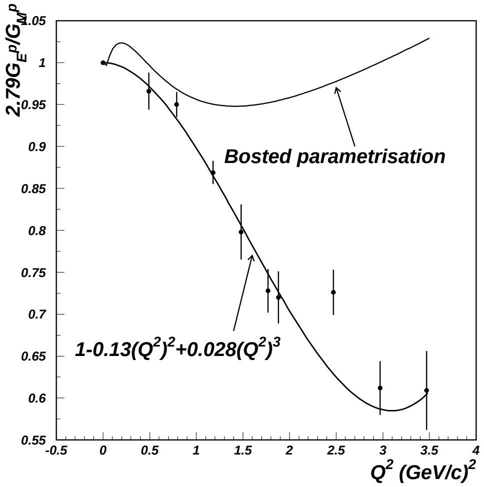

*Figure 1-2: Data points for the ratio 2.79* $G_E^p/G_M^p$ *from the TJNAF experiment [5]. The Bosted parametrisation and the third degree polynomial fit* $(1-0.13(Q^2)^2+0.028(Q^2)^3)$ *are indicated with the full lines.*

Recently, the ratio $G_E^p(Q^2)/G_M^p(Q^2)$ has been measured at TJNAF. The results of this experiment show for the first time that the $Q^2$-dependence of $G_E^p(Q^2)$ and $G_M^p(Q^2)$ are not at all alike [5]. $G_E^p(Q^2)$ decreases faster than $G_M^p(Q^2)$ when $Q^2$ increases. In figure 1-2 the data are plotted. For details on the calculation method and uncertainties, see reference [5]. To these data points a third degree polynomial was fitted. It is indicated by the rapidly falling full line in the figure. This fit will be used to determine $G_E^p(Q^2)$ that will be applied in the analysis of the VCS experiment at TJNAF. Note that in the regions of interest (around 1.0 and 1.9 (GeV/c)$^2$) the fit is pretty good. For completeness, also the ratio $2.79 G_E^p(Q^2)/G_M^p(Q^2)$ determined by the Bosted parametrisation is drawn in the figure.

## 1.3 The Nucleon Structure in Terms of Polarizabilities

The quantity called polarizability is a measure of the stiffness or rigidity of a system. The electric polarizability for example describes the ease with which a system containing charges adapts its internal structure to an applied quasi-static electromagnetic field.

In order to get an idea of the physics underlying the polarizability of a system, let's consider two constituents of opposite charge ($q$ and $-q$, respectively), bound together with springs and emerged in a constant electric field. The electric field forces the two particles to move in opposite directions. Since the centres of mass of the positive and negative charges do not coincide anymore, a dipole moment $\vec{d} = \alpha_E \vec{E}$ is induced, where $\alpha_E$ is the electric polarizability and $\vec{E}$ is the electric field. If one now considers the force between the two charged particles to be governed by Hooke's law ($q\vec{E} = k\vec{r}$, with $k$ the spring constant that gives information on how strong the spring is), an equilibrium will be obtained when $\alpha_E = 2q^2/k$. Given the fact that $k$ is a measure of how strong the two charges are bound together, one sees clearly that $\alpha_E$ gives us a measure of the ease with which the system can be polarised in the presence of an external electric field.

Extending this classical example to the nucleon which is a composite system, one sees that the electromagnetic polarizabilities can give us important information on the binding force acting between the constituents of the nucleons, hence on their internal structure. The electric polarizability of the hydrogen atom is about $0.66 \times 10^6 fm^3$. This is of the order of the atom's size ($\approx (10^2 fm)^3$). The world global averages of the electric and magnetic polarizabilities of the proton (see section 1.4.2) are $\bar{\alpha}_E = 12.1 \times 10^{-4} fm^3$ and $\bar{\beta}_M = 2.1 \times 10^{-4} fm^3$. Comparing these small values with the proton's size ($\approx (1 fm)^3$), one learns that the proton is a very rigid object, with strong "springs" between its constituents.

Classical scattering of light in the earth's atmosphere can also be considered in terms of the electric polarizability : if an electric field has a wavelength $\lambda$ that is much larger than the atom on which it impinges, the induced dipole moment will also contribute to the resultant field. The incident field polarises dipoles that then re-radiate their energies. As derived by Rayleigh [6] the total time-average scattered power increases with the fourth power of the frequency ($\omega^4$), so shorter wavelengths ($\lambda \sim \omega^{-1}$) of light, which consist of violet and blue, are scattered more than longer wavelengths. This is the reason why during daytime, the sunlight apparently lacks blue, which makes the sun look yellow. This missing blue is scattered by the earth's atmosphere, and is visible for us as the sky having a blue color. So the light of the sky is in fact the sun's scattered blue light. As evening falls, the light coming from the sun has to traverse a longer path through the atmosphere. So the filtering effect of the atmosphere increases, causing the sun to become apparently orange and finally even red. The cross section for Rayleigh scattering is also proportional to the electric polarizability. So it is clear that if one can measure the scattered power of a certain system at large distance, one also has access to the polarizability of this system. This is the basic idea behind Real and Virtual Compton Scattering experiments.

Analogous to the electric field, the magnetic field induces a magnetic moment according to $\vec{\mu} = \beta_M \vec{B}$ with $\beta_M$ the magnetic polarizability or magnetic susceptibility. In this case, the magnetic field forces the already present magnetic moments of the quarks inside the nucleon to align with the direction of the magnetic field, generating a paramagnetic contribution to the induced magnetic dipole moment. Induced electric currents, generated by the charged pions on the nucleon's surface, will lead to a diamagnetic contribution to the induced magnetic moment, weakening the resulting dipole moment by Lenz's law.

Note that in Compton Scattering experiments, $\bar{\alpha}_E$ and $\bar{\beta}_M$ are used. They combine the effects of the static polarizabilities $\alpha_E$ and $\beta_M$ with retardation corrections.

As seen in section 1.2.3, the nucleon form factors describe the electric and magnetic distributions of the nucleon. VCS in its turn gives access to the deformation of these distributions caused by an electromagnetic field perturbation. To describe these deformations, new observables have been defined : Generalized Polarizabilities (GPs). They generalize the electric $\bar{\alpha}_E$ and magnetic $\bar{\beta}_M$ polarizabilities obtained in RCS and can be thought of as giving information on local polarisation densities in the nucleon. While the form factors describe only the ground state of the nucleon, polarizabilities are sensitive to the entire excitation spectrum of the nucleon, providing therefore important nucleon structure observables. They complement the nucleon formfactors and can contribute valuable knowledge in the quest for understanding the ensemble of quarks and gluons within the nucleon.

A variety of theoretical model-calculations of the GPs exist. They will be reviewed in section 1.6.

## 1.4 Real Compton Scattering

### 1.4.1 Formalism

The well known Compton effect refers to the scattering of photons on atomic electrons. Nevertheless one also has assigned the name Compton to the process where photons scatter on nucleons. This process is called Compton Scattering. Depending on whether the incoming photon is real or virtual, one deals with Real Compton Scattering (RCS) or Virtual Compton Scattering (VCS). In both cases the outgoing photon is real. This section covers the RCS process off the proton, the next section deals with VCS.

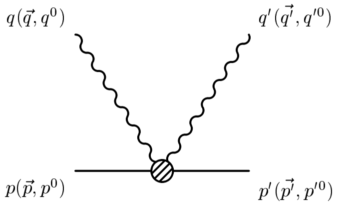

*Figure 1-3: Schematic for real Compton scattering.*

A schematic for RCS is shown in figure 1-3. $q$ and $q'$ are the four-momenta of the incoming and scattered real photon, respectively, $p$ and $p'$ denote the four-momenta of the target and recoil proton. In this process, the incoming photon plays the role of electromagnetic field, inducing a time dependent electric and magnetic dipole moment in the nucleon. The time dependence of the electric dipole moment leads to a secondary electromagnetic radiation : the outgoing photon. This radiation depends on the electric and magnetic polarizabilities of the nucleon.

Below pion production threshold, the amplitude for RCS off a proton can be expressed as an expansion in the photon energies $q^0$ and $q'^0$. According to the low energy theorem [7], the unpolarised differential cross section for RCS in the laboratory frame can be written in the form :

$$\begin{aligned} \frac{d\sigma}{d\Omega} &= \left(\frac{d\sigma}{d\Omega}\right)^{Born} \\ &\quad - \frac{e^2}{4\pi m_p}\left[\frac{q'^0}{q^0}\right]^2 q^0 q'^0 \left[\frac{\bar{\alpha}_E + \bar{\beta}_M}{2}(1+cos\theta)^2 + \frac{\bar{\alpha}_E - \bar{\beta}_M}{2}(1-cos\theta)^2\right] + \mathcal{O}(q^{0^4}) \end{aligned} \tag{1-13}$$

with $\theta$ the angle between the incoming and the scattered photon. Figure 1-4 shows the relative importance of the different contributions to the cross section. The first term of equation (1-13) is the model-independent Born contribution that describes the scattering off a spin-1/2 point particle with an anomalous magnetic moment ($\kappa$). This term can be written in terms of the nucleon global properties (charge, mass and anomalous magnetic moment). It significantly differs from the relativistic "Klein-Nishina" cross section that does not take into account the anomalous magnetic moment. The second term contains the nucleon structure effects in the form of the electric ($\bar{\alpha}_E$) and magnetic ($\bar{\beta}_M$) polarizabilities. As can be seen in figure 1-4, these structure effects ($\bar{\alpha}_E, \bar{\beta}_M$) mainly compensate the effect coming from the anomalous magnetic moment. The solid curve in the figure is the complete cross section due to all order terms in $q^0$. It is calculated in a dispersive approach by L'vov [8]. This figure shows that below the pion production threshold the relative difference between the quadratic approximation (Born+($\alpha$+$\beta$)qq') and the complete calculation (L'vov) reaches up to 25%. This indicates that it is not that evident to neglect higher order terms. This causes the main difficulty for extracting the scalar polarizabilities from experimental data.

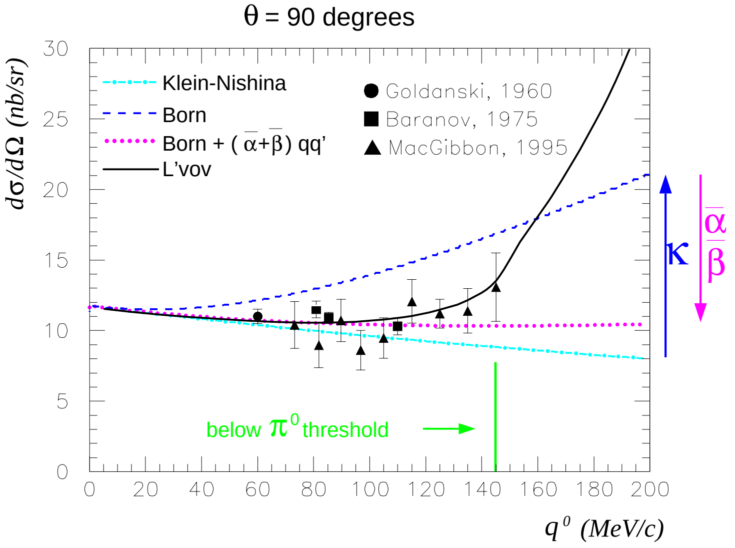

*Figure 1-4: Differential cross section for real Compton scattering off the proton. Figure from reference [9].*

Equation (1-13) shows clearly that the unpolarised differential cross section for RCS when performing forward scattering ($\theta$ small) experiments, is extremely sensitive to the sum of the electric and magnetic polarizabilities, while backwards scattering ($\theta$ near 180°) is mostly sensitive to the difference. For $\theta = 90°$, information on $\bar{\alpha}_E$ can be obtained.

When performing double polarisation experiments, one has additional access to the four spin-dependent polarizabilities $\gamma_i$. These spin-dependent polarizabilities originate from the spin-1/2 nature of the nucleon. They describe the response of the nucleon's spin distribution to an external quasi-static electromagnetic field.

### 1.4.2 RCS experiments

Measurements of the proton polarizabilities have only been performed by Compton scattering experiments. The polarizabilities are determined by measuring the deviation of the measured cross sections from the Born cross section. The effect of the polarizabilities one expects from theory is not large. Hence the statistical precision and systematic accuracy of the experiments have to be outstanding in order to be able to determine the values of the polarizabilities with an acceptable precision. As equation (1-13) suggests, one could think of raising the photon energy in order to increase the sensitivity of the cross section to the polarizabilities. But if the energy becomes too high ($q^0 > 100\ MeV$), the low energy expansion is not valid any longer and theoretical uncertainty is introduced in the extraction of the polarizabilities. So it is obvious that, when measuring absolute cross sections, attention has to be paid to the following aspects : the energy and angular range have to be chosen as a balance between sensitivity to the polarizabilities and insensitivity to any theoretical model.

The first experimental indication that the proton structure affects the differential cross section for elastic photon-proton scattering was obtained at the FIAN in 1956 [10], while the first values for the proton electromagnetic polarizabilities were published in 1960 [11]. Since then, a number of experiments has been performed in order to determine the proton electric and magnetic polarizabilities. In reference [12] a brief overview of a series of these experiments is given. Table 1-1 summarizes the published proton polarizability values. For details on extraction methods and errors used by the authors, see references [11, 12, 13, 14, 15, 16, 17].

A model-independent dispersion sum rule has been derived by Baldin [18]. It yields a rather precise value for $\bar{\alpha}_E + \bar{\beta}_M$ :

$$\bar{\alpha}_E + \bar{\beta}_M = \frac{1}{2\pi^2}\int_{m_\pi}^{\infty} \frac{\sigma_\gamma(q^0)}{(q^0)^2} dq^0 = 14.2 \pm 0.5 \times 10^{-4} fm^3 \qquad (1\text{-}14)$$

| Data set | $\bar{\alpha}_E$ $(10^{-4} fm^3)$ | $\bar{\beta}_M$ $(10^{-4} fm^3)$ |
|---|---|---|
| Gol'danski et al. (1960)[11] | $9 \pm 2$ | $2 \pm 2$ |
| Baranov et al. (1975)[13] | $10.7 \pm 1.1$ | $-0.7 \pm 1.6$ |
| Federspiel et al. (1991)[14] | $10.9 \pm 2.2 \pm 1.3$ | $3.3 \mp 2.2 \mp 1.3$ |
| Zieger et al. (1992)[15] | $10.6 \pm 1.2 \pm 1.1$ | $3.6 \mp 1.2 \mp 1.1$ |
| Hallin et al. (1993)[16] | $9.8 \pm 0.4 \pm 1.1$ | $4.4 \mp 0.4 \mp 1.1$ |
| MacGibbon et al. (1995)[12] | $12.5 \pm 0.6 \pm 0.7 \pm 0.5$ | $1.7 \mp 0.6 \mp 0.7 \mp 0.5$ |
| Olmos (2000)[17] | $11.89 \pm 0.57$ | $1.17 \pm 0.75$ |

Table 1-1: *Published values for electric ($\bar{\alpha}_E$) and magnetic ($\bar{\beta}_M$) polarizabilities of the proton.*

where $\sigma_\gamma(q^0)$ is the total photo-absorption cross section on the proton. The numerical value is obtained using the available experimental data and applying reasonable theoretical considerations for extrapolating the integral to infinite energy [19]. A lot of published values for $\bar{\alpha}_E$ and $\bar{\beta}_M$ have been obtained by imposing this constraint to the experimental results. This is indicated in table 1-1 by inverting the signs of the errors on $\bar{\beta}_M$. In reference [20] the Baldin sum rule lead to the following value for $\bar{\alpha}_E + \bar{\beta}_M$ :

$$\bar{\alpha}_E + \bar{\beta}_M = 13.69 \pm 0.14 \times 10^{-4} fm^3 \tag{1-15}$$

The world global average, calculated by MacGibbon et al., for $\bar{\alpha}_E$ and $\bar{\beta}_M$ at $Q^2 = 0\ (GeV/c)^2$ is [12]:

$$\bar{\alpha}_E = (12.1 \pm 0.8 \pm 0.5) 10^{-4} fm^3 \qquad \bar{\beta}_M = (2.1 \mp 0.8 \mp 0.5) 10^{-4} fm^3 \tag{1-16}$$

At present, large efforts are made at MAMI, TJNAF, SAL and LEGS to improve the values of the electromagnetic polarizabilities of the proton and neutron, as well as to investigate the proton spin polarizabilities in double polarisation experiments.

## 1.5 Virtual Compton Scattering

### 1.5.1 Introduction

As already stated before, VCS is the process : $\gamma^* + p \to p' + \gamma$. This reaction can be accessed experimentally through photon electro-production off the proton : $e + p \to e' + p' + \gamma$. A schematic for this reaction is shown in figure 1-5. Again, $k$ ($k'$) denotes the four-momentum of the incoming (scattered) electron, $p$ ($p'$) the four-momentum of the target (recoil) proton and $q$ ($q'$) the four-momentum of the incoming virtual (outgoing real) photon.

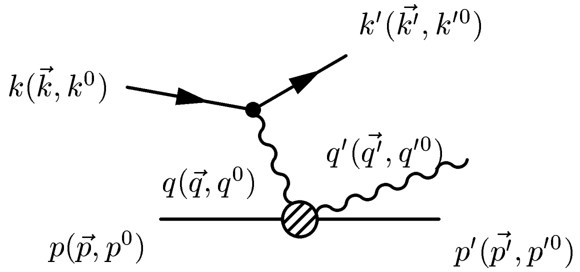

*Figure 1-5: Schematic for photon electro-production off the proton.*

As described in [21], the VCS process at threshold can be pictured as the electron scattering off a proton that is placed in the electromagnetic field of the final (real) photon. Since the energy of this final photon is small, one can consider the applied field $\vec{A}^{ext}$ to be constant in time and space.

Under the influence of this quasi-constant electromagnetic field, the charge and current distributions $J^0$ and $\vec{J}$ inside the proton will be modified. Since the field is weak, these modifications will vary linearly with this field and the proportionality constants are the "famous" generalized polarizabilities. From a general point of view, one will need a tensor of polarizabilities $P^{\mu\nu}$ in order to describe how the system rearranges its internal structure as an answer to the applied field. The current density will be modified with [21]:

$$\delta J^{\mu}(x) = \int d^4y P^{\mu\nu}(x, y) A_{\nu}^{ext}(y) \tag{1-17}$$

Measuring $\delta J^{\mu}(x)$, will give us means to quantify this polarizability tensor.

Here one can see how VCS is complementary to electron scattering on a free target (no external field) : in the same way that electron scattering yields form factors that are the Fourier transform of current $J^\mu(x)$ and charge $J^0$ distributions, VCS will give access to the Fourier transform of $\delta J^\mu(x)$, i.e. the modification of this current distribution under the influence of an electromagnetic field perturbation.

At this point, also the link between RCS and VCS can be made clearer. Since the virtuality of the interacting particle in RCS is not existent, one only has access to the Fourier transform of $\delta J^\mu(x)$ along the real photon line $q^0 = \mathsf{q}$ ($Q^2 = 0\ (GeV/c)^2$). Only the transverse component of $\delta J^\mu(x)$ plays a role, giving access to the well known electric ($\bar{\alpha}_E$) and magnetic ($\bar{\beta}_M$) polarizabilities. In the case of VCS, the interaction is generated by a virtual photon ($q^0$ and $\mathsf{q}$ can be varied independently) providing another channel of observation, namely $Q^2$. Moreover, VCS gives in addition access to the longitudinal components of $\delta J^\mu(x)$ and thus to a much greater variety of structure information.

Up to now, one has pretended that $\delta J^\mu(x)$ only contains the reaction of the internal degrees of freedom of the proton. However, $\delta J^\mu(x)$ also contains a trivial and dominant part that characterizes the global response of the proton to the applied electromagnetic field : due to its charge, the proton moves as a whole under the influence of the electric field and the magnetic field causes a precession of the magnetic moment. Since one is only interested in the response of the internal structure, one needs to subtract this global response of the proton. At low energies, the response is dominated by the global motion of the proton in the external field. This is the origin of the low Energy Theorem (LET) for VCS [22]. To calculate this global motion, one only needs to know the mass, charge and magnetic moment of the proton. Once the motion is characterized, one has to calculate the amplitude for electron scattering on this moving proton. This can be done, since one knows the proton elastic form factors.

### 1.5.2 Electron scattering in an external field

To elaborate the above considerations in a more quantitative way, the approach from reference [21] will be summarized in this section. For a more detailed explanation, this reference can be consulted.

The general expression to the order $e^2$ for the total current in the presence of an external field is given by :

$$J^\mu = ej^\mu + e^2 S^{\mu\nu} A_\nu^{ext} \tag{1-18}$$

with $j^\mu$ the hadronic current and $S^{\mu\nu}$ the contact (or Seagull) term which only has space components because of the Hamiltonian formulation.

To evaluate the effect of $A^{ext}$ on the proton states, perturbation theory is used. The effective Hamiltonian is given by :

$$H = H_s + V \tag{1-19}$$

with $H_s$ the strong interaction Hamiltonian and V the perturbation given by :

$$V = e \int d\vec{x}\; j^{\mu} A_{\mu}^{ext} \tag{1-20}$$

The Schrödinger equation can be written as :

$$i\frac{\partial}{\partial t}|t >= (H_s + V)|t > \tag{1-21}$$

with $j^{\mu}$ not depending on time.

When considering low energy photons, one knows that the proton essentially sees a constant electric and magnetic field $(\vec{E}, \vec{B})$. In this limit, the perturbation $V$ is time independent. The intrinsic induced current is defined as :

$$\begin{aligned} \delta J^{\mu}_{int}(\vec{r}) &= e^2 < N_f|S^{\mu\nu}(\vec{r})A_{\nu}^{ext}(\vec{r})|N_i > \\ &+ e^2 \sum_{n\neq N} \left( \frac{< N_f|V|n >< n|j^{\mu}(\vec{r})|N_i >}{E_f - E_n} + \frac{< N_f|j^{\mu}(\vec{r})|n >< n|V|N_i >}{E_i - E_n} \right) \end{aligned} \tag{1-22}$$

It contains a complete set of intermediate states $|n >$ (energy $E_n$) between $V$ and $j^{\mu}$, except the state corresponding to the proton itself, because this state leads to a singularity which is the quantum manifestation of the global motion of the proton. $E_i$ $(E_f)$ is the energy of initial (final) state $|N_i >$ $(|N_f >)$.

Let's now consider the effect of a constant electric and a constant magnetic field on a proton, neglecting recoil effects $(E_i = E_f = m_p)$. The gauge potential corresponding to a constant electric field is :

$$A^0_{ext} = -\vec{r}.\vec{E}, \qquad \vec{A}_{ext} = 0 \tag{1-23}$$

Using (1-20) and remembering that the Seagull term has no time dependent component, (1-22) becomes :

$$\delta J^{\mu}_{int,E}(\vec{r}) = e^2 \sum_{n\neq N} \left( \frac{< N_f|\vec{d}\vec{E}|n >< n|j^{\mu}(\vec{r})|N_i >}{E_n - m} + complex\ conjugate \right) \tag{1-24}$$

where the dipole moment operator $\vec{d}$ is defined as

$$\vec{d} = \int d\vec{r}\; \vec{r}\; j^0(\vec{r}) \tag{1-25}$$

For a constant magnetic field, the gauge field is :

$$A^0_{ext} = 0, \qquad \vec{A}_{ext} = -\frac{1}{2}\vec{r} \times \vec{B} \tag{1-26}$$

which yields for (1-22) :

$$\begin{aligned} \delta J^{\mu}_{int,B}(\vec{r}) &= \frac{e^2}{2} < N_f | S^{\mu i}(\vec{r}) \epsilon_{ijk} r^j | N_i > B^k \\ &+ e^2 \sum_{n \neq N} \left( \frac{< N_f | \vec{\mu}\vec{B} | n >< n | j^{\mu}(\vec{r}) | N_i >}{E_n - m} + complex\ conjugate \right) \end{aligned} \tag{1-27}$$

with the magnetic dipole operator defined as

$$\vec{\mu} = \frac{1}{2} \int d\vec{r}\, \vec{r} \; \times \; \vec{j}(\vec{r}) \tag{1-28}$$

If one is able to eliminate the global motion of the proton, a VCS experiment below the pion production threshold will allow to measure the Fourier transform of the induced currents (1-24) and (1-27). From equations (1-24) and (1-27), the induced dipole moments can be calculated :

$$\delta\vec{d} \;\; = \int d\vec{r}\, \vec{r}\, \delta J^0_{int,E} \;\; = \bar{\alpha}_E \vec{E} \tag{1-29}$$

$$\delta\vec{\mu} \;\; = \tfrac{1}{2} \int d\vec{r}\, \vec{r} \times \vec{J} \;\; = \underbrace{(\bar{\beta}_{para} + \bar{\beta}_{dia})}_{\beta_M} \vec{B} \tag{1-30}$$

After averaging over the proton spin projection ($\sigma$), the electric and magnetic polarizabilities are obtained :

$$\bar{\alpha}_E = \frac{e^2}{3} \sum_{n \neq N, \sigma, \sigma'} \frac{| < N, \sigma | \vec{d} | n, \sigma' > |^2}{E_n - m} > 0 \tag{1-31}$$

$$\bar{\beta}_{para} = \frac{e^2}{3} \sum_{n \neq N, \sigma, \sigma'} \frac{| < N, \sigma | \vec{\mu} | n, \sigma' > |^2}{E_n - m} > 0 \tag{1-32}$$

$$\bar{\beta}_{dia} = -\frac{e^2}{6} \sum_{\sigma} < N, \sigma | \int d\vec{r}\, r^2\, j^0(\vec{r}) | N, \sigma' > < 0 \tag{1-33}$$

These formulas show that the polarizabilities $\bar{\alpha}_E$ and $\bar{\beta}_M$ are sensitive to the complete excited spectrum of the proton, but because of the threshold condition the excited states only contribute virtually, they can not decay and therefore have no width. Note that the polarizabilities are given in Heaviside-Lorentz units.

### 1.5.3 Notation and kinematics of the reaction $e + p \rightarrow e' + p' + \gamma$

In the reaction of the photon electro-production off the proton $e + p \rightarrow e' + p' + \gamma$, 6 particles are involved : the incoming electron ($e$), the outgoing electron ($e'$), the virtual photon ($\gamma^*$), the real photon ($\gamma$), the target proton ($p$) and the recoil proton ($p'$). Table 1-2 summarizes the notations for the variables associated with these particles.

| | $e$ | $e'$ | $\gamma^*$ | $p$ | $p'$ | $\gamma$ |
|---|---|---|---|---|---|---|
| four-momentum | $k$ | $k'$ | $q = k - k'$ | $p$ | $p'$ | $q'$ |
| (rest mass)$^2$ | $m_e^2$ | $m_e^2$ | $q^2 < 0$ | $m_p^2$ | $m_p^2$ | 0 |
| energy | $k^0$ | $k'^0$ | $q^0 = k^0 - k'^0$ | $p^0$ | $p'^0$ | $q'^0$ |
| momentum | $\vec{k}$ | $\vec{k'}$ | $\vec{q} = \vec{k} - \vec{k'}$ | $\vec{p}$ | $\vec{p'}$ | $\vec{q'}$ |
| modulus of momentum | k | k’ | q=$\lvert\vec{k} - \vec{k'}\rvert$ | p | p’ | q’ |
| helicity and spin projection | $h$ | $h' = h$ | $\lambda$ | $\sigma$ | $\sigma'$ | $\lambda'$ |

Table 1-2: *Notation of variables associated with the photon electro-production process off the proton.*

The electron helicity is conserved because the electron mass can be neglected with respect to its energy. Since one is interested in VCS below the pion production threshold it is natural from the theoretical point of view to work in the center of mass ($cm$) frame defined by $\vec{p}_{cm} + \vec{q}_{cm} = \vec{p'}_{cm} + \vec{q'}_{cm} = 0$, but from the experimental point of view the laboratory frame is preferred. In the following, variables in the laboratory frame will have the index $lab$, the variables in the center of mass frame will have the index $cm$.

In order to be able to describe the reaction $e + p \rightarrow e' + p' + \gamma$ where no polarisations are detected, 5 variables are needed [23]. The first set of 3 measurable variables describes the leptonic part of the interaction : $(\mathsf{k}_{lab}, \mathsf{k}'_{lab}, \theta^e_{lab})$ where $\theta^e_{lab}$ is the scattering angle of the electron. There exists a complete bijection between this set of $lab$ variables, a set of $cm$ variables ($\mathsf{q}_{cm}$, $\mathsf{q}'_{cm}$, $\epsilon$) and a set of invariant variables $(Q^2, s, \epsilon)$ where $\epsilon$ is the linear polarisation rate of the virtual photon, $Q^2$ the opposite of the virtual photon invariant mass squared and $s$ the total energy squared of the $cm$ system $\gamma^* p$. The relations between these sets are given by :

$$Q^2 = 4\mathsf{k}_{lab}\mathsf{k}'_{lab} sin^2(\frac{\theta^e_{lab}}{2}) \qquad (1\text{-}34)$$

$$s = -Q^2 + m_p^2 + 2m_p q^0_{lab} \tag{1-35}$$

$$\epsilon = \frac{1}{1 + 2\frac{\mathsf{q}^2{}_{lab}}{Q^2} tan^2(\frac{\theta^e_{lab}}{2})} \tag{1-36}$$

$$\mathsf{q}^2{}_{cm} = Q^2 + \frac{(s - Q^2 - m_p^2)^2}{4s} \tag{1-37}$$

$$\mathsf{q}'{}_{cm} = \frac{s - m_p^2}{2\sqrt{s}} \tag{1-38}$$

The variables $Q^2$ and $s$ allow to calculate all energies and momenta of the photons and protons in the *cm* system. They are tabulated in table 1-3.

| particle | energy | momentum |
|---|---|---|
| $\gamma^*$ | $q^0_{cm} = \frac{s-Q^2-m_p^2}{2\sqrt{s}}$ | $\mathsf{q}_{cm} = \sqrt{Q^2 + q^{0^2}_{cm}}$ |
| $\gamma$ | $q'^0_{cm} = \frac{s-m_p^2}{2\sqrt{s}}$ | $\mathsf{q}'{}_{cm} = q'^0_{cm}$ |
| $p$ | $p^0_{cm} = \frac{s+Q^2+m_p^2}{2\sqrt{s}}$ | $\mathsf{p}_{cm} = \mathsf{q}_{cm}$ |
| $p'$ | $p'^0_{cm} = \frac{s+m_p^2}{2\sqrt{s}}$ | $\mathsf{p}'{}_{cm} = \mathsf{q}'{}_{cm}$ |

Table 1-3: *Energies and momenta of the photons and protons of the VCS interaction in the cm system.*

Besides the 3 variables describing the leptonic part of the interaction, two other variables are used in the analysis of the VCS reaction. These variables define the hadronic arm. They are $\theta^{\gamma^*\gamma}_{cm}$, the polar angle between the incoming virtual and the outgoing real photon and $\varphi$, the angle between the leptonic and hadronic plane. This last one is the same in the *cm* and in the *lab* system. In figure 1-6 the leptonic and hadronic planes and the VCS kinematics in the laboratory frame are shown.

The Lorentz transformation that characterizes the relation between the *cm* and the *lab* frame is given by :

$$\vec{\beta} = \frac{\vec{p}_{tot}}{E_{tot}} = \frac{\vec{q}_{lab}}{q^0_{lab} + m_p} \tag{1-39}$$

$$\gamma = \frac{1}{\sqrt{1-\beta^2}} = \frac{E_{tot}}{\sqrt{s}} = \frac{q^0_{lab} + m_p}{\sqrt{s}} \tag{1-40}$$

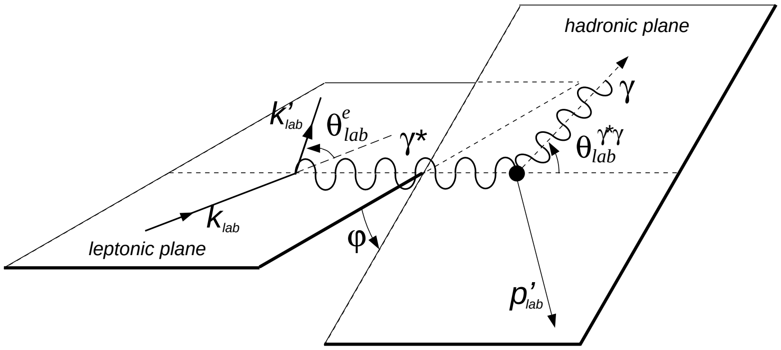

*Figure 1-6: VCS kinematics in the laboratory frame.*

Due to this Lorentz boost from *cm* to *lab*, the outgoing proton momentum is focused in a small cone around the virtual photon direction, while the outgoing real photon can be emitted in all directions. This is drawn in figure 1-7. As can be seen, the momentum vector of the recoil proton describes the surface of an ellipsoid. The value of $\vec{p'}_{lab}$ is linked to the value of $\theta_{cm}^{\gamma^*\gamma}$ : $\mathsf{p}'_{\mathsf{lab}}$ reaches a minimum/maximum for $\theta_{cm}^{\gamma^*\gamma} = 0°/180°$. The angle between $\vec{p'}_{lab}$ and $\vec{q}_{lab}$ can be calculated as :

$$tg\theta_{lab}^{\gamma^*p'} = \frac{sin\theta_{cm}^{\gamma^*p'}}{\beta\gamma\frac{p'^{0}_{cm}}{\mathsf{p}'_{\mathsf{cm}}} + \gamma cos\theta_{cm}^{\gamma^*p'}} \tag{1-41}$$

This angle reaches a maximum for :

$$cos\theta_{cm}^{\gamma^*p'} = \frac{-\mathsf{p}'_{cm}}{\beta p'^{0}_{cm}} \tag{1-42}$$

It is clear that the higher $Q^2$, the smaller this maximum, and hence the stronger the focusing of the outgoing proton momentum around the virtual photon direction.

The reference $\varphi = 0°$ is defined when the real photon is present in the leptonic half-plane defined by $\vec{k}_{lab}$ and $\vec{k'}_{lab}$.

The energy of the recoil proton in the *lab* and $\theta_{cm}^{\gamma^*\gamma}$ are linked together following [4] :

$$p'^{0}_{lab} = \frac{(q^0_{lab} + m_p)(s + m_p^2)}{2s} - \frac{q_{lab}}{2s}(s + m_p^2)cos\theta_{cm}^{\gamma^*\gamma} \tag{1-43}$$

consequently, if one measures the momentum of the recoil proton and one knows the variables of the leptonic arm $(q^0_{lab}, s, q_{lab})$, one is able to calculate $cos\theta_{cm}^{\gamma^*\gamma}$.

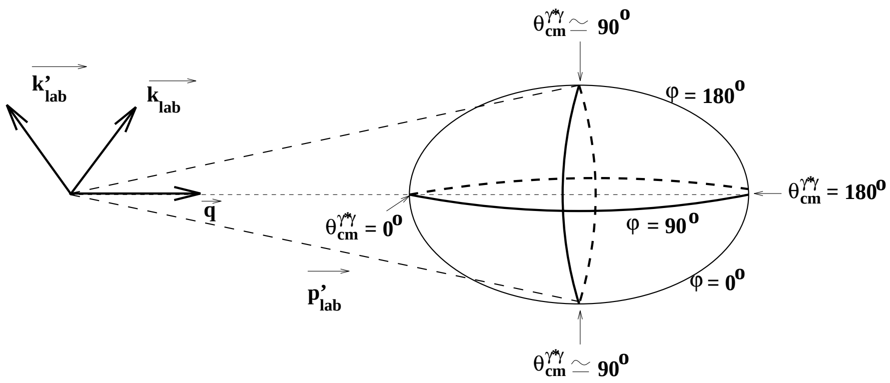

*Figure 1-7: Phase space of the proton around the virtual photon direction due to the Lorentz cm to lab boost.*

To conclude : the kinematics of the reaction is completely described by one of the following, equivalent sets of variables :

$$\begin{pmatrix} \mathsf{k}_{lab} \\ \mathsf{k'}_{lab} \\ \theta^e_{lab} \\ p'_{lab} \\ \varphi \end{pmatrix} \leftrightarrow \begin{pmatrix} Q^2 \\ s \\ \epsilon \\ \theta_{cm}^{\gamma^*\gamma} \\ \varphi \end{pmatrix} \leftrightarrow \begin{pmatrix} \mathsf{q}_{cm} \\ \mathsf{q'}_{cm} \\ \epsilon \\ \theta_{cm}^{\gamma^*\gamma} \\ \varphi \end{pmatrix} \tag{1-44}$$

Measuring the scattered electron and the recoil proton in the *lab* is sufficient to characterize completely the kinematics of photon electro-production off the proton.

### 1.5.4 VCS cross section and amplitudes

In subsection 1.5.1, the photon electro-production is considered as shown in figure 1-5. But one has to be careful. In reality, the photon electro-production below the pion production threshold covers two different processes : the final (real) photon can be emitted either by the (incoming/outgoing) electron, or by the proton. The first process is described by the Bethe-Heitler (BH) amplitude which is calculable in QED. The second process is described by the Full Virtual Compton Scattering (FVCS) amplitude. In the one photon exchange approximation, the latter is a linear combination of VCS amplitudes. Note that FVCS includes the leptonic part of the interaction. In experiments, it is impossible to know whether the real photon is emitted by the electron or the proton. Thus it is necessary to consider all three diagrams in figure 1-8.

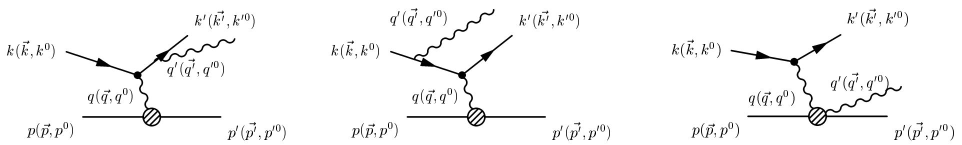

(a) BH (b) BH (c) FVCS

*Figure 1-8: Bethe-Heitler (BH) and Full Virtual Compton Scattering (FVCS) amplitudes.*

In the following one considers the unpolarised case of VCS in the kinematic regime defined by a center of mass energy ($\sqrt{s}$) of the final photon-proton system below the pion production threshold : $m_p c^2 < \sqrt{s} < (m_p + m_{\pi^0})c^2$ (with $m_p$ and $m_{\pi^0}$ the rest mass of the proton and the pion, respectively). This considerably simplifies the description of the process since the intermediate resonances of the proton can not decay. The only possible final state is the proton-photon(s) system. Experimentally the scattered electron and recoil proton are detected in coincidence. The pion production and real photon production are distinguished by checking the invariant missing mass squared $M_X^2 = (k+p-k'-p')^2$. In the case of a radiated real photon, this missing mass squared is $(0 \text{ MeV/c}^2)^2$, in the case of pion production it is about $(135 \text{ MeV/c}^2)^2$.

The main aspects of the formalism established by P.A.M. Guichon et al. [24] in order to define the Generalized Polarizabilities (GPs) will be briefly discussed here.

In the laboratory frame, the non polarised photon electro-production cross section corresponding to all three graphs in figure 1-8 is given by :

$$\frac{d^5\sigma}{d\mathsf{k'}_{lab} d\Omega_{k'_{lab}} d\Omega_{p'_{cm}}} = \frac{(2\pi)^{-5}}{64 m_p} \left(\frac{\mathsf{k'}_{lab}}{\mathsf{k}_{lab}}\right) \frac{s - m_p^2}{s} \mathcal{M} = \frac{(2\pi)^{-5}}{64 m_p} \left(\frac{\mathsf{k'}_{lab}}{\mathsf{k}_{lab}}\right) \frac{2\mathsf{q'}_{cm}}{\sqrt{s}} \mathcal{M} \tag{1-45}$$

with $\mathcal{M}$ the Lorentz invariant probability for interaction. In this thesis, this five fold differential cross section will be denoted as $\frac{d\sigma}{d\Omega}$. Since one considers an unpolarised experiment, one has to take into account all possible spin-states of initial and final particles. This yields for $\mathcal{M}$ the following expression :

$$\mathcal{M} = \frac{1}{4} \sum_{\sigma\sigma' h' \lambda'} \left| T^{ee'\gamma} \right|^2 \tag{1-46}$$

with $T^{ee'\gamma}$ the amplitude for the interaction ($ep \rightarrow ep\gamma$). As already pointed out, the photon electro-production process covers two different processes (see figure 1-8) that are experimentally indistinguishable : the Bethe-Heitler process with amplitude $T^{BH}$ and the FVCS process with amplitude $T^{FVCS}$. The measured cross section for photon electro-production contains the coherent sum of these two processes :

$$T^{ee'\gamma} = T^{BH} + T^{FVCS} \tag{1-47}$$

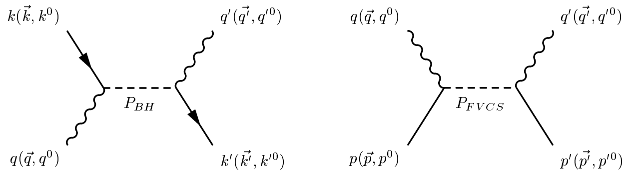

(a) BH

(b) FVCS

*Figure 1-9: Bethe-Heitler (BH) and Full Virtual Compton Scattering (FVCS) propagators.*

In the one photon exchange approximation the propagators for these two amplitudes are shown in figure 1-9. For the BH amplitude with the outgoing electron radiating the photon, this propagator can be written as :

$$P_{BH} = \frac{1}{(k' + q')^2 - m_e^2} = \frac{1}{2k'q'} \tag{1-48}$$

When the photon is emitted by the incoming electron, the propagator is expressed in an analogue way. It is clear that the BH amplitude will have a singularity when developing in powers of $\mathsf{q}'_{cm}$. This amplitude can be written as :

$$T^{BH} = \frac{a_{-1}^{BH}}{\mathsf{q}'_{cm}} + a_0^{BH} + a_1^{BH} \mathsf{q}'_{cm} + \mathcal{O}(\mathsf{q}'^2_{cm}) \tag{1-49}$$

Since one considers the kinematics below the pion production threshold, the only possible intermediate on mass shell state for FVCS is the proton. Thus the propagator can be written as :

$$P_{FVCS} = \frac{1}{(p' + q')^2 - m_p^2} = \frac{1}{2p'q'} \tag{1-50}$$

Also here, a development in powers of $\mathsf{q}'_{cm}$ of the amplitude will show a singularity in $\mathsf{q}'_{cm}$.

In the one photon exchange approximation, the FVCS amplitude can be written as a linear combination of VCS amplitudes :

$$T^{FVCS} = \frac{-e^3}{Q^2} \sum_{\lambda} \Omega(h,\lambda) T^{VCS}(\lambda',\lambda) \tag{1-51}$$

with $\Omega(h,\lambda)$ the lepton current. This decoupling of the lepton current allows to take the limit $Q^2 \to 0$ for $T^{VCS}$. In this limit, the transverse part of $T^{VCS}$ $(\lambda = \pm 1)$ coincides (up to a factor $e^2$) with the RCS amplitude. Hence it will be possible to define observables describing $T^{VCS}$ in such a way that, in this limit, they correspond to the polarizabilities encountered in RCS.

One chooses to decompose the hadronic tensor $T^{VCS}$ in two gauge invariant terms :

$$T^{VCS} = T^{Born} + T^{NonBorn} \tag{1-52}$$

The Born (denoted as $B$ in what follows) amplitude represents the process where the photon is emitted by the proton. This term is divergent in the limit $\mathsf{q}'_{cm} = 0$. Thus it can developed as follows :

$$T^{B} = \frac{a^{B}_{-1}}{\mathsf{q}'_{cm}} + a^{B}_{0} + a^{B}_{1}\mathsf{q}'_{cm} + \mathcal{O}(\mathsf{q}'^{2}_{cm}) \tag{1-53}$$

The NonBorn (denoted as $NB$ in what follows) amplitude describes the process where the photon is emitted by the proton intermediate states. This amplitude is proton structure dependent and can be parametrized by generalized polarizabilities. According to the low energy theorem for VCS [24], which is an extension of the low energy theorem for RCS [7], this amplitude is at least linear in $\mathsf{q}'_{cm}$. The development of this amplitude in powers of $\mathsf{q}'_{cm}$ becomes :

$$T^{NB} = a^{NB}_{1}\mathsf{q}'_{cm} + \mathcal{O}(\mathsf{q}'^{2}_{cm}) \tag{1-54}$$

The above considerations imply that the photon electro-production amplitude can be written as :

$$\begin{aligned} T^{ee'\gamma} &= T^{BH} + T^{B} + T^{NB} \\ &= \frac{a^{BH}_{-1} + a^{B}_{-1}}{\mathsf{q}'_{cm}} + (a^{BH}_{0} + a^{B}_{0}) + ((a^{BH}_{1} + a^{B}_{1}) + a^{NB}_{1})\mathsf{q}'_{cm} + \mathcal{O}(\mathsf{q}'^{2}_{cm}) \\ &= \frac{a_{-1}}{\mathsf{q}'_{cm}} + a_0 + (a_1 + a^{NB}_{1})\mathsf{q}'_{cm} + \mathcal{O}(\mathsf{q}'^{2}_{cm}) \end{aligned} \tag{1-55}$$

The interesting feature of this separation in BH, Born and NonBorm terms of the amplitude $T^{ee'\gamma}$ is that the BH and Born terms are completely calculable in QED once the proton form factors are known. In figure 1-10 a numerical calculation of the BH+Born cross section as a function of $\theta_{cm}^{\gamma^*\gamma}$ is shown, the kinematical variables $\mathsf{q}_{cm}$, $\epsilon$ and $\varphi$ are kept at fixed values corresponding to TJNAF kinematics of $Q^2 = 1.0(GeV/c)^2$. The used proton elastic form factors are as explained in section 1.2.3. As a convention one defines $\theta_{cm}^{\gamma^*\gamma}$ to be negative and $\varphi = 0°$ when in fact $\varphi = 180°$. In this figure one sees that the BH amplitude is very high near the angles that match the directions of the incoming and scattered electron, the "cat ears". The information on the internal structure of the proton in which one is interested and which is present in the NonBorn term will show up as a deviation from the BH+Born curve. It is clear that the regions in which one is interested are the backward angles, away from region of the two cat ears where the relative contribution of BH to the cross section is extremely high. Equation (1-55) combined with (1-45) learns that the five fold differential cross section for photon electro-production leads to a singularity for $\mathsf{q}'_{cm} \to 0$. This divergence associated with the emission of a soft photon is known as the "infrared divergence" and is discussed in [23, 25].

The coefficients $a$ of the amplitude $T^{ee'\gamma}$ are functions of the other 4 variables of the kinematics of photon electro-production off the proton $(\mathsf{q}_{cm}, \epsilon, \theta_{cm}^{\gamma^*\gamma}, \varphi)$.

The Low energy theorem [22] learns that at $\mathsf{q}'_{cm} \to 0$ and fixed $\mathsf{q}_{cm}$, the coefficients $a_{-1}$ and $a_0$ in (1-55) are completely determined by the global properties of the proton (charge, mass, anomalous magnetic moment) and the elastic form factors. The first apparition of the excited proton states is in the third term that consists of a known part $a_1$ and a non-trivial part $a_1^{NB}$ that hides new information on the internal proton structure. It is this part that will be parametrized by 6 generalized polarizabilities.

### 1.5.5 Generalized polarizabilities

P.A.M. Guichon et al. [24] have derived the generalized polarizabilities from an analysis of $T^{NB}$ in terms of reduced electromagnetic multi-poles $H_{NB}^{(\rho' L', \rho L)S}(\mathsf{q}'_{cm}, \mathsf{q}_{cm})$, where $\rho$ ($\rho'$) indicates the type of the initial (final) photon ($\rho = 0$ : longitudinal or charge, C ; $\rho = 1$ : magnetic, M; $\rho = 2$ : electric, E); the initial (final) orbital angular moment is denoted by $L$ ($L'$) and the quantum number $S$ characterizes the non-spin-flip ($S = 0$) and spin-flip ($S = 1$) transitions. The multi-poles characterize the electromagnetic transitions of the proton.

Conservation of parity and angular momentum leads to the following selection

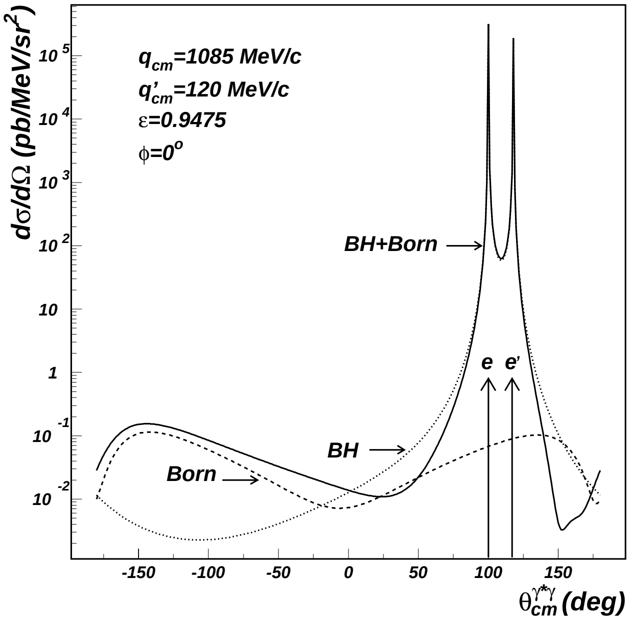

*Figure 1-10: Born, BH and BH+Born contributions to the* $e + p \to e' + p' + \gamma$ *differential cross section as a function of* $\theta_{cm}^{\gamma^*\gamma}$ *in TJNAF kinematics.* $\mathsf{q}_{\mathsf{cm}}, \mathsf{q}'_{\mathsf{cm}}, \epsilon$ *and* $\varphi$ *are fixed, the incident and scattered electron directions are indicated with arrows.*

rules :

$$\begin{aligned} (-1)^{\rho'+L'} &= (-1)^{\rho+L} && (\rho', \rho = 0, 1, 2) \\ |L'-S| \leq L &\leq |L'+S| && (S = 0, 1) \end{aligned} \qquad (1\text{-}56)$$

Since the outgoing photon is real, it can only be transverse which cancels the possibility $\rho' = 0$. If one restricts himselve to the lowest order of the NonBorn term in the amplitude (i.e. linear terms in $\mathsf{q}'_{cm}$), only the electric and magnetic dipole radiation in the final state contribute to the amplitude. In that case $L' = 1$. This is called the dipole approximation.

The above considerations show that 10 multi-poles will be necessary to describe $T^{NB}$ at low energies. They are summarized in the 6th column of table 1-4.

| $\rho'$ | $\rho$ | $L$ | $S$ | transition $(\gamma, \gamma^*)$ | $H_{NB}^{(\rho' L', \rho L)S}$ | GP |
|---|---|---|---|---|---|---|
| 1 | 0 | 0,2 | 1 | $(M1, L0)$,$(M1, L2)$ | $H_{NB}^{(11,00)1}$,$H_{NB}^{(11,02)1}$ | $P^{(11,00)1}$,$P^{(11,02)1}$ |
|  | 2 | 2 | 1 | $(M1, E1)$ | $H_{NB}^{(11,22)1}$ | $\hat{P}^{(11,2)1}$ |
|  | 1 | 1 | 0,1 | $(M1, M1)$ | $H_{NB}^{(11,11)0}$,$H_{NB}^{(11,11)1}$ | $P^{(11,11)0}$,$P^{(11,11)1}$ |
| 2 | 0 | 1 | 0,1 | $(E1, L1)$ | $H_{NB}^{(21,01)0}$,$H_{NB}^{(21,01)1}$ | $P^{(01,01)0}$,$P^{(01,01)1}$ |
|  | 2 | 1 | 0,1 | $(E1, E1)$ | $H_{NB}^{(21,21)0}$,$H_{NB}^{(21,21)1}$ | $\hat{P}^{(01,1)0}$,$\hat{P}^{(01,1)1}$ |
|  | 1 | 2 | 1 | $(E1, M2)$ | $H_{NB}^{(21,12)1}$ | $P^{(01,12)1}$ |

Table 1-4: *Allowed quantum numbers, electromagnetic multi-poles and corresponding generalized polarizabilities in the development of* $T^{NB}$ *to order* $\mathsf{q}'_{cm}$.

For the definition of the generalized polarizabilities it is necessary to know the low energy behaviour of the multi-poles when $(\mathsf{q}_{cm}, \mathsf{q}'_{cm}) \rightarrow (0, 0)$. One could think of defining 10 polarizabilities that correspond to the limits of the multi-poles at $\mathsf{q}_{cm} = 0$. But as one wants to relate some of the generalized polarizabilities to the polarizabilities defined in RCS, one has to be sure that the transition of the virtual photon does not depend on the path along which the origin in the $(\mathsf{q}_{cm}, \mathsf{q}'_{cm})$-plane is approached. This is not obvious as can be seen from figure 1-11. Here the paths in the $(\mathsf{q}_{cm}, \mathsf{q}'_{cm})$-plane to approach the zero energy point for RCS and VCS are drawn. In the *cm*, RCS always approaches this point via $(\mathsf{q}_{cm} = \mathsf{q}'_{cm} \rightarrow 0)$, while VCS approaches the limit $\mathsf{q}'_{cm} \rightarrow 0$ with arbitrary fixed $\mathsf{q}_{cm}$. For the Coulomb $(\rho, \rho' = 0)$ and magnetic $(\rho, \rho' = 1)$ transitions there is no problem [24]. But for the electric $(\rho, \rho' = 2)$ transitions it is suitable to replace them. Siegert's theorem [26]

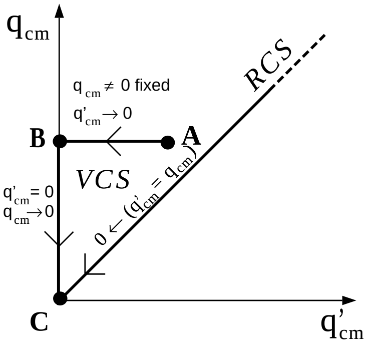

*Figure 1-11: Behaviour of RCS and VCS when approaching the limit ($\mathsf{q}_{cm}$, $\mathsf{q}'_{cm}$)=($0$,$0$).*

implies that electric transitions of the outgoing photon ($\rho' = 2$) can be expressed in terms of the charge transitions ($\rho' = 0$). Thus the only annoying case left is $\rho = 2$. Studying this has lead to so-called mixed multi-poles $\hat{H}_{NB}^{(\rho' L', L)S}(\mathsf{q}_{cm}, \mathsf{q}'_{cm})$. They are no longer characterized by a well-defined multi-pole type of the incoming photon but they describe a well defined mixture of an electric and a charge transition in the initial state.

The above considerations have lead to the following definition of the generalized polarizabilities :

$$P^{(\rho' L', \rho L)S}(\mathsf{q}_{cm}) = \left[ \frac{1}{\mathsf{q}'^{L'}_{cm} \mathsf{q}^{L}_{cm}} H_{NB}^{(\rho' L', \rho L)S}(\mathsf{q}'_{cm}, \mathsf{q}_{cm}) \right]_{\mathsf{q}'_{cm}=0} \qquad (\rho, \rho' = 0, 1) \quad (1\text{-}57)$$

$$\hat{P}^{(\rho' L', L)S}(\mathsf{q}_{cm}) = \left[ \frac{1}{\mathsf{q}'^{L'}_{cm} \mathsf{q}^{L+1}_{cm}} \hat{H}_{NB}^{(\rho' L', L)S}(\mathsf{q}'_{cm}, \mathsf{q}_{cm}) \right]_{\mathsf{q}'_{cm}=0} \qquad (\rho' = 0, 1) \quad (1\text{-}58)$$

They are tabulated in the last column of table 1-4. More details on the low energy behaviour of the multi-poles and of the generalized polarizabilities can be found in [24]. Recently has been proven [27] that, using crossing symmetry and charge conjugation invariance, four constraining relations exist so that only six of the ten GPs defined before are independent. The choice of them is arbitrary. A convenient choice, used in the following is $P^{(01,01)0}, P^{(01,01)1}, P^{(11,11)0}, P^{(11,11)1}, P^{(01,12)1}$ and $P^{(11,02)1}$.

Some of the GPs are related to the electromagnetic polarizabilities that are found in the low energy expansion of the RCS amplitude. The scalar ($S = 0$) polarizabilities $P^{(01,01)0}(\mathsf{q}_{\mathsf{cm}})$ and $P^{(11,11)0}(\mathsf{q}_{\mathsf{cm}})$ generalize $\bar{\alpha}_E$ and $\bar{\beta}_M$ to the case of virtual photons :

$$P^{(01,01)0}(0) = -\sqrt{\frac{2}{3}}\frac{\bar{\alpha}_E}{e^2} \qquad P^{(11,11)0}(0) = -\sqrt{\frac{8}{3}}\frac{\bar{\beta}_M}{e^2} \tag{1-59}$$

In this dipole approximation, two of the vector ($S = 1$) GPs are connected with the spin polarizabilities $\gamma_i$ as follows [28] :

$$P^{(01,12)1}(0) = -\frac{\gamma_3}{e^2}\frac{\sqrt{2}}{3} \qquad P^{(11,02)1}(0) = -\frac{(\gamma_2+\gamma_4)}{e^2}\frac{2\sqrt{2}}{3\sqrt{3}} \tag{1-60}$$

Moreover it was shown in [28] that :

$$P^{(01,01)1}(0) = P^{(11,11)1}(0) = 0 \tag{1-61}$$

### 1.5.6 Extraction of generalized polarizabilities from VCS cross sections

Combining equations (1-45), (1-46) and (1-55) yields for the photon electroproduction cross section :

$$\begin{aligned} d^5\sigma^{exp} &= \phi \mathsf{q}'_{cm}\{ \underbrace{a_{-1}^2}_{\mathcal{M}_{-2}^{BH+B}} \mathsf{q}'^{-2}_{cm} + \underbrace{(a^*_{-1}a_0 + a_{-1}a^*_0)}_{\mathcal{M}_{-1}^{BH+B}} \mathsf{q}'^{-1}_{cm} + \underbrace{a_0^2 + (a^*_{-1}a_1 + a_{-1}a^*_1)}_{\mathcal{M}_{0}^{BH+B}} \\ &\quad + \underbrace{(a^*_{-1}a_1^{NB} + a_{-1}a_1^{*NB})}_{\mathcal{M}_0^{NB}} + \mathcal{O}(\mathsf{q}'_{cm})\} \qquad (1\text{-}62) \\ &= \phi \mathsf{q}'_{cm}(\mathcal{M}_{-2}^{exp}\mathsf{q}'^{-2}_{cm} + \mathcal{M}_{-1}^{exp}\mathsf{q}'^{-1}_{cm} + \mathcal{M}_0^{exp} + \mathcal{O}(\mathsf{q}'_{cm})) \qquad (1\text{-}63) \end{aligned}$$

where $d^5\sigma^{exp}$ is the five-fold differential experimental cross section as defined in (1-45) and $\phi$ a phase space factor. From the previous subsection one knows that the polarizabilities come into play in the NonBorn term of the amplitude. It is this term $a_1^{NB}$ that has been parametrized in terms of 6 GPs. Thus for the cross section the term containing $\mathcal{M}_0^{exp}$ reveals the effect of the polarizabilities. $\mathcal{M}_{-2}^{exp}$ and $\mathcal{M}_{-1}^{exp}$ are exactly calculable with the four kinematical variables $(\mathsf{q}_{cm}, \epsilon, \theta_{cm}^{\gamma^*\gamma}, \varphi)$ and the proton form factors. Considering equations (1-62) and (1-63) one sees that the contribution of the polarizabilities will be measured experimentally, using the Low Energy Expansion (LEX) :

$$\mathcal{M}_0^{NB} = \mathcal{M}_0^{exp} - \mathcal{M}_0^{BH+B} = \left[\mathcal{M}^{exp} - \mathcal{M}^{BH+B}\right]_{\mathsf{q}'_{cm}=0} \tag{1-64}$$

Defining the completely calculable cross section :

$$\begin{aligned} d^5\sigma^{BH+B} &= \phi \mathsf{q}'_{cm}\ \mathcal{M}^{BH+B} \\ &= \phi \mathsf{q}'_{cm}(\mathcal{M}^{BH+B}_{-2}\mathsf{q}'^{-2}_{cm} + \mathcal{M}^{BH+B}_{-1}\mathsf{q}'^{-1}_{cm} + \mathcal{M}^{BH+B}_{0} + \mathcal{O}(\mathsf{q}'_{cm})) \end{aligned} \tag{1-65}$$

yields for the experimental five fold differential photon electro-production cross section :

$$d^5\sigma^{exp} = d^5\sigma^{BH+B} + \phi \mathsf{q}'_{cm}((\mathcal{M}^{exp}_0 - \mathcal{M}^{BH+B}_0)) + \mathcal{O}(\mathsf{q}'^2_{cm}) \tag{1-66}$$

This formula is the basis for filtering GPs out of the experimental data. This analysis is done in three steps :

First one has to be sure that the LET (Low Energy Theorem) is verified. This implies validating :

$$\lim_{\mathsf{q}'_{cm}\to 0} d^5\sigma^{exp}(\mathsf{q}'_{cm}) = d^5\sigma^{BH+B}(\mathsf{q}'_{cm}) \tag{1-67}$$

This justifies the analysis method and also tests the radiative corrections (see section 5.4) and values for the proton electric and magnetic form factors that are used to calculate $d^5\sigma^{BH+B}$.

The second step is studying the behaviour of $(d^5\sigma^{exp} - d^5\sigma^{BH+B})/\phi\mathsf{q}'_{cm}$ as a function of $\mathsf{q}'_{cm}$ and extrapolating this value to $\mathsf{q}'_{cm} = 0$. This results in knowing $\mathcal{M}^{exp}_0 - \mathcal{M}^{BH+B}_0$ which is parametrized in terms of the 6 GPs. Note that the behaviour of $(d^5\sigma^{exp} - d^5\sigma^{BH+B})/\phi\mathsf{q}'_{cm}$ as a function of $\mathsf{q}'_{cm}$ can indicate the importance of higher order terms $(\mathcal{O}(\mathsf{q}'_{cm}))$.

Finally the values for $\mathcal{M}^{exp}_0 - \mathcal{M}^{BH+B}_0$ at different kinematical settings at fixed $\mathsf{q}_{cm}$ have to be determined in order to extract information on GPs.

For a non polarised experiment, $\mathcal{M}^{exp}_0 - \mathcal{M}^{BH+B}_0$ can be expressed as a linear combination of 5 GPs [24, 21]. The coefficients of this expression are completely calculable with $(\mathsf{q}_{cm}, \epsilon, \theta^{\gamma^*\gamma}_{cm}, \varphi)$ :

$$\mathcal{M}^{exp}_0 - \mathcal{M}^{BH+B}_0 = v_{LL}(\varphi, \theta^{\gamma^*\gamma}_{cm})(\mathbf{P_{LL}}(\mathsf{q}_{cm}) - \frac{1}{\epsilon}\mathbf{P_{TT}}(\mathsf{q}_{cm})) + v_{LT}(\varphi, \theta^{\gamma^*\gamma}_{cm})\mathbf{P_{LT}}(\mathsf{q}_{cm}) \tag{1-68}$$

with

$$\begin{aligned} v_{LL}(\varphi, \theta^{\gamma^*\gamma}_{cm}) &= \epsilon K sin\theta^{\gamma^*\gamma}_{cm}(\omega'' sin\theta^{\gamma^*\gamma}_{cm} - \omega' \mathsf{k}_T cos\varphi cos\theta^{\gamma^*\gamma}_{cm}) \\ v_{LT}(\varphi, \theta^{\gamma^*\gamma}_{cm}) &= -\epsilon K\sqrt{2\epsilon(1+\epsilon)}((\omega'' sin\theta^{\gamma^*\gamma}_{cm} cos\varphi - \mathsf{k}_T \omega' cos\theta^{\gamma^*\gamma}_{cm}) \\ &\quad + \frac{\tilde{q}_0}{\mathsf{q}_{cm}}(\omega'' sin\theta^{\gamma^*\gamma}_{cm} cos\theta^{\gamma^*\gamma}_{cm} cos\varphi - \omega' \mathsf{k}_T(1 - cos^2\varphi sin^2\theta^{\gamma^*\gamma}_{cm}))) \\ K &= \frac{4m_p e^6 \mathsf{q}_{cm}}{\tilde{Q}^2(1-\epsilon)}\sqrt{\frac{2E(\mathsf{q}_{cm})}{E(\mathsf{q}_{cm}) + m_p}} \end{aligned} \tag{1-69}$$

and

$$\begin{aligned}
\tilde{Q} &= [Q]_{\mathsf{q'}_{cm}=0} & \tilde{q}_0 &= -\frac{\tilde{Q}^2}{2m_p} \\
\omega &= -\left[\mathsf{q'}_{cm}\left(\frac{1}{pq'}+\frac{1}{kq'}\right)\right]_{\mathsf{q'}_{cm}=0} & \omega' &= \left[\mathsf{q'}_{cm}\left(\frac{1}{k'q'}-\frac{1}{kq'}\right)\right]_{\mathsf{q'}_{cm}=0} \\
\mathsf{k}_T &= \tilde{Q}\sqrt{\frac{\epsilon}{2(1-\epsilon)}} & \omega'' &= \left[\omega \mathsf{q}_{cm} - \omega'\sqrt{\mathsf{k'}^2_{cm}-\mathsf{k}^2_T}\right]_{\mathsf{q'}_{cm}=0} \\
E(\mathsf{q}_{cm}) &= \sqrt{\mathsf{q}^2_{cm}+m_p^2} & \tilde{q}_0 &= -\frac{\tilde{Q}^2}{2m_p}
\end{aligned}$$

The structure functions $\mathbf{P_{LL}}(\mathsf{q}_{cm})$, $\mathbf{P_{TT}}(\mathsf{q}_{cm})$ and $\mathbf{P_{LT}}(\mathsf{q}_{cm})$ are defined as the following combinations of GPs :

$$\mathbf{P_{LL}}(\mathsf{q}_{cm}) = -2\sqrt{6}m_p G_E P^{(01,01)0}(\mathsf{q}_{cm}) \tag{1-70}$$

$$\mathbf{P_{TT}}(\mathsf{q}_{cm}) = 3G_M \mathsf{q}^2_{cm}\left(\sqrt{2}P^{(01,12)1}(\mathsf{q}_{cm}) - \frac{1}{\tilde{q}^0}P^{(11,11)1}(\mathsf{q}_{cm})\right) \tag{1-71}$$

$$\mathbf{P_{LT}}(\mathsf{q}_{cm}) = \sqrt{\frac{3}{2}}m_p\frac{\mathsf{q}_{cm}}{\tilde{Q}}G_E P^{(11,11)0}(\mathsf{q}_{cm}) + \frac{3}{2}\frac{\mathsf{q}_{cm}}{\tilde{q}_0}\tilde{Q}G_M P^{(01,01)1}(\mathsf{q}_{cm}) \tag{1-72}$$

With $G_E$ and $G_M$ the proton electromagnetic form factors.

To be able to determine experimentally the two structure functions $(\mathbf{P_{LL}}(\mathsf{q}_{cm}) - \frac{1}{\epsilon}\mathbf{P_{TT}}(\mathsf{q}_{cm}))$ and $\mathbf{P_{LT}}(\mathsf{q}_{cm})$ that are accessible in an unpolarised VCS experiment, one needs at least 2 couples of $(\varphi, \theta_{cm}^{\gamma^*\gamma})$-values at fixed values for $\mathsf{q}_{cm}$ and $\epsilon$ to separate them. Equations (1-70), (1-71) and (1-72) show that these two structure functions are the sum of a scalar and a spin dependent quantity. This last one vanishes as $Q^2 \to 0$. To separate $\mathbf{P_{LL}}(\mathsf{q}_{cm})$ and $\mathbf{P_{TT}}(\mathsf{q}_{cm})$, at least 2 values for $\epsilon$ are needed. Note that $\mathbf{P_{LL}}(\mathsf{q}_{cm})$ is of particular interest since it is proportional to $P^{(01,01)0}(\mathsf{q}_{cm})$ which is the generalization of the usual electric polarizability $\bar{\alpha}_E$. To go one step further and determine independently all 6 GPs, double polarisation experiments are needed [29, 30].

## 1.6 Theoretical Models for Polarizabilities

The first estimation of the values of generalized polarizabilities has been made by Guichon, Liu and Thomas in a Non Relativistic Constituant Quark Model (NR-CQM) [24]. This estimation guided the first generation of experiments. It is based on the assumption that baryons are composed of three massive quarks that are subject to a harmonic oscillator confining potential and additional hyperfine interactions. Later, this calculation has been extended to include recoil effects [31]. This model does not respect the fundamental symmetries such as relativistic invariance and chiral and crossing symmetry. Hence the predictive possibilities of this model are limited. Recently Pasquini, Scherer and Drechsel reviewed this model [32].

A phenomenological approach of the problem is made in the Effective Lagrangian Model (ELM) by M. Vanderhaeghen [33]. Nucleon resonance effects are included in this model. Also the polarisation of the pion cloud is taken into account. Since the parameters of this model are adjusted to experimental values it is clear that the description made by this model is close to reality if all the dominating processes are taken into account. A limitation of this model is the lack of chiral symmetry.

Metz and Drechsel have performed a one-loop calculation in the Linear Sigma Model (LSM) in the limit of an infinite sigma mass [34]. Although this model fulfills all the relevant symmetries (Lorentz, gauge, chiral invariance) it is very simple and does not give a very realistic description of the nucleon. In particular the calculation of the magnetic polarizability is not at all in agreement with experimental obtained estimates (see table 1-5). It is in the framework of this model that the four constraining relations for the polarizabilities (see section 1.5.5) have been developed.

A very systematic and consistent approach has been made in the Heavy-Baryon Chiral Perturbation Theory (HBChPT). Calculations to third order in the initial and final photon momentum expansion have been performed by Hemmert, Holstein, Knöchlein and Scherer [35]. Another calculation up to third order has been performed in reference [36]. The results obtained in this last calculation are not at all satisfying.

Table 1-5 summarizes the values for $\bar{\alpha}_E(0)$ and $\bar{\beta}_M(0)$ obtained in the four different models.

In figure 1-12 the evolution of $\bar{\alpha}_E$ and $\bar{\beta}_M$ with $Q^2$ is presented for the four models mentioned above. It is clear that the variation with $Q^2$ of the polarizabilities is very model dependent. Especially for $\bar{\beta}_M$ the model-dependence is important.

Figure 1-13 shows the evolution of the two structure functions $(\mathbf{P_{LL}}(\mathsf{q}_{cm}) - \frac{1}{\epsilon}\mathbf{P_{TT}}(\mathsf{q}_{cm}))$ and $\mathbf{P_{LT}}(\mathsf{q}_{cm})$ as a function of $Q^2$ in the framework of the HBChPT and the ELM. The dotted lines represent the scalar (spin independent) contributions, the full lines are the spin dependent plus the spin independent contributions. The experimental results from RCS are also indicated. As can be seen, the behaviour of the spin dependent contribution to the structure functions is rather different in both models. This indicates that considering the pion-cloud or not, which is the main difference between the two models, largely influences the spin polarizabilities. Large spin polarizabilities for example might explain why in RCS, which only has

| Model | $\bar{\alpha}_E(0)$ $10^{-4} fm^3$ | $\bar{\beta}_M(0)$ $10^{-4} fm^3$ |
|---|---|---|
| Experiment[12] | $12.1 \pm 1$ | $2.1 \mp 1$ |
| NRCQM[32] | 5.5 | 4.7 |
| ELM[33] | 7.3 | 1.6 |
| LSM[34] | 7.5 | -2.0 |
| HBChPT[35] | 12.8 | 1.3 |
| HBChPT[37] | 10.5 | 3.5 |
| HBChPT[36] | 17.1 | 9.2 |

Table 1-5: *Values for $\bar{\alpha}_E(0)$ and $\bar{\beta}_M(0)$ obtained in different theoretical models, compared to the experimentally obtained result.*

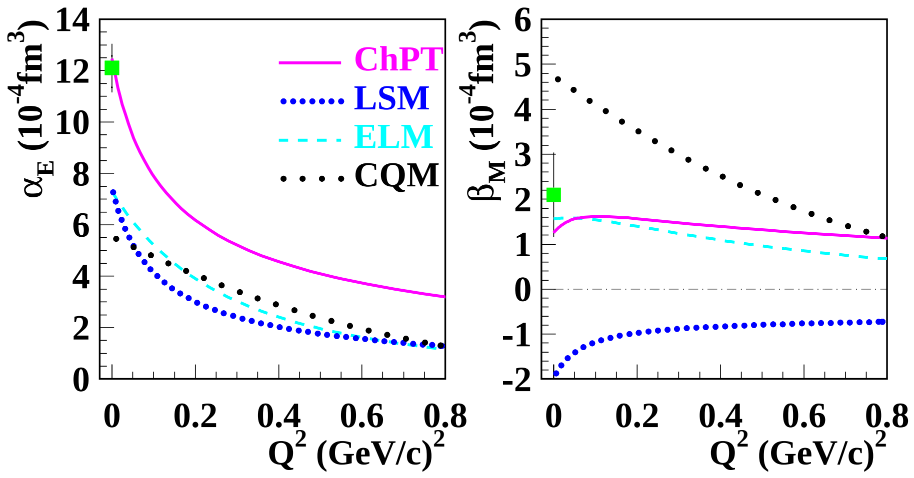

*Figure 1-12: Electric and magnetic polarizabilities as a function of $Q^2$ as calculated in four theoretical models: HBChPT [35], LSM [34], ELM [33] and NRCQM [32]. The experimental results at $Q^2 = 0(GeV/c)^2$ [12] are also indicated.*

scalar polarizabilities in the first order of the cross section expansion as a function of the real photon energy, higher order terms can not really be neglected (see section 1.4). VCS on the other hand contains in the first order scalar and spin dependent information which might reduce the importance of higher order terms.

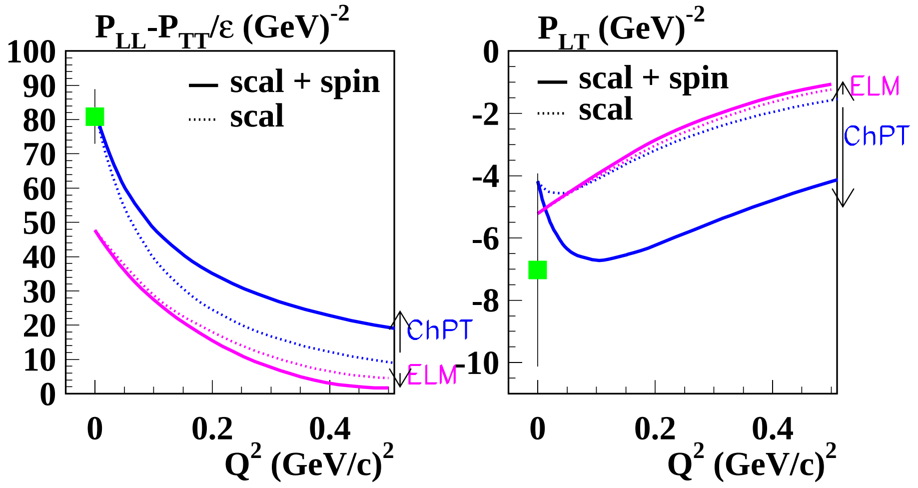

*Figure 1-13: Calculations for the two structure functions made in the ELM and HBChPT frameworks. The scalar (dotted lines) and scalar+spin dependent (solid lines) contributions are drawn. The RCS results are also indicated.*

These two figures (1-12 and 1-13) illustrate the need for measuring polarizabilities at different values of $Q^2$, in order to eliminate or confirm approximations that have been made in the various models.

Figure 1-14a shows the BH+Born cross section and the BH+Born cross section plus the polarizability effect, as predicted by HBChPT for Mainz kinematics (see section 1.7). This figure shows that the effect from the polarizabilities one expects is rather small (10% at most). Figures 1-14b and 1-14c are an attempt to show the same, but for TJNAF kinematics. As the calculations done in HBChPT do no cover high $Q^2$-values, a very rough speculation has been made. One has chosen the following values for the two structure functions in TJNAF kinematics at $Q^2 = 1(GeV/C)^2$ : $(\mathbf{P_{LL}}(\mathsf{q}_{cm}) - \frac{1}{\epsilon}\mathbf{P_{TT}}(\mathsf{q}_{cm})) = 4.0\ GeV^{-2}$ and $\mathbf{P_{LT}}(\mathsf{q}_{cm}) = -1.0\ GeV^{-2}$. The values for MAMI kinematics are : $(\mathbf{P_{LL}}(\mathsf{q}_{cm}) - \frac{1}{\epsilon}\mathbf{P_{TT}}(\mathsf{q}_{cm})) = 26.0\ GeV^{-2}$ and $\mathbf{P_{LT}}(\mathsf{q}_{cm}) = -5.3\ GeV^{-2}$ [35]. As can be seen for TJNAF kinematics, and supposing the values for the structure functions are realistic, even at

$\mathsf{q}'_{\mathsf{cm}}$=45 MeV/c, there is a visible effect (up to 20 % near $\theta_{cm}^{\gamma^*\gamma} = 0°$) of the polarizabilities.

Recently one has shown [38, 39] that 4 of the 6 GPs can be evaluated using dispersion relations. This dispersion formalism provides a new tool to analyse VCS experiments above the pion production threshold. As such it increases significantly the sensitivity to the GPs, since the sensitivity of the VCS cross section to the GPs boosts with the photon energy. The dispersive integrals are calculated taking into account the pion-nucleon intermediate states by using the state of the art MAID2000 [40] analysis for the pion photo- and electro-production. A comparison with calculations made in the HBChPT at $\mathcal{O}(p^3)$ raises questions about the convergence of the chiral expansion [38, 39]. This is also shown for the spin polarizabilities in RCS for which 3 independent HBChPT calculations have been performed to $\mathcal{O}(p^4)$ [41, 42, 43]. The corrections to e.g. $\gamma_0$ ($\gamma_0 = \gamma_1 - \gamma_2 - 2\gamma_4$) from $\mathcal{O}(p^3)$ to $\mathcal{O}(p^4)$ are of the order of 100%. So HBChPT predictions have to be interpreted carefully.

## 1.7 VCS Experiments below the Pion Production Threshold

As described in the previous sections, the polarizabilities will be investigated by studying the total photon electro-production cross section as a function of the outgoing photon energy $\mathsf{q}'_{cm}$ and $\theta_{cm}^{\gamma^*\gamma}$ . As can be seen in figure 1-14, $\theta_{cm}^{\gamma^*\gamma}$ gives the possibility to choose a domain where the effect of the GPs is visible, while $\mathsf{q}'_{cm}$ sets the size of the visibility of this effect (see equation 1-66). The choice of the other 3 kinematical variables of the problem ($Q^2$ or $\mathsf{q}_{cm}$, $\epsilon$, $\varphi$) will be discussed below, as well as the chosen kinematical settings of the three VCS experiments below the pion production threshold that have been performed up to now.

From the theoretical point of view, the only constraint on $Q^2$ is that $\mathsf{q}_{cm}$ has to be significantly larger than $\mathsf{q}'_{cm}$ to justify the multi-pole expansion used to analyse the experimental data [24, 27]. From the experimental point of view, there are more issues to be considered :

As seen in section 1.5.3, the Lorentz boost from *cm* to *lab* focuses the recoil proton direction in a cone around the virtual photon direction. This focusing becomes stronger when $\mathsf{q}_{cm}$ increases (see equation 1-42). So when performing experiments with large $Q^2$ and spectrometers with reasonable large acceptance, it is possible to explore a large part of the photon phase space ($\theta_{cm}^{\gamma^*\gamma}, \varphi$) since in this case almost the complete phase space for the proton is covered by the spectrometers.

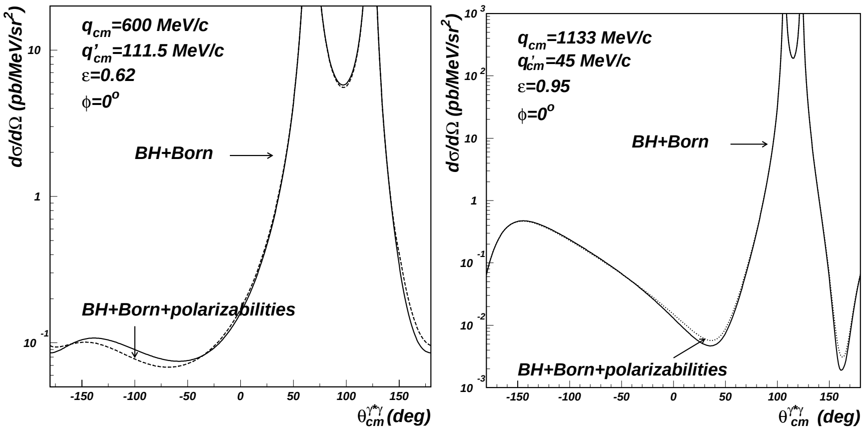

(a) Mainz kinematics, polarizability effect from HBChPT

(b) TJNAF kinematics, speculation for polarizability effect

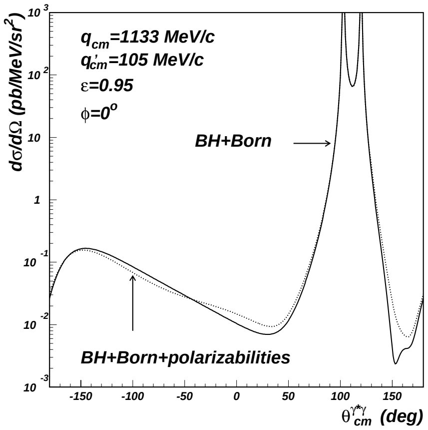

(c) TJNAF kinematics, speculation for polarizability effect

*Figure 1-14: BH+Born and BH+Born+polarizabilities effect for MAMI and TJNAF kinematics.*

This is the case for the two experiments at MAMI and TJNAF that are focussed on measuring the GPs of the proton. Performing experiments at low values for $\mathsf{q}_{\mathsf{cm}}$ allows to test chiral perturbation theory predictions. But since the kinematical focusing of the proton weakens when considering low momentum transfer, it is recommended to perform also measurements out of the scattering plane ($\varphi \neq 0°$). The possibility of measuring out of plane is an important capability for VCS experiments. By going above or below the scattering plane, the BH contribution to the cross section can be suppressed relative to the VCS contribution since one can move away from the incident and scattered electron directions. The experiment at Bates, that has the ability to measure out of plane, is focussed on measuring the polarizabilities at low momentum transfer in order to test predictions made by chiral perturbation theory.

For coincidence experiments, the limitations of upper and lower limits for $Q^2$ come from the constraints on the proton detection. The upper limit is imposed by the maximum momentum that can be accepted by the hadron spectrometer. When going too low in $Q^2$, the proton momentum becomes very low and resolution deteriorating effects due to energy loss and collision within the target become too important. Moreover, when the proton momentum becomes too low, the proton's chances to leave the target vanish.

The virtual photon flux varies with $1/(1-\epsilon)$. So it is clear that an $\epsilon$-value close to 1 is recommended. In order to separate $\mathbf{P_{LL}}(\mathsf{q}_{cm})$ and $\mathbf{P_{TT}}(\mathsf{q}_{cm})$ one needs at least 2 values for $\epsilon$. The smallest/largest value for $\epsilon$ at fixed value of $\mathsf{q}_{cm}$ is determined by the maximum/minimum angle of the electron spectrometer (see formula 1-36). If it is possible to have a good separation of 2 different $\epsilon$-values with one of them close to 1, one might perform an experiment with 2 different virtual photon polarisations.

It has already been mentioned that by going out of plane, thus varying $\varphi$, the BH contribution to the cross section can be suppressed relative to VCS. Of course, this can experimentally only be obtained when the spectrometers have the possibility to go out of plane. Bates has three out of plane spectrometers at its disposal and hence has the possibility to perform measurements out of plane. The MAMI and TJNAF experiments are using spectrometers that are moving in the reaction plane ($\varphi = 0°$). But their vertical acceptance is significant so they also have the possibility to study a range in $\varphi$ which is not so small. Moreover, the range in $\varphi$ that is acceptable increases when $\mathsf{q}_{cm}$ increases due to the Lorentz boost.

Table 1-6 summarizes the kinematical conditions of the three VCS experiments below the pion production threshold.

| experiment | BATES | MAMI | TJNAF |
|---|---|---|---|
| $Q^2(\mathrm{GeV/c})^2$ | 0.05 | 0.33 | 1.0 and 1.9 |
| $\mathsf{q}_{cm}(\mathrm{MeV/c})$ | 240 | 600 | $\geq 1000$ |
| $\epsilon$ | 0.90 | 0.62 | $\geq 0.85$ |
| $\theta_{cm}^{\gamma^*\gamma}$ | $90°$ | $[-180°, 180°]$ | $[-180°, 180°]$ |
| $\varphi$ | $0°, 90°, 180°, 270°$ | $0°, 180°$ | $[0°, 180°]$ |
| max opening angle cone | $\pm 24°$ | $\pm 10°$ | $\pm 6°$ and $\pm 4°$ |

Table 1-6: *Kinematical settings for the VCS experiments below the pion production threshold at Bates, MAMI and TJNAF.*

# Chapter 2

# First dedicated VCS Experiment at MAMI

## 2.1 Introduction

In this chapter, a concise report will be given on the first VCS experiment that was specifically designed for a determination of the Generalized Polarizabilities (GPs)[44]. For more detailed information on any facet of this experiment, see the PhD works [4, 23, 45]. This experiment has been performed at the 855 MeV Mainz Microtron (MAMI) in Germany in 1995-1997. Absolute differential unpolarised cross sections for the reaction $e + p \rightarrow e' + p' + \gamma$ have been measured in a wide angular range for $\theta_{cm}^{\gamma^*\gamma}$ at five values of the outgoing photon momentum $\mathsf{q}'_{cm}$, ranging from 33.6 MeV/c to 111.5 MeV/c. The virtual photon momentum and polarisation were kept fixed at $\mathsf{q}_{cm}$=600 MeV/c ($\mathrm{Q}^2$=0.33$(\mathrm{GeV/c})^2$) and $\epsilon = 0.62$, respectively. The range of the out-of-plane angle $\varphi$ was determined by the acceptance of the two high resolution magnetic spectrometers that served for the detection of the scattered electron and recoil proton in coincidence. To distinguish real photon production events from pion production events, a cut on the missing mass around zero was made. This was possible due to the excellent resolution of the facility (momentum resolution of $10^{-4}$ and angular resolution better than 3 mrad), as illustrated in figure 2-1 where a missing mass squared distribution is presented. Typical electron currents of 30$\mu$A and a liquid hydrogen target of 49.5 mm yielded a luminosity of $\mathcal{L} \approx 4 \times 10^{37}\ cm^{-2}s^{-1}$. The analysis of this experiment lead to the extraction of two structure functions that are related to the GPs.

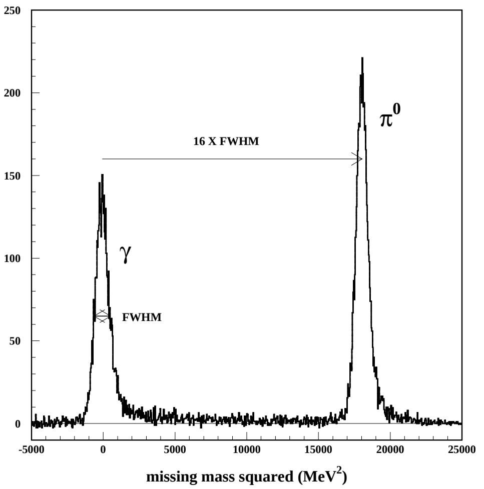

*Figure 2-1: Experimental spectrum of the missing mass squared for one kinematical setting at Mainz. The separation between photons and pions is very clean.*

## 2.2 Analysis of the Experiment

### 2.2.1 Kinematics

The measured kinematics for the VCS experiment at MAMI are presented in table 2-1.

The variables defining the leptonic part of the photon electro-production reaction ($\mathsf{k}_{lab}$,$\mathsf{k}'_{lab}$,$\theta^e_{lab}$) $\leftrightarrow$ ($\mathsf{q}_{cm}$,$\mathsf{q}'_{cm}$,$\epsilon$) are defined considering the remarks made in section 1.7 :

- $\mathsf{q}_{cm}$ is chosen as large as possible to favour the focusing of the proton (see section 1.5.3), but keeping in mind the restraints imposed by the momentum acceptance of the spectrometers and the maximum energy of the electron beam
- one has chosen 5 values of $\mathsf{q}'_{cm}$ below the pion production threshold to measure the evolution of the cross section with $\mathsf{q}'_{cm}$
- since one needs the same value of $\epsilon$ for all kinematical settings (see section 1.5.6), the angular range for the electron spectrometer restricts the interval

| $q_{cm}$= 600 MeV/c | | | $\epsilon$ = 0.62 | | |
|---|---|---|---|---|---|
| $q'_{cm}$ MeV/c | $k_{lab}$ MeV/c | $k'_{lab}$ MeV/c | $\theta^e_{lab}$ deg | $p'_{lab}$ MeV/c | $\theta^p_{lab}$ deg |
| 111.5 | 855 | 539.4 | 52.18 | 655.0 | -30.6 |
| 111.5 | 855 | 539.4 | 52.18 | 596.0 | -30.6 |
| 111.5 | 855 | 539.4 | 52.18 | 536.0 | -30.6 |
| 111.5 | 855 | 539.4 | 52.18 | 483.0 | -34.9 |
| 111.5 | 855 | 539.4 | 52.18 | 483.0 | -39.2 |
| 90.0 | 825 | 537.5 | 53.02 | 636.4 | -33.2 |
| 90.0 | 825 | 537.5 | 53.02 | 572.8 | -33.2 |
| 90.0 | 825 | 537.5 | 53.02 | 521.0 | -33.2 |
| 90.0 | 825 | 537.5 | 53.02 | 500.0 | -37.1 |
| 90.0 | 825 | 537.5 | 53.02 | 500.0 | -41.0 |
| 67.5 | 795 | 536.5 | 53.78 | 636.3 | -36.8 |
| 67.5 | 795 | 536.5 | 53.78 | 556.0 | -36.8 |
| 67.5 | 795 | 536.5 | 53.78 | 536.0 | -41.7 |
| 45.0 | 765 | 534.7 | 54.51 | 601.2 | -38.4 |
| 45.0 | 765 | 534.7 | 54.51 | 550.0 | -40.2 |
| 33.6 | 750 | 533.85 | 54.87 | 583.2 | -39.7 |
| 33.6 | 750 | 533.85 | 54.87 | 546.3 | -40.7 |

Table 2-1: *Measured kinematics of the VCS experiment at MAMI.*

in which $\epsilon$ can be chosen to $0.54 < \epsilon < 0.62$. Given these two extreme polarisation values, the lever arm for a good separation of the two structure functions $\mathbf{P_{LL}}(\mathsf{q}_{cm})$ and $\mathbf{P_{TT}}(\mathsf{q}_{cm})$ is too small. So one has chosen only one value for $\epsilon$, as high as possible to favour the FVCS amplitude over the BH amplitude.

The variables defining the hadronic arm $(\mathsf{p}'_{lab},\, \theta^{p}_{lab}) \leftrightarrow (\theta^{\gamma^*\gamma}_{cm},\, \varphi)$ are chosen in such a way that the intersection of the phase space of the recoil proton and the hadron spectrometer is optimised, avoiding the large contribution of the elastic scattering and BH events. In figure 2-2 the recoil proton momentum is presented as a function of its angle for one kinematical setting at MAMI. The leptonic variables are kept fixed at $Q^2 = 0.33(GeV/c)^2$, $\epsilon = 0.62$ and $\mathsf{q}'_{cm} = 111.5 MeV/c$. Each point $(\mathsf{p}'_{lab},\, \theta^{p}_{lab})$ corresponds to two precise values in $(\theta^{\gamma^*\gamma}_{cm},\, \varphi)$. Since the phase space $(\mathsf{p}'_{lab},\, \theta^{p}_{lab})$ increases with increasing $\mathsf{q}'_{cm}$, more hadron spectrometer settings are necessary to cover a large part of the recoil proton phase space. Note that due to the limited vertical acceptance of the hadron spectrometer (±70 mrad) and limited Lorentz boost, the central region on figure 2-2 can not be accessed.

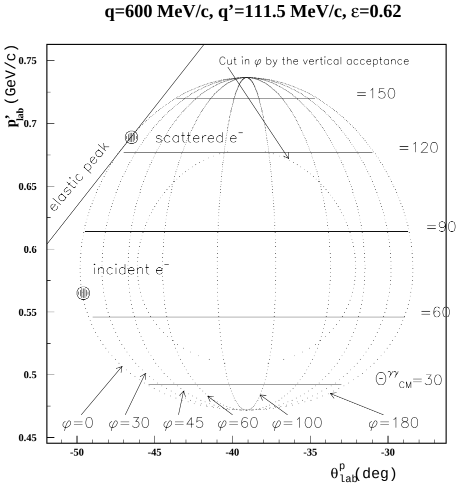

*Figure 2-2: Momentum and angle of the outgoing proton for* $\mathsf{q}'_{cm} = 111.5 MeV/c$ *at MAMI kinematics.* $\theta^{\gamma^*\gamma}_{cm}$ *and* $\varphi$ *are also indicated. The central region is experimentally not accessible due to the limited spectrometer vertical acceptance.*

### 2.2.2 Cross sections

As pointed out in section 1.6, the effect of the generalized polarizabilities causes only a small deviation from the BH+Born cross section. For MAMI kinematics, theory expects this deviation to be about 10 % at the highest $q'_{cm}$-values (see figure 1-14a). It is clear that identifying such a tiny effect, requires a very good accuracy on the measured cross sections.

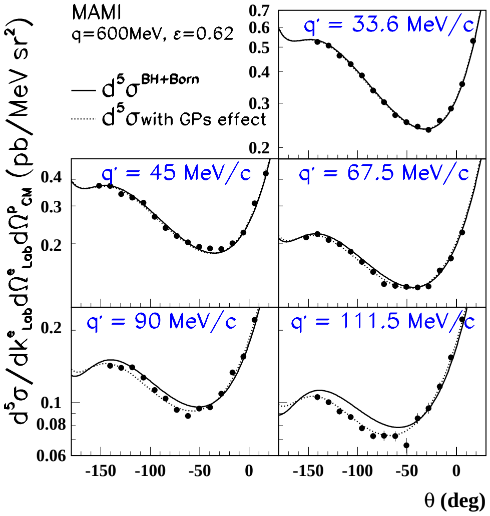

*Figure 2-3: Differential unpolarised cross sections for the photon electro-production reaction measured at MAMI. Figure from [44].*

In the MAMI-experiment, the cross sections are measured with a statistical accuracy within ± 3%. In addition, a careful analysis of possible systematic errors has been made. Section 1.2.3 already indicated that the proton form factors are not exactly known. So absolute elastic scattering cross sections for each of the kinematical settings have been measured. They endorsed the use of the Höhler form factor parametrisation at a precision better than ±1%. The same accuracy has been obtained for the luminosity and the spectrometer efficiencies. M. Vanderhaeghen et al. [46] have calculated the radiative corrections taking into account all the diagrams up to order $\alpha^4$ in the VCS cross section. They are of the order of 20%

of the cross section and are determined with a systematic uncertainty equal to ± 2%. The verification of missing mass spectra and the determination of the solid angles have been performed by a Monte Carlo simulation (see chapter 4). This yielded solid angles within an accuracy of ± 2%. Besides the above systematic uncertainties that are constant over the angular range of the real photon, another systematic uncertainty that causes distortions of these angular distributions has to be taken into account. It is caused by small imperfections in the optics calibration of the spectrometers and is responsible for an additional systematic uncertainty of ± 2.5%. In the following these two types of systematic errors (constant and not constant over the angular range of the real photon) will sometimes be mentioned separately.

The obtained results for the cross sections as a function of $\theta_{cm}^{\gamma^*\gamma}$ are shown for the 5 different $\mathsf{q}'_{cm}$ values in figure 2-3. Only the statistical errors are indicated. The BH+Born cross sections, calculated with the Höhler form factors are drawn as solid lines. Note that these calculated BH+Born cross sections have been normalized by an additional normalization factor $x = 0.987$ [47]. At small outgoing photon momentum, the agreement between experiment and calculated BH+Born cross section is certified. This is the first, indispensable step in the analysis of any VCS experiment focused on the extraction of GPs (see section 1.5.6). When $\mathsf{q}'_{cm}$ increases, one observes a growing deviation of the experimental cross section from the BH+Born cross section. This is the effect of the proton polarizabilities.

### 2.2.3 Extraction of information on generalized polarizabilities

The next step in the analysis consists of studying $(d^5\sigma^{exp} - d^5\sigma^{BH+Born})/\phi\mathsf{q}'_{cm}$ as a function of $\mathsf{q}'_{cm}$ for the 14 different values of $\theta_{cm}^{\gamma^*\gamma}$ one has chosen and to determine for each $\theta_{cm}^{\gamma^*\gamma}$ its value at $\mathsf{q}'_{cm} = 0$ (see section 1.5.6). This yields 14 values for $\mathcal{M}_0^{exp} - \mathcal{M}_0^{BH+Born}$ as defined in equation (1-68).

Figure 2-4 shows $(d^5\sigma^{exp} - d^5\sigma^{BH+Born})/\phi\mathsf{q}'_{cm}$ as a function of the real photon momentum $\mathsf{q}'_{cm}$ at the 14 different angles $\theta_{cm}^{\gamma^*\gamma}$. This figure also demonstrates the main difficulty of this experiment : as $\mathsf{q}'_{cm}$ decreases, the statistical error becomes larger. The intercept of $(d^5\sigma^{exp} - d^5\sigma^{BH+Born})/\phi\mathsf{q}'_{cm}$ with the ordinate axis has been determined in several ways. The methods that were applied can be divided into 2 main groups : one group takes into account possible $\mathsf{q}'_{cm}$ dependences of $(d^5\sigma^{exp} - d^5\sigma^{BH+Born})/\phi\mathsf{q}'_{cm}$, and the other one supposes there is no $\mathsf{q}'_{cm}$ dependence at all. This last hypothesis is based on the fact that figure 2-4 shows only -if any- a very weak $\mathsf{q}'_{cm}$ dependence which suggests that higher order terms in the expansion of formula (1-66) can be neglected. This is in contrast with the case of RCS (see section 1.4) where, even below the pion production threshold, higher order terms are responsible for a substantial contribution to the amplitude.

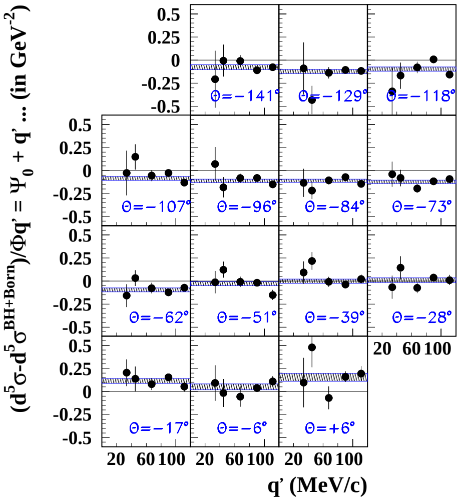

*Figure 2-4:* $(d^5\sigma^{exp} - d^5\sigma^{BH+Born})/\phi \mathsf{q}'_{cm}$ *as a function of* $\mathsf{q}'_{cm}$ *for the 14 different angles* $\theta_{cm}^{\gamma^*\gamma}$*, in the figure marked as* $\theta$*, measured at MAMI.* $\Psi_0$ *stands for* $\mathcal{M}_0^{exp} - \mathcal{M}_0^{BH+Born}$*. Figure from [44].*

### 2.2.3.1 First method : no $\mathsf{q}'_{cm}$ dependence of $\mathcal{M}^{exp} - \mathcal{M}^{BH+Born}$

In this method, the intercept at the origin of $(d^5\sigma^{exp} - d^5\sigma^{BH+Born})/\phi \mathsf{q}'_{cm}$ as a function of $\mathsf{q}'_{cm}$, is determined in different ways. All of them give results that are comparable within the error bars. The first method calculates $\mathcal{M}_0^{exp} - \mathcal{M}_0^{BH+Born}$ at each $\theta_{cm}^{\gamma^*\gamma}$ as the weighted mean value of the 5 data points. The other method determines the value of $\mathcal{M}_0^{exp} - \mathcal{M}_0^{BH+Born}$ for a single real photon energy. The shaded bands on figure 2-4 represent the uncertainty in the extrapolation to $\mathsf{q}'_{cm} = 0$ using the weighted mean method.

Following equation (1-68), one can write :

$$\frac{\mathcal{M}_0^{exp} - \mathcal{M}_0^{BH+Born}}{v_{LT}(\varphi, \theta_{cm}^{\gamma^*\gamma})} = \frac{v_{LL}(\varphi, \theta_{cm}^{\gamma^*\gamma})}{v_{LT}(\varphi, \theta_{cm}^{\gamma^*\gamma})}(\mathbf{P_{LL}}(\mathsf{q}_{cm}) - \frac{1}{\epsilon}\mathbf{P_{TT}}(\mathsf{q}_{cm})) + \mathbf{P_{LT}}(\mathsf{q}_{cm}) \quad (2\text{-}1)$$

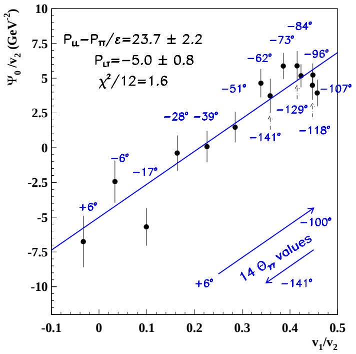

*Figure 2-5: $(\mathcal{M}_0^{exp} - \mathcal{M}_0^{BH+Born})/v_{LT}(\varphi, \theta_{cm}^{\gamma^*\gamma})$ (in the figure denoted as $\Psi_0/\mathsf{v}_2$) as a function of $v_{LL}(\varphi, \theta_{cm}^{\gamma^*\gamma})/v_{LT}(\varphi, \theta_{cm}^{\gamma^*\gamma})$ (in the figure $\mathsf{v}_1/\mathsf{v}_2$). The solid line represents the linear fit to the data points with coefficients as indicated. The structure functions are in $GeV^{-2}$. Figure from [44].*

Figure 2-5 shows the 14 values of $(\mathcal{M}_0^{exp} - \mathcal{M}_0^{BH+Born})/v_{LT}(\varphi, \theta_{cm}^{\gamma^*\gamma})$, determined by the weighted mean method, as a function of $v_{LL}(\varphi, \theta_{cm}^{\gamma^*\gamma})/v_{LT}(\varphi, \theta_{cm}^{\gamma^*\gamma})$. This figure shows that the data are reasonably well aligned, which might indicate that the higher order terms in equation (1-66) are rather negligible. The two obtained structure functions $(\mathbf{P_{LL}}(\mathsf{q}_{cm}) - \frac{1}{\epsilon}\mathbf{P_{TT}}(\mathsf{q}_{cm}))$ and $\mathbf{P_{LT}}(\mathsf{q}_{cm})$ that are combinations of 5 GPs are given by the slope and intercept of the linear fit to the data. The result is given in table 2-3. The first error is the statistical error only, the other two errors are the systematic errors as previously explained. The theoretical cross sections that are calculated using these two extracted structure functions are presented in figure 2-3 with the dotted lines.

#### 2.2.3.2 Second method : $\mathsf{q}'_{cm}$ dependence of $\mathcal{M}^{exp} - \mathcal{M}^{BH+Born}$

This method, developed by P.A.M. Guichon, supposes that the evolution of $(d^5\sigma^{exp} - d^5\sigma^{BH+Born})/\phi\mathsf{q}'_{cm}$ with $\mathsf{q}'_{cm}$ is determined by the interference between the complete BH+Born amplitude considered at all orders in the $\mathsf{q}'_{cm}$ expansion and the first term of the NonBorn amplitude (first order in the $\mathsf{q}'_{cm}$ expansion). So the only parameters in this method are the 6 GPs that are present in the only term of the NonBorn amplitude that is taken into account. They are determined with a best fit to the complete set of data (5×14 cross sections). Since $P^{(11,02)1}(Q^2)$ is expected to be very small (the corresponding quadrupole deformation of the $\Delta$ state is expected to be very small), it is fixed at zero. $P^{(01,01)0}(Q^2)$ is also kept fixed, since it is sufficiently well known at $Q^2$=0 (GeV/c)$^2$, and its theoretically predicted evolution with $Q^2$ is comparable to the evolution with $Q^2$ of the electric form factor. Fixing these two polarizabilities also causes a better convergence for the calculation method for the GPs.

Note that although the polarizabilities are introduced in section 1.5 as being a function of $\mathsf{q}_{cm}$, they can also be expressed as a function of $\tilde{Q}^2$, with $\tilde{Q}^2 = \left[-2m_p^2 + 2m_p\sqrt{m_p^2 + \mathsf{q}_{cm}^2}\right]_{\mathsf{q}'_{cm}=0}$. Remark that sometimes the notation $Q^2$ instead $\tilde{Q}^2$ is used.

| SF | GP | Experiment[47] | HBChPT[35] | units |
|---|---|---|---|---|
| | $P^{(11,02)0}$ | 0.0 fixed | +0.003 | $fm^4$ |
| $\mathbf{P_{LL}}$ | $P^{(01,01)0}$ | -0.0626 fixed | -0.056 | $fm^3$ |
| $\mathbf{P_{LT}}$ | $P^{(01,01)1}$ | +0.0086±0.0055 | +0.007 | $fm^3$ |
| | $P^{(11,11)0}$ | -0.0321±0.0186 | -0.034 | $fm^3$ |
| $\mathbf{P_{TT}}$ | $P^{(11,11)1}$ | +0.0035±0.0033 | +0.001 | $fm^3$ |
| | $P^{(01,12)1}$ | -0.0107±0.0026 | -0.008 | $fm^4$ |

Table 2-2: *Results for the GPs obtained at MAMI using the second method (see text), compared to the HBChPT predictions. SF indicates Structure Function.*

The results for the 6 GPs, obtained by this method are tabulated in table 2-2. The errors mentioned are statistical only. When interpreting these results, one has to keep in mind the 2 assumptions that are made : keep only one term of the Non-Born amplitude and fix the values for $P^{(11,02)1}(Q^2)$ and $P^{(01,01)0}(Q^2)$. This method mainly serves to confirm the rather flat $\mathsf{q}'_{cm}$ evolution of $\mathcal{M}^{exp} - \mathcal{M}^{BH+Born}$ and it allows to determine some spin polarizabilities with a good accuracy. The precision on the scalar magnetic polarizability in contrary, is not very good. This causes the determination of the two structure functions to be less precise in comparison to the first method. The values for the structure functions are given in table 2-3.

## 2.3 MAMI Results

In table 2-3, the result for the two structure functions is summarized for each of the two previously explained methods. The first error is the statistical error. Since the second method allowed to extract more information, the error on the recombined quantities (structure functions) is larger than the error on the structure functions obtained in the first method. Also the predictions made by different theoretical models are given. The experiment clearly favours the HBChPT calculation. In the case of $\mathbf{P_{LT}}(Q^2)$ this is not so surprising. HBChPT respects chiral symmetry, thus it correctly describes the pion cloud. This pion cloud dominates the spin dependent part of $\mathbf{P_{LT}}(Q^2)$. The calculations done in the ELM and NRCQM models lack chiral symmetry which is an important characteristic of QCD. This is why the experimental results do not agree as well with these predictions. Although the LSM calculation takes into account this chiral symmetry, other hypotheses are too restrictive to give a realistic prediction for the GPs and hence the two structure functions.

| Model | $\mathbf{P_{LL}}(Q^2) - \frac{1}{\epsilon}\mathbf{P_{TT}}(Q^2)$ $GeV^{-2}$ | $\mathbf{P_{LT}}(Q^2)$ $GeV^{-2}$ |
|---|---|---|
| 1st method[44] | $23.7 \pm 2.2 \pm 0.6 \pm 4.3$ | $-5.0 \pm 0.8 \pm 1.1 \pm 1.4$ |
| 2nd method[47] | $33.6 \pm 11.7$ | $-6.5 \pm 4.2$ |
| HBChPT[35] | 26.0 | -5.3 |
| HBChPT[48] | 26.3 | -5.7 |
| LSM[34] | 11.5 | 0.0 |
| ELM[33] | 5.9 | -1.9 |
| NRCQM[31] | 11.1 | -3.5 |
| NRCQM[32] | 14.9 | -4.5 |

Table 2-3: *Results for the two structure functions obtained at MAMI, compared to the theoretical predictions.* $Q^2 = 0.33 (GeV/c)^2$ *and* $\epsilon = 0.62$.

In figure 2-6 the two structure functions, calculated in the HBChPT and the ELM formalism are shown as a function of $Q^2$. Also the experimentally obtained values for RCS and VCS at MAMI using the first method are indicated.

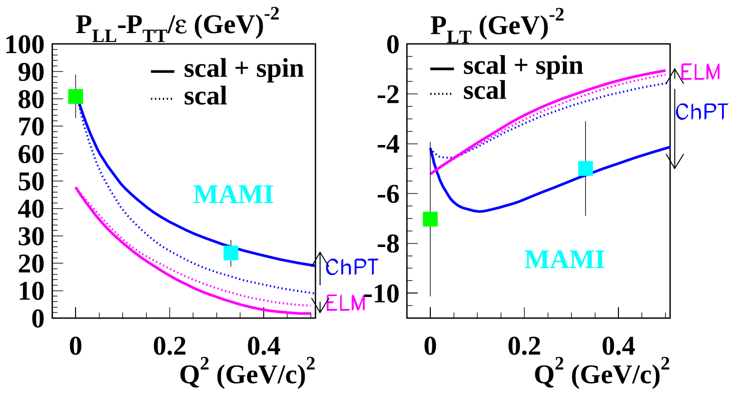

*Figure 2-6: Calculations for the two structure functions in the ELM and HBChPT formalism. The RCS results and VCS at MAMI results using the first method (see text) are also indicated. Details about the ELM and HBChPT formalism can be found in section 1.6.*

## 2.4 Summary

This first VCS experiment at MAMI showed that VCS experiments are feasible, but not that easy due to the high accuracy one needs on the cross sections in order to identify a polarizability effect. This experiment succeeded in extracting two structure functions that are combinations of GPs at $Q^2 = 0.33(GeV/c)^2$ and $\epsilon = 0.62$. These observables that are linked to the internal structure of the nucleon, are very efficient to judge theoretical models. The results obtained in this experiment favour the Heavy Baryon Chiral Perturbation theory predictions which indicates a large contribution of the spin-dependent polarizabilities.

# Chapter 3

# Experimental Setup for the VCS Experiment at TJNAF

## 3.1 Overview

In the spring of 1998, experiment E93-050 “Nucleon Structure Study by Virtual Compton Scattering” took place in the experimental Hall A of the Thomas Jefferson National Accelerator Facility (TJNAF, formerly known as CEBAF, Continuous Electron Beam Accelerator Facility) in Newport News, Virginia (USA). The research program of this institute is focused on bridging the hadronic and quark descriptions of nuclear matter. It has been recognized from the 1960s that high-energy electron beams (probing spatial scales down to a fraction of the nucleon’s size) with 100% duty factor would provide a unique and powerful new tool to extend electromagnetic interaction studies to a broad range of coincidence reactions. As such, Jefferson Lab has set its principal scientific goal to use the power of the electromagnetic interaction to investigate this transition region from the nucleon-based description of nuclei to the underlying quark-based description. The TJNAF accelerator was designed to provide independent continuous-wave (CW) electron beams to three experimental halls simultaneously, permitting three experiments to run in parallel. Each one of these three halls (A, B and C) is built with equipment designed to provide complementary capabilities for probing the nucleon and nuclear structure. Hall C was the first experimental facility to come into operation (May 1995). It has the possibility to be adapted to a large variety of experiments by adding more spectrometers and/or detecting devices . Hall B possesses a large acceptance spectrometer (CLAS, CEBAF Large Acceptance Spectrometer), so this hall is very well suited for experiments that require the simultaneous detection of several loosely correlated particles, and permitting measurements at limited luminosity. Finally, Hall A is equipped with two identical high resolution spectrometers (HRS). This makes this hall a good place for high-precision studies of (exclusive) reactions where two particles have to be detected in coincidence, as is the case for the VCS experiment E93-050.

## 3.2 Accelerator

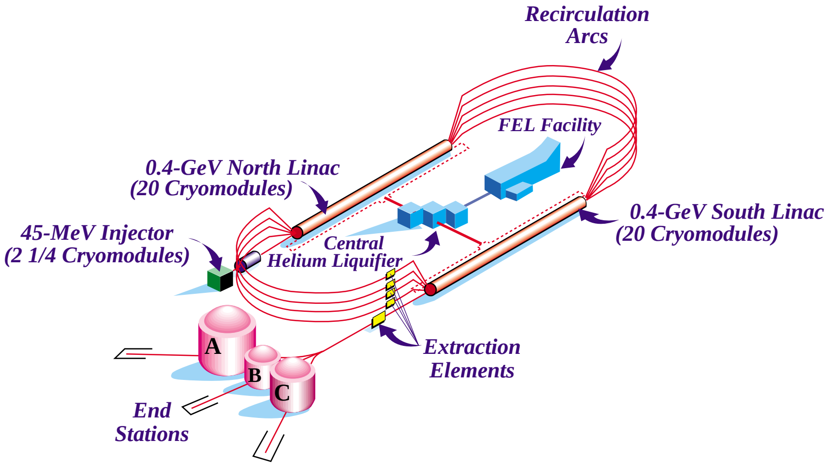

*Figure 3-1: Schematic view of the TJNAF accelerator.*

The TJNAF accelerator is a super-conducting radio frequency (RF) electron accelerator that was commissioned during the early 1990s and that produced the first experimental beam in October 1994. A schematic layout of the almost 1500 m long racetrack shaped accelerator is shown in figure 3-1.

The electron beam begins its journey in the 45 MeV injector that can deliver polarised or unpolarised electrons with an energy of 45 MeV. Then it is injected in the North linac consisting of 20 cryomodules that contain super conducting niobium cavities, functioning at 1497MHz. Each pass through a linac gives the electrons an additional 400 MeV. By tuning the accelerating electric field of the cavities, this energy can be higher or lower. After travelling through the first magnetic recirculation arc, which has a radius of 80 m, it obtains another 400 MeV in the South linac. At this point, the electron beam can either be extracted to go into any of the experimental halls, or it can continue its way through the second recirculation arc to go for another ride around the accelerator. The beam can travel this racetrack up to 5 times, in this way gaining up to 4 GeV. With the 45 MeV from the injector, this yields a beam energy of maximum 4045 MeV.

Because of the particular design of the TJNAF accelerator, beams with different energies and currents can be delivered to the different halls simultaneously. The beam has a micro-structure that consists of short pulses at a frequency of 1497 MHz. Generally, each hall receives one third of the pulses, resulting in a quasi-continuous train of pulses at a frequency of 499 MHz.

Table 3-1 summarizes the beam characteristics at the time of E93-050.

| | |
|---|---|
| Minimum energy | 445 MeV |
| Maximum energy | 4045 MeV |
| Duty cycle | 100%, CW |
| Emittance | 2x$10^{-9}$mrad |
| Energy spread ($\delta$E/E) | $10^{-4}$ |
| Maximum intensity | 200$\mu$A |

Table 3-1: *TJNAF beam characteristics.*

In the near future, Jefferson Lab expects to upgrade the accelerator's maximum energy to the 8-10 GeV regime.

A beam energy of 4045 MeV was used for the E93-050 experiment. Typical current-values were 50-70 $\mu$A.

## 3.3 Hall A

A diameter of 53 m makes Hall A the largest of the three circularly shaped experimental halls at TJNAF. Figure 3-2 shows its configuration. The beam enters the hall in the lower left-hand corner and follows the beamline which is equipped with instrumentation for measurement of beam current, position, energy and polarisation. Subsequently the beam is incident on the target that is located in a cylindrical aluminium scattering chamber. This vacuum can is placed at the pivot point of the two nominally identical high resolution spectrometers. In the figure, these spectrometers are labeled "Electron Spectrometer" and "Hadron Spectrometer", but each spectrometer can be configured to detect either type of particle by changing the polarity of its magnetic elements. Most of the electrons incident upon the target do not interact and are transported to a well shielded, isolated beam dump (not shown in the figure). Part of the electrons that scatter are detected in the electron spectrometer. Protons that are knocked out from the target nuclei may be detected in the hadron spectrometer. The two spectrometers can be moved independently clockwise or counter-clockwise around the hall. The range of scattering angle for the electron spectrometer is 12.5° to 165°, while the hadron arm can be moved from 12.5° to 130°.

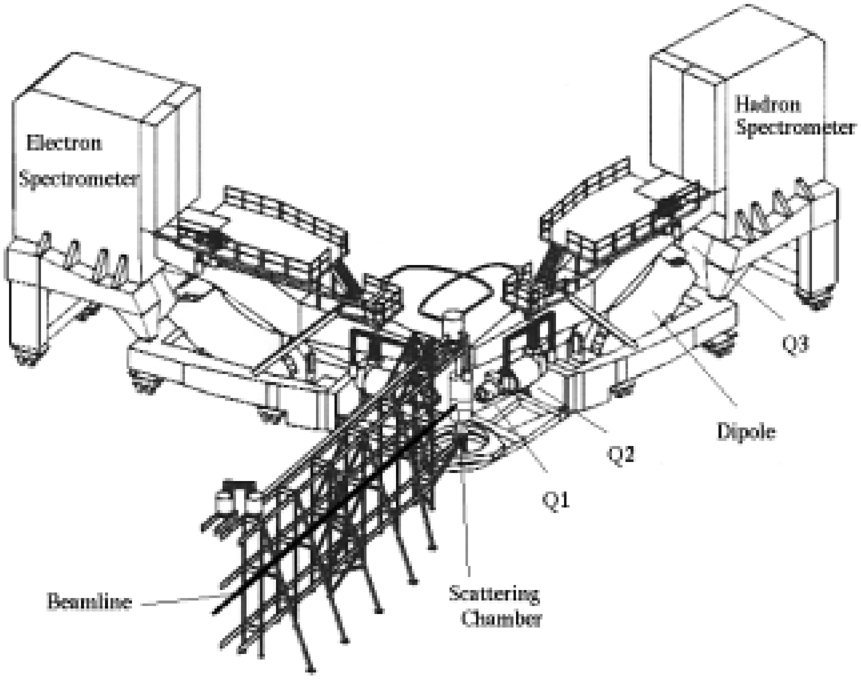

*Figure 3-2: Hall A configuration (diameter of 53 m).*

## 3.4 Hall A Arc and Beamline

Once the beam has been accelerated to the desired energy, it is bent into Hall A through an arc of eight identical dipoles. Knowing the strength of these magnets and the path of the beam travelling through them, the incident beam energy can be deduced with a precision of $10^{-4}$. At the moment the E93-050 experiment took place, this energy measurement method was not yet available.

The beam can now start its straight journey to the scattering chamber where the target is located. As seen in figures 3-3 and 3-4, the section of the beamline between the shielding wall and the target contains major beamline devices, such as a Compton and a Möller polarimeter. These systems are used to determine the polarisation of the incident beam. Since for E93-050 no polarised beam was required, these devices were not used. Also the e-p energy measurement setup was not used since it was not fully operational yet. More information on these systems can be found on the Hall A web page [49].

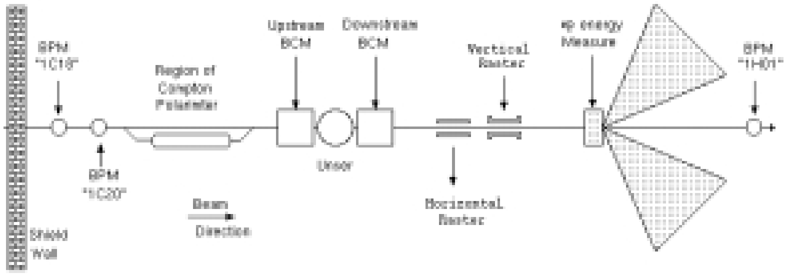

*Figure 3-3: Schematic view of the first part of the Hall A beamline (not to scale). This section of the beamline spans about 26 m.*

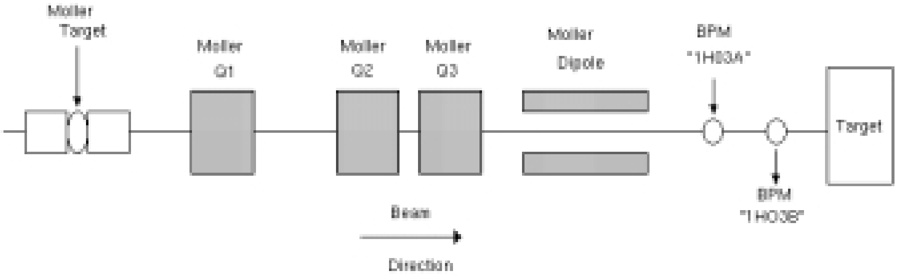

*Figure 3-4: Continuation of figure 3-3 (again not to scale). This section spans about 18 m.*

Many smaller devices that are important for the E93-050 experiment are also located in the beamline.

This experiment requires a cryogenic liquid hydrogen target and a high beam intensity (see section 3.5). Therefore it is mandatory to vary the beam position on the target in order to prevent damage to the target cell and to reduce target density changes due to local boiling. This wiggling of the beam position is done by the rastering system [50]. As a consequence of this beam movement, one needs to have the means to reconstruct its position on the target event-by-event. This is essential for the analysis. One can of course use the raster information, but also the information coming from the Beam Position Monitors (BPMs denoted BPM 1H03A and BPM 1H03B on figure 3-4) is used [51]. During E93-050 the beam had to be stable on the target within 250 $\mu$m, as measured by the two BPMs 1H03A and 1H03B. Finally the Beam Current Monitors (BCMs) [52] are used to measure the charge incident on the target, again a very important feature for the analysis of this experiment. The beam current had to be more than 5 $\mu$A all the time since charge measurements become less accurate below this level. The nominal beam energy was 4045 MeV. Since there was no direct way to measure the actual beam energy, indirect methods were used to obtain this beam energy. These methods indicate that the value of the beam energy during this experiment was about 4030.5 MeV (see section 5.2.10).

## 3.5 Targets

Most of the TJNAF physics program, including the VCS experiment E93-050, is focused on the few nucleon systems H, D, $^3$He and $^4$He and requires high target luminosities ($>10^{38} cm^{-2} sec^{-1}$) to obtain acceptable counting rates. As such, within the limited geometrical acceptance of a magnetic focusing spectrometer, extended high-density targets and high beam currents are required. Since the density of a liquid typically is about 1000 times larger than the density of a gas or a solid, cryogenic liquids are used (H, D) as a target. The energy/heat transferred by the beam to the target is proportional to the beam intensity. So if one uses high beam currents this can cause target boiling. This is why the target has to be permanently cooled down. This can be done by making the cryogenic target a loop which is constantly been cooled down.

A schematic of the Hall A target ladder that was used for the E93-050 experiment is shown in figure 3-5. It consists of 3 cryogenic target loops (2 deuterium and 1 hydrogen), 3 aluminium dummy targets (4, 10 and 15 cm) and 5 solid targets. The whole ladder is connected to a vertical lifting mechanism so that one can place the right target cell in the path of the beam.

During the VCS experiment E93-050 the 15 cm hydrogen target, the 3 dummy targets and the $C^{12}$ target were used. Since 1999 the first deuterium loop has been changed to a high pressure helium loop.

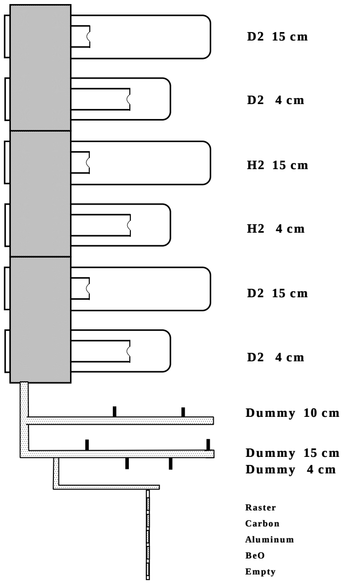

*Figure 3-5: Schematic view of the Hall A cryotarget with the attached dummy and solid target ladder.*

### 3.5.1 Cryotargets

In the following only the liquid hydrogen target will be considered, since this is the target used for this experiment. The liquid hydrogen target is a target loop, consisting of a 15 cm and a 4 cm “beer can” cell, filled with liquid hydrogen. During normal operation, it should have already been liquefied and should be in a stable state. Figure 3-6 shows a single target loop with its main components.

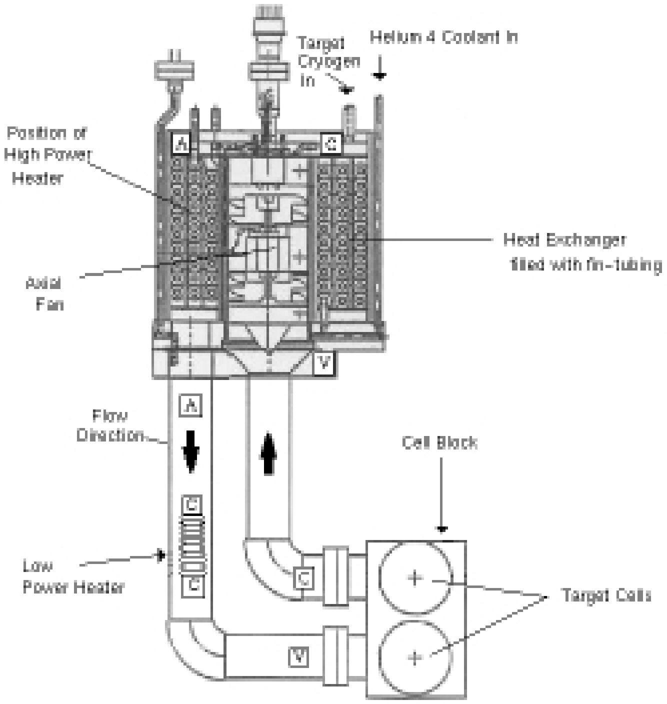

*Figure 3-6: Diagram of a single target loop. All of the main components are shown. The squares indicate the three types of temperature sensors : C(ernox), A(llen-Bradley) and V(apor pressure bulbs).*

#### 3.5.1.1 Target loop components

In the heat exchanger, gaseous target “fluid” (which is already pre-cooled down to 30-80 K) becomes liquid and is kept at a constant temperature. Because of its particular geometry, the heat exchanger yields a lot of "cooling surface" for the target fluid and provides up to 500 W/s of cooling power for the Hall A cryotarget.

The loop pump, or axial fan, which is placed at the center of the heat exchanger makes circulate the target fluid through the target cells and the heat exchanger, as shown by the arrows on the figure.

These target cells are made of aluminium beer cans and contain a flow diverter that forces the target liquid into the beamline. The nominal target lengths are 15 cm and 4 cm. The actual target lengths vary with construction and operating temperature and pressure. The lengths (without beam) at their centers (without windows), corrected for operating pressures and thermal contraction at the operating temperature, are listed in table 3-2. For all target measurements see reference [53].

| Target Cell | Cold Length (cm) | Upstream Window Thickness (cm) | Downstream Window Thickness (cm) |
|---|---|---|---|
| $H_2$ 15 cm | 14.95±0.02 | 0.0071±0.0003 | 0.0094±0.0005 |
| $H_2$ 4 cm | 3.78±0.01 | 0.0071±0.0003 | 0.0089±0.0005 |
| $D_2$ 15 cm | 14.94±0.02 | 0.0071±0.0003 | 0.0097±0.0005 |
| $D_2$ 4 cm | 3.93±0.01 | 0.0071±0.0003 | 0.0091±0.0005 |

Table 3-2: *Cryotarget dimensions without beam.*

To keep the target density constant during the experiment, the target temperature has to be kept constant all the time. Two types of heaters are used to adjust the temperature of the cryogen during periods when the beam is off or when there are temperature fluctuations due to small changes in coolant flow or coolant temperature. The high power heaters are used when there is no beam, they can provide more than 700 W of power. The low power heaters, that can provide up to 50 W, are used for fine-tuning.

The temperature in each target loop is monitored by 3 different types of thermometers. They are placed at different locations in the target loop (see fig 3-6). There are 4 Cernox Temperature Sensors. They provide resistive temperature measurements and are the most accurate at the cryogenic temperatures. Also 2 Allen-Bradley temperature sensors are used. They provide again a resistive temperature measurement and are mostly used during cool-down periods and to check whether the temperature is within the correct range. Finally there are 2 hydrogen-filled vapour pressure bulbs located in the target loop. They serve as a third type of thermometry and, unlike the other 2, they do not use a resistive measurement, but they measure a pressure. Like the Allen-Bradley sensors, these vapour pressure bulbs are used as a visual check that the cryogen's temperature is about correct.

#### 3.5.1.2 Target operating parameters

Table 3-3 shows the operating temperature and pressure of the hydrogen and deuterium target loops, as well as the corresponding densities and boiling and freezing temperatures in this state.

| Target | Temperature (K) | Pressure (atm) | Density (g/cm$^3$) | Boiling (K) | Freezing (K) |
|---|---|---|---|---|---|
| $LH_2$ | 19 | 1.8 | 0.0723±0.00005 | 23 | 14 |
| $LD_2$ | 22 | 1.5 | 0.1670±0.00005 | 25 | 19 |

Table 3-3: *Cryotarget operating parameters (without beam).*

The temperature is determined by the Cernox resistive sensors. The pressure is measured by two pressure transducers located in the target fill and the target return lines, respectively. The error on the target density calculation (without beam) is about 0.1% for $H_2$ and about 0.3% for $D_2$ [54].

#### 3.5.1.3 Target performance

The hydrogen and deuterium targets are operational since September 1997. A record high luminosity was achieved during commissioning : up to 120 $\mu$A beam current on 15 cm $LH_2$ and $LD_2$ (beam power $>$ 700 W), which yielded a luminosity of about $5.10^{38}$ cm$^{-2}$s$^{-1}$. Table 3-4 lists the luminosity achieved at 100 $\mu$A beam current and the energy deposited by the beam at this current.

### 3.5.2 Dummy and solid targets

Attached to the cryotarget ladder is a solid target ladder, which consists of three aluminium dummy targets and five solid target foils. Each dummy target is a set of two flat plates of aluminium, separated by empty space (10 cm, 15 cm

| | Hydrogen | Deuterium |
|---|---|---|
| Density (g/cm$^3$) | 0.07230 | 0.1670 |
| Length (cm) | 15.0 | 15.0 |
| $\frac{1}{\rho}\frac{dE}{dx}$ (MeV cm$^2$ g$^{-1}$) | 5.4 | 2.7 |
| Power (W) | 586 | 676 |
| Luminosity (cm$^{-2}$ s$^{-1}$) | 4.1 $\times 10^{38}$ | 4.7 $\times 10^{38}$ |
| Radiation Length (R.L.)(g/cm$^2$) | 61.28 | 122.4 |
| Thickness (R.L.) | 0.0177 | 0.0205 |

Table 3-4: *Luminosity and heat deposition in the target at 100 $\mu$A beam current.*

and 4 cm). These targets can be used to estimate the contribution of the target aluminium windows to the measured data.

Below these dummy targets are the solid target foils. First sits an aluminium target with two holes in it, used for fast raster commissioning. Also a carbon and a second aluminium target that can be used for spectrometer studies, are present. As a beryllium-oxide target starts to glow from incident beam, this target is used to visually check that the beam is present and in the correct position. Finally at the bottom of the solid target ladder the empty target is mounted. It is used when there doesn't have to be a target in the beam's path, and the beam can go straight to the beam dump. For the experiment E93-050 the C$^{12}$ and dummy targets are used (e.g. for Y$_{tg}$ optimization [55]).

## 3.6 High Resolution Spectrometers

Hall A is equipped with two spectrometers that are nominally identical in terms of magnetic properties. They are designed to have a high resolution in the determination of particle momentum, position and angle. The super-conducting spectrometer magnets have a QQDQ (quadrupole, quadrupole, dipole, quadrupole) configuration as shown in figure 3-7.

Shown are the scattering chamber, the spectrometer magnetic elements and the detector shield house which contains the detectors. Between the spectrometer

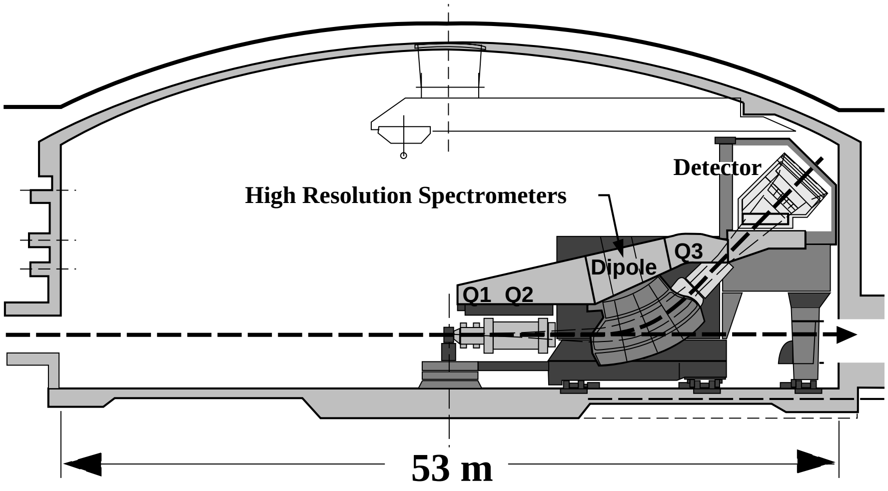

*Figure 3-7: Side view of the Hall A High Resolution Spectrometers.*

entrance window and the first quadrupole (Q1) of the spectrometer, a box is positioned that contains three movable tungsten collimators. The first one is a sieve slit that is used for spectrometer optics studies. The second is a 6 msr rectangular collimator that can be used to define the limits of the spectrometer acceptance. The last collimator is a dummy collimator that performs no collimation at all. Between the last quadrupole (Q3) and the detector shield house, a titanium exit window is present.

Each spectrometer provides point-to-point focusing in the dispersive (vertical) direction and mixed focusing in the transverse (horizontal) direction. Q1 is convergent in the dispersive plane, Q2 and Q3 provide transverse focusing. The magnetic field of the dipole increases with the radial distance, which provides a natural focusing in the dispersive direction. The field in the magnets is monitored by an NMR probe (dipoles) and by the current in the magnets (quadrupoles). As mentioned before, both spectrometers can be used to detect either particle (electrons or hadrons), by simply changing the polarity of the magnetic elements.

After a particle has travelled through the spectrometer magnets, it enters the shield house that contains several detecting devices (see section 3.7). The position and angle of the particles that arrive at the "spectrometer focal plane" are measured with a pair of Vertical Drift Chambers (VDCs) that are placed at 45° with respect to the spectrometer axis. Note that the actual physical focal plane that was meant to coincide with the first wire plane (spectrometer focal plane), is tilted by 26° from the last one (thus 71° from the spectrometer axis) due to the absence of a sextupole [56]. These measured focal plane parameters (position and angle) can be used to reconstruct the trajectory and momentum of the particle at the reaction point in the target. Optimizing the relation between the focal plane and target parameters, called transport matrix, has been subject of many studies during the analysis of this experiment [55, 57, 58, 59].

The angles of the spectrometers are measured by comparing the position of marks on the back of the spectrometers with marks on the Hall A floor. When rotating the spectrometers, the central axis may not point to the center of the target. This mispointing is monitored by Linear Voltage Differential Transformers (LVDTs) (see section 5.2.3).

The main characteristics of each of the spectrometers is summarized in table 3-5 [60].

## 3.7 Detector Packages

As shown in figure 3-7, the detector package is located inside a metal and concrete shielding house that is closed during data taking. This is done to protect the detectors from radiation damage and to minimize cosmic and beam-induced background. The detector packages of the two spectrometers are shown in figures 3-8 and 3-9.

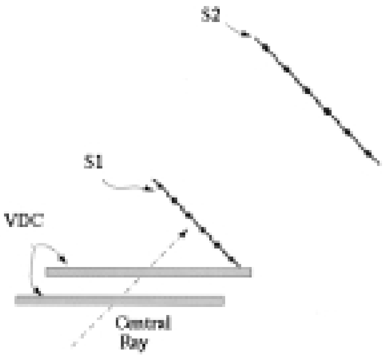

*Figure 3-8: Hadron arm detector package.*

| H.R.S. Characteristics | Commissioning | C.D.R. |
|---|---|---|
| Momentum range | 0.3 – 4.0 GeV/c | 0.3 – 4.0 GeV/c |
| Configuration | QQDQ | QQDQ |
| Bending Angle | 45° | 45° |
| Optical Length | 23.4 m | 23.4 m |
| Momentum Acceptance | ±4.5% | ±4.95% |
| Dispersion (D) | 12.4 cm/% | 12.4 cm/% |
| Radial Linear Magnification (M) | 2.5 | 2.5 |
| D/M | 5 | 5 |
| Momentum resolution (FWHM) | $2.5 \times 10^{-4}$ | $10^{-4}$ |
| Angular Acceptance:<br>Horizontal<br>Vertical | <br>±28 mr<br>±60 mr | <br>±30 mr<br>±65 mr |
| Solid Angle:<br>rectangular approximation<br>elliptical approximation | <br>6.7 msr<br>5.3 msr | <br>7.8 msr<br>6.1 msr |
| Angular resolution :(FWHM)<br>horizontal<br>vertical | <br>2 mr<br>6 mr | <br>0.5 mr<br>1.0 mr |
| Transverse Length Acceptance | ±5 cm | ±5 cm |
| Transverse position resolution (FWHM) | 3 mm | 1.0 mm |
| Spectrometer Angle Accuracy | 0.1 mr | 0.1 mr |

Table 3-5: *Main characteristics of the Hall A High Resolution Spectrometers. The first values are obtained during the commissioning, the last values are the ones needed as described in the Conceptual Design Report [61].*

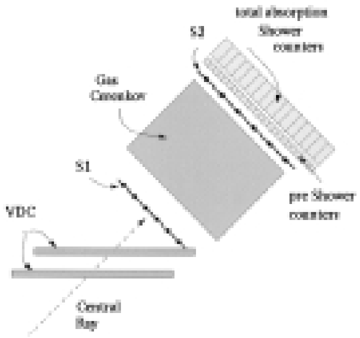

*Figure 3-9: Electron arm detector package.*

Each arm has two VDCs to define the trajectories of the charged particles, and two scintillator planes (S1 and S2) to generate an event-trigger and to provide time-of-flight information. The C̃erenkov counters in both arms and the (pre)shower in the electron arm serve to identify particles. The hadron arm has additional equipment to measure the polarisation of protons (straw chambers and carbon analyzer) and a third scintillator plane (S3). For the E93-050 experiment, all devices (except for the hadron arm polarimeter and S3) were operational. By today, only data from the VDCs and scintillators S1 and S2 are used for the analysis. These devices will be discussed briefly in the following subsections.

### 3.7.1 Vertical drift chambers

Each HRS detector stack is equipped with two VDCs in order to determine the position and angle of incidence of particles passing through the detector's focal plane. For both spectrometers, the lower VDC is located at the detector focal plane (at 15 cm from the titanium entrance window) and the second VDC is placed 50 cm downstream (perpendicular distance is about 30 cm) such that the nominal central ray of the spectrometer passes through the center of each VDC at an angle of 45° (see figures 3-10 and 3-11). Each VDC has two wire planes, perpendicular to each other, enabling the detection of the two coordinates of a particle track in the plane of the VDC with a resolution of about $225\mu$m (FWHM). Therefore the information obtained with the two wire planes results in the knowledge of the angles of the track passing through with a resolution of 0.3 mrad (FWHM). For a more detailed description see reference [62].

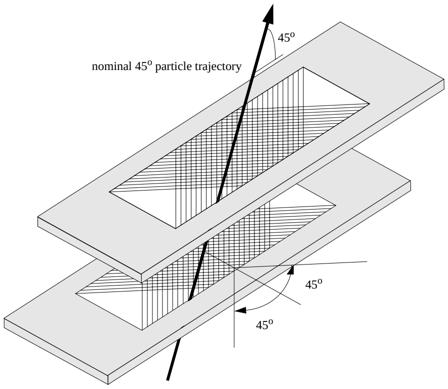

Figure 3-10: *Schematic layout of the VDC package (not to scale).*

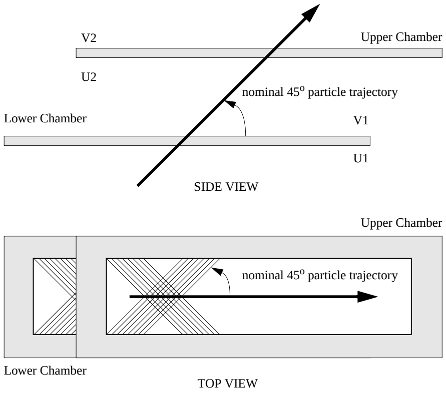

Figure 3-11: *Schematic layout of the VDC package (not to scale).*

### 3.7.2 Scintillator planes

The detector package of each spectrometer contains also two scintillator planes S1 and S2 (see figures 3-8 and 3-9). These planes are separated by 1.933 m in the electron arm and 1.854 m in the hadron arm and consist of 6 plastic scintillator paddles with an overlap of 0.5 cm in order to ensure complete coverage of the detector plane. The S1 scintillator plane has an active area of about 170 cm x 35 cm, while the S2 scintillator has an active area of about 220 cm x 54 cm. These surfaces are larger than the particle envelope at the location of that plane. This ensures a high trigger (see section 3.8) efficiency. The paddles are placed in such a way that their long axes are perpendicular to the spectrometer dispersive direction. A photo-multiplier tube is mounted on either end of each paddle. A schematic view of a scintillator plane is presented in figure 3-12. The scintillator efficiencies will be described in section 5.2.7.

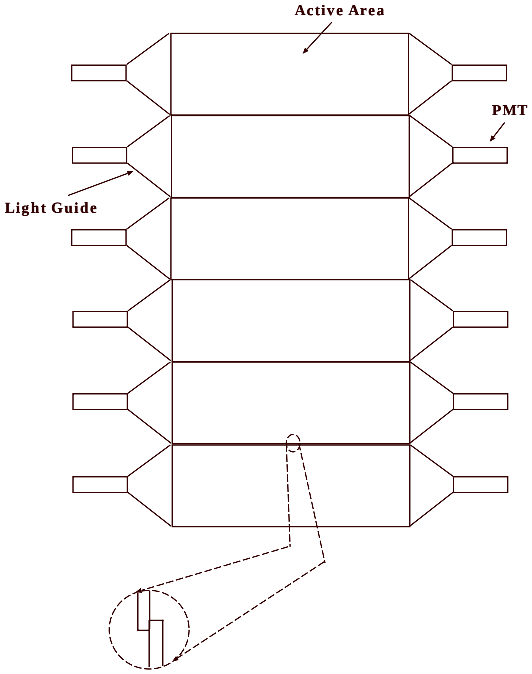

*Figure 3-12: Schematic of a scintillator plane.*

## 3.8 Trigger Electronics

The trigger electronics determines whether or not an event is to be recorded by the data acquisition system. Since the two spectrometers are alike, also their trigger systems are similar.

The HRS trigger detector packages for the electron and hadron arm are slightly different : for the electron arm the trigger package consists of two scintillator planes (S1 and S2), a gas C̃erenkov counter, a lead-glass shower detector and a lead-glass pre-shower detector. For the hadron arm, the package includes three scintillator planes, a gas and an aerogel C̃erenkov counter. For this experiment, only the S1 and S2 scintillator planes in each spectrometer and the electron C̃erenkov were used to generate the triggers. Figure 3-13 shows the logic diagram of the trigger electronics used in this experiment.

| Type | Description | Definition |
|---|---|---|
| T1 | electron single | $S1 \cap S2 \cap$ S-ray |
| T2 | electron junk | $(S1 \cap S2 \cap !\text{S-ray}) \cup (!S1 \cap S2 \cap \tilde{C}) \cup (S1 \cap !S2 \cap \tilde{C})$ |
| T3 | hadron single | $S1 \cap S2 \cap$ S-ray |
| T4 | hadron junk | $(S1 \cap S2 \cap !\text{S-ray}) \cup (!S1 \cap S2) \cup (S1 \cap !S2)$ |
| T5 | coincidence | $T1 \cap T3$ |
| T8 | random | |

Table 3-6: *Trigger types for E93-050.*

There are 6 basic trigger types (T1, T2, T3, T4, T5 and T8) that lead to the formation of an event buffer with the readout of all detectors into the CODA (see section 3.9) data file. The "good" electron and hadron arm single triggers are called T1 and T3, respectively. The coincidence trigger T5 is formed when a T1 and a T3 are detected within a 100 ns window. T8 is a random trigger fired by a 1024 Hz clock. T2 and T4 finally are the "bad" electron and hadron arm single triggers, respectively.

An S-ray configuration coincidence of at least one paddle in the S1 and at least one paddle in the S2 scintillator planes of the electron (hadron) spectrometer, leads to a T1 (T3) trigger. For the S-ray requirement, both planes (S1 and S2) must have a signal in coincidence and the number of the paddle(s) that fired in

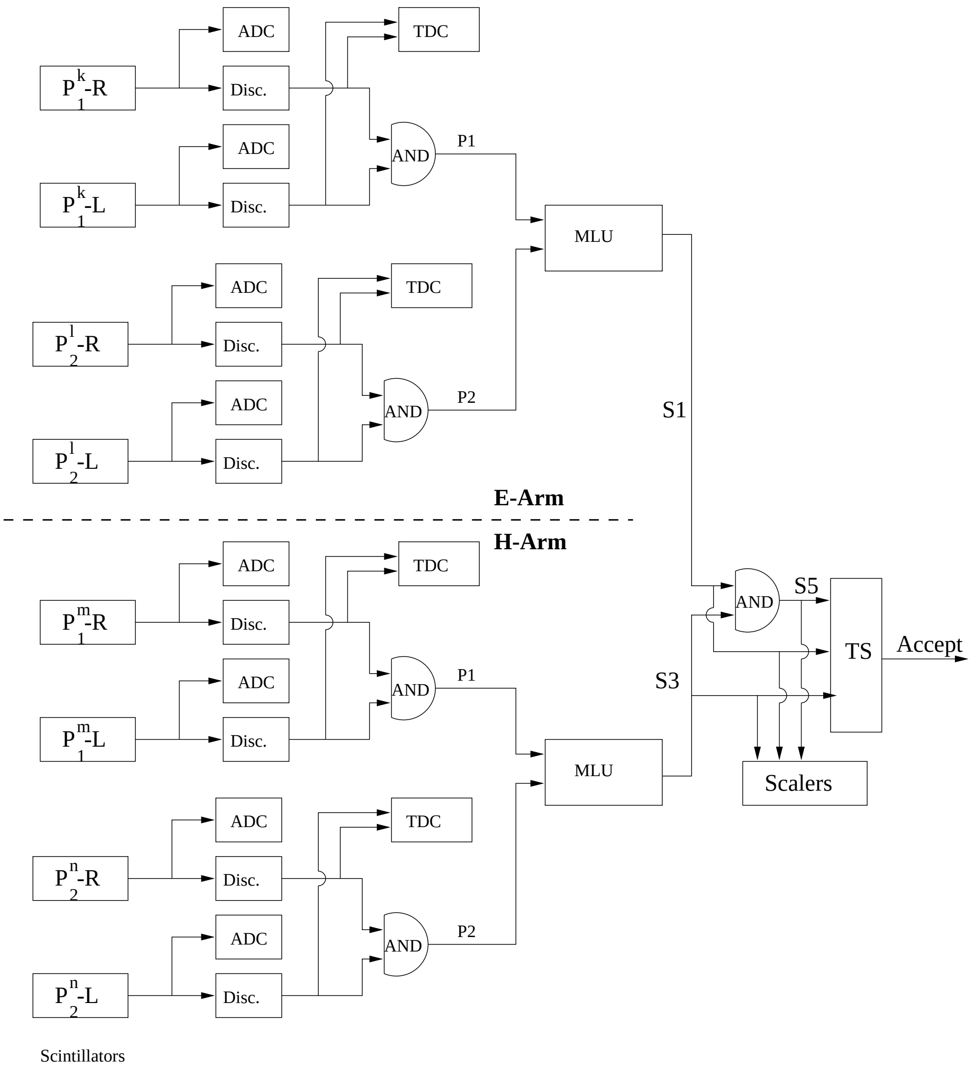

*Figure 3-13: Logic diagram of the trigger electronics for E93-050.* $P^i_{1(2)}$*-R(L) indicates the right(left) PMT mounted on paddle* $i$ *of scintillator plane 1(2). P1(2) denotes the accepted signal from scintillator plane 1(2). S1, S3 and S5 indicate electron single, hadron single and coincidence trigger, respectively.*

S2 must be the same or an adjacent paddle number(s) as in S1. This is shown in figure 3-14a. To have a good hit on any of the scintillator planes, there has to be a coincidence between the left and the right PMT of an individual scintillator paddle (see figure 3-14b).

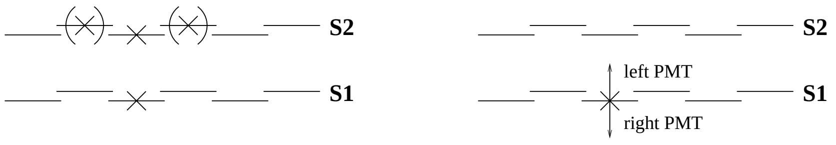

(a) S-ray configuration for a T1(T3) trigger

(b) Left-right coincidence of the two PMTs of one scintillator paddle

*Figure 3-14: S-ray configuration and good scintillator hit.*

A trigger type T2 is formed in the electron arm when either the S-ray configuration is not fulfilled, or when in one of the scintillator planes no paddle is hit. In the latter case, a valid signal in coincidence in the C̃erenkov is required. The trigger type T4 is formed in the hadron arm and is similar to T2 except that here is no C̃erenkov. So trigger T4 is formed by any valid hit in either S1 or S2 in the hadron arm. Table 3-6 gives an overview of the basic trigger types for this experiment and their definitions.

The trigger dead times and efficiencies will be discussed in sections 5.2.6 and 5.2.7.

## 3.9 Data Acquisition

All data acquisition (DAQ) during E93-050 is done using a system built under the CODA environment. CODA (CEBAF Online Data Acquisition) is a toolkit developed at Jefferson Lab and is used to manage the data acquisition system in Hall A. This system is controlled using a graphical user interface, called RunControl. A schematic of this Hall A data acquisition system is shown in figure 3-15.

On each spectrometer, there is one VME crate, one Fastbus crate and one Trigger Supervisor (TS) inside the spectrometer shielding house. The TS causes an event to be recorded by the data acquisition when the trigger electronics classifies the trigger as an allowed one (see section 3.8). At this moment, the ReadOut

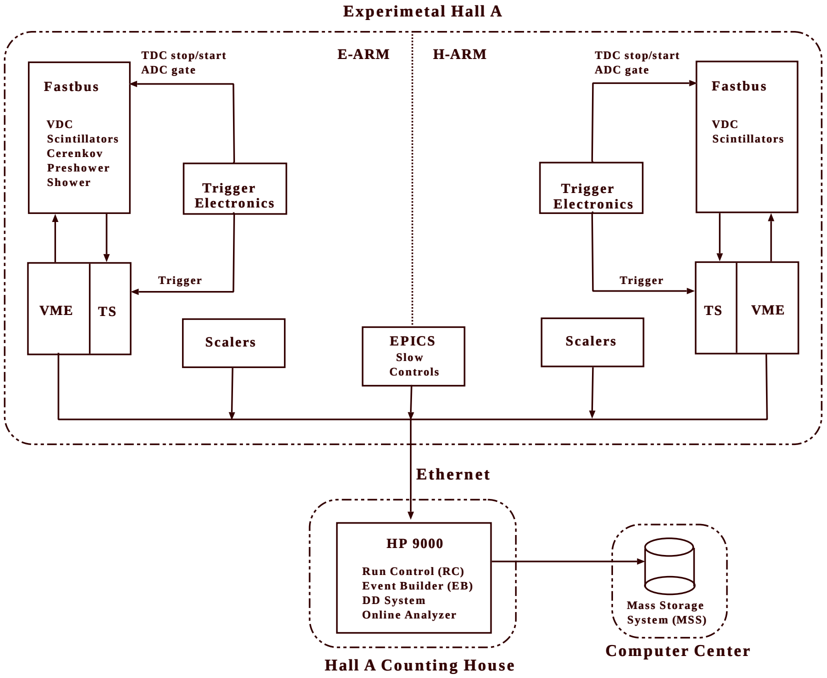

*Figure 3-15: Hall A data acquisition system.*

Controllers (ROC) which interface with the detector systems, are read out. These ROCs are single board computers in the VME and Fastbus crates. The Fastbus crate contains all TDC and Analogue-to-Digital Converter (ADC) modules that register data from the focal plane detectors. The VME crate contains scalers. The information gathered by the ROCs is then collected by the Event Builder which incorporates all of the necessary header and identifying information and puts it together into the CODA event format. The CODA Data Distribution system (DD) and online analyzer are used to analyze and/or send the events to the disk of the computer in the counting house. At specified times this data is copied to the Mass Storage System (MSS) where they are put on data tapes.

There are several types of events in the data stream. The first few events and the last event in the CODA data file of each run are status events like 'prestart', 'go', 'end', ... that were generated whenever the state of the run changed. Most events in the data file are physics events that contain "header" information (how long is the event, what trigger type, ...) followed by the physics information from the ROCs. Besides these two types of events, there are also scaler events that are read out every 10 seconds and the so-called EPICS (Experimental Physics and Industrial Control System) events that provide readouts of beam current, beam position, magnetic fields in the spectrometer magnets, ... . The latter data allows to scan the runs for malfunction of the hardware equipment.

# Chapter 4

# Monte Carlo Simulation for VCS

## 4.1 Introduction

Analysing VCS experiments requires the determination of experimental differential cross sections for the photon electro-production reaction $e + p \rightarrow e' + p' + \gamma$ (see section 1.5). These five fold differential cross sections $d^5\sigma/dk'_{lab}d\Omega_{k'_{lab}}d\Omega_{\gamma^*\gamma_{cm}}$ have to be determined very precisely since one wants to observe and quantify small deviations with respect to the BH+Born cross section (see section 1.6). The three main components one needs in order to calculate experimental differential cross sections are the collected number of good events, the experimental luminosity that yields these events and last but not least the solid angle one considers when accumulating the events (see section 5.5). The latter component is the one that justifies the presence of this chapter. The calculation of the solid angles one uses for the analysis of the VCS experiments at MAMI and at TJNAF is performed using an extensive Monte Carlo simulation. This simulation generates events according to the BH+Born cross section behaviour and takes into account resolution deteriorating effects. A Monte Carlo simulation for the VCS experiment at MAMI has been developed in Gent by L. Van Hoorebeke. For the VCS experiment at TJNAF another Monte Carlo simulation has been created, based on the MAMI simulation. Although the code has already proven to be very reliable and detailed, it is still subject to changes and ameliorations. In this chapter, the main aspects of this Monte Carlo simulation will be outlined.

## 4.2 Differential Cross Section versus Solid Angle

In general, calculating the cross section of a certain reaction for a specific kinematical setting implies evaluating the ratio of the number of counts detected in a given phase space bin ($N_{bin}$) and the integrated luminosity ($\mathcal{L}$). This ratio can be expressed as the mean differential cross section over this bin, multiplied with the solid angle of the phase space bin that is considered ($\Delta\Omega_1$). This is derived in equation (4-1). An other formulation is given in equation (4-2), where the ratio is written as the product of an actual cross section value somewhere in the bin (e.g. the central point), multiplied with a solid angle $\Delta\Omega_2$, that slightly differs from $\Delta\Omega_1$ by a factor $\epsilon$. This factor $\epsilon$ depends on the cross section behaviour within the considered bin, relative to the cross section value $\left(\frac{d\sigma}{d\Omega}\right)_0$.

$$\begin{aligned}
\frac{N_{bin}}{\mathcal{L}} &= \int \frac{d\sigma}{d\Omega} d\Omega \\
&= \frac{\int \frac{d\sigma}{d\Omega} d\Omega}{\int d\Omega} \int d\Omega = \left\langle \frac{d\sigma}{d\Omega} \right\rangle \Delta\Omega_1 && \text{(4-1)} \\
&= \left(\frac{d\sigma}{d\Omega}\right)_0 \int \left( 1 + \frac{\frac{d\sigma}{d\Omega} - \left(\frac{d\sigma}{d\Omega}\right)_0}{\left(\frac{d\sigma}{d\Omega}\right)_0} \right) d\Omega \\
&= \left(\frac{d\sigma}{d\Omega}\right)_0 (\Delta\Omega_1 + \epsilon) = \left(\frac{d\sigma}{d\Omega}\right)_0 \Delta\Omega_2 && \text{(4-2)}
\end{aligned}$$

It is clear that $\Delta\Omega_1$ is a pure "geometrical" quantity, while $\Delta\Omega_2$ depends on the cross section behaviour in the bin. Since the analysis of the VCS experiments is based on comparing theoretical and experimental differential cross sections, it is more suitable to use the second formulation of the ratio $\frac{N_{bin}}{\mathcal{L}}$. In that way, we obtain the experimental cross section in a well defined point in the phase space bin we consider.

From the experimental point of view, $N_{bin}$ is the number of events we detect and $\mathcal{L}$ can be obtained once we know the characteristics of target and beam (see section 5.3). The only unknown left, besides the differential cross section which we want to obtain, is $\Delta\Omega$. Obtaining a precise value for this solid angle is not that evident. Indeed, in reality the number of particles that are actually being detected in a given phase space bin ($N_{bin}$) is not equal to the number of particles that were present in that bin at the point of interaction. This is caused by resolution deteriorating effects (energy losses in target, multiple scattering, spectrometer resolutions). Thus we need to know the value for $\Delta\Omega$ that is corrected for these effects. This is where the Monte Carlo simulation comes into play. This extensive simulation generates events in a given phase space, according to a given cross section behaviour and implementing all resolution effects and effective detector geometries. Such a simulation provides the means to obtain a $\Delta\Omega$, corrected for the above effects. Depending on whether we use a constant cross section behaviour or the actual cross section behaviour, it will yield $\Delta\Omega_1$ ($\epsilon$ is 0) or $\Delta\Omega_2$.

As already mentioned, the knowledge of $\Delta\Omega_2$ is of particular interest. To obtain this solid angle, the real cross section behaviour of the process considered in the given phase space has to be known. And this real cross section behaviour is exactly the main unknown in the experiment. However, for VCS experiments below the pion production threshold, theory predicts that the five fold differential photon electro-production cross section only slightly differs from the BH+Born cross section (see section 1.6), so we can use this theoretically calculable cross section as a good approximation. Moreover, when considering small bins, the effect of using this slightly different cross section behaviour will be weakened since the number of events we will consider to calculate solid angles is also generated by this slightly different cross section behaviour (see section 4.5). If necessary, the value obtained for $\Delta\Omega_2$ can be improved by a (rather complicated) iterating process [63].

## 4.3 Journey through the Monte Carlo Simulation for VCS

The Monte Carlo simulation is in fact a package that consists of 3 separate Fortran codes. Each one of these codes has its own specific task. The first part, VCSSIM, simulates all processes that happen from the beam impinging on the target up to the generated particles arriving at the spectrometer collimators. This code generates 2 output files : an ntuple containing the generated events and a data file, containing general information on the simulation run. The second code, RESOLUTION, applies the spectrometer resolution effects to the ntuple generated by VCSSIM. This results in a second ntuple. Finally ANALYSIS analyses the ntuple resulting from RESOLUTION in order to obtain a third ntuple, containing for each event physics observables. This is done in exactly the same way the actual experimentally obtained events are analysed. So we have an ntuple at our disposal that should resemble the ntuple generated by the actual experiment, on the condition that the kinematical conditions in which the experiment and simulation have run are the same and on the condition that we understand and describe well everything that is happening during the experiment.

The modular structure of this simulation package has its advantages. One can change the spectrometer resolutions and/or the analysis (e.g. adding/changing physics variables) without having to re-simulate everything happening in the target. Since VCSSIM is the most time-consuming part of the three, this feature is very welcome. The next subsections will describe the three codes more in detail. The simulation codes for the two experiments (TJNAF and MAMI) are mainly alike. Since the simulation for the TJNAF experiment has been developed during this PhD work and the construction of the grids (see later) for it were part of this PhD work, the TJNAF version will be considered in what follows.

### 4.3.1 VCSSIM

In order to run this part of the simulation package, an extensive input file is needed. This file contains the name of the output files, experimental setup parameters (beam energy, spectrometers angular and momentum settings, target and rastering parameters, ... ), target resolution effects to be applied, cross section behaviour to be implemented, ... . For a complete list of all necessary input data, see reference [64]. All this information is needed to be able to simulate the real experiment as close to reality as possible. Here we already see that knowledge of the experimental setup is crucial for the analysis. As will be shown later (see section 5.2.3), small errors in some of the input parameters can cause large discrepancies in the obtained solid angles. At this point, an interesting feature of this simulation can be pointed out. By changing experimental parameters in the input file for the simulation and comparing the obtained results for the solid angles, systematic uncertainties that are introduced in the analysis of the experiment can be quantified. This will be illustrated in the analysis chapters further in this thesis.

The way this code generates events is very intuitive, and can be followed step by step. In figure 4-1 a schematic of the event generation process of VCSSIM is displayed. First a beam energy is sampled following a Gaussian distribution, simulating the beam energy resolution, with parameters given in the input file. Next, the beam position on the liquid hydrogen target is generated, following the rastering parameters that are also given in the input file. One can choose a uniform raster distribution or a realistic distribution. Next, an interaction point in the target is chosen, uniformly distributed along the beam line and in agreement with the beam position on the target. Given these two points (interaction point and beam position on the target), the target length and the path length through the target wall travelled by the incoming electron can be calculated. Travelling through these materials causes the electron to undergo multiple scattering which changes its momentum direction, and to loose energy by collision and real external radiation

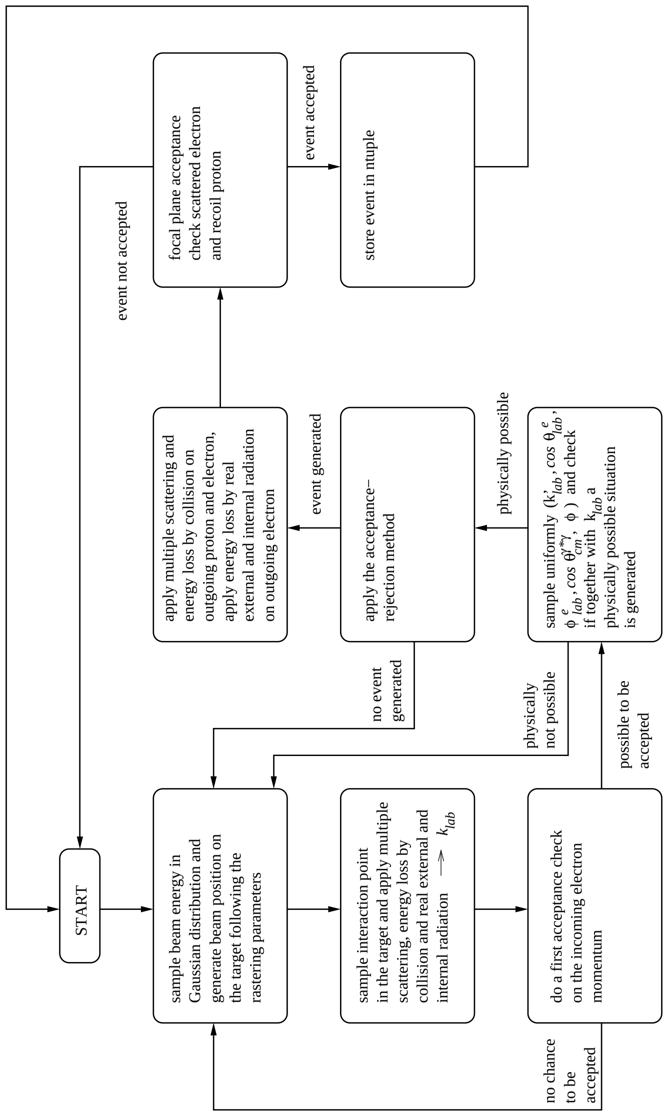

Figure 4-1: Flow diagram for the generation of events in VCSSIM.

(Bremsstrahlung). Also electron energy loss due to real internal radiation [25] is taken into account in the simulation. Flags that are given in the input file of the simulation indicate which of these effects have to be generated. For detailed considerations on these energy losses and how they are implemented in the simulation, see references [63, 65].

After applying all these effects, the actual electron four-momentum $k$, inducing the VCS interaction is obtained. Since the energy lost by real radiation can be very high, a first check is made at this point to see whether this electron still has any chance to be detected in the electron spectrometer. For that purpose, its momentum is compared to the minimum momentum value an incoming electron needs to have in order to be detected by the electron spectrometer. This value is calculated once in the beginning of the code as the incoming momentum value an electron needs to scatter elastically at the minimum scattering angle and having the lowest momentum detectable by the electron spectrometer. If this calculated momentum is larger than the momentum of the generated electron, it is of no use to continue with this event and the sampling starts all over again. If this calculated momentum is larger, a sample in phase space is made.

As can be seen in equation (4-2), the number of counts in a phase space bin is proportional to the integrated luminosity, the cross section value in the bin and the bin size. Thus the events will have to be generated with a probability that is proportional to the cross section behaviour. Since the five fold differential cross section is defined in the phase space $\Delta k' \Delta\Omega_{k'_{lab}} \Delta\Omega_{\gamma^*\gamma_{cm}}$, one samples uniformly in $\mathsf{k}'_{lab}$, $cos(\theta^{e}_{lab})$, $\varphi^{e}_{lab}$, $cos(\theta^{\gamma^*\gamma}_{cm})$ and $\varphi$. If the combination of this sampled set of variables and $\mathsf{k}_{lab}$ is physically possible, the acceptance-rejection method [66] with a constant value as an envelope is applied. This might result in a generated event, sampled following a probability distribution that is proportional to the cross section behaviour. It is clear that when using a constant cross section behaviour, one does not need to apply this acceptance-rejection method. In that case all physically possible samples lead to an event.

Once an event has been generated, a check has to be made whether this event will be detected. This means one has to verify whether the scattered electron and recoil proton arrive in the spectrometer focal planes. Before doing this check, again resolution worsening effects have to be applied. Analogue to the incoming electron, the scattered electron undergoes real internal and external radiation energy loss, energy loss by collision and multiple scattering. The recoil proton will be subject to multiple scattering and energy loss by collision. Again all these effects can be switched on or off independently. For checking whether the particle is detected or not, an acceptance routine written by S. Jaminion [55] is used. Once the acceptance check is made, we can start all over again, trying to generate a next event. The generation of events continues until the ntuple contains the number of events that is asked for in the simulation input file.

Depending on what option is chosen in the simulation input file, the simulation code stores only the accepted events or all the generated events in the ntuple. For each event, relevant information on how the event arrived at the spectrometer entrance is kept (momentum components, vertex (i.e. point of interaction in the target) coordinates). Since the simulation almost completely generates the $4\pi$ phase space for the real photon, the complete recoil proton phase space is covered. To benefit from this, all hadron spectrometer settings (see section 5.1) can be treated in one simulation run. To know which spectrometer setting accepted the event, a spectrometer setting index is also stored for each event. Besides this ntuple, VCSSIM also generates a data file. This file contains some statistical data on the simulation run and a summary of the inputs that have been given to the program. Also the integrated luminosity is stored in this file. This integrated luminosity is given by :

$$\mathcal{L}^{sim} = \frac{N^{sim}}{\int \frac{d^5\sigma}{dk' d\Omega_{k'_{lab}} d\Omega_{\gamma^*\gamma_{cm}}} d\Omega^{sim}} \tag{4-3}$$

where $N^{sim}$ is the number of events that are generated in $d\Omega^{sim}$, which is a well defined part of the total simulation phase space. $d^5\sigma / dk' d\Omega_{k'_{lab}} d\Omega_{\gamma^*\gamma_{cm}}$ represents the cross section as used to generate events. More details on the determination of the simulation integrated luminosity can be found in [67].

### 4.3.2 RESOLUTION

This second program in the simulation package has as the objective the application of the resolution effects of the spectrometers to the events that are present in the ntuple resulting from VCSSIM. For each event, this results in a change of momentum size, momentum direction and vertex point. This code also needs a proper input file. This input file contains the characteristics that will be used to apply the resolution effects. Also the names of the input ntuple and output ntuple are given in this file.

One can choose to use constant resolution effects, or to follow the actual transport of the particle to the focal plane, to apply multiple scattering in the focal plane detectors and to transport the particle back to the target.

The first option implements resolution effects by sampling in Gaussian distributions that have the spectrometer resolution values as FWHM. These resolution effects are constant, they do not depend on the position in the focal plane where the

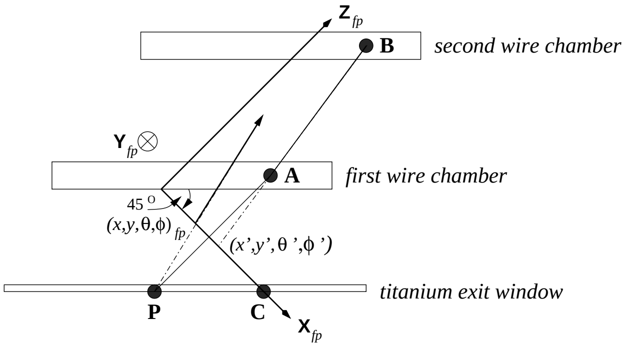

*Figure 4-2: Spectrometer resolution effects in RESOLUTION program of Monte Carlo Simulation for VCS (not to scale). Explanation in text.*

particle arrives. Typical FWHM values are $1\times10^{-4}$ for the momentum resolution, 2 and 6 mrad for the horizontal and vertical angular resolution ($\varphi_{tg}$ and $\theta_{tg}$ in the Target Coordinate System as defined in Appendix B), 2 mm for the z-resolution and 0.35 mm for the x and y resolutions. These x, y and z are defined in the Hall A Laboratory Coordinate System (see Appendix B). Note that, although this option is not used when analysing the TJNAF experiment, it is valuable for the study of the influence of resolution effects on solid angles, thus on cross section values.

The second option is the one used for the analysis of the TJNAF experiment. Since the focal plane is tilted over 45° with respect to the detector devices, the presence of this second method is justified. Indeed, depending on where the particle arrives in the focal plane, the resolution effects due to multiple scattering will be more or less pronounced. This is explained in figure 4-2. The transport of the particles from target to the focal plane is calculated using the first order 4×4 transport matrices taken from reference [68]. This yields the coordinates $(x, y, \theta, \varphi)_{fp}$ as indicated on the figure, they are given in the Transport Coordinate System (see Appendix B). Given these coordinates, the intersection of a track, corresponding to those coordinates and the titanium exit window of the spectrometer magnets is determined (point P in the figure). At this point the multiple scattering in all windows, gas chambers etc. starts, yielding a point A and a point B in the two wire chambers (see section 3.7.1). These 2 points A and B are used to build the resolution affected coordinates $(x', y', \theta', \varphi')_{fp}$. These coordinates are then transported again to the target, yielding target coordinates that are influenced by the multiple scattering effects in the focal plane detectors. It is clear that the $x$ and $y$ coordinates of particles that arrive at the focal plane near the intersection of the XY-plane with the titanium exit window (in the figure denoted C), will be less affected by multiple scattering in the spectrometer than the $x$ and $y$ coordinates of particles arriving further from this point. This is due to the titanium exit window that causes a lot more scattering than all other windows and gases together [69].

These changed events are stored in a second ntuple. This ntuple can be considered as the equivalent of an experimental ntuple that contains the reconstructed particle momenta at the reconstructed point of origin in the target.

### 4.3.3 ANALYSIS

This last part of the simulation package does in principle the same as one does in the analysis of the real experiment : reconstructing physically relevant variables, starting from particle momenta and vertices in the target. Before doing this reconstruction, the particle momenta are corrected for the mean energy loss in the target, the same way one does in the experiment. This results in a third ntuple that can be used for comparing experimental and simulated spectra (see sections 6.2 and 7.4), and for calculating solid angles that are necessary to obtain experimental cross section values (see section 4.5).

## 4.4 Grids for the Monte Carlo Simulation

As seen in section 1.5.4, the BH+Born cross section increases very rapidly when the real outgoing photon direction approaches the incoming and scattered electron directions. This causes the acceptance-rejection method with a constant envelope to become rather inefficient in the region away from these electron directions, slowing down the generation of events. The efficiency of this acceptance-rejection method, with well chosen envelope values, is of the order of 10%. As such one needs a fast method to calculate the BH+Born cross section values. The code one uses to calculate these BH+Born cross sections is written by M. Vanderhaeghen [33]. Unfortunately, the rate at which it generates cross section values is rather low. To overcome this problem, a simulation grid is used. This grid is a five dimensional cross section matrix, having $\mathsf{q}_{cm}$, $\mathsf{q}'_{cm}$, $\epsilon$, $\theta_{cm}^{\gamma^*\gamma}$ and $\varphi$ as variables. At each matrix point, the cross section point is calculated using the code mentioned above. The cross section value at a random point in phase space is then obtained by performing a logarithmic interpolation in the matrix, i.e. a linear interpolation in the logarithms of the cross section values. Using this method, the cross section values are generated up to 1000 times faster than when using the cross section code. The construction of this grid is done, keeping in mind several considerations : the grid has to cover at least the complete phase space in which the simulation samples, the size of the grid has to be kept reasonably while the accuracy of the grid has to be as good as possible.

### 4.4.1 Simulation sampling phase space

Since one wants to generate events according to the BH+Born cross section which has the form $d^5\sigma/dk'_{lab}d\Omega_{k'_{lab}}d\Omega_{\gamma^*\gamma_{cm}}$ and which depends on the variables $\mathsf{k}_{lab}$, $\mathsf{k'}_{lab}$, $\theta^e_{lab}$, $\theta^{\gamma^*\gamma}_{cm}$ and $\varphi$, the phase space in which to sample will be a product $\Delta\mathsf{k'}_{lab}\Delta\Omega_{k'_{lab}}\Delta\Omega_{\gamma^*\gamma_{cm}}$. This means one has to define a range in each of these 3 sub-phase spaces. In order to keep the simulation as efficient as possible, one wants to define this phase space as small as possible, but containing at least all regions that might lead to an event that can be detected. In that way, one prohibits the sampling of most of the events that a priori do not have any chance to arrive in the spectrometer focal planes and that would thus worsen the efficiency of the simulation. For the TJNAF simulation, the ranges are defined as follows :

- $\Delta\Omega_{k'_{lab}}$ is defined as the product $\Delta cos(\theta^e_{lab})\Delta\varphi^e_{lab}$. So the ranges for $\theta^e_{lab}$ and $\varphi^e_{lab}$ have to be determined. This is done in an intuitive way : scanning the edges of the target in combination with scanning the borders of the collimator of the electron spectrometer, yields values for those 2 angles. Their extreme values are used to define the sampling ranges for $cos(\theta^e_{lab})$ and $\varphi^e_{lab}$.
- for $\Delta\mathsf{k'}_{lab}$, the minimum value $(\mathsf{k'}_{lab})_{min}$ is determined by the minimum momentum acceptance of the electron spectrometer :

  $$(\mathsf{k'}_{lab})_{min} = P_e * (1 - |relative\ acceptance\ range|) \tag{4-4}$$

  The momentum setting $P_e$ and the relative acceptance range are given in the input file for the simulation, the acceptance range is typically ±5.5%. The maximum value is calculated as the maximum momentum an elastically scattered electron, having the maximum beam energy ($(\mathsf{k}_{lab})_{max}$), can have in the $\Delta\Omega_{k'_{lab}}$ range defined above :

  $$(\mathsf{k'}_{lab})_{max} = \frac{(\mathsf{k}_{lab})_{max}}{1 + \frac{(\mathsf{k}_{lab})_{max}}{m_p}(1 - cos(\theta^e_{min}))} \tag{4-5}$$

- finally $\Delta\Omega_{\gamma^*\gamma_{cm}}$ covers the complete $4\pi$ phase space, thus $cos(\theta^{\gamma^*\gamma}_{cm})$ covers [-1,+1], while $\varphi$ varies from 0 to $2\pi$.

For completeness I recall that the simulation samples in a Gaussian distribution with a relative FWHM of $1 \times 10^{-4}$ to obtain the momentum of the electron that impinges on the target.

### 4.4.2 Construction of the simulation interpolation grid

When constructing the interpolation grid, one has to make sure the complete phase space defined above in which the simulation samples, is covered. The most straightforward way for doing this would be taking the ranges in $\mathsf{k}'_{lab}, \theta^e_{lab}$, $\theta^{\gamma^*\gamma}_{cm}$ and $\varphi$ from above and define a range in $\mathsf{k}_{lab}$. But this would yield very large matrices, containing a lot of meaningless values. Indeed, for a given value of $\mathsf{k}_{lab}$, it is needless to have cross section values at our disposal that correspond to $\mathsf{k}'_{lab}$ values that are larger than $\mathsf{k}'^{elas}_{lab}$, since this situation is physically not possible. The smaller $\mathsf{k}_{lab}$, the more grid-space would be filled with nonsense. As shown in section 1.5.3 there exists a complete bijection between the *lab* variables $(\mathsf{k}_{lab}, \mathsf{k}'_{lab}, \theta^e_{lab})$ and the *cm* variables$(\mathsf{q}_{cm}, \mathsf{q}'_{cm}, \epsilon)$. Since the three *cm* variables are decorrelated of each other, a grid constructed with these variables is more efficient. Defining the ranges for these variables is done by scanning the ranges in the *lab* variables $(\mathsf{k}_{lab}, \mathsf{k}'_{lab}, \theta^e_{lab})$, calculating the corresponding *cm* variables $(\mathsf{q}_{cm}, \mathsf{q}'_{cm}, \epsilon)$ and storing their extreme values. The ranges in $\mathsf{k}'_{lab}$, $\theta^e_{lab}$, $\theta^{\gamma^*\gamma}_{cm}$ and $\varphi$ are determined as in the simulation sampling phase space. Note that the grid only needs to cover $\varphi$ from 0 to $\pi$, since there is a cross section symmetry around the leptonic plane. The range for $\mathsf{k}_{lab}$ in the cross section matrix is defined as follows :

$$(\mathsf{k}_{lab})_{max} = \text{nominal beam energy} + 2MeV \tag{4-6}$$

$$(\mathsf{k}_{lab})_{min} = \frac{(\mathsf{k}'_{lab})_{min}}{1 - \frac{(\mathsf{k}'_{lab})_{min}}{m_p}(1 - cos(\theta^e_{min}))} \tag{4-7}$$

Once the ranges in $\mathsf{q}_{cm}, \mathsf{q}'_{cm}, \epsilon, \theta^{\gamma^*\gamma}_{cm}$ and $\varphi$ are defined, the binning of these ranges has to be carefully chosen. By considering the size of the final matrix and the overall interpolation accuracy within the covered phase space, one arrives at a satisfying binning for the 5 dimensional grid. Unlike what was done for the Mainz grids, one was obliged to make the binning for some of the variables non-equidistant. This is due to the fact that the cross section value changes enormously with the variation of some of the variables (especially $\mathsf{q}'_{cm}$). The binning has to be tighter in regions where the cross section value changes a lot in order to obtain an interpolation accuracy that is the same all over the phase space. Moreover, the regions that are most probable to generate events have to be very accurate while the regions that barely produce any event are less important. Since the phase spaces for the two experimental regions that are subject to the VCS experiment at TJNAF are too

| | bins | | DA_1 | | DA_2 | |
|---|---|---|---|---|---|---|
| | # | equidist. | low | high | low | high |
| $\mathsf{q}_{cm}$ | 10 | yes | 705.8 MeV | 1480.6 MeV | 1067.1 MeV | 2001.2 MeV |
| $\mathsf{q}'_{cm}$ | 36 | no | 1.0 MeV | 363.2 MeV | 1.0 MeV | 411.8 MeV |
| $\epsilon$ | 8 | no | 0.920 | 0.977 | 0.841 | 0.934 |
| $\theta_{cm}^{\gamma^*\gamma}$ | 44 | yes | 0° | 180° | 0° | 180° |
| $\varphi$ | 30 | yes | 0° | 180° | 0° | 180° |
| $\mathsf{k}_{lab}$ | - | - | 3476.0 MeV | 4047.0 MeV | 3297.4 MeV | 4047.0 MeV |
| $\mathsf{k}'_{lab}$ | - | - | 3227.0 MeV | 3713.4 MeV | 2773.0 MeV | 3284.7 MeV |
| $\theta_{lab}^{e}$ | - | - | 11.7° | 19.7° | 18.9° | 27.6° |
| accuracy | | | <1% | | <1% | |

Table 4-1: *Configuration of simulation grids for settings DA_1 and DA_2 of the VCS experiment at TJNAF.*

different, two different grids have been constructed. All the above reasoning led to the grid configurations for DA_1 and DA_2 (see later) as summarized in table 4-1. The corresponding ranges in $\mathsf{k}_{lab}, \mathsf{k}'_{lab}$ and $\theta_{lab}^{e}$ are also given.

Each of these two cross section grids contains about 5110000 cross section values and is contained in a binary file of 20.4 MB. In figure 4-3 the BH+Born cross section values as a function of $\theta_{cm}^{\gamma^*\gamma}$ and $\varphi$ are shown for $\mathsf{q}_{cm}$=1093 MeV/c, $\mathsf{q}'_{cm}$=45.5 MeV/c and $\epsilon$=0.9485. These values are extracted from the grid for DA_1. One can clearly see the two "cat ears" that correspond to the incoming and outgoing electron directions.

## 4.5 Solid Angles

Once one disposes of the output ntuple from ANALYSIS and the integrated luminosity $\mathcal{L}^{sim}$ from VCSSIM, one is able to calculate solid angles. The solid angle for a phase space bin for which one wants to obtain the differential cross section value, can be calculated using the following equation :

$$\Delta\Omega_{bin}^{sim} = \frac{N_{bin}^{sim}}{\mathcal{L}^{sim}\left(\frac{d^5\sigma}{dk'\,d\Omega_{k'_{lab}}\,d\Omega_{\gamma^*\gamma_{cm}}}\right)_0} \tag{4-8}$$

where $N_{bin}^{sim}$ is the number of simulated events that are present in the defined bin and $(d^5\sigma/dk'd\Omega_{k'_{lab}}d\Omega_{\gamma^*\gamma_{cm}})_0$ is the differential cross section in a certain point in that

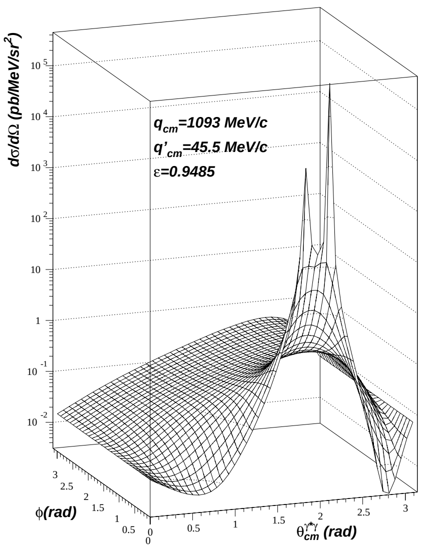

*Figure 4-3: BH+Born cross section values as a function of $\theta_{cm}^{\gamma^*\gamma}$ and $\varphi$, extracted from the DA_1 grid at $\mathsf{q}_{cm}$=1093 MeV/c, $\mathsf{q}'_{cm}$=45.5 MeV/c and $\epsilon$=0.9485.*

bin and corresponding to the cross section behaviour that is used for generating these $N_{bin}^{sim}$ events in VCSSIM (i.e. BH+Born or constant cross section value). The obtained solid angle will be $\Delta\Omega_{1,bin}^{sim}$ or $\Delta\Omega_{2,bin}^{sim}$, depending on whether one used a constant cross section behaviour or the BH+Born cross section behaviour to generate events in VCSSIM. At this point one sees how the effect on the solid angle of using a slightly different cross section behaviour is weakened. Indeed, the number of events used to calculate this solid angle is also slightly different from what one should obtain with the real cross section behaviour. Thus the imperfection in the denominator of formula (4-8) is weakened by an analogue imperfection in the numerator. Note that this is only true when the following two conditions are met : the considered bin is small and the used cross section behaviour only slightly differs from the real cross section behaviour.

The two upper plots of figure 4-4 show solid angles for the kinematical setting DA_1_15 (see section 5.1) that are obtained using a constant cross section behaviour and using the BH+Born cross section behaviour as a function of $\theta_{cm}^{\gamma^*\gamma}$. The ranges in $\theta'^{\gamma^*\gamma}_{cm}$ (as defined in section 7.2) that are considered are mentioned. Note that the other 3 kinematical variables $\mathsf{q}_{cm}$, $\mathsf{q}'_{cm}$ and $\epsilon$ are kept fixed. The errors indicated are the statistical errors (they are barely visible on the plot). The systematic errors

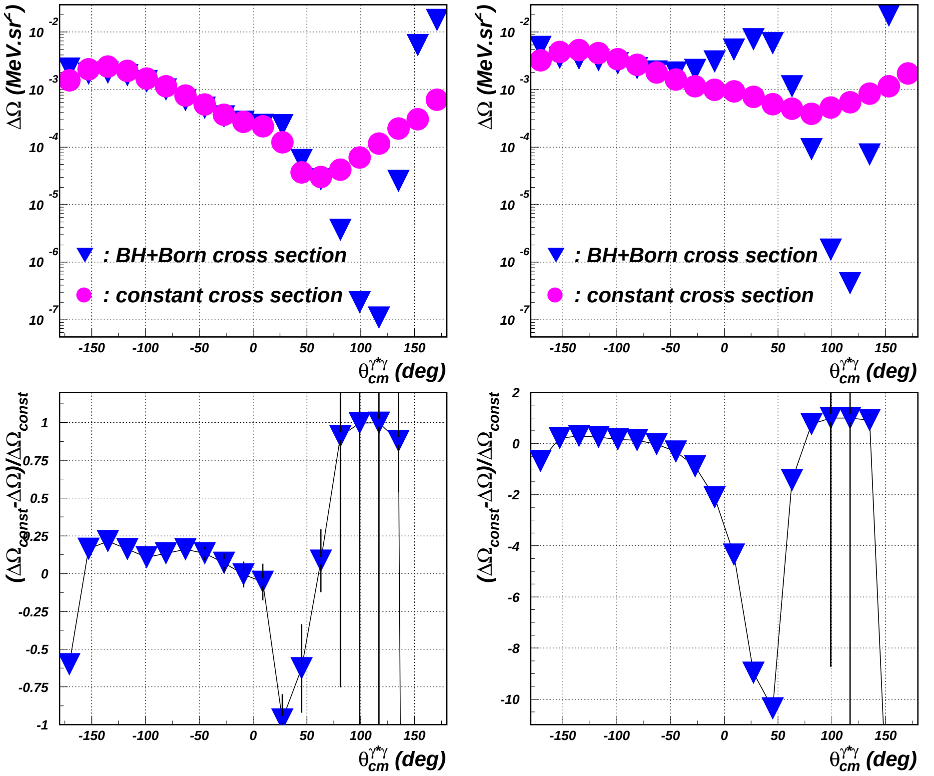

(a) $60° < \theta'^{\gamma^*\gamma}_{cm} < 120°$ (b) $0° < \theta'^{\gamma^*\gamma}_{cm} < 180°$

*Figure 4-4: Top : solid angles for setting DA_1_15 as a function of* $\theta_{cm}^{\gamma^*\gamma}$*, using the BH+Born and constant cross section behaviour. Bottom : relative difference between these solid angles.*

would only give rise to a global shift up or down of the two curves. The lower plots give an indication of how much the BH+Born cross section value in a point of a bin (here the center point) differs from the mean cross section value in the bin. Note that the results obtained in the region $60° < \theta_{cm}^{\gamma^*\gamma} < 160°$ for the BH+Born cross section behaviour are not reliable due to limitations applied in the simulation. As can be clearly seen, in the region of interest (i.e. away from the cat ears) the solid angles obtained with a constant cross section and the BH+Born cross section behaviour differ up to 20% when one considers relative small bins in $\theta'^{\gamma^*\gamma}_{cm}$. Indeed, in this region, the BH+Born cross section comportment is rather "flat", not changing much within the considered bins. This can be seen in figure 4-3. On the contrary, when one considers large bins in $\theta'^{\gamma^*\gamma}_{cm}$, the solid angles significantly differ near $\theta_{cm}^{\gamma^*\gamma} = 0°$. This is expected since in this region, the BH+Born cross section considerably changes with $\varphi$. These plots illustrate that the difference in solid angles when one uses a constant cross section or the BH+Born cross section behaviour, becomes more important when the cross section within the bin significantly fluctuates. As such, using the BH+Born cross section to calculate solid angles will yield better results for VCS experiments than using a constant cross section. Indeed, theory predicts that the photon electro-production cross section only slightly differs from the BH+Born cross section behaviour (see section 1.6). Moreover, because of this small difference one can expect the relative difference between the "real solid angle" and the solid angle obtained with the BH+Born cross section behaviour to be smaller than the relative difference between using a constant cross section behaviour and using the BH+Born cross section behaviour. Since the aim of the VCS experiments is to obtain experimental cross sections values with a very good accuracy (up to a few percent), it is clear that the effect of using an approximative cross section behaviour to obtain solid angles might be non-negligible.

Figure 4-5 gives an idea of the effect that the resolution effects, as described in section 4.3, have on the solid angles. The points represent the relative difference between the the solid angles that are obtained when applying resolution effects and the ones obtained when applying no resolution effects. The kinematical conditions are the same as in figure 4-4b. Again only the statistical errors are indicated. As can be seen, in the region of interest the resolution effects cause the solid angles to change only a few percent.

Finally the obtained solid angles can be applied to the experimental data in order to obtain the experimental cross section value for a point in the bins :

$$\frac{d^5\sigma^{exp}}{d\mathsf{k}'_{lab} d\Omega_{\mathsf{k}'_{lab}} d\Omega_{\gamma^*\gamma_{cm}}} = \frac{N_{bin}^{exp}}{\mathcal{L}^{exp}\Delta\Omega_{bin}^{sim}} \tag{4-9}$$

In the case one uses $\Delta\Omega_{1,bin}^{exp}$, the obtained cross section value will be the mean cross

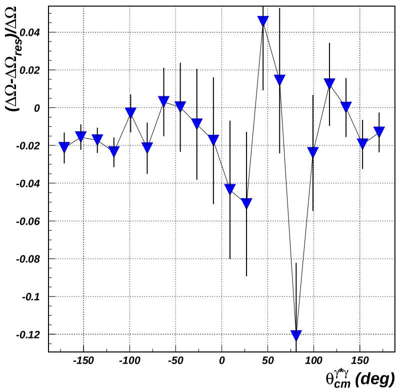

*Figure 4-5: Relative difference between the solid angles that are obtained applying the spectrometer resolution effects and the solid angles obtained not applying these effects. DA_1_15 is the considered kinematical setting.*

section value over the phase space bin considered (see equation (4-1)). When one uses $\Delta\Omega^{exp}_{2,bin}$ a good approximation for the actual cross section value in a point of the bin will be obtained (see equation (4-2)).

It is clear that the accuracy of the solid angle one uses for obtaining experimental five fold differential cross sections is very important. At the time of writing of this thesis, the systematic uncertainty on the obtained solid angle for the Monte Carlo simulation for VCS at TJNAF is estimated to be 4 to 5% [70]. This will become better as the simulation will be improved and tested in the future. The statistical error depends on the amount of simulated data and will be discussed in the analysis chapters of this thesis.

## 4.6 Concluding Remarks

Besides this Monte Carlo simulation for VCS, there also exists a Monte Carlo simulation for elastic scattering. This simulation has the same structure and coding as the VCS simulation, but as the cross section for elastic scattering is quasi exactly calculable, there is no need to approximate the cross section behaviour. Moreover, since the calculation of the elastic scattering cross section is less complicated than the calculation of the BH+Born cross section, the generation of events is very fast, not needing interpolation in a grid. The systematic accuracies (about 3% [70]) are better than for the VCS simulation. Furthermore the elastic scattering cross section behaves smoother than the VCS cross section and as such, the acceptance-rejection method is far more efficient, yielding much better statistical accuracies given the same effort and processor time. This elastic Monte Carlo simulation is extensively used to analyse the elastic scattering data (see chapter 6).

As can be conceived, such a Monte Carlo simulation can be used for many more tasks than just obtaining solid angles. As already mentioned, it can be used to study resolution effects. Comparing experimentally obtained distributions with distributions generated by the simulation gives a very good indication whether one understands everything that is happening. Moreover it is a very useful tool to study systematic uncertainties in the analysis of the experiment. These and other applications will be illustrated in the analysis chapters, further in this thesis.

# Chapter 5

# Analysis of the TJNAF Data at $Q^2$=1.0(GeV/c)$^2$

## 5.1 Overview of the Data

The Virtual Compton Scattering experiment E93-050 that took place in March-April 1998 in Hall A at TJNAF has two main physics goals : studying the photon electro-production reaction below pion production threshold at $Q^2 = 1.0\ (GeV/c)^2$ and $Q^2 = 1.9\ (GeV/c)^2$ in order to extract the generalized polarizabilities, and studying the photon electro-production reaction in the nucleon resonance region in order to extract for the first time VCS cross sections in this region. In order to be able to reach these goals, and in particular the first one, one needs to measure absolute cross sections for the photon electro-production reaction with a very good accuracy (see section 1.6).

The TJNAF VCS data are taken using an electron beam of 4.045 GeV and a duty cycle of 100%, impinging on the 15 cm long liquid hydrogen target. The scattered electron and recoil proton are detected in coincidence in the two Hall A high resolution spectrometers. Details about these experimental components can be found in chapter 3. After reconstructing the momentum and vertex information of the recoil proton and the scattered electron, the four-momentum of the missing (undetected) particle can be reconstructed. This four-momentum gives the means to identify the missing particle : VCS events require the missing mass to be the photon mass $m_\gamma = 0\ MeV/c^2$, while pion production events are characterized by a missing mass $m_{\pi^0} \approx 135\ MeV/c^2$. The phase-space accessible by the kinematical settings for this experiment does not allow other reaction channels to be detected. Thanks to the good energy resolution of the TJNAF facility, the separation of pions and photons by missing mass reconstruction is possible, hence there is no need to detect this missing particle.

The choice of the kinematics to be studied, was on one hand conditioned by the maximum electron energy available and by the limitations of the spectrometers. On the other hand, also physics considerations guided the selection of kinematical settings. Studying VCS below the pion production threshold is done at $Q^2 = 1.0\ (GeV/c)^2$ and $Q^2 = 1.9\ (GeV/c)^2$. The analysis presented in this thesis is focused on the data at $Q^2 = 1.0\ (GeV/c)^2$, hence only these kinematics will be considered in what follows.

The electron spectrometer was set at an angle of 15.42° and a momentum of 3.433 GeV/c, while the proton spectrometer was used at 17 different angle and momentum settings. These settings are chosen in such a way that as much as possible of the accessible photon-proton phase space is covered, avoiding the angular regions where the BH contribution is dominant and avoiding the “elastic line”. Thanks to the high $Q^2$-value, which causes the Lorentz boost to imply a strong focusing of the recoil proton direction along the virtual photon direction (see section 1.5.3) and thanks to the large vertical acceptance of both spectrometers (see section 3.6), the experiment has a large out-of-(leptonic)-plane acceptance. This makes it possible to cover most of the real photon phase space. In figure 5-1 the proton arm kinematics are shown. Each “circle” corresponds to a different value of $s$, and hence $\mathsf{q}'_{\mathsf{cm}}$ (see section 1.5.3). $s$ covers the range : $m_p^2c^4 = 0.88GeV^2 \leq s \leq (m_p + m_{\pi^0})^2c^4 = 1.15GeV^2$, thus $\mathsf{q}'_{\mathsf{cm}}$ is limited to 126.5 MeV/c. The line that is tangent to the circles, represents the recoil proton kinematics of the elastic peak ($Q^2$ is variable and $s = m_p^2c^4$ fixed). The rectangles on the figure indicate the nominal acceptances of the 17 different hadron spectrometer settings. Note that the higher the value for $\mathsf{q}'_{\mathsf{cm}}$, the more hadron spectrometer settings are necessary to cover the complete photon-proton phase space. The kinematics for these 17 settings are summarized in table A-2 in Appendix A, they are denoted DA_1_X with X indicating the number of the considered setting (X=1,2,...,17).

Since this experiment was one of the Hall A commissioning experiments, besides the VCS data, also spectrometer optics and acceptance calibration data were taken. These calibration studies are done mostly using elastic scattering data on the 15 cm long liquid hydrogen target. Also data with empty targets and/or using the sieve slit on the electron or hadron arm are taken. The kinematics for these calibration data and all other data that are taken during the experiment are also summarized in Appendix A.

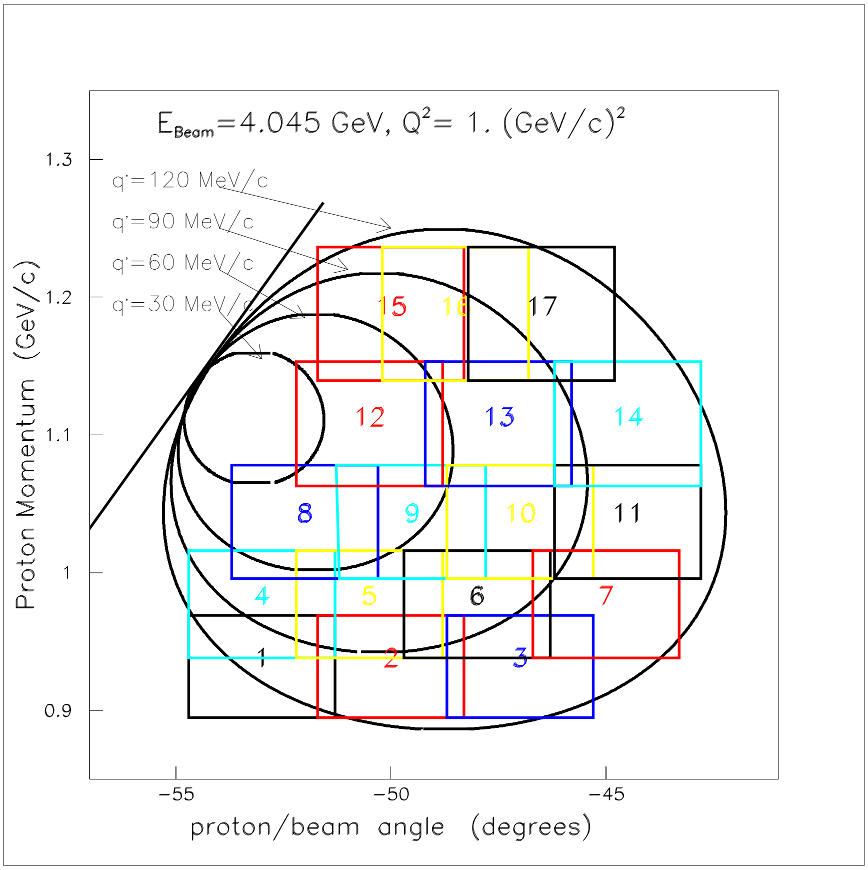

*Figure 5-1: Hadron arm kinematical settings for the data taking below pion production threshold at $Q^2 = 1.0(GeV/c)^2$. The electron spectrometer nominal angle is 15.42° and the central momentum is 3.433 (GeV/c). See text for explanation.*

## 5.2 Making the Data ready for Physics Analysis

More than 450 Gigabytes of data has been taken during the experiment E93-050. About 170 Gigabytes of it represent the VCS data below the pion production threshold at $Q^2 = 1.0\ (GeV/c)^2$ while the elastic data at $Q^2 = 1.0\ (GeV/c)^2$ almost cover 90 Gigabytes. These data contain a lot of useful, but also useless input for the analysis. So the primary concern is to extract all the useful information and to filter out only the data that are relevant for the analysis. In that way, the data to be analysed will be cleaner and significantly reduced, rendering the analysis more efficient and less time consuming. To give an idea, this filtering leaves only 50 Gigabytes of data from the original 170 Gigabytes of VCS data left to analyse. In order to perform this "cleaning-up" and filtering, a systematic approach was used. This is schematically presented in figure 5-2. This diagram gives an overview of all major steps that are taken for each run to obtain clean and filtered data. During this cleaning process, the analyser ESPACE (see section 5.2.1) is used, as well as a number of software tools among which most of them have been developed by the E93-050 collaboration.

The analysis starts with the raw data file e93050_#.dat that is generated during the data taking of the experiment (see section 3.9), # denotes the run number. For each run, a proper header file that is necessary to run any ESPACE kumac is created. The raw data file serves as input for two ESPACE kumacs (EFFICIENCY and CHECKCAL) and the codes GEO and STRIPPER. The ESPACE kumac EFFICIENCY yields information on the trigger efficiencies. The ESPACE kumac CHECKCAL gives the means to determine the electron spectrometer $x$ and $z$ offsets. The software code GEO serves as a tool to verify the quality of a run and to identify the parts of the data that had problems during data taking. Next, STRIPPER filters out the "good" parts of the data, based on the output of GEO and on event type. A next ESPACE kumac (VCS or ELAS, depending on whether one is using VCS data or elastic scattering data) that needs these filtered events and the spectrometer offsets obtained by CHECKCAL, yields an ntuple (vcs_#.hbook/elas_#.hbook) that contains all event information that will be needed to perform the physics analysis. Before doing this analysis, the minimisation code OFFSET optimises (see later) the ntuple and adds relevant flags to the events, using input from different software tools (see figure 5-2). This results in the final ntuple to be analysed.

In the following subsections all relevant steps and software tools that are used to obtain the final input for the physics analysis will be reviewed. The ones that were part of this work will be discussed more in detail. The schematic in figure 5-2 will serve as "fil rouge" throughout this section. Note that although the elastic

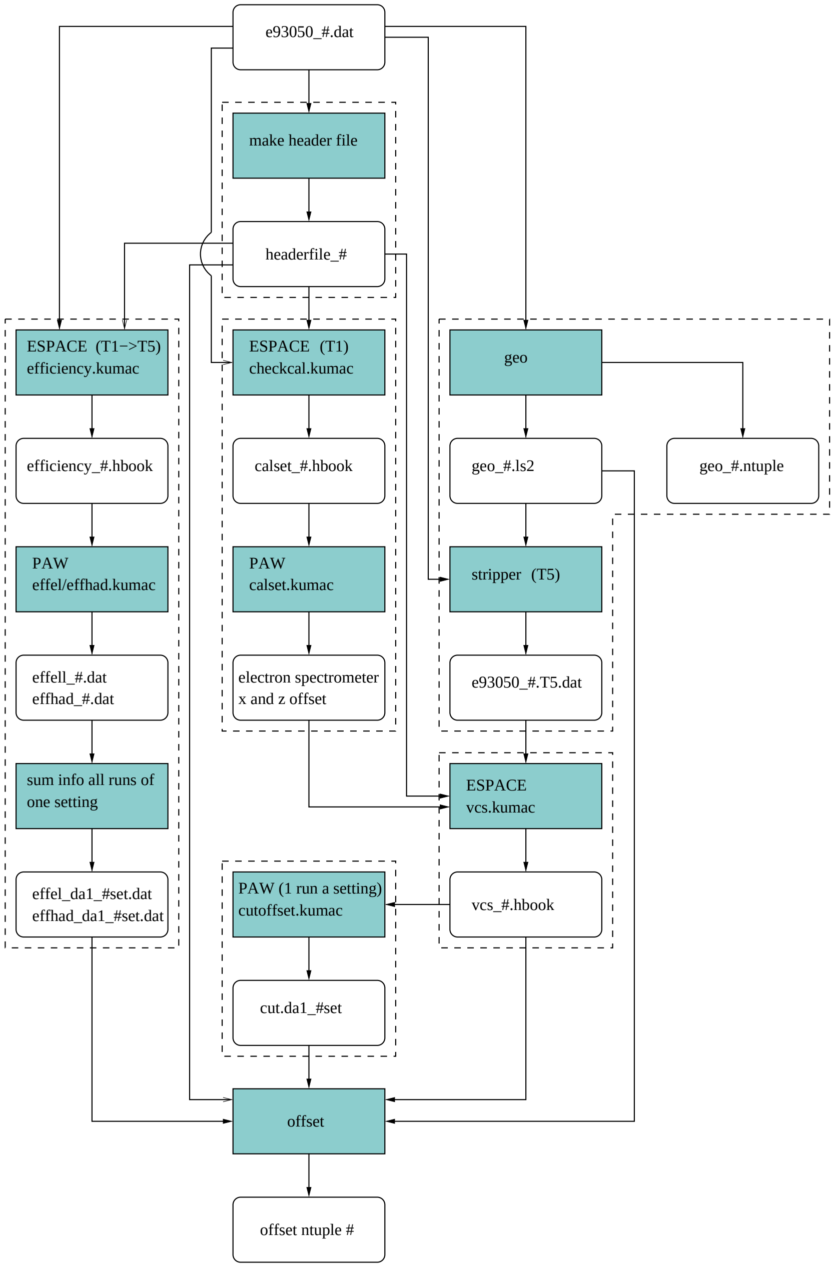

*Figure 5-2: Filtering and preparing processes, applied to the raw data files in order to obtain clean ntuples that are ready to be analysed. The hatched boxes represent the software tools, the blank boxes indicate input/output files.*

scattering data as well as the VCS data have been dealt with following the schematic 5-2, there are differences. They will be explained in the appropriate subsections.

### 5.2.1 ESPACE

ESPACE (Event Scanning Program for Hall A Collaboration Experiments) is a data analysis code that is used to analyse data that are taken in the Hall A at TJNAF. It is a tool that takes the raw data file and filters, histograms and/or calibrates variables of the experimental setup while applying conditions on the incoming data. These variables range from raw detector signals (e.g. ADC and TDC information), focal plane positions and angles, to more elaborate ones like the momentum and direction of a particle.

In order to run, ESPACE needs the following input :

- a *header file* that contains run-specific information such as spectrometer magnetic fields, target parameters, spectrometer offsets, ... . A number of software tools have been developed by the E93-050 collaboration in order to extract this necessary information from the CODA data files. For each data file, a proper header file has been created (see schematic 5-2).

- a *detector map file* that includes the correspondence between the event readout electronics and the physical detector outputs; it contains a description of the physical detectors. The file used for the analysis of this experiment is *detmap6.config*; it was readily available.

- a *database file* that contains basic calibration constants of the detectors (offsets, physical positions, ... ) and the optical matrix database used to reconstruct the target variables of a detected particle, given the focal plane detectors information. The optimisation of this file has been subject to many efforts made by the E93-050 collaboration. For detailed discussions about this topic, one should consult [57, 58, 55, 59]. The database used for the analysis presented in this thesis is *db_lpc_1*.

- a *kumac file* that gives the appropriate commands to ESPACE (where to find/put information, what information to get from the data file, ... ).

Although ESPACE might have been used to do the complete analysis, one has chosen to limit the use of ESPACE to the minimum. It is only used to perform database optimisation and to generate histograms and ntuples containing “basic” variables. To do the physics analysis, proper software tools have been developed (see section 5.5). More details about ESPACE can be found in the ESPACE manual [71].

### 5.2.2 Filtering good and useful events out of the raw data

The decoding program GEO is a utility tool that looks at EPICS and CODA (see section 3.9) information present in the raw data files. It decodes all these informations and allows to display them as a function of time. This permits to identify problems that occurred during the data taking. To give an idea, table 5-1 summarizes the problems encountered while analysing the VCS data at $Q^2 = 1.0\ (GeV/c)^2$ with this code. Note that one run can be affected by more than one problem.

| problem | number of runs (total : 126) | percentage of runs |
|---|---|---|
| no problems | 20 | 16 |
| desynchronisation | 24 | 19 |
| dipole problem | 1 | 1 |
| quadripole problem | 6 | 5 |
| VDC problem | 7 | 6 |
| beam interruptions | 93 | 74 |
| apply additional cut | 13 | 10 |

Table 5-1: *Overview of problems in VCS data at* $Q^2 = 1.0\ (GeV/c)^2$ *identified with GEO.*

Depending on the origin and possible consequence(s) of these problems, one can decide whether one wants to leave out parts of the runs or whether one can/needs to fix certain problems before continuing the analysis. The beam interruptions are left out automatically by GEO, taking into account a target relaxation time of 100 s. As can be seen, a lot of the data suffers from a desynchronisation problem of the BPMs and raster ADCs, so one could not afford to leave out these data. This problem prohibits an event by event determination of the beam position on the target. Hence, a software tool has been developed in order to "fix" this problem. Details about this problem and how it was solved can be found in reference [72]. Some problems could be identified afterwards as being "no problem at all", but just a temporary malfunctioning of a readout device implying no problems for the analysis, hence no action had to be taken. The table shows that 84 percent of the runs had parts that had to be left out.

The code itself generates 2 output files. First an ntuple (geo_#.ntp) containing most of the information present in the raw data file. This ntuple allows to display all kinds of readout, so problems can be associated to event numbers and/or time intervals. Also a text file (geo_#.ls2) is generated. This text file contains the event numbers and time stamps that correspond to the beginning and end of good parts of data as well as the number of different triggers present in these pieces and the corresponding computer life times (see section 5.2.6). This text file serves as input for the code STRIPPER (see below) and the code OFFSET (see section 5.2.10).

After the run has been verified by GEO, STRIPPER scans the raw data file and makes a new data file, containing only the CODA information for events specified in geo_#.ls2. One can choose which trigger types have to be kept. For the analysis of the VCS data, only the T5 trigger types are stored. For the analysis of the elastic scattering data, T1 and T5 events are kept. The different trigger types are defined in section 3.8.

### 5.2.3 Electron spectrometer mispointing

Under ideal circumstances, the central axis of the two spectrometers go through the origin of the Hall A coordinate system (see Appendix B). But in reality, there is a mispointing of the order of millimeters. This mispointing causes a shift in the angle and the acceptance of the spectrometer that is considered. So it is important to know this mispointing in order to correct the assumed angle to the real value. These offsets are essential inputs for the Monte Carlo simulation (see chapter 4) and the ESPACE header file (see section 5.2.1). To measure a mispointing, a Linear Voltage Differential Transformer (LVDT) is used. It measures the off radial distance OO' (indicated by $d$ in figure 5-3) of the spectrometer axis. An accurate determination of $d$ gives means to determine the spectrometer $x$ and $z$ offsets.

To obtain a value for $d$ from the raw LVDT readouts, two calibration constants are needed. They can be obtained from the Jefferson Lab Surveys [73]. For the hadron arm and the vertical mispointing of the electron arm there is no problem, but for the electron arm horizontal LVDT, two sets that are incompatible are available. So a systematic study has been performed to determine which set to use.

This study consisted of running an ESPACE kumac (CHECKCAL) on a number of runs throughout the experiment. For all T1 events $z$ was reconstructed, using

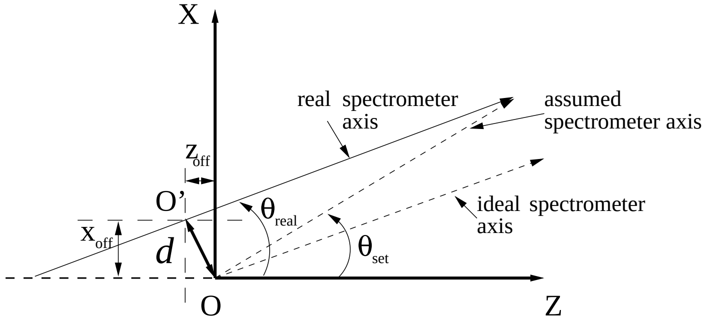

*Figure 5-3: Spectrometer mispointing in the Hall A Laboratory Coordinate System.*

data coming from the electron arm and the given calibration constants. This reconstruction should give an image of the target. Figure 5-4 shows the distributions that were obtained for a run at the beginning of the data taking for DA_1, using both sets of calibration constants. The vertical lines indicate the edges of the target with an uncertainty of ±1mm [74]. Also the $x$ and $z$ offsets obtained with the respective calibration sets are indicated.

It is clear that for this run, the use of the calibration set 0 yields a good image of the target, while calibration set 1 is totally off. This study has been done for many runs, and all of them exclude calibration set 1. However, when the run number increases (time passes by during the experiment), the reconstruction of the target, using calibration set 0, becomes systematically worse. This is shown in figure 5-5. This plot gives a qualitative idea of how the reconstructed target "shifts" along the $z$ axis during the experiment. It shows the "reconstructed target center" as a function of run number. The large error bars on the plot are mainly due to the inaccuracy of the calculation method. The main conclusion that can be drawn from this plot is that there is a "shift" of about 3 mm between the beginning of the data taking at $Q^2 = 1.0\ (GeV/c)^2$ and the end.

Since the origin of this "shift" is not clear, and since there are suspicions that the horizontal LVDT on the electron arm did not work properly [73], one decided not to rely on the horizontal LVDT readout and to "adjust" manually the $x$ and $z$ offsets in order to have a "centered" image of the target. In practice, for the analysis of the experiment, one kept calibration set 0 for the first part of the DA_1 data (up to run number 1654), i.e. the offsets calculated with the information coming from

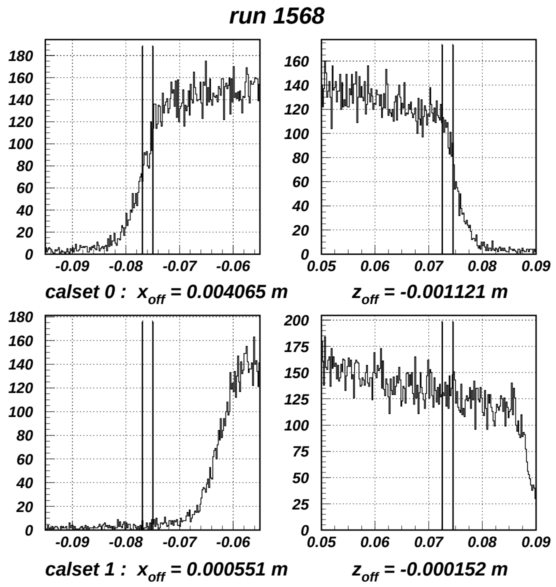

*Figure 5-4: Target reconstruction along the Z axis of the Hall A Laboratory Coordinate System for T1 events, using the two available calibration sets.*

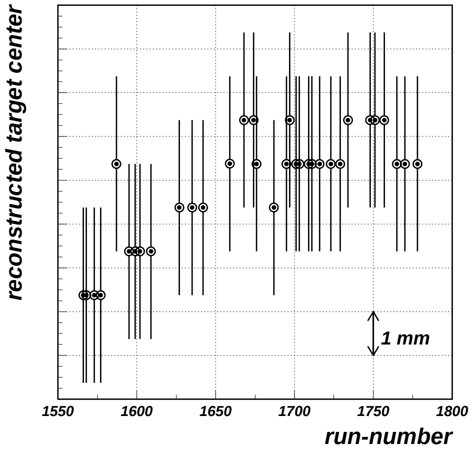

*Figure 5-5: Qualitative shift of the (T1) reconstructed target center along the Z axis of the Hall A Laboratory Coordinate System during DA_1.*

the LVDT. For the second part, 0.9 mm was added systematically to the $x$ offset given by calset 0, the $z$ offset was changed accordingly ($z_{off}^{new} = -x_{off}^{new} * tan(15.389°)$ where 15.389° is the nominal angle of the electron spectrometer). This "re-centered" the image of the target back to the supposed position. This is shown in figure 5-6.

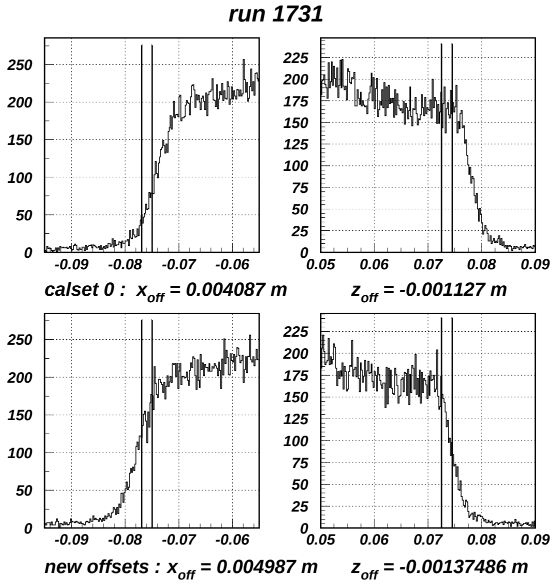

*Figure 5-6: Target reconstruction along the Z axis of the Hall A Laboratory Coordinate System for T1 events, using calibration set 0 (upper figures) and using the manually changed offsets (lower figures).*

A brief study has been performed in order to see what systematic error is introduced in the analysis, caused by a mispointing uncertainty of the electron arm. This study has been done using the Monte Carlo simulation for elastic scattering (see chapter 4). Two simulations have been done with all input parameters alike, except for the $x$ (and accordingly the $z$) offset of the electron spectrometer. A difference of 1 mm for the $x$ offset was introduced. Solid angles have been calculated and their relative differences are considered. The main conclusion that can be drawn from this study is that a mispointing uncertainty of 1mm of the electron arm yields a systematic error on the solid angle of 1-2% up to 4% near the acceptance edges.

Note that the real electron angle setting during the data taking for CA_1 and DA_1 was 15.389° and not 15.42°, as mentioned in the proposal.

### 5.2.4 Prescaling

The number of events that are recorded in the data file, does not match the number of events that arrived at the scalers. This is due to an intentional decrease of the number of events of a certain trigger type. This is done in order not to overload the data file with less interesting trigger types. Indeed, since for most of the data, we are especially interested in coincidence events (trigger type T5), it is useless to fill the data file with lots of single trigger types (T1 and T3) that occur much more than coincidence events. To avoid this, each trigger type has been assigned a certain prescale factor $PS$. This factor indicates that for each $PS$ events of that certain trigger type, only one has to be recorded in the data stream. These run dependent prescale factors are known and can be applied without any problem. Note that for the T5 triggers, the prescale factor was always 1, so all T5 events are recorded in the data files.

### 5.2.5 Electronic dead time correction

As repeatedly mentioned, calculating cross sections requires counting measured events. Unfortunately the number of events one measures does not match the number of events that actually had to be detected. This is due to inefficiency problems present everywhere in the experimental equipment. A first correction one has to apply to the measured number of events comes from the electronic dead time. Since the counting rates in the scintillators were high during the experiment and since one aims at measuring cross sections with a high accuracy, the electronic dead time becomes important. Details on this electronic dead time and how it was calculated can be found in references [75, 76].

For the analysis presented in this thesis, the correction on the elastic scattering data is 0.3%. The correction on the VCS data is 3%. These values are an overall estimate, based on the electronic dead time of a sample of runs.

### 5.2.6 Computer dead time correction

A second correction one has to apply to the measured number of events originates from the computer dead time. Indeed, each time the computer is handling the formation of an event record and putting it in the data file, the computer is blind for other events arriving. To account for this loss of events, the computer dead time has to be determined.

The computer dead time varies over time (depending on computer load, prescale factors), as such it has to be determined for each portion of the runs. Moreover it has been shown [77] that different trigger types can have different dead times. The determination of these computer dead times, denoted as $DT$, is done in a simple-minded way. It is calculated as 1 minus the ratio between the number of events found in the data file and the expected number of events :

$$DT1 = 1 - \frac{PS1.T1}{S1 - S5} \tag{5-1}$$

$$DT2 = 1 - \frac{PS2.T2}{S2} \tag{5-2}$$

$$DT3 = 1 - \frac{PS3.T3}{S3 - S5} \tag{5-3}$$

$$DT4 = 1 - \frac{PS4.T4}{S4} \tag{5-4}$$

$$DT5 = 1 - \frac{PS5.T5}{S5} \tag{5-5}$$

with $PS1$-$PS5$ the prescale factors of the different trigger types, S1-S5 the number of triggers that arrived during the data acquisition as counted by the scalers and T1-T5 the number of trigger types, present in the data file. Note that for the trigger types T1 and T3, one has to take into account that a coincidence of a trigger type T3 and a trigger type T1 is only recorded as a trigger type T5, however the scalers record a trigger type S5 also as a trigger type S1 and S3, so one has to avoid double counting of these scalers.

Typical values for the computer dead time for elastic data are 10 % to 20 %, for VCS data, the computer dead times range from 10 % to 40 %.

### 5.2.7 Scintillator and trigger efficiency

Another inefficiency correction that has to be applied to the measured number of events is due to the inefficiency of the scintillators and the trigger logic (see sections 3.7.2 and 3.8). Due to this inefficiency there are some good triggers that are classified as being junk triggers (e.g. VDC information (see section 3.7.1) combined with information form the S1 scintillator plane matches a possible track, but a valid S2 signal is missing). So it is important to be able to quantify this fraction of “missed” events and to correct the measured number of events accordingly.

The basic idea behind this study is to divide the scintillator planes S1 and S2 for the electron and hadron arm in 2-dimensional bins (along the paddle and perpendicular to the paddle axes) and to define for each bin the appropriate efficiency. In that way we can apply an event-by-event weight to the measured data, depending on the place where the particle hit the scintillator planes. This method is preferred over applying an overall weight that is the same all over the scintillator planes since it takes into account possible differences in efficiency for different places on the scintillator planes. Indeed, for example one observed, especially at the beginning of the experiment and thus during the data taking for DA_1, a strong difference in efficiency between the different paddles in S2 of the electron arm. This is illustrated in the 4 top figures of figure 5-7 where the inefficiencies of the electron and hadron arm S1 and S2 planes are plotted as a function of *xdetgeom*, which is the spatial coordinate related to the paddle that is hit. These figures show that the inefficiencies of paddles number 1, 3 and 5 of the electron arm S2 plane are less than 0.5 %, while paddle number 4 has an inefficiency of almost 3%. This is due to inefficient working photo-multipliers. For the hadron arm, the inefficiencies are almost negligible. The high inefficiency values for the extreme paddle numbers are due to low statistics when calculating the inefficiencies. Besides the fact that the inefficiencies are place-dependent, also a time-dependency has been observed. This can be seen for example by comparing the two top figures with the two bottom figures in figure 5-7. They represent the same inefficiencies, but with a time-difference of about 4 days. So also a time-dependency has to be taken into account when defining the corrections that have to be applied to the measured number of events.

In order to construct such “weight-grids”, an ESPACE kumac (EFFICIENCY) gathering all the necessary information, has been applied to all the runs. The resulting hbook files are analysed, yielding 2 files for each run. One that contains the inefficiencies of each bin in the two electron scintillator planes and one that contains the same information for the hadron arm. The binning of the scintillator planes has been chosen in such a way that the inefficiency within a bin is rather constant. Moreover, to have enough statistics on the inefficiencies in order to keep the error low, and still minimise the effect of possible time-dependencies of the scintillator inefficiencies, all “inefficiency-grids” belonging to runs of one setting were merged, yielding one “inefficiency-grid” for each setting of DA_1. Details about the binning and the calculation method of these inefficiencies can be found in [78].

The corrections that have to be applied to the measured number of events due to this scintillator inefficiency are typically a few percent. The error on the inefficiencies mainly comes from statistics and is very low [78].

### 5.2.8 Random coincidence subtraction

The variable *tc_cor* gives the time, corrected for difference in path-length of the particles, that passed between the two spectrometer triggers of a coincidence event. It is an important criterium to identify true coincidence events. As already

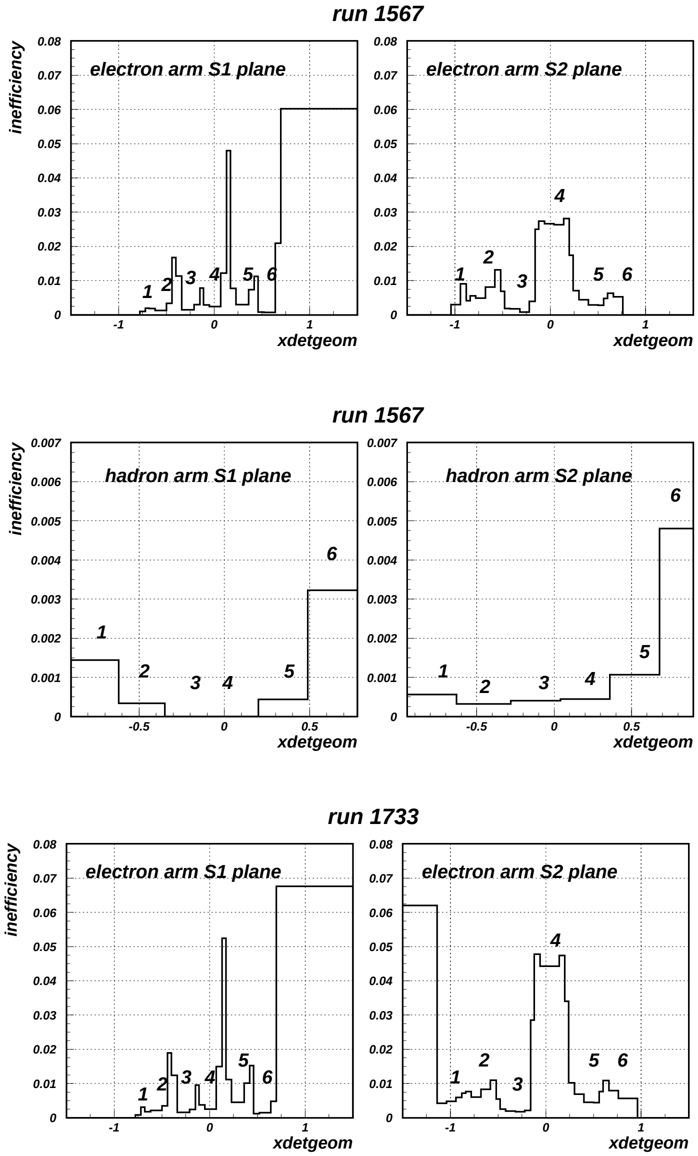

*Figure 5-7: Inefficiencies of the electron and hadron arm scintillator planes S1 and S2 for run number 1567 and the electron arm scintillator planes for run number 1733. The numbers on the figure indicate the paddle numbers. The values are averaged along the paddle axes.*

mentioned (section 3.8) the coincidence time window is 100 ns. The time between 2 beam pulses is about 2 ns (section 3.2), as such 50 beam pulses are present in the considered time window. Different scattering events can cause accidental coincidences. This is illustrated in the top plot of figure 5-8.

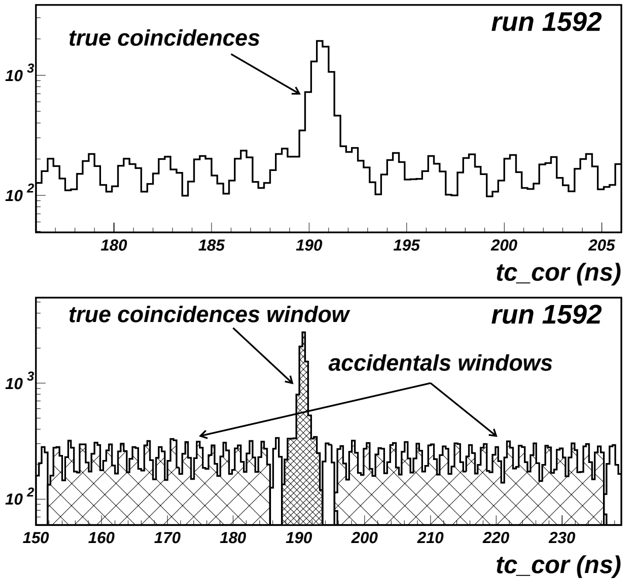

*Figure 5-8: Method to correct for random coincidence events, illustrated on run 1592.*

The corrected coincidence time of flight of run 1592 is shown. One clearly sees the true coincidences peak around 191 ns and the accidental coincidence events, generated by different scattering events. The minimal cut one should apply to identify real coincidences is this main peak. Since accidental coincidences also are present in this main peak region, one has to correct for them. The way this is done, is explained on the basis of the bottom plot in figure 5-8. The events one defines as being good coincidence events are the ones from the main coincidence peak and the two nearby beam pulses. The probability to have accidental coincidences in this time window is the same as the probability to have accidental coincidences in any other time window. As such, one considers two other “accidentals” time windows, one before and one after the true coincidence peak. The complete analysis of the data is done, taking into account all events in these 3 time windows, but when evaluating the number of events present in the analysis, the events that are in the

2 accidentals windows are given a weight defined by minus the ratio of the size of the true coincidence window over the size of the sum of the two accidental time windows. In that way, one corrects for the accidentals that are present in the true coincidences window.

In figure 5-9 the effect of random subtraction on the missing mass squared distribution for setting DA_1_15 is shown. The dashed/dotted line represents the missing mass squared distribution without random subtraction, the full line is the same distribution, but with random subtraction.

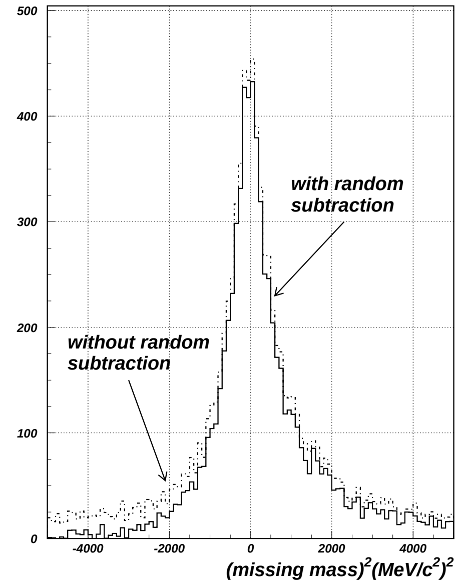

*Figure 5-9: Effect of random coincidence subtraction on the missing mass squared distribution for setting DA_1_15. Additional cuts have been applied to the events (see section 7.3) in order to clean the plot.*

### 5.2.9 Multiple track correction

The analysis that is presented in this thesis is performed on T1 events (for elastic scattering) with only 1 reconstructed track in the electron arm, and T5 events (for elastic scattering and VCS) with exactly 1 reconstructed track in the electron arm and 1 reconstructed track in the hadron arm. Using this approach, one does not have to bother with events that have more than one reconstructed track and that might thus introduce uncertainties in the reconstruction of vertex variables.

By eliminating all events that have multiple tracks, one also eliminates good events (e.g. good event + cosmic ray), so one has to correct for this. The way this is done in the analysis is straightforward. The basic assumption that is made is that the ratio of good events to bad events is the same for events that have 1 track in both arms (for T1 events 1 track in the electron arm) and events that have multiple tracks in one or both arms (for T1 events multiple tracks in the electron arm). The variables that are used to make the selection 1 track or multiple tracks are the variables *spec_e.track* and *spec_h.track* generated by ESPACE. These variables give the number of reconstructed tracks in the electron arm and hadron arm [71]. In the following they will be denoted as $et$ and $ht$, respectively. The number of “missed” events due to this track selection and for which one has to correct afterwards the measured number of events is :

$$T1_{cor} = T1_{meas}.\frac{T1(et > 1)}{T1(et = 1)} \tag{5-6}$$

$$T5_{cor} = T5_{meas}.\frac{T5\left((et \neq 0).and.(ht \neq 0).and.[(et > 1).or.(ht > 1)]\right)}{T5[(et = 1).and.(ht = 1)]} \tag{5-7}$$

These correction factors are calculated setting per setting and applied after the good event selection (see diagram 5-13). Typical correction values are 3-4%.

### 5.2.10 Minimization procedure

Before starting the physics analysis, all ntuples resulting from the ESPACE kumac VCS are optimized by the code OFFSET. This minimization code can determine and correct remaining offsets on the vertex variables and also their correlations with some experimental variables. One condition for being able to do so is that the corrections have to be small, so that a linear expansion is justified. Details on this code can be found in reference [79].

For the analysis of the VCS data at $Q^2 = 1.0$ $(GeV/c)^2$ the code is used to determine the offset on the beam energy by optimizing the missing mass squared and the offset on $y_{tg}$ in the hadron arm by optimizing $d$. $y_{tg}$ is defined in the target coordinate system (see Appendix B) and $d$ is the difference between the crossing of the reconstructed tracks in the electron and hadron arm and the beam position along the Hall A X-axis (see figure 5-10). The result of these optimizations is illustrated in figures 5-11a and 5-11b where the missing mass squared and $d$ are plotted for one run of DA_1 before and after the optimization. These optimizations have been systematically performed on all runs of DA_1. The optimizations of the missing mass squared indicate there was a beam energy offset of about -13.4 to

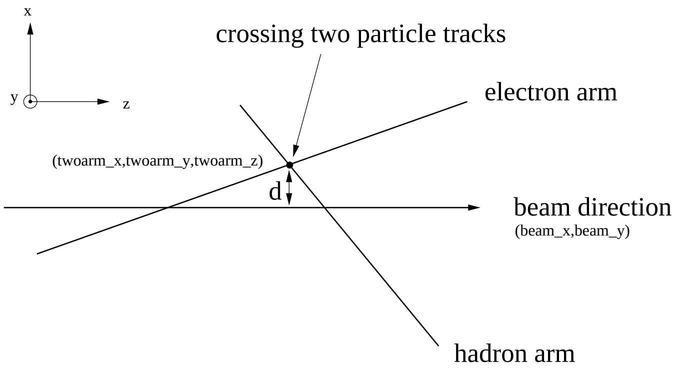

*Figure 5-10: Definition of the observable d=twoarm_x-beam_x.*

-15.3 MeV. As such the analysis is performed assuming the beam energy was not 4045 MeV, but 4030.5 MeV. This is important in order to run the simulation and to run any ESPACE kumac. As will be seen in section 6.2, also the analysis of elastic scattering data indicates the beam energy was lower than what one assumed.

The ntuple that is generated by the OFFSET code contains besides the original variables that are modified following the minimization processes, some additional reconstructed variables (e.g. physics variables like missing mass) and weights to account for scintillator inefficiencies, computer dead times and accidental coincidences. These have been described in the previous subsections.

The optimization procedures of this code can not be applied to elastic scattering data since these data only cover a small part of the focal plane. As such. in the elastic case the code is only used to add the weights to the events in the ntuple. Consequently, no optimizations have been performed for the elastic scattering data.

## 5.3 Luminosity Determination

Calculating cross sections requires the knowledge of the integrated luminosity. This integrated luminosity is calculated as [1]:

$$\int \mathcal{L} dt = \int L N_a n_t dt \tag{5-8}$$

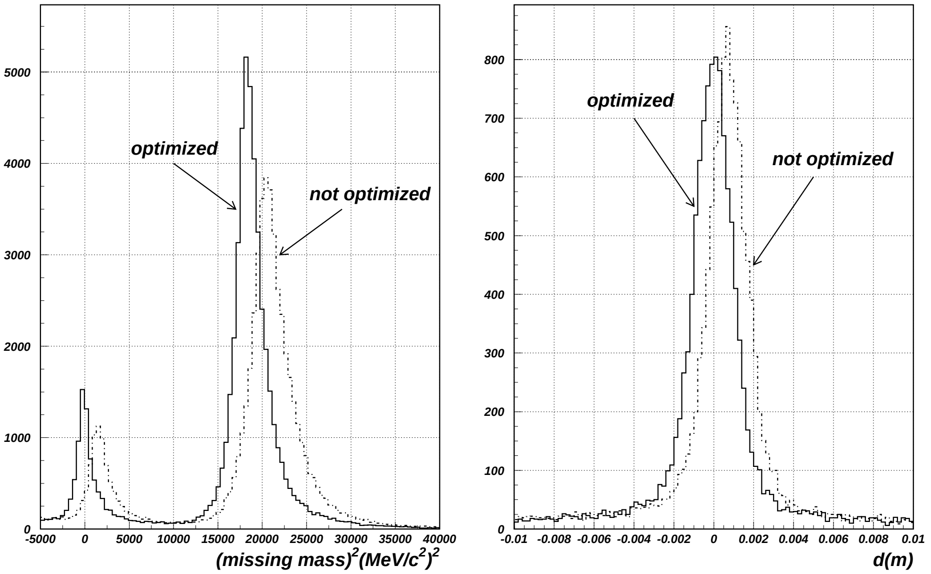

(a) Missing mass distribution of run 1645. To clean the plot, the following cuts are applied : $abs(d) < 0.0025$; $185 < tc\_cor < 195$; $etrack = 1$ and $htrack = 1$.

(b) $d$ distribution of run 1728. To clean the plot, the following cuts are applied : $7500 < m\_miss2 < 35000$;$185 < tc\_cor < 195$; $etrack = 1$ and $htrack = 1$.

*Figure 5-11: Missing mass and d distributions before and after optimizing with the OFFSET code.*

with $N_a$ the number of electrons impinging per second on the target, $n_t$ the number of target particles per $cm^3$, $L$ the target length in units $cm$ and $dt$ the time interval (in seconds) that is considered. Assuming that the target density stayed constant during the time intervals that are considered, the following formula is used :

$$\int \mathcal{L} dt = \frac{Q \rho N_A L}{e} \tag{5-9}$$

where $Q$ (Coulomb) is the total charge that is accumulated during $dt$, $\rho$ is the target density ($0.0723 g/cm^3$ [53]), $N_A$ is Avogadro's constant ($6.0221367 \times 10^{23} mol^{-1}$) and $e$ is the electron charge ($1.602177 \times 10^{-19}$C).

The luminosity is determined with an accuracy better than 1% [80]. The target density plays an important role when calculating the luminosity. Indeed, it has been shown that the target density diminishes by 2% when the current changes by $80 \mu A$ [80]. As such also the target boiling has been studied. For details about these studies, see reference [80].

## 5.4 Calculation of Radiative Corrections

In all electron scattering experiments, it is necessary to take into account radiative effects when determining experimental cross sections. Indeed, in order to be able to compare experimentally obtained cross section values with theoretical predictions, the measured cross sections have to be corrected for these effects. In this work, one wants to measure cross section values for the photon electro-production reaction. Unfortunately, when performing the experiment, it is impossible to study the "pure" reaction, since in the reaction process additional real and virtual photons can be emitted. This gives rise to measured cross section values that are affected by these additional processes. As such, one will have to correct the measured cross section values for these radiative processes in order to obtain the "pure" photon electro-production reaction cross section values.

Two types of radiative corrections can be distinguished :

- external radiative corrections : these take into account the Bremsstrahlung radiation that is emitted by the incoming and/or outgoing electron(s) in the presence of a charged particle that is not the scattering proton.
- internal radiative corrections : they take into account the emission of additional real photons (real internal radiation) and the emission and re-absorption of additional virtual photons (virtual internal radiation) at the scattering proton. The latter do not change the final kinematics, they only have an effect

on the measured cross section value.

For elastic scattering, these external and real internal radiation effects cause the energy spectrum of the scattered electron to have a “tail”. This is due to the energy losses associated with real radiation effects. For photon electro-production reactions, these real radiative effects can be observed as a tail in the missing mass spectrum. This is illustrated in figures 5-12a and 5-12b.

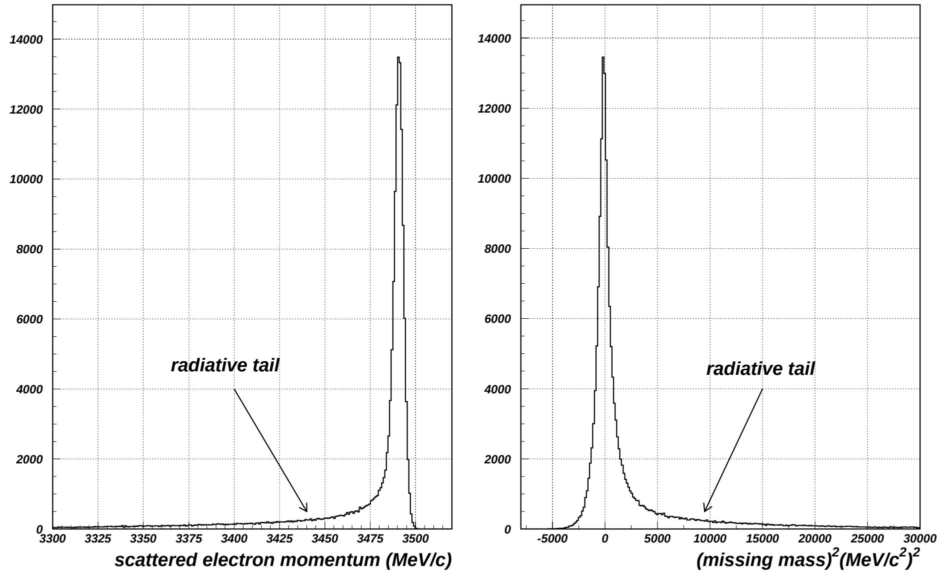

(a) elastic scattering

(b) photon electro-production

*Figure 5-12: Simulated distributions, illustrating the radiative tail, caused by the external and part of the real internal radiation processes.*

The external radiative corrections are completely taken into account in the Monte Carlo simulation (see chapter 4) by means of the electron energy loss distribution for Bremsstrahlung. As such, they are already present in the deduced solid angle and it is not needed to correct for them.

For the internal radiative effects, one can write :

$$d^5\sigma^0 = d^5\sigma^{measured} \ \times \ e^{-\delta} \tag{5-10}$$

where $d^5\sigma^0$ is the “pure” photon electro-production reaction cross section, $d^5\sigma^{measured}$

the experimentally obtained one and $\delta$ can be written as :

$$\delta = \delta_V + \delta_R \tag{5-11}$$

$\delta_V$ corresponds to the internal virtual radiation and is quasi constant in the considered phase space, $\delta_R$ corresponds to the real internal radiation correction and can be written as :

$$\delta_R = T_{anal} + F(\Delta M^2_{cut}) \tag{5-12}$$

with $T_{anal}$ an analytic function that only depends on the kinematics and that is nearly constant for the considered phase space. $F(\Delta M^2_{cut})$ (for elastic scattering $F(\Delta E_{cut})$) is the part of $\delta_R$, depending on the experimental cut in missing mass squared, that generates the radiative tail. Also this radiative correction ($F(\Delta M^2_{cut})/F(\Delta E_{cut})$) has been included in the Monte Carlo simulation; as such, also this part of the real internal radiative correction is already taken into account in the obtained solid angle.

All radiative corrections that are discussed above are on the electron side of the interaction. Besides these, an additional small correction $\delta_{cont}$ has to be taken into account. This correction deals with virtual radiative corrections on the proton side, the two-photon exchange corrections and the soft-photon emission from the proton.

| kinematic | $\delta_V$ | $T_{anal}$ | $\delta_{cont}$ | $e^{-\delta_V-T_{anal}-\delta_{cont}}$ |
|---|---|---|---|---|
| VCS at $Q^2 = 1.0(GeV/c)^2$ | -18.3% | +26.7% | -1.3% | +93.1% |
| elastics at $Q^2 = 1.0(GeV/c)^2$ | -18.6% | +26.8% | -1.0% | +93.1% |

Table 5-2: *Radiative corrections to be considered when calculating experimental cross sections at $Q^2 = 1$ $(GeV/c)^2$. Values are taken from reference [81].*

To summarize, the "pure" photon electro-production reaction cross section can be obtained as :

$$d^5\sigma^0 = d^5\sigma^{measured} \ \times \ e^{-(\delta_V+T_{anal}+\delta_{cont})} \tag{5-13}$$

where $d^5\sigma^{measured}$ is the cross section that is obtained with a solid angle that already takes into account the corrections for external radiation and $F(\Delta M^2_{cut})$ ($F(\Delta E_{cut})$). Table 5-2 summarizes the values for the corrections one has to apply to the measured cross section values in the analysis of the E93-050 experiment.

For details about all these radiation effects, see references [82], [23] and [25], for a description of how they are implemented in the elastic and the VCS simulation see reference [63].

## 5.5 Extracting Experimental Cross Sections

The cross sections that are presented in this thesis, are calculated as follows :

$$\left(\frac{d^5\sigma}{d\Omega}\right)^{exp} = f_{radcor} \times \frac{f_{globalcor} \times N^{exp}}{\mathcal{L}^{exp}\Delta\Omega^{sim}} \tag{5-14}$$

with

- $N^{exp}$ the number of measured events in a certain chosen phase-space bin, applying well-chosen cuts
- $\Delta\Omega^{sim}$ the solid angle, obtained with the Monte Carlo simulation (see chapter 4), describing the chosen phase-space bin, applying the same cuts
- $\mathcal{L}^{exp}$ the integrated luminosity that yielded these $N^{exp}$ events (see section 5.3)
- $f_{radcor}$ the radiative correction that has to be applied (see section 5.4)
- $f_{globalcor}$ the correction that has to be applied to the measured number of events. This correction includes prescaling, electronic and computer dead times, scintillator inefficiencies, random subtraction and multiple track correction (see sections 5.2.4 to 5.2.9). Note that this correction has to be applied event by event.

Experimental cross sections are obtained using MARGHARITA, a software tool that has been developed as part of this thesis work. This program serves to calculate photon electro-production cross sections. The schematic 5-13 gives an overview of the structure and actions of MARGHARITA.

The two main inputs that are needed in order to obtain experimental cross sections are the ntuple generated by OFFSET and the ntuple generated by the Monte Carlo simulation. These two ntuples are treated in exactly the same way, applying the same cuts and parameters, in order to obtain the number of events present in the chosen phase-space bins. The definition and parametrisation of these phase-space bins and cuts is done in the files cuts.dat and param_#.dat. Since for the analysis of the data, we have chosen to run the simulation without a raster profile (using a flat raster), MARGHARITA takes the real raster profile from the experimental ntuple and applies this to the simulated events (see reference [83]).Moreover,

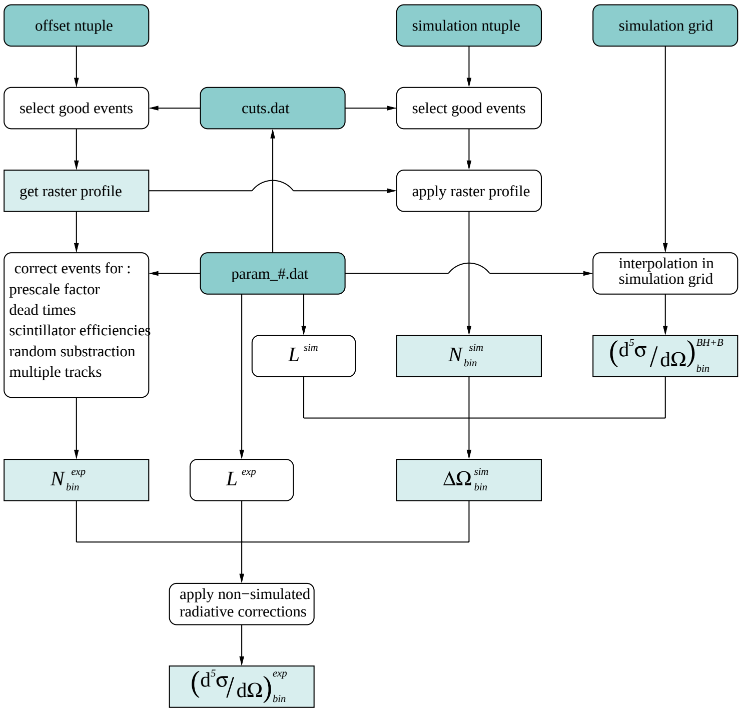

*Figure 5-13: Schematic representing the structure of MARGHARITA. See text for explanation.*

the number of measured events is corrected as mentioned in the schematic. After these corrections, the number of events in each phase-space bin is counted for the simulation and the experiment. The number of simulated events in a certain well-defined phase-space bin, together with the interpolated BH+Born cross section in the center of that phase-space bin and the simulation luminosity yields the solid angle (see chapter 4). The number of measured events in that same phase-space bin, together with the experimental luminosity (see section 5.3) and the obtained solid angle of that phase-space bin, yields the cross section value in the center of the phase-space bin. After applying radiative corrections as described in section 5.4, we dispose of the five fold differential cross section that can be compared with theoretical predictions.

The way elastic scattering cross sections are obtained is similar to the procedure described above.

## 5.6 Error Analysis

The cross section values that are presented in this thesis are subject to systematical and statistical errors. The systematical errors can be divided into two categories. The first kind is connected to the global normalisation, they affect all cross section values in the same way and do not disturb the form of any distribution. The second kind might deform the angular and/or momentum distribution(s) (e.g. due to optical aberrations in the spectrometers). Up to now, no detailed study has been performed in order to define the systematical uncertainty on the obtained cross section values. As such, only rather crude estimates and results of some preliminary studies will be given here (see this thesis and reference [55]).

For the global errors, not having any effect on the distributions, but only generating a normalisation effect, one estimates the systematical error to be at most 3%. This error originates from the luminosity calculation (<1%), dead time determination (<1%), radiative corrections (±2%), ... .

The errors, deforming the cross section distributions are estimated to cause a maximum systematical error of 20%. This error originates from the uncertainty on the simulated solid angle (hypotheses that are made in the simulation, resolution effects that are not perfectly well reproduced in the simulation, ... )(<5%), offsets of the experimental apparatus (±10%), offsets still present in the database (±5%), radiative corrections depending on the cut in $(missing\ mass)^2$, absolute position of the beam on the target (±7%), systematical errors related to cuts that are applied to the data (±10%), ... .

For this analysis, one estimates the overall systematical uncertainty on the obtained cross section values to be at most 20%. Note that a detailed study of this problem is not that trivial. Many sources are related to other sources and can not be treated independently. For example the systematical error caused by the cut in $(missing\ mass)^2$ can be due to offsets, resolutions, radiation effects in the simulation, ... .

In order to explain how the statistical errors are calculated, one has to remind how experimental cross section values are obtained (formula 5-14) :

$$d^5\sigma = \frac{N^{exp}}{\mathcal{L}^{exp}\Delta\Omega^{sim}} \tag{5-15}$$

with $N^{exp}$ the corrected number of events present in the considered bin, $\mathcal{L}^{exp}$ the experimental luminosity and $\Delta\Omega^{sim}$ the solid angle obtained with the simulation. The error on this cross section value is calculated as :

$$\sigma(d^5\sigma) = d^5\sigma \times \sqrt{\frac{\sigma^2(N^{exp})}{(N^{exp})^2} + \frac{\sigma^2(\Delta\Omega^{sim})}{(\Delta\Omega^{sim})^2}} \tag{5-16}$$

where one supposes that the experimental luminosity is only responsible for a systematical uncertainty on the cross section value.

$\sigma(N^{exp})$ and $\sigma(\Delta\Omega^{sim})$ are given by the following expressions

$$\sigma(N^{exp}) = \sqrt{\sum_{i=1}^{n^{exp}} (w_i^{exp})^2} \tag{5-17}$$

$$\sigma(\Delta\Omega^{sim}) = \frac{1}{\mathcal{L}^{sim} d^5\sigma^{sim}} \sqrt{\sum_{i=1}^{n^{sim}} (w_i^{sim})^2} \tag{5-18}$$

with $w_i$ the weight of event $i$. For the experimental events, $w_i$ represents the correction factor that includes all corrections that are described in sections 5.2.4 to 5.2.9. For the solid angle, $w_i$ is the weight that is used to apply the raster profile to the simulated events (see section 5.5). Note that for the calculation of the solid angle, the inaccuracy on the simulated luminosity ($\mathcal{L}^{sim}$) and cross section value ($d^5\sigma^{sim}$) are supposed to be negligible compared to the statistical uncertainty. Combining formula's (5-16), (5-17) and (5-18) yields for the statistical error on the experimental cross section value :

$$\sigma(d^5\sigma) = d^5\sigma \times \sqrt{\frac{\sum_{i=1}^{n^{exp}} (w_i^2)}{\left(\sum_{i=1}^{n^{exp}} w_i^{exp}\right)^2} + \frac{\sum_{i=1}^{n^{sim}} (w_i^2)}{\left(\sum_{i=1}^{n^{sim}} w_i^{sim}\right)^2}} \tag{5-19}$$

These statistical errors are plotted as error bars on all cross section values presented in this thesis.

The solid angles in this thesis are obtained with a number of counts that is 5 to 10 times higher than the experimental number of counts. The statistical accuracy of the solid angles has to be increased in the future.

# Chapter 6

# Elastic Scattering Cross Sections at $Q^2$=1.0(GeV/c)$^2$ as a Calibration Check of the Measurements

## 6.1 Overview

The elastic scattering data that were taken during the experiment were not only useful to perform calibrations of the experimental equipment, they also serve as a very important tool to check the absolute calibration of our measurements, to test the radiative corrections that are calculated and to justify the choice of the proton form factors that are used to calculate the BH+Born cross sections. Indeed, since the elastic scattering cross section can be exactly calculated once the electric and magnetic form factors of the proton are known (see section 1.2), a comparison between the experimentally obtained elastic scattering cross sections and the calculated cross sections will give an idea of the quality of the analysis. The elastic scattering data that are presented in this thesis, are summarized in table 6-1. The different elastic scattering kinematical settings at $Q^2 = 1.0 (GeV/c)^2$ are denoted CA_1_X with X indicating the number of the considered setting.

In figure 6-1 a schematic of the electron arm kinematics of these settings is shown. The dotted rectangle represents the electron spectrometer acceptance. The vertical axis is the momentum acceptance, while the horizontal axis represents the scattering angle acceptance. The “elastic peak”, represented by the diagonal lines, moves across the focal plane by changing the magnetic field by 2%.

Since the elastic scattering cross section value changes significantly within

| | electron spectrometer | | | | hadron spectrometer | | |
|---|---|---|---|---|---|---|---|
| setting | $\frac{\delta P}{P}$(%) | P (GeV/c) | $\theta_E(^\circ)$ | colli | P (GeV/c) | $\theta_H(^\circ)$ | colli |
| ca_1_10 | -2 | 3.433 | 15.42 | 6 msr | 1.143 | -54.28 | 6 msr |
| ca_1_16 | +0 | 3.496 | 15.42 | 6 msr | 1.143 | -54.28 | 6 msr |

Table 6-1: *Elastic scattering kinematics for which cross sections are presented. For each spectrometer, its central momentum setting P is given, as well as its angle setting and the collimator that is used. For the electron spectrometer the momentum setting relative to the elastic peak momentum is also given ($\delta P/P$).*

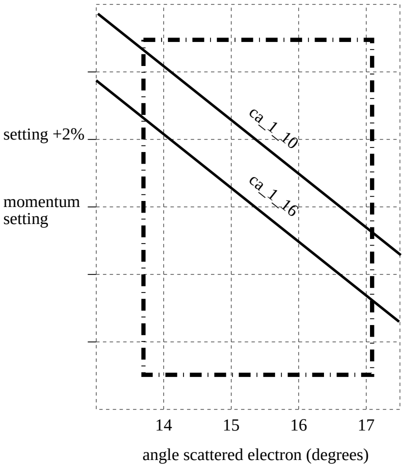

*Figure 6-1: Schematic representing the focal plane coverage of the presented elastic scattering kinematics at $Q^2 = 1.0(GeV/c)^2$.*

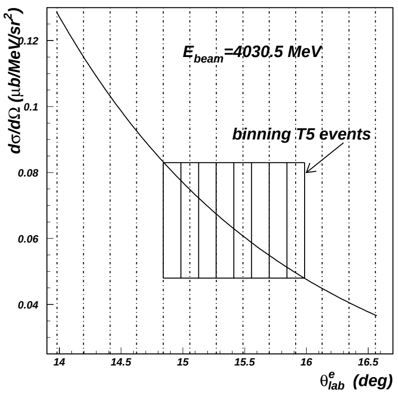

*Figure 6-2: Elastic scattering cross section as a function of the electron scattering angle. The vertical dashed lines represent the 12 bins one has defined to study the T1 elastic scattering cross sections. The full lines represent the binning for the T5 elastic scattering analysis.*

the horizontal electron spectrometer angular acceptance, one has chosen to divide this horizontal acceptance in bins. This is shown in figure 6-2. In this figure the elastic scattering cross section is drawn as a function of the electron scattering angle. The aim of the elastic scattering studies will be to reproduce this curve. As a consequence of the angular settings of the 2 spectrometers, T5 events will only cover a part of the electron spectrometer acceptance. As such, the binning for T5 events is different. This is also indicated in the figure.

## 6.2 Comparing the Elastic Simulation with the Experiment

Before looking at actual cross section values, it is necessary to compare experimental distributions with distributions generated by the Monte Carlo simulation. This study will give an idea of how well one controls the resolutions and offsets that come into play. There are mainly 2 types of observables that are studied : single arm observables (electron or hadron arm) and double arm observables. Since different observables are sensitive to different spectrometer variables and/or offsets, a selection of well chosen observables will allow to make conclusions on (combinations of) different resolutions and/or offsets. The observables that are used for this study are summarized in table 6-2. All of them are sensitive to some of the spectrometer reconstructed variables and/or the beam energy at the vertex (denoted as $E_{beam}$ in the following). The spectrometer reconstructed variables at the target are : $y_{tgE}$, $\varphi_{tgE}$, $\theta_{tgE}$ and $p_E$ for the electron arm and $y_{tgH}$, $\varphi_{tgH}$, $\theta_{tgH}$ and $p_H$ for the hadron arm. $p$ is the momentum of the particle, after energy loss correction. $y_{tg}$, $\varphi_{tg}$ and $\theta_{tg}$ are defined in the spectrometer coordinate system (see Appendix B).

| observable | type | definition | sensitive to |
|---|---|---|---|
| *epkin* | single | momentum outgoing electron, corrected for energy loss and recoil effects | $E_{beam}, p_E, \varphi_{tgE}$ |
| *hpkindif* | single | $p_{Hmeasured} - p_{Hcalculated}$ | $E_{beam}, p_H, \varphi_{tgH}$ |
| *d* | double | difference between $x$ position of the crossing of the tracks determined by the E-arm and H-arm and the beam position (figure 5-10) | $y_{tgE}, y_{tgH}$ |
| *thdif* | double | difference of azimuthal angle electron and proton | $\theta_{tgE}, \theta_{tgH}$ |
| *emiss* | double | missing energy | $E_{beam}, p_E, p_H$ |
| $(missing\ mass)^2$ | double | | all |

Table 6-2: *Elastic scattering observables for comparing simulated and experimental distributions.*

The plots that are presented in figure 6-3 are for all CA_1_16 T5 events. The solid line shows the simulation result while the dashed line represents the experiment. No cuts have been applied to the events. In order to improve the experimental distributions, additional offsets had to be applied to various variables. The additional offsets that have been introduced for setting CA_1_16 are summarized in table 6-3. Note that other settings required other additional offsets.

The plots show that for the elastic scattering kinematics, the resolutions and offsets are reasonably well controlled. As such, it is justified to use the elastic scattering Monte Carlo simulation to define the solid angles that will be used to obtain experimental cross sections.

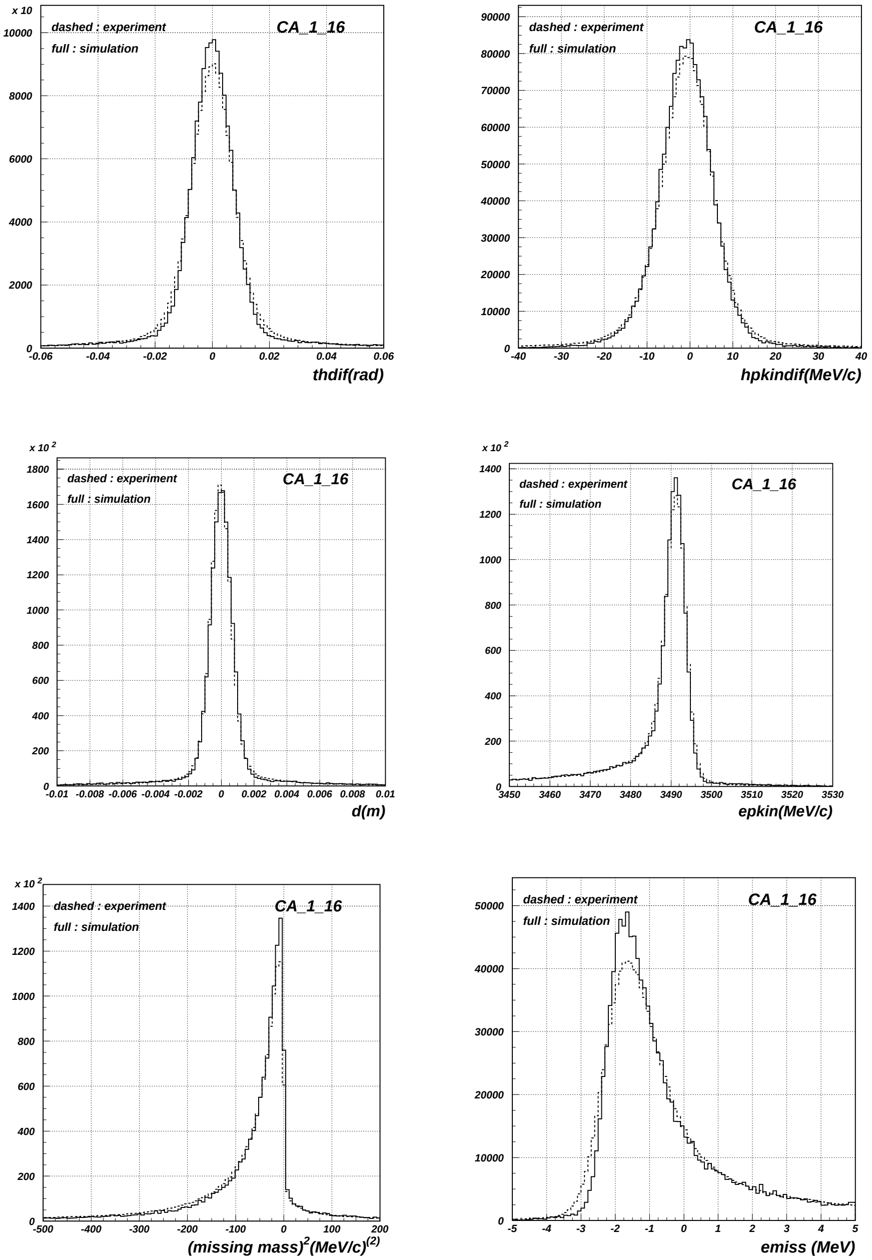

*Figure 6-3: Comparing experimental and simulated distributions of observables in elastic scattering for setting CA_1_16.*

| variable | additional offset |
|---|---|
| $E_{beam}$ | +2.0 MeV |
| $epkin$ | -1.0 MeV/c |
| $hpkin$ | +1.2 MeV/c |
| $\theta_{tgE}$ | -1.6 mrad |
| $\theta_{tgH}$ | +1.2 mrad |
| $\varphi_{tgE}$ | -0.3 mrad |
| $\varphi_{tgH}$ | -0.1 mrad |

Table 6-3: *Additional offsets applied to the CA_1_16 experimental data.*

## 6.3 Elastic Scattering Cross Sections

Two types of elastic scattering cross sections have been extracted : elastic scattering cross sections obtained with only T1 (single electron) events and elastic scattering cross sections obtained with T5 (coincidence) events. Evaluating the T1 cross sections will give an idea of how well the leptonic part of the experiment is calibrated. Evaluating the T5 events validates the calibration of the coincidence measurements.

The method used to obtain elastic scattering cross sections is illustrated in figure 6-4. First, elastic scattering cross sections are obtained considering increasing intervals in *epkin*. The intervals are defined starting from the "elastic peak" position value + 15 MeV/c to lower *epkin*-values (starting with the "elastic peak" -2 MeV/c) in steps of 2 MeV/c. Two intervals ($\Delta E_1$ and $\Delta E_2$) are indicated on the figure. The cross section values for these different intervals are plotted as a function of $\Delta E$ in the bottom figure. Note that although the considered bin in *epkin* is taken from the "elastic peak" position value +15 MeV/c, the value of $\Delta E$ is calculated as the difference between the "elastic peak" value and the lower *epkin*-value of the considered bin in $\Delta E$. As can be seen, with increasing $\Delta E$, the cross section values rapidly reach a "plateau". This plateau indicates that the obtained cross section values no longer depend on the experimental cut in $\Delta E$, and as such one can be confident that the generation of the radiative tail in the Monte Carlo simulation is done correctly. The error bars show the statistical errors. The quality of most of the plateaus used to determine elastic scattering cross sections that are presented here,

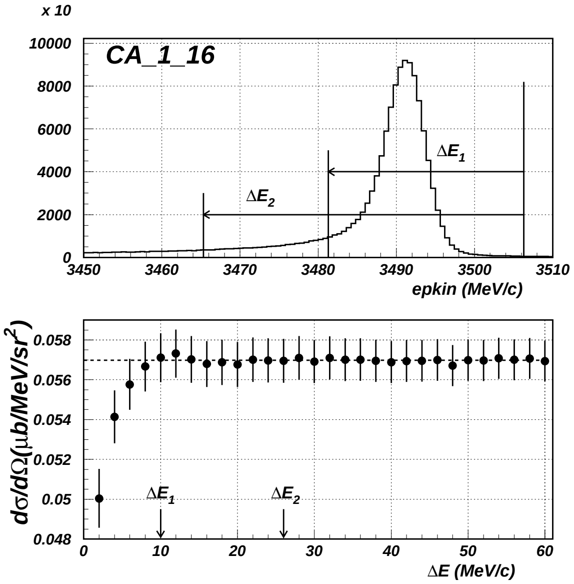

*Figure 6-4: Method to determine elastic scattering cross sections, illustrated on the experimental setting CA_1_16. The top figure shows the epkin-distribution that is used to study cuts in $\Delta E$. The bottom figure represents the corresponding elastic scattering cross section plateau for $15.556^\circ < \theta^e_{lab} < 15.699^\circ$. Two different cuts in $\Delta E$ are indicated on both figures.*

is typically such as shown in the figure. The elastic scattering cross section values corresponding to these plateaus are calculated as the mean of the cross section values for which $20(MeV/c) < \Delta E < 60(MeV/c)$.

The elastic scattering cross sections are presented in figure 6-5. The top plots are the results for T1 and T5 events of setting CA_1_16. The bottom plots are the results for setting CA_1_10. The solid lines represent the elastic scattering cross section, calculated with the proton form factors as explained in section 1.2.3, the dotted and dashed lines represent these calculated values plus/minus 5% and 10%, respectively. The statistical errors on the experimentally obtained cross section values are indicated. As can be seen, for CA_1_16 one succeeds in reproducing the single arm (T1) elastic scattering cross section over almost all of the horizontal electron spectrometer acceptance within 3%. For T5 events, one has the same accuracy in the center of the acceptance, near the edges of the horizontal hadron spectrometer acceptance however the accuracy is less good. For CA_1_10, again one finds an accuracy better than 3% in the center of the horizontal electron spectrometer acceptance. As can be seen, near the lower electron scattering angles, the reproduction of the cross section values is not good at all. Looking at figure 6-1 shows that these points are situated at the edge of the electron spectrometer acceptance. For T5 events, one sees an agreement between experiment and theory within 3% except for higher electron scattering angles where the obtained cross sections are not good. However, cutting in the hadron arm acceptance, improves the form of the cross section distribution significantly, as can be seen in figure 6-6.

The systematical error on these cross section values is estimated to be about at most 5% in the center of the acceptance and up to 10% near the edges.

## 6.4 Conclusion

As illustrated in the previous section, in the center of the electron and hadron spectrometer acceptance, the reproduction of the elastic scattering cross section yields an accuracy better than 3%. As such one can conclude that the calibration and resolutions in the center of the acceptance of both spectrometers are reasonably well understood. Near the edges of the acceptances, however, the situation is less favourable. There the resolutions and systematic uncertainties are not so well understood. This will have an impact on the VCS cross sections, since for VCS data, almost the complete spectrometer acceptances are covered.

The results that are presented also indicate that the use of the proton form factors as described in section 1.2.3 is justified and the calculation of the radiative corrections in the simulation is tested. Also the calculation of the luminosity seems

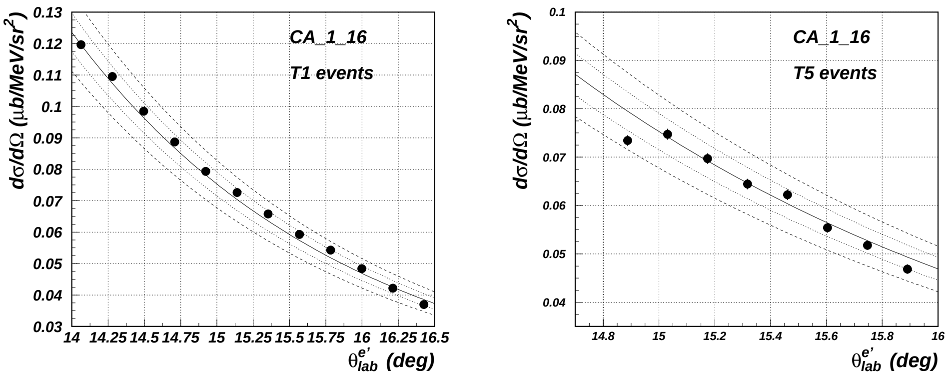

(a) setting CA_1_16, single electron events (T1)

(b) setting CA_1_16, coincidence events (T5)

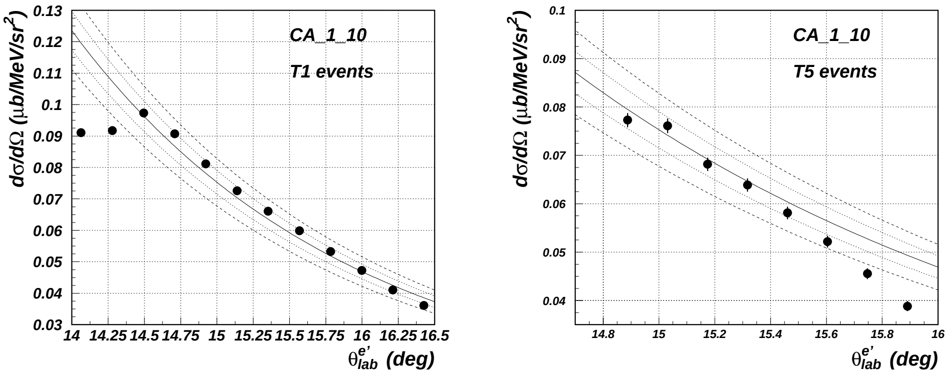

(c) setting CA_1_10, single electron events (T1)

(d) setting CA_1_10, coincidence events (T5)

*Figure 6-5: Experimental elastic scattering cross sections, compared to the theoretically calculated cross section, using the proton form factors as described in section 1.2.3. The full line represents the theoretically calculated cross section, the dashed and dotted lines are these calculated values plus/minus 5% and 10%, respectively. No cuts have been applied to the events. The statistical errors are very low and hardly visible.*

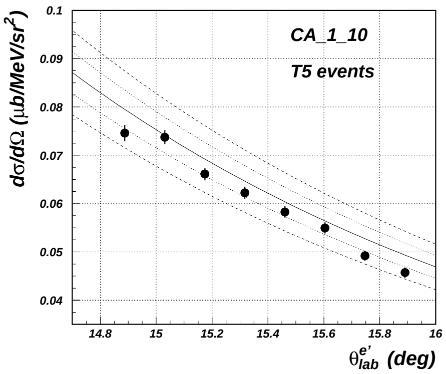

*Figure 6-6: Experimental elastic scattering cross sections for the CA_1_10 T5 events, compared to the theoretically calculated elastic scattering cross section. Additional cuts on the hadron arm acceptance have been applied to the events (*$abs(\varphi_{tgH}) < 0.02rad$ *and* $abs(\theta_{tgH}) < 0.04rad$*).*

to be well controlled.

# Chapter 7

# Cross Sections for the Photon Electro-production Reaction at $Q^2$=1.0(GeV/c)$^2$

## 7.1 Definition of VCS Photon kinematical Variables

In this section, the definition of the photon kinematical variables in the center of mass frame that are used in this thesis will be given. In principle there are two ways to reconstruct the outgoing photon variables : first, one can identify the outgoing photon as the missing particle; however its mass will not necessarily equal zero due to resolution and radiation effects. Second, one can impose the reconstructed photon to have mass zero. The second approach is not used in this analysis. Either of the two methods is justified, as long as one makes sure one uses the same definitions in the experiment and in the simulation and as long as the simulation reproduces the observed experimental resolutions in an acceptable way.

Given the missing mass ($M_{miss}$), the outgoing photon energy $q'^{0}_{cm}$ and momentum $\mathsf{q}'_{cm}$ are expressed as :

$$q'^{0}_{cm} = \frac{s - m_p^2 + M_{miss}^2}{2\sqrt{s}} \tag{7-1}$$

$$(\mathsf{q}'_{cm})^2 = (q'^{0}_{cm})^2 - M_{miss}^2 \tag{7-2}$$

The polar angle between the incoming real and the outgoing virtual photon is given by :

$$tan(\theta_{cm}^{\gamma^*\gamma}) = \frac{\mathsf{q}'_{lab}.sin\theta_{lab}^{\gamma^*\gamma}}{\gamma.\left[\mathsf{q}'_{lab}.cos\theta_{lab}^{\gamma^*\gamma} - \beta.q'^{0}_{lab}\right]} \tag{7-3}$$

with $\gamma$ and $\beta$ defining the Lorentz transformation along the virtual photon direction (see section 1.5.3). The azimuthal angle $\varphi$ is given by :

$$cos(\varphi) = \frac{q3(1)}{sin\theta_{cm}^{\gamma^*\gamma}.\mathsf{q}'_{lab}} \tag{7-4}$$

with $q3(1)$ the component of $\vec{q}'_{lab}$ transverse to $\vec{q}_{lab}$ and contained in the plane defined by $\vec{k}_{lab}$ and $\vec{k}'_{lab}$. If $p3(2) < 0$ then $\varphi = 2\pi - \varphi$. $p3(2)$ is the component of $\vec{q}'_{lab}$ transverse to $\vec{q}_{lab}$ and transverse to $p3(1)$.

## 7.2 Getting familiar with the Phase Space and Solid Angles used in the Analysis

Before showing experimental cross sections for the photon electro-production reaction, it is necessary to clearly define the points in phase space for which one has obtained cross section values. Note that the cross section values that are obtained in the presented analysis are cross section values in a certain point in phase space and are not mean cross section values over a certain bin (see section 4.2).

As explained in section 1.5.6, the aim of this experiment is to study the behaviour of the photon electro-production reaction cross section in the leptonic plane as a function of $\theta_{cm}^{\gamma^*\gamma}$ and $\mathsf{q}'_{cm}$ at fixed $\mathsf{q}_{cm}$ and $\epsilon$. Thus, bins and values for $\theta_{cm}^{\gamma^*\gamma}$ and $\mathsf{q}'_{cm}$ have to be defined, as well as the values for $\mathsf{q}_{cm}$ and $\epsilon$.

The initial choice that is made is to derive cross section values in the leptonic plane ($\varphi = 0°, 180°$). In this plane, $\theta_{cm}^{\gamma^*\gamma}$ varies between $-180°$ and $+180°$ (see section 1.5.4). One has chosen to divide this angular range in 20 equally sized bins, yielding cross section values for 20 different $\theta_{cm}^{\gamma^*\gamma}$ values. The range in $\mathsf{q}'_{cm}$ that is considered is limited by the pion production threshold on the one hand, and by the cut in $s$ (see section 7.3.5) on the other hand. Although very recently [38, 39] it has been shown that using a dispersion formalism, information on the generalized polarizabilities can also be extracted above the pion production threshold, the analysis presented here is not yet suited to use this formalism. However, in the future the analysis will be expanded above the pion production threshold, so that this formalism can be applied. As such, the range in $\mathsf{q}'_{cm}$ is limited to $30\ MeV/c \leq \mathsf{q}'_{cm} \leq 120\ MeV/c$ and is divided in 3 bins : [30 MeV/c, 60 MeV/c], [60 MeV/c, 90 MeV/c] and [90 MeV/c, 120 MeV/c]. The cross sections have been derived at a certain point in each of these 3 bins, namely $q'_{cm}$=45 MeV/c, $q'_{cm}$ =75 MeV/c and $q'_{cm}$=105 MeV/c.

In table 7-1 the values for the leptonic variables of the points in phase space for which photon electro-production reaction cross sections will be shown, are summarized. These values together with the 20 values for $\theta_{cm}^{\gamma^*\gamma}$ and $\varphi = 0°$ or $180°$, depending on whether we are looking at backward angles or not, define the complete kinematics.

| $k_{lab}$ MeV/c | $Q^2$ $(MeV/c)^2$ | $q'_{cm}$ MeV/c | $q_{cm}$ MeV/c | $\epsilon$ | $\sqrt{s}$ MeV | $k'_{lab}$ MeV/c | $\theta^e_{lab}$ deg |
|---|---|---|---|---|---|---|---|
| 4032.5 | $10^6$ | 45 | 1102.0 | 0.953 | 984 | 3452 | 15.4 |
| 4032.5 | $10^6$ | 75 | 1083.5 | 0.952 | 1016 | 3418 | 15.5 |
| 4032.5 | $10^6$ | 105 | 1066.8 | 0.950 | 1049 | 3382 | 15.6 |

Table 7-1: *Values of the variables describing the leptonic part of the photon electro-production reaction, used to represent cross section values in this thesis.*

Note that the values for $q_{cm}$ and $\epsilon$ are not the same for the 3 kinematical settings. But since their differences are rather small, for a first analysis one can suppose them to be constant. So the results in chapter 8 will be shown at the mean values for $q_{cm}$ and $\epsilon$, i.e. $q_{cm}^{mean} = 1084.1\ MeV/c$ and $\epsilon^{mean} = 0.951$; this corresponds to $\tilde{Q}^2 = 0.93\ (GeV/c)^2$.

Besides the points in phase space for which one will derive cross section values, also the phase space bins that are used to obtain these cross section values have to be defined. In figure 7-1a the standard spherical coordinate system is presented. The polar axis is defined by the virtual photon momentum $\vec{q}_{cm}$, $\theta_{cm}^{\gamma^*\gamma}$ is the polar angle and $\varphi$ the azimuthal angle. In the figure they are denoted by *thqgcm* and *phi*, respectively. Also two equally sized phase space bins are indicated by the hatched areas. It is clear that using this coordinate system, possible offsets in the determination of the virtual photon direction have a direct impact on the results. Indeed, the shape of the phase space bins changes a lot when approaching the virtual photon direction. Because of this particular shape of the phase space bins near the virtual photon direction, there is a large sensitivity to bad angle reconstruction of the particles in this region. To overcome this inconvenience, another coordinate system has been introduced. It is presented in figure 7-1b. Here the virtual photon momentum direction $\vec{q}_{cm}$ has no crucial role anymore with regard to the shape of the bins. Indeed, the shape of the phase space bins is identical everywhere, as such the sensitivity to a bad reconstruction near the virtual photon direction is much smaller. The relations between the outgoing photon angles in these two frames are given by :

$$\begin{aligned} cos(\theta'^{\gamma^*\gamma}_{cm}) &= sin(\theta^{\gamma^*\gamma}_{cm}).sin(\varphi) && \text{(7-5)} \\ cos(\varphi') &= cos(\theta^{\gamma^*\gamma}_{cm})/sin(\theta'^{\gamma^*\gamma}_{cm}) && \text{(7-6)} \\ sin(\varphi') &= sin(\theta^{\gamma^*\gamma}_{cm}).cos(\varphi)/sin(\varphi') && \text{(7-7)} \end{aligned}$$

where $\varphi'$ is the new azimuthal angle and $\theta'^{\gamma^*\gamma}_{cm}$ the new polar angle.

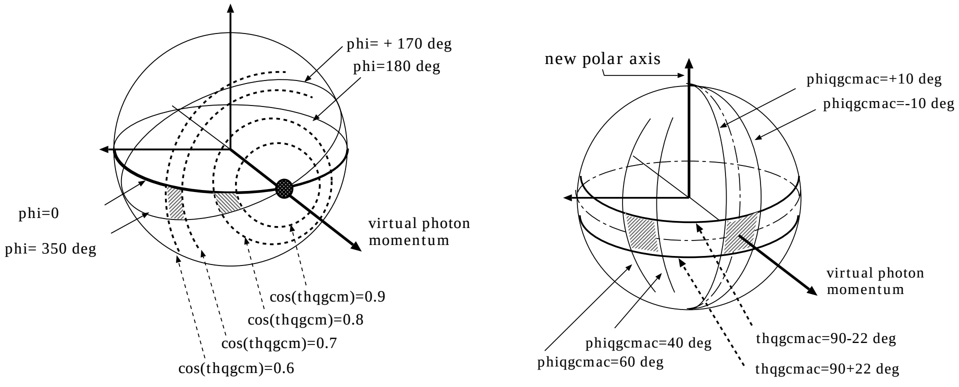

(a) standard spherical coordinate system

(b) new coordinate system

*Figure 7-1: Standard spherical and new coordinate system, with the definition of their respective phase space bins (hatched areas).* $\varphi$ *is denoted by phi,* $\theta^{\gamma^*\gamma}_{cm}$ *by thqgcm,* $\varphi'$ *by phiqgcmac and* $\theta'^{\gamma^*\gamma}_{cm}$ *by thqgcmac.*

For obtaining cross section values in this thesis, the phase space bins that are used are defined by 20 equally sized bins in $\varphi'$ ($[0°, 18°], [18°, 36°], ..., [342°, 360°]$) and well-defined ranges in $\theta'^{\gamma^*\gamma}_{cm}$. Counting experimental events and obtaining the solid angles with the Monte Carlo simulation is performed using this binning. Since the cross section values that will be obtained are values in a certain point in phase space, the use of this new coordinate system is justified.

An important remark that has to be made is that choosing the complete range for $\theta'^{\gamma^*\gamma}_{cm}$ and projecting the results on the leptonic plane, can cause errors in the obtained results. Indeed, the effect of the polarizabilities is not necessarily the same all over the region $0° \leq \theta'^{\gamma^*\gamma}_{cm} \leq 180°$; however, using the complete range in $\theta'^{\gamma^*\gamma}_{cm}$ will cause the overall effect to be projected on the leptonic plane. As such, it is necessary to perform an iteration in the analysis; this means using the initial obtained "polarizability effect" to run a new Monte Carlo simulation and using these new solid angles to perform a second analysis. An other option to minimize the "projection effect" is performing the analysis, using smaller bins in $\theta_{cm}^{\prime\gamma^*\gamma}$. This has been done for the analysis presented in this thesis. One has chosen 3 different ranges in $\theta_{cm}^{\prime\gamma^*\gamma}$ : $20° \leq \theta_{cm}^{\prime\gamma^*\gamma} \leq 60°$,$60° \leq \theta_{cm}^{\prime\gamma^*\gamma} \leq 120°$ and $120° \leq \theta_{cm}^{\prime\gamma^*\gamma} \leq 160°$. Normally, the 2 out-of-(leptonic)-plane ranges in $\theta_{cm}^{\prime\gamma^*\gamma}$ should give the same results, as there is a cross section symmetry around the leptonic plane.

## 7.3 Selecting the good Photon Electro-production Events

In order to "clean" the experimental events and to consider only the relevant ones, i.e. the photon electro-production events, additional cuts have been applied to the data. These cuts will be detailed in this section. Also here, the strength of the simulation has to be stressed : as long as one applies the same cuts to the experimental and the simulated data, there is no problem, since the conditions for counting experimental events and the conditions for counting simulated events (and hence solid angles) are alike. Of course, the simulation has to reproduce the spectra in a reasonable way.

Since in principle, the cuts that are imposed on the data should from a certain point on not have any effect on the obtained cross section values, systematic studies have been performed to test the stability of different cuts on the cross section values. These studies will also give a first estimation of some of the systematic uncertainties that are present in the analysis. The global result of these studies will be summarized in section 7.6.

### 7.3.1 Elimination of transmission protons

As mentioned in section 5.1, the hadron spectrometer kinematical settings are chosen in such a way that the elastic scattering coincidence events are not detected. However, looking at the actual data that were taken, one sees a lot of background events due to transmission protons. These protons, generated by elastic scattering events, have a momentum that is high enough to go through the 8 cm tungsten collimator, loosing a few 100 MeV/c, and finally arriving in the momentum acceptance of the hadron spectrometer. Filtering these events out of the data is done, using only information coming from the electron beam and the electron spectrometer since this information is not affected by this "collimator walk-through".

In order to be able to filter out these events, the impact coordinate in the hadron arm collimator is calculated, supposing that all events are elastic scattering events, and using only the beam energy at the vertex, the scattered electron angles $(\theta_{tgE}, \varphi_{tgE})$, the vertex point formed by the reconstructed electron track and the raster information, and the two body *ep* kinematics. This impact coordinate $(y^{colli}_{elastH})$ is compared to the actual impact coordinate of the proton in the hadron arm $(y^{colli}_{H})$, measured by the hadron arm, using the vertex point formed by the reconstructed hadron track and the raster information. If these two coordinates do not differ significantly, one can suspect the event to be a transmission proton.

The cut that is applied to the events is :

$$y^{colli}_{elastH} - y^{colli}_{H} \leq -0.012m \tag{7-8}$$

Note that the spectrometers do not give vertical position information, as such the cut is only considered in the horizontal direction.

### 7.3.2 Reducing the considered target length

In order to define the target length that is considered, the variable $y_{tgE}$ (see Appendix B) has been used. A systematic study, evaluating the effect on the cross section values of using different target lengths has been performed. The 5 different target lengths that have been considered varied between 5 cm and 15 cm. This study showed that diminishing the considered target length has no significant influence on the obtained results. As such, in order to keep the statistics as high as possible, only a weak cut in $y_{tgE}$ has been defined. This cut ensures that no events, originating from outside the target come into play. When defining this cut, one has to be careful since the distribution of $y_{tgE}$ is not centered around zero, but around -0.007 m. Thus the cut that allows to consider the complete target is defined as :

$$-0.027\ m < y_{tgE} < 0.013\ m \tag{7-9}$$

### 7.3.3 Narrowing the spectrometer acceptances

It is known that there still is a problem with the acceptance function that is used in the simulation (see section 4.3) [55]. This imperfection causes the simulated spectrometer acceptances to be larger that what is experimentally observed. This discrepancy is especially important for events at low $\mathsf{q}'_{cm}$ and backwards $\theta^{\gamma^*\gamma}_{cm}$ angles. As such, additional cuts have been applied in order to overcome this discrepancy.

These cuts are defined in the phase spaces $(\theta_{tg}, \varphi_{tg})$ for the electron and the hadron arm. A rather severe cut has been imposed on both spectrometer acceptances in order to be sure that the region where the simulated acceptance is larger than the experimental acceptance is excluded. The cuts for both arms are defined as :

$$|\theta_{tg}| < 0.04\ rad \tag{7-10}$$

$$|\varphi_{tg}| < 0.02\ rad \tag{7-11}$$

### 7.3.4 Cut in $(missing\ mass)^2$

As already mentioned, the kinematical settings of this experiment allow pion production events also to be detected. A way to distinguish between photon electro-production events and pion production events is calculating the mass of the missing particle. The $(missing\ mass)^2$ distribution for setting DA_1_16 is shown in figure 7-2. As can be seen, it is not possible to completely separate photon and pion electro-production events. As such, a well-chosen window in the $(missing\ mass)^2$ distribution has to be defined. Again a systematic study has been performed in order to verify which cut on the $(missing\ mass)^2$ has to be applied. The considered ranges in $(missing\ mass)^2$ varied between [-5000, +3000] and [-5000, +7000]. This study learns that the cut in missing mass does not really influence the results, except when going too high in missing mass squared (up to $7000(MeV/c^2)^2$ and higher), since for these values, pions are introduced in the acceptance. This also indicates that the radiative tail in the simulation is rather well reproduced. One has chosen the cut in missing mass to be :

$$|(missing\ mass)^2| < 5000(MeV/c^2)^2 \tag{7-12}$$

### 7.3.5 Defining the range in $s$

As described in section 1.5.3, $s$ is the total energy squared of the $cm$ system $\gamma^* p$. The elastic scattering events are characterized by $s \approx m_p^2 c^4$, the pion production events are characterized by $s \approx (m_p c^2 + m_{\pi^0} c^2)^2$. As such, the cut $m_p^2 c^4 \leq s \leq (m_p c^2 + m_{\pi^0} c^2)^2$ could be imposed. Since in this thesis, $\mathsf{q}'_{cm}$ values are only considered from $\mathsf{q}'_{cm}$=30 MeV/c on, the following cut on $s$ has been imposed :

$$(m_p c^2 + 30MeV)^2 \leq s \leq (m_p c^2 + m_{\pi^0} c^2)^2 \tag{7-13}$$

This cut ensures that no elastic scattering events and no other disturbing events that are present at low $s$ values, are accepted.

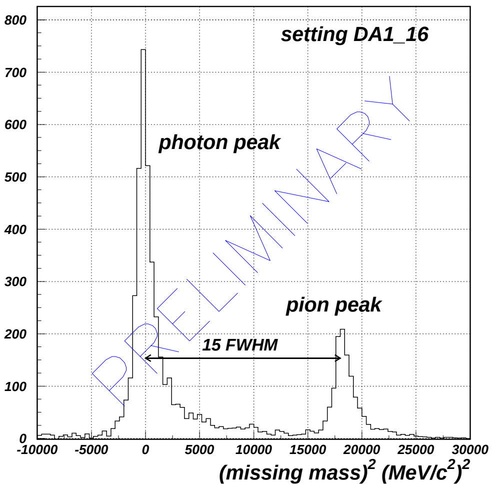

*Figure 7-2: Missing mass distribution for setting DA1_16. The cuts that are applied to the events are as described in section 7.3. The FWHM of the photon peak is taken as reference.*

### 7.3.6 Cut in collimator aperture

An additional cut on the collimator variables has been imposed in order to overcome possible effects due to the edges of the acceptances of the spectrometers. The cuts that are imposed on both spectrometers are the following :

$$|x_{colli}| \leq 0.059m \tag{7-14}$$

$$|y_{colli}| \leq 0.030m \tag{7-15}$$

with $y_{colli}$ the collimator horizontal coordinate and $x_{colli}$ the vertical coordinate. These cuts slightly diminish the actual aperture of the collimators.

### 7.3.7 Restriction of the relative momentum acceptance $\delta P/P$

Also on the momentum of the events relative to the spectrometer settings a cut has been applied. Again this is done to avoid possible acceptance edge-effects, but also because of the limited momentum phase-space defined in the simulation grid (see section 4.4). A systematic study showed that from a certain cut in the relative momentum acceptance on, the obtained cross section values stabilise. Cross section values have been obtained with relative momentum acceptances ranging from 3.5%

to 5% in steps of 0.5%. A rather severe cut on both spectrometers has been imposed :

$$|\delta P/P| < 0.04 \tag{7-16}$$

### 7.3.8 Overview of cuts that are applied in the analysis

In table 7-2, all cuts that are defined above, are summarized. These cuts have been applied to all DA_1 data.

| variable | minimum | maximum |
|---|---|---|
| $y^{colli}_{elastH} - y^{colli}_{H}$ | | -0.012 m |
| $y_{tgE}$ | -0.027 m | 0.013 m |
| $\theta_{tg^E_H}$ | -0.04 rad | 0.04 rad |
| $\varphi_{tg^E_H}$ | -0.02 rad | 0.02 rad |
| $(missing\ mass)^2$ | -5000 $(MeV/c^2)^2$ | +5000 $(MeV/c^2)^2$ |
| $s$ | 937024 $MeV^2$ | 1151329 $MeV^2$ |
| $x_{colli^E_H}$ | -0.059 m | 0.059 m |
| $y_{colli^E_H}$ | -0.030 m | 0.030 m |
| $\delta P/P^E_H$ | -0.04 | 0.04 |

Table 7-2: *Overview of the cuts that are used in the analysis of DA_1.*

### 7.3.9 Number of analysed events

The total number of events used in the analysis for all settings of DA_1 is summarized in table 7-3. These numbers take into account all the cuts defined above and all corrections that are described in section 5.2.

## 7.4 Comparing the VCS Simulation with the Experiment

Again it is necessary to compare experimental distributions with simulated distributions before extracting cross section values from the experimental data. This

| setting | # events | setting | # events | setting | # events |
|---|---|---|---|---|---|
| 01 | 962 | 07 | 639 | 13 | 4500 |
| 02 | 1217 | 08 | 2150 | 14 | 157 |
| 03 | 812 | 09 | 5665 | 15 | 12322 |
| 04 | 1381 | 10 | 939 | 16 | 5964 |
| 05 | 1048 | 11 | 678 | 17 | 1645 |
| 06 | 1113 | 12 | 17822 | total | 58915 |

Table 7-3: *Overview of the number of events used in the analysis of DA_1.*

will show how well offsets and resolutions that are playing a role are controlled, and it will also show whether there are still background or disturbing events left in the analysis. It will also allow us to justify additional cuts that have been imposed on the experimental (and accordingly simulated) events to be analysed. Indeed, sometimes it is necessary to apply non-trivial cuts to the data in order to throw away non-relevant and even disturbing events (see e.g. section 7.3.1).

In this subsection experimental and simulated distributions of some important variables will be compared. A first set of variables are the target reconstructed variables : $\delta P_E/P_E$, $\delta P_H/P_H$, $\varphi_{tgE}$, $\varphi_{tgH}$, $\theta_{tgE}$, $\theta_{tgH}$, $y_{tgE}$ and $y_{tgH}$. They are defined in the target coordinate system (see Appendix B). A second set of variables are those that are used to do the optimisations on the experimental ntuple : $(missing\ mass)^2$ and $d$ (see section 5.2.10). Finally one has the variables that define the points in phase space where the cross sections values are evaluated : $\mathsf{q}_{cm}$, $\mathsf{q}'_{cm}$, $\epsilon$, $\theta_{cm}^{\gamma^*\gamma}$ and $\varphi$. They are defined in section 1.5.3.

The distributions that are shown here are for the accepted events of setting DA_1_16, corresponding to all cuts defined in section 7.3. Note that for the target reconstructed variables, the cut on the variable that is shown, is not applied. The distributions are normalised to their respective luminosities (experiment and simulation).

As can be seen, the correspondence between the experimental and simulated distributions for the target reconstructed variables is generally good, except for $\delta P_H/P_H$ and $\theta_{tgH}$ where one clearly sees the discrepancy between the experiment and the simulation near the acceptance edges (see section 7.3.3). As already explained, these regions are left out of the analysis. Unlike for the target reconstructed variables, the agreement between the experimental and simulated distributions for the $(missing\ mass)^2$ and $d$ is not yet fully satisfying. Looking at the position of the distributions, the offsets seem to be understood quite well, at least for this setting, but the resolutions are not yet simulated as they are found in the experimental data. The experimental distributions of the physics variables that are used in the analysis are in reasonable good agreement with the simulated distributions.

As already mentioned, the distributions that are shown are for only one setting of the data. Most of the settings show distributions of the same quality as the ones that are shown. Some settings however still have problems, especially concerning the missing mass distribution. This indicates that there are still resolution and offset problems which will certainly introduce systematic errors (shape and absolute value of cross section distribution) on the presently obtained cross sections.

The main conclusion that can be drawn from this study is that the experiment and the simulation are in reasonable good agreement. However, optimisations on offsets and especially resolutions are certainly still necessary.

## 7.5 Preliminary Cross Section Values for the Photon Electro-production Reaction at $Q^2$=1.0(GeV/c)$^2$

In figure 7-7 the experimental cross section values, obtained using the cuts that are defined in section 7.3 are plotted as a function of $\theta_{cm}^{\gamma^*\gamma}$. The range in $\theta'^{\gamma^*\gamma}_{cm}$ that is considered is $0° \leq \theta'^{\gamma^*\gamma}_{cm} \leq 180°$. The results are obtained, accumulating all 17 different settings. The top plot shows the results for $\mathsf{q}'_{cm} = 45 MeV/c$, the middle plot for $\mathsf{q}'_{cm} = 75 MeV/c$ and the bottom plot for $\mathsf{q}'_{cm} = 105 MeV/c$. Note that $\theta_{cm}^{\gamma^*\gamma}$ varies between -243° and 117°, where the range [-243°,-180°] corresponds in fact to the range [117°,180°]. This is done in order to make the presentation more appealing. The solid line represents the theoretically calculated BH+Born cross section using the proton form factors as described in section 1.2.3.

Figure 7-8 shows the relative difference between the BH+Born cross section and the experimental cross section that is shown in figure 7-7. Analogue to figure 7-7, this is done as a function of $\theta_{cm}^{\gamma^*\gamma}$ as defined above and for the 3 different values of $\mathsf{q}'_{cm}$. The horizontal lines on the figures indicate a relative difference of 10% and 20%, respectively.

In the region of interest for a first analysis ($-175° < \theta_{cm}^{\gamma^*\gamma} < 45°$, see chapter 8) at the lowest $\mathsf{q}'_{cm}$ value, the cross section values are obtained within ±10% deviation from the BH+Born cross section value. If everything is under control, at $\mathsf{q}'_{cm} = 0$, one should find exactly the BH+Born cross section value; however as seen

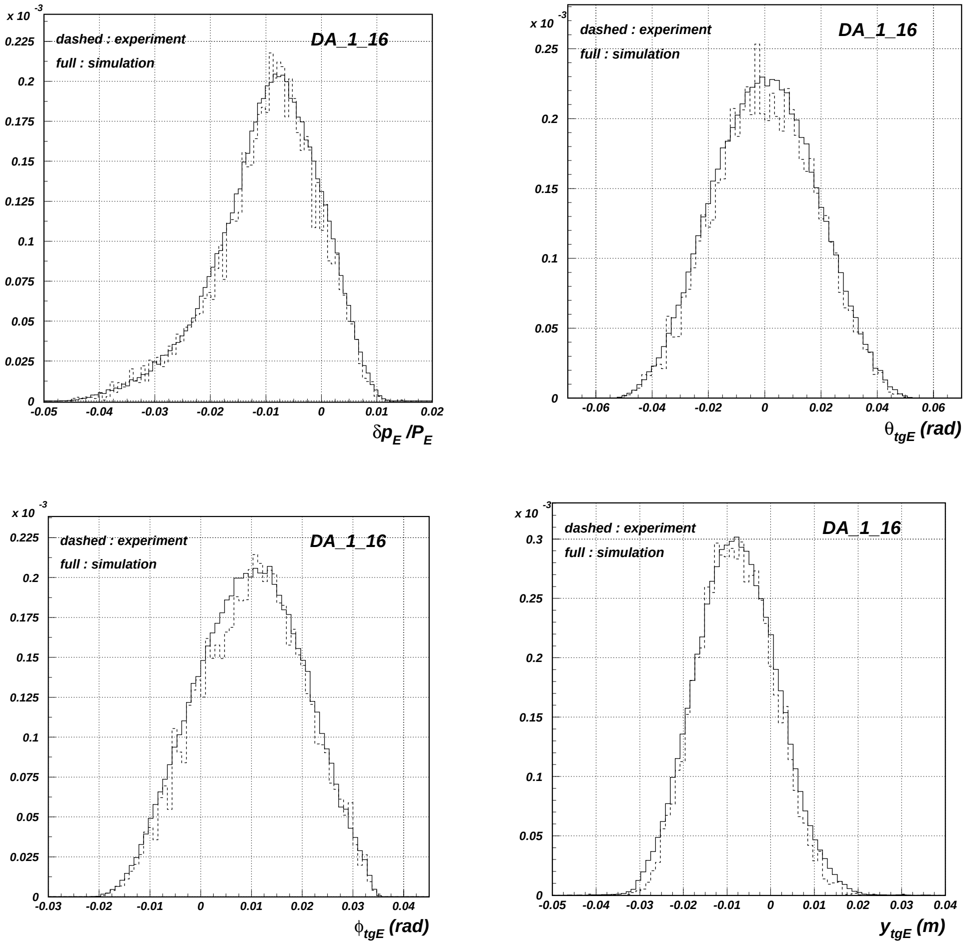

*Figure 7-3: Comparing experimental and simulated distributions of the electron spectrometer reconstructed variables for setting DA_1_16.*

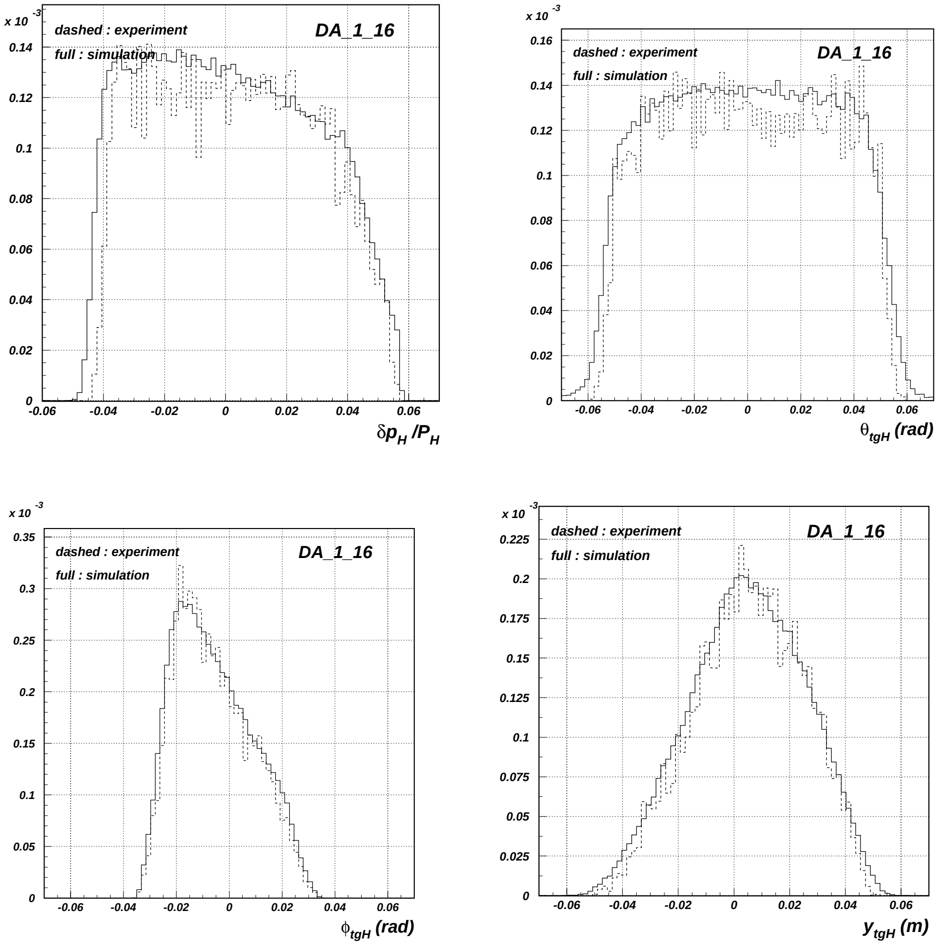

*Figure 7-4: Comparing experimental and simulated distributions of the hadron spectrometer reconstructed variables for setting DA_1_16.*

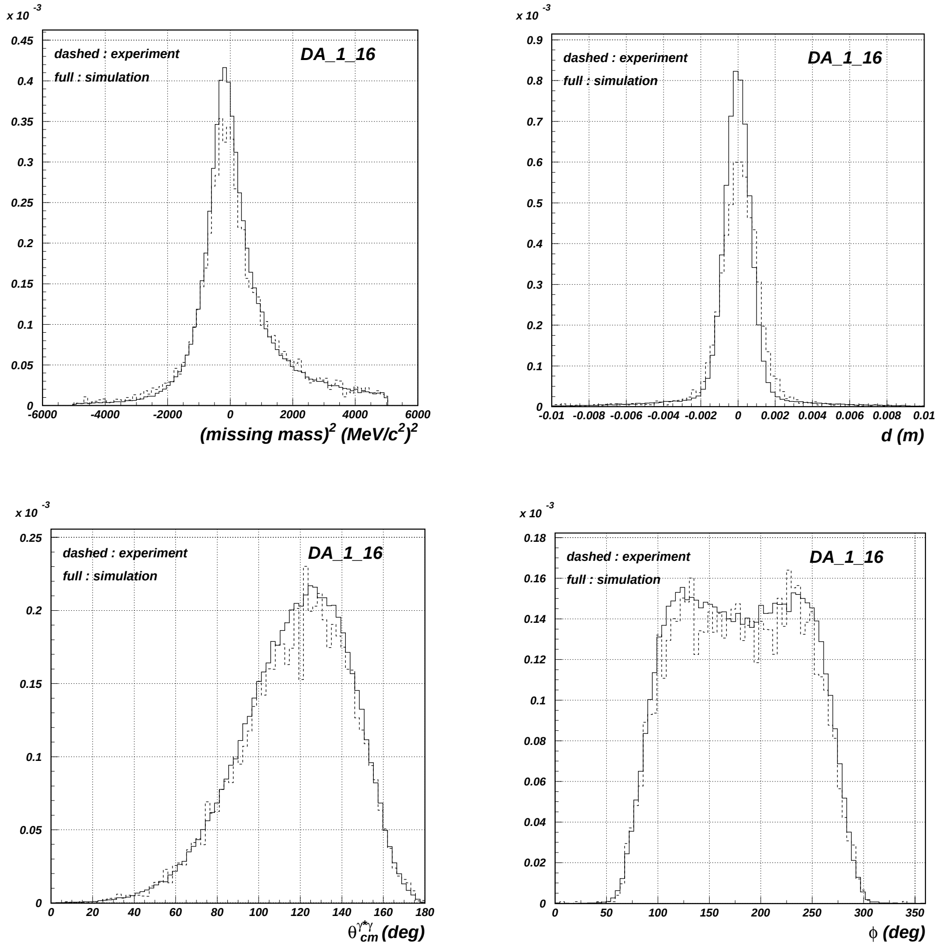

*Figure 7-5: Comparing experimental and simulated distributions of variables for setting DA_1_16.*

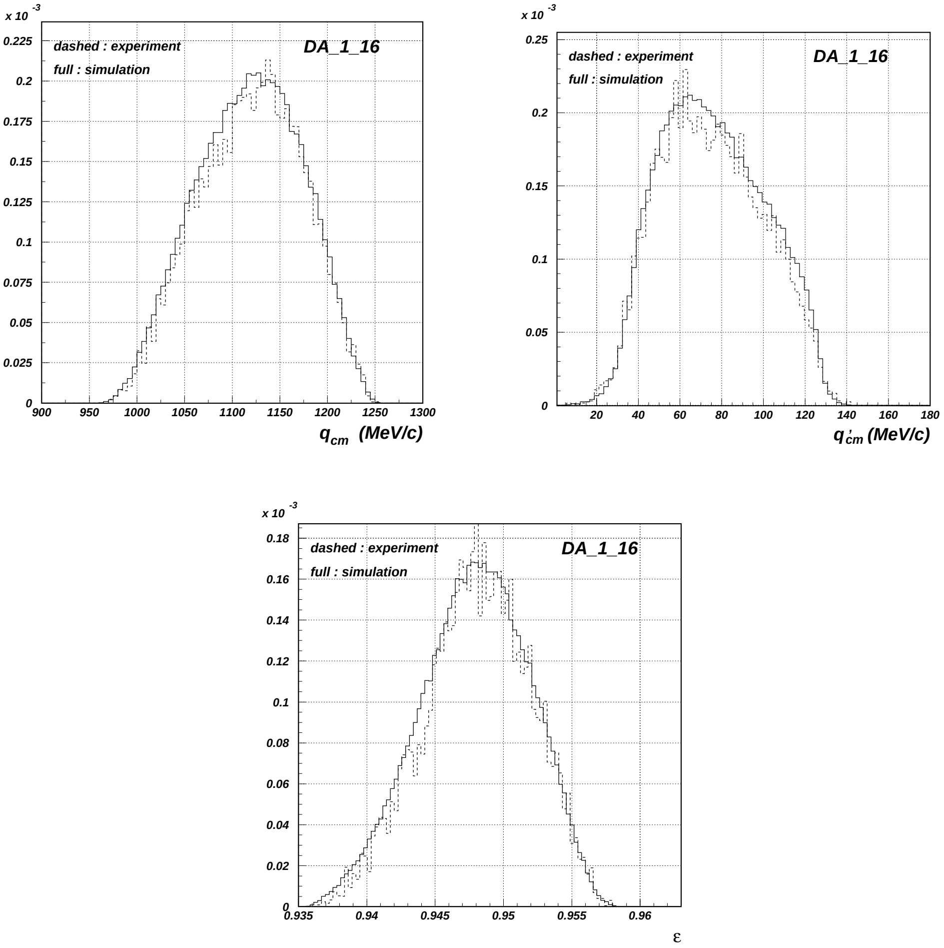

*Figure 7-6: Comparing experimental and simulated distributions of variables for setting DA_1_16.*

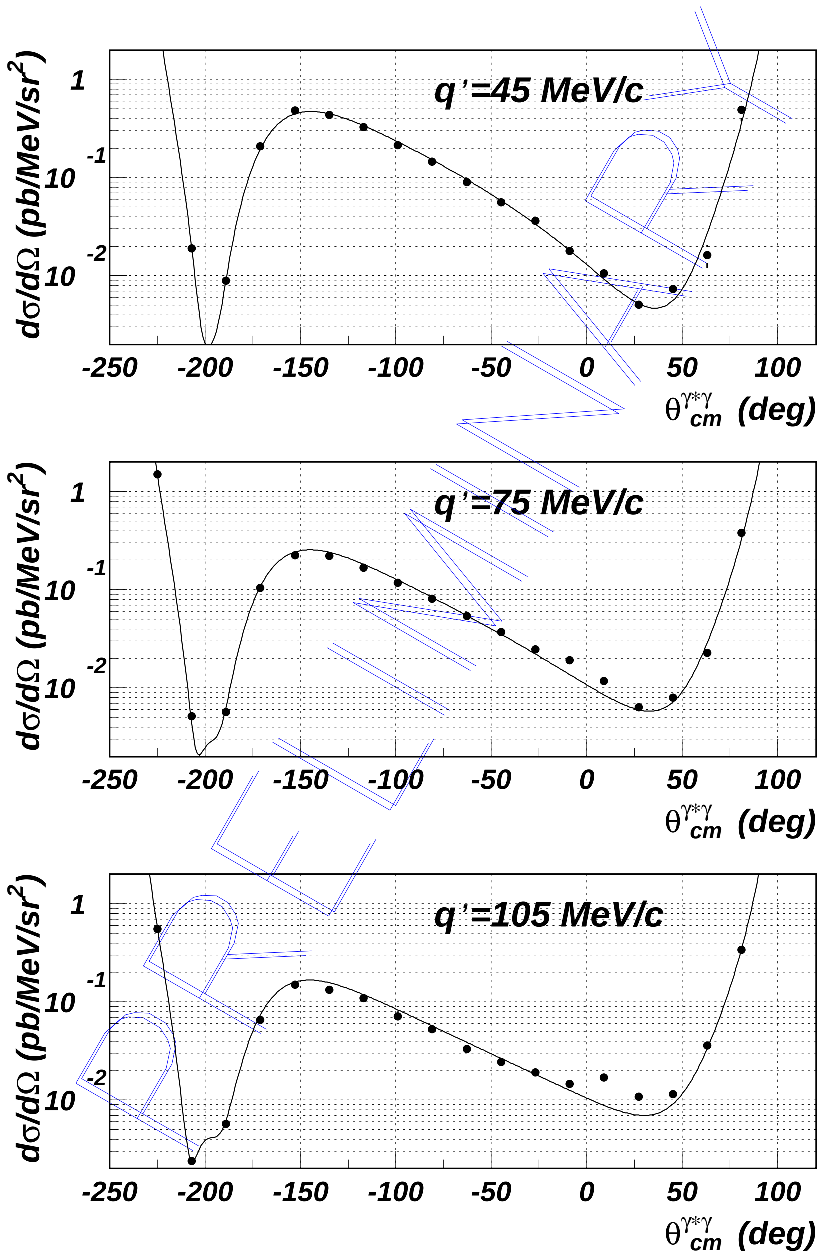

*Figure 7-7: Photon electro-production cross sections at $Q^2$=1.0(GeV/c)$^2$ as a function of $\theta_{cm}^{\gamma^*\gamma}$ for 3 values of $\mathsf{q}'_{cm}$ and fixed $\epsilon$. The solid lines represent the BH+Born cross section values. The considered range in $\theta'^{\gamma^*\gamma}_{cm}$ is $[0°, 180°]$.*

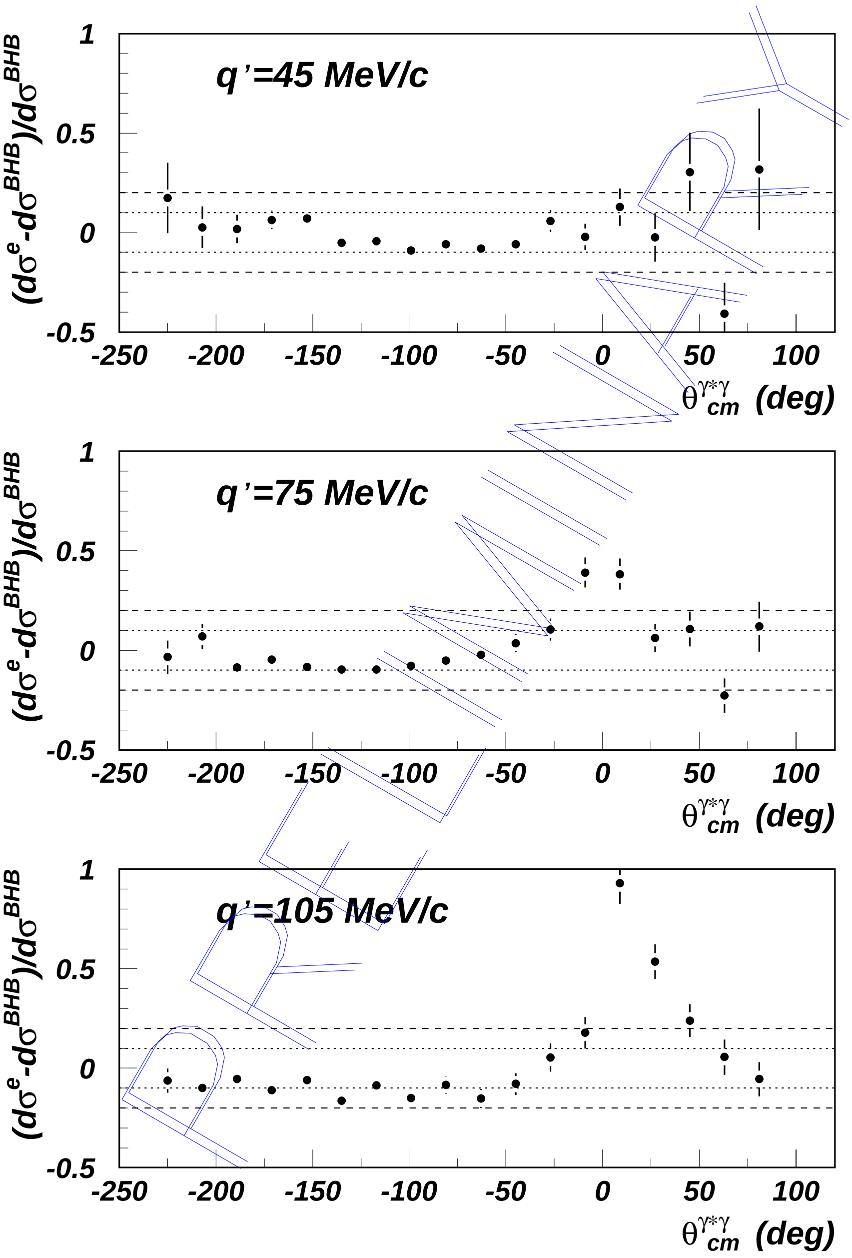

Figure 7-8: Relative difference between the experimentally obtained cross section values and the BH+Born cross section values at $Q^2$=1.0(GeV/c)$^2$ as a function of $\theta_{cm}^{\gamma^*\gamma}$ for 3 values of $\mathsf{q}'_{cm}$ and fixed $\epsilon$. The considered range in $\theta_{cm}'^{\gamma^*\gamma}$ is $[0°, 180°]$.

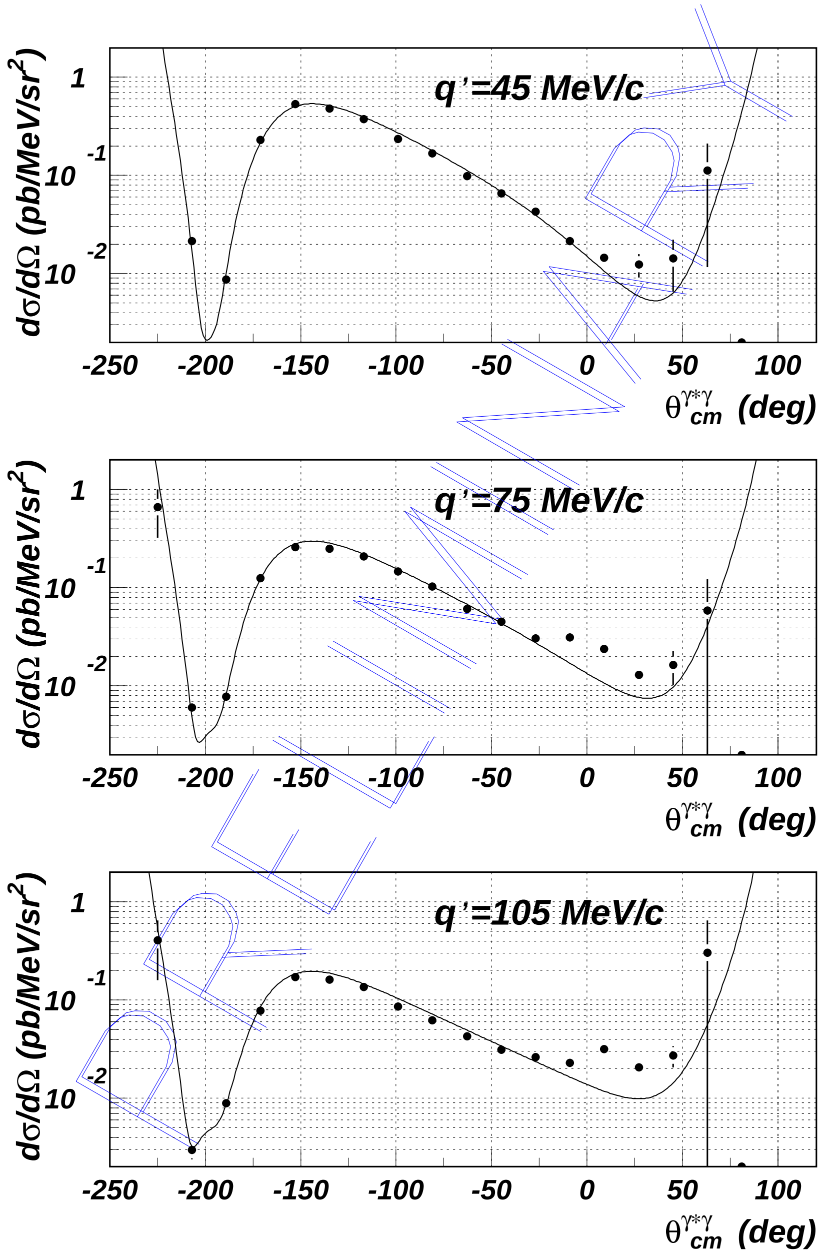

*Figure 7-9: Photon electro-production cross sections at $Q^2$=1.0(GeV/c)$^2$ as a function of $\theta_{cm}^{\gamma^*\gamma}$ for 3 values of $\mathsf{q}'_{cm}$ and fixed $\epsilon$. The solid lines represent the BH+Born cross section values. The considered range in $\theta_{cm}'^{\gamma^*\gamma}$ is $[60°, 120°]$.*

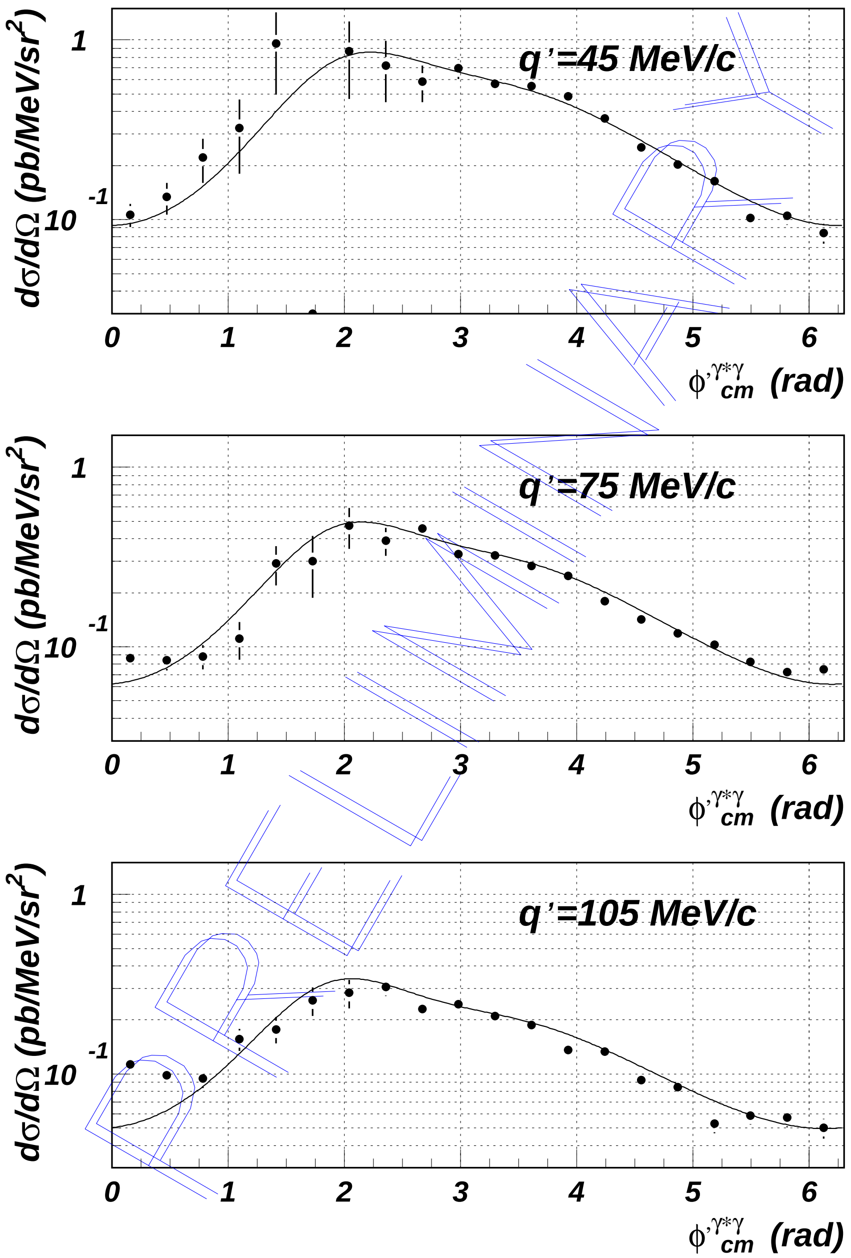

*Figure 7-10: Photon electro-production cross sections at* $Q^2$*=1.0(GeV/c)*$^2$ *as a function of* $\varphi'^{\gamma^*\gamma}_{cm}$ *for 3 values of* $\mathsf{q}'_{cm}$ *and fixed* $\epsilon$*. The solid lines represent the BH+Born cross section values. The considered range in* $\theta'^{\gamma^*\gamma}_{cm}$ *is [20°, 60°].*

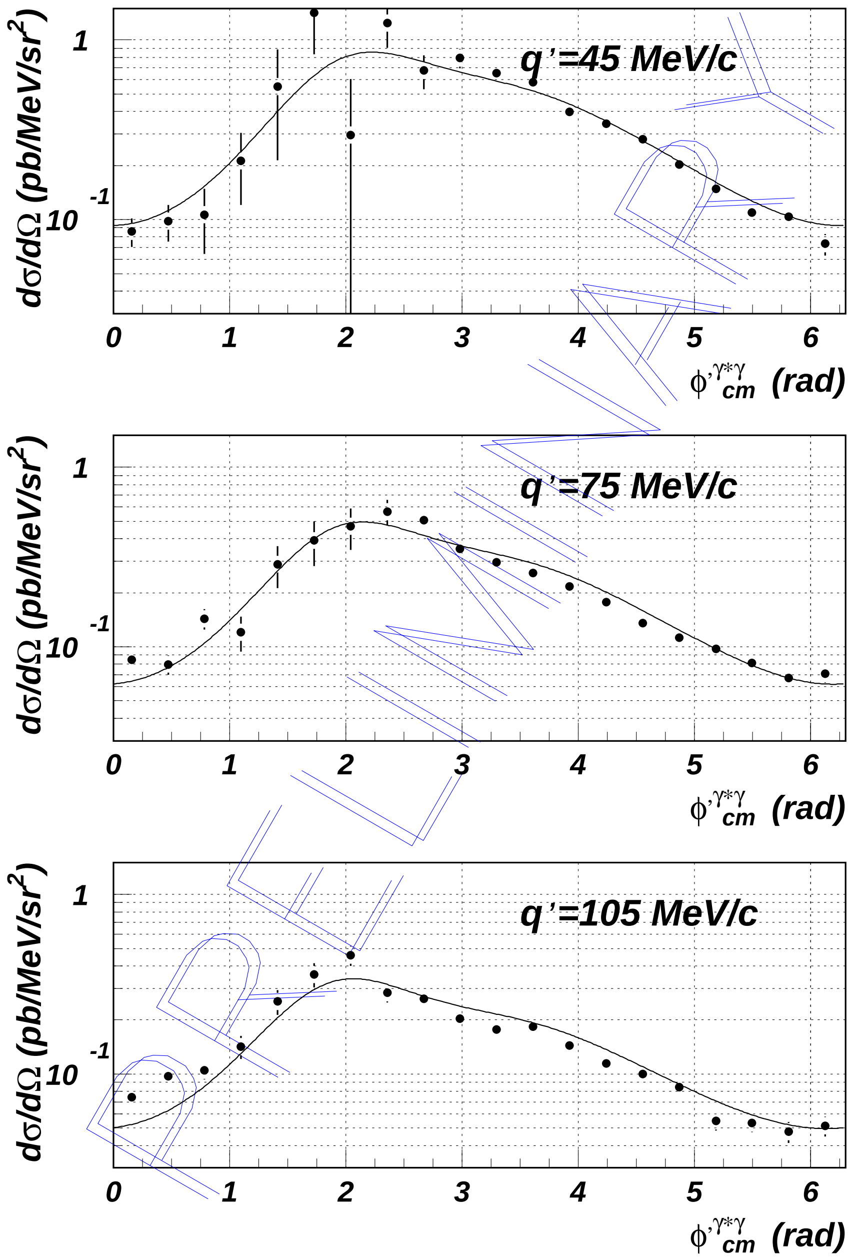

*Figure 7-11: Photon electro-production cross sections at* $Q^2$*=1.0(GeV/c)*$^2$ *as a function of* $\varphi'^{\gamma^*\gamma}_{cm}$ *for 3 values of* $\mathsf{q}'_{cm}$ *and fixed* $\epsilon$*. The solid lines represent the BH+Born cross section values. The considered range in* $\theta'^{\gamma^*\gamma}_{cm}$ *is* $[120°, 160°]$*.*

in section 1.6, at $\mathsf{q}'_{cm} = 45 MeV/c$ for the present kinematics one can expect already a slight effect of the generalized polarizabilities. For higher $\mathsf{q}'_{cm}$ values one sees the deviation from the BH+Born cross section increasing : for $\theta^{\gamma^*\gamma}_{cm}$ between -200° and -100° and for $\theta^{\gamma^*\gamma}_{cm}$ between -50° and 50°, the absolute value of the relative difference increases significantly. This might be interpreted as an effect of the generalized polarizabilities. In order to be able to do so, more systematical studies will have to be performed.

In figure 7-9, the same is presented as in figure 7-7, but with $60° \leq \theta'^{\gamma^*\gamma}_{cm} \leq 120°$. As such, a relatively small range around the leptonic plane is considered. One sees that, even at the lowest $\mathsf{q}'_{cm}$-value and for the forward angles, there seems to be too much yield. As such it might be that there are real physical offsets and/or resolutions that are not yet sufficiently understood. Figures 7-10 and 7-11 also represent photon electro-production cross section values, but out-of-(leptonic)-plane. The ranges in $\theta'^{\gamma^*\gamma}_{cm}$ that are considered are $20° \leq \theta'^{\gamma^*\gamma}_{cm} \leq 60°$ and $120° \leq \theta'^{\gamma^*\gamma}_{cm} \leq 160°$, respectively. The cross section values are presented as a function of $\varphi'^{\gamma^*\gamma}_{cm}$. One sees that the results are in reasonable good agreement, as such one can be confident about the analysis method.

In the next chapter, a first attempt will be made to extract preliminary information on the generalized polarizabilities, using the cross section values presented in figure 7-9.

## 7.6 Systematic Study of the Stability of the Cross Section Values

A very preliminary conclusion about the systematical studies that have been performed when defining the cuts on the data (see section 7.3), is presented in figure 7-12. Here, the representation is again for the 3 different values of $\mathsf{q}'_{cm}$ and as a function of $\theta^{\gamma^*\gamma}_{cm}$. In this figure, R represents the relative difference between obtained cross section values, using a well-defined set of cuts, and the cross section values obtained with the cuts as defined in section 7.3 and that one considers to be the “standard” cross section values. The band that is formed with the 2 lines, represents the extreme values between which all cross section values that are obtained, are situated. The systematical studies have been performed on 20 sets of different cuts. As such, this band gives a maximum systematical uncertainty on the obtained experimental cross section values, due to the cuts that are applied to the data.

As can be seen, almost all over the region of interest ($-175° < \theta^{\gamma^*\gamma}_{cm} < 45°$), the results that are obtained with the different cuts are stable within ±10%. This

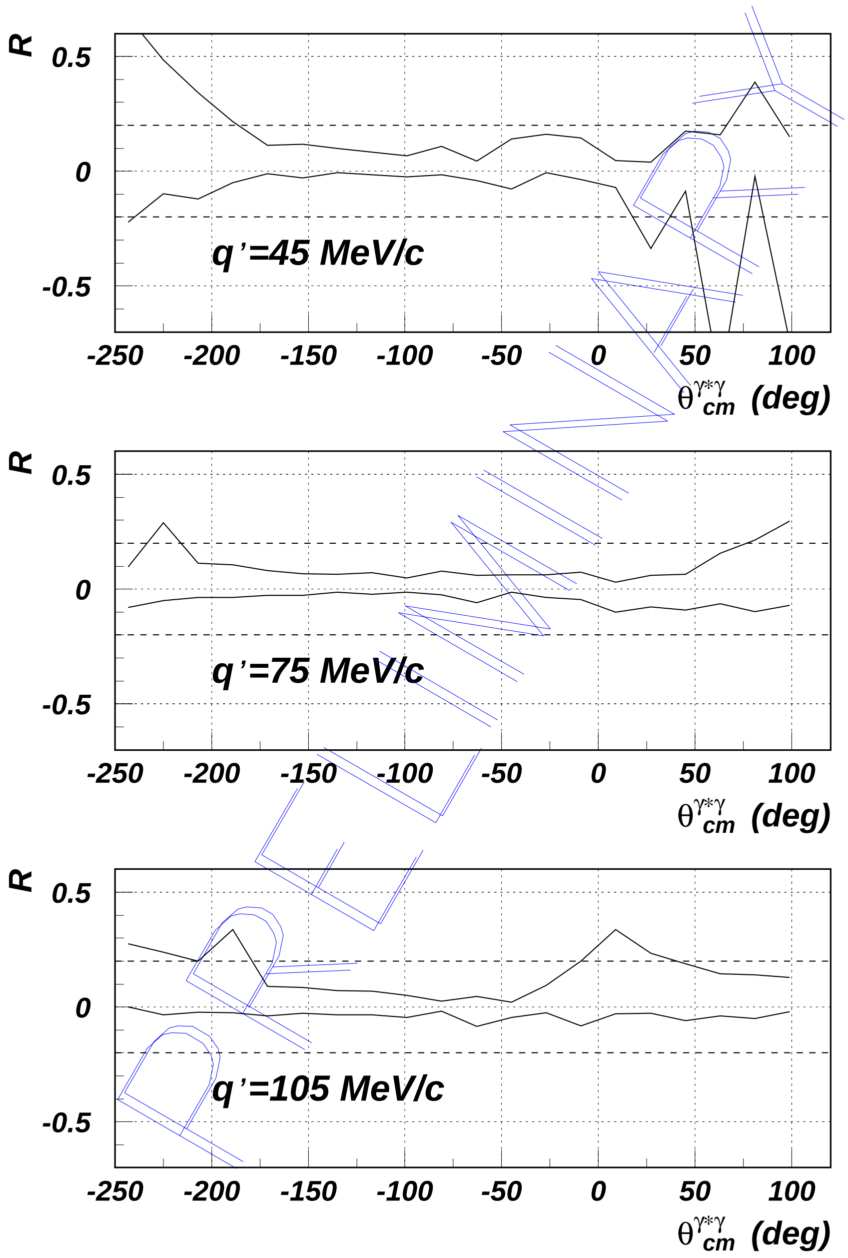

*Figure 7-12: Extreme relative differences encountered when performing systematical studies defining the cuts to be applied on the data.*

means the cuts that are applied to the data yield reasonably stable results.

An important remark that has to be made here, is that these studies have been performed, considering the complete range in $\theta'^{\gamma^*\gamma}_{cm}$ ($0° \leq \theta'^{\gamma^*\gamma}_{cm} \leq 180°$). When analysing cross section values with the intention to extract information on generalized polarizabilities however, it is necessary to restrict the ranges in $\theta'^{\gamma^*\gamma}_{cm}$ (see section 7.2). As such, these systematic studies of the cuts applied to the data should be redone, considering small ranges in $\theta'^{\gamma^*\gamma}_{cm}$. However, for a first analysis, one supposes that the result will not be very different.

## 7.7 Conclusion

In this chapter, preliminary cross section values for the photon electro-production reaction at $Q^2$=1.0(GeV/c)$^2$ have been presented. One should keep in mind however that there still is a lot of work to be done in order to improve the results and to be confident no offsets or other uncertainties are responsible for the observed deviation of the experimental cross section from the BH+Born cross section. As such, more systematical studies are needed, one should raise the statistical accuracy of the simulated solid angles, the cuts applied on the data should be optimized, the effect of considering different ranges in $\theta'^{\gamma^*\gamma}_{cm}$ has to be studied, ... . Nevertheless, in the next chapter a first attempt will be made to extract information on the generalized polarizabilities at $Q^2$=1.0(GeV/c)$^2$, using cross section values as presented in this chapter.

**at $Q$ =1.0(GeV/c)**

# Chapter 8

# Extracting Information on Generalized Polarizabilities

## 8.1 Introduction

A first, preliminary attempt has been made to extract information on the generalized polarizabilities using the photon electro-production cross sections that are presented in chapter 7. The kinematics where they have been determined are defined by : $Q^2$=1.0(GeV/c)$^2$, $\mathsf{q}_{cm}^{mean}$=1084.1 MeV/c and $\epsilon^{mean}$=0.951, corresponding to $\tilde{Q}^2 = 0.93$ $(GeV/c)^2$ (see section 7.2). As already mentioned, only the cross section values obtained in a rather small range around the leptonic plane ($60° \leq \theta_{cm}^{\prime\gamma^*\gamma} \leq 120°$) are used (see figure 7-9). The method that is applied to extract this information has been explained in section 1.5.6 and is similar to the one applied to the data of the VCS experiment at MAMI (see chapter 2). Only the main steps and equations that are needed to extract information on the generalized polarizabilities will be recalled here.

As seen in equation 1-66, the photon electro-production reaction cross section can be written as :

$$d^5\sigma^{exp} = d^5\sigma^{BH+Born} + \phi\mathsf{q}'_{cm}(\mathcal{M}_0^{exp} - \mathcal{M}_0^{BH+Born}) + \mathcal{O}(\mathsf{q}'^2_{cm}) \tag{8-1}$$

A first step in the procedure is to check whether the experimental cross section value converges to the BH+Born value when $\mathsf{q}'_{cm}$ decreases. This has already been done in chapter 7, where one has noticed that with decreasing $\mathsf{q}'_{cm}$, the experimental cross section values tend towards the BH+Born ones.

The next step is to study, for different values of $\theta_{cm}^{\gamma^*\gamma}$, the behaviour of $(d^5\sigma^{exp} - d^5\sigma^{BH+Born})/\phi\mathsf{q}'_{cm}$ as a function of $\mathsf{q}'_{cm}$ and to extrapolate its values to $\mathsf{q}'_{cm} = 0$. For each value of $\theta_{cm}^{\gamma^*\gamma}$, this results in knowing $\mathcal{M}_0^{exp} - \mathcal{M}_0^{BH+Born}$ which is, for a non polarised experiment, parametrized in terms of 5 GPs.

The final step is to study $\mathcal{M}_0^{exp} - \mathcal{M}_0^{BH+Born}$ as a function of $v_{LL}/v_{LT}$. This will yield information on 2 combinations of GPs (see equation 1-68) :

$$\mathcal{M}_0^{exp} - \mathcal{M}_0^{BH+Born} = v_{LL}(\varphi, \theta_{cm}^{\gamma^*\gamma})(\mathbf{P_{LL}}(\mathsf{q}_{cm}) - \frac{1}{\epsilon}\mathbf{P_{TT}}(\mathsf{q}_{cm})) + v_{LT}(\varphi, \theta_{cm}^{\gamma^*\gamma})\mathbf{P_{LT}}(\mathsf{q}_{cm}) \tag{8-2}$$

Note that all results that will be shown here are very preliminary and that a more detailed and accurate analysis of the data will be needed in order to extract more precise information.

## 8.2 Extracting Preliminary Information on Generalized Polarizabilities at Q$^2$=1.0(GeV/c)$^2$

In order to extract preliminary information on the generalized polarizabilities, only the relevant range in $\theta_{cm}^{\gamma^*\gamma}$ is considered. This range covers $-175° < \theta_{cm}^{\gamma^*\gamma} < 45°$. So only 12 data points are considered. The region $\theta_{cm}^{\gamma^*\gamma} > 45°$ is left out because the statistical accuracy of the points in that region is not good (see figure 7-9) and one approaches the cat ears. The reason why the points in the region $\theta_{cm}^{\gamma^*\gamma} < -175°$ are disregarded is twofold : the cross section value changes a lot in that region, making an interpolation in the simulation grid less accurate; moreover in that region, the expected polarizability effect is high (see figure 1-14c, note that the representation is on a logarithmic scale), as such the BH+Born approximation that has been made in the simulation is not sufficient to produce good solid angles. In figure 8-1, $(d^5\sigma^{exp} - d^5\sigma^{BH+Born})/\phi \mathsf{q}'_{cm}$ (indicated as $\Delta\mathcal{M}^{exp}$ in the figure) is shown as a function of $\mathsf{q}'_{cm}$ for the 12 different values of $\theta_{cm}^{\gamma^*\gamma}$. For a first analysis, one supposes there is no $\mathsf{q}'_{cm}$-dependence of $(\mathcal{M}^{exp} - \mathcal{M}^{BH+Born})$. The intercept at the origin of $(d^5\sigma^{exp} - d^5\sigma^{BH+Born})/\phi \mathsf{q}'_{cm}$ is determined as the weighted mean value of the 3 data points. The middle of the shaded bands represent the value that is extrapolated to $\mathsf{q}'_{cm}$=0 MeV/c using the weighted mean method, the shaded bands indicate the statistical error on this value.

Following equation (8-2), $(\mathcal{M}_0^{exp} - \mathcal{M}_0^{BH+Born})/v_{LT}(\varphi, \theta_{cm}^{\gamma^*\gamma})$ is plotted as a function of $v_{LL}(\varphi, \theta_{cm}^{\gamma^*\gamma})/v_{LT}(\varphi, \theta_{cm}^{\gamma^*\gamma})$ in figure 8-2. A linear fit has been made to the data points. This fit is represented by the solid line. The slope and intercept of this linear fit yield values for the two structure functions $(\mathbf{P_{LL}}(\mathsf{q}_{cm}) - \frac{1}{\epsilon}\mathbf{P_{TT}}(\mathsf{q}_{cm}))$ and $\mathbf{P_{LT}}(\mathsf{q}_{cm})$ that are combinations of 5 GPs :

$$P_{LL} - \frac{1}{\epsilon}P_{TT} = 6.3 \pm 0.6 \pm 3 \ (GeV)^{-2} \quad P_{LT} = -1.7 \pm 0.3 \pm 1 \ (GeV)^{-2} \tag{8-3}$$

The first error is the statistical error, the second error is the estimated systematical

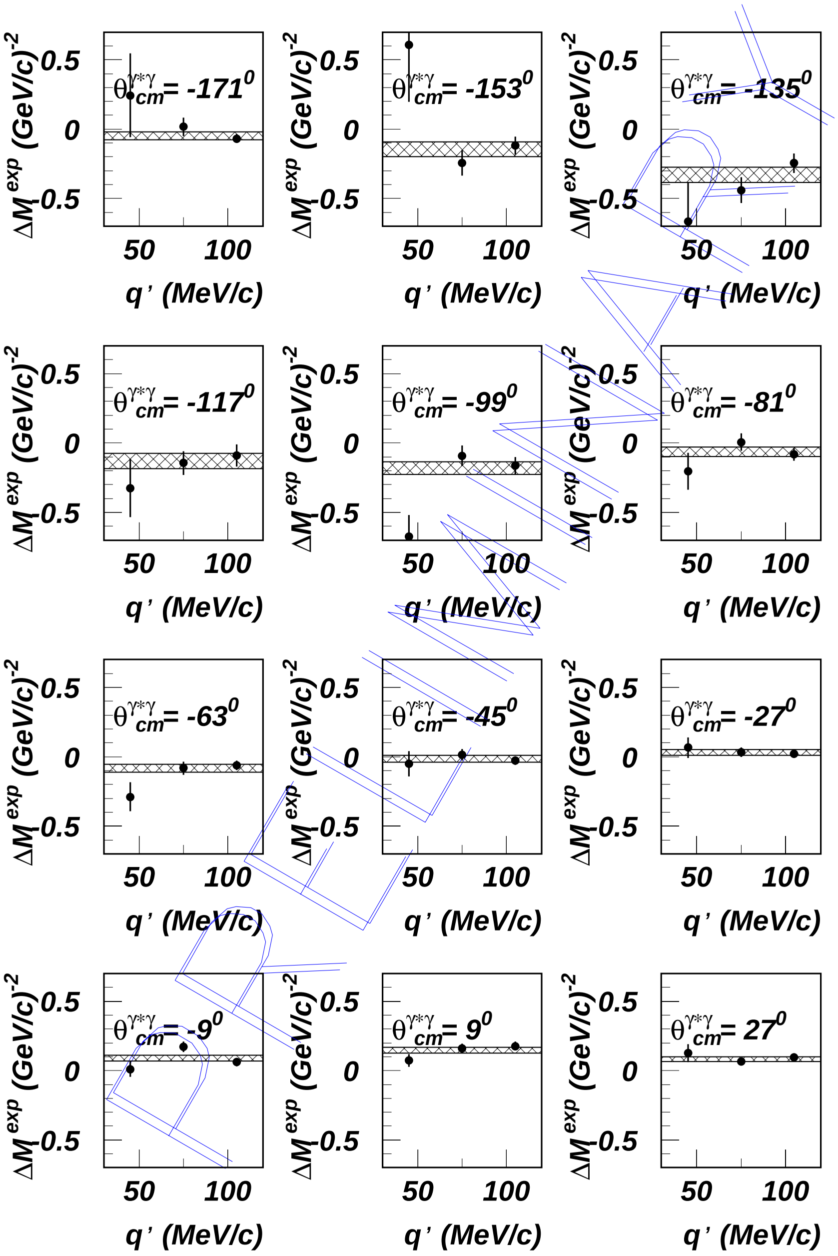

*Figure 8-1:* $(d^5\sigma^{exp} - d^5\sigma^{BH+Born})/\phi \mathsf{q}'_{cm}$ *(denoted as* $\Delta\mathcal{M}^{exp}$ *in the figure) as a function of* $\mathsf{q}'_{cm}$ *for the 12 different angles* $\theta^{\gamma^*\gamma}_{cm}$.

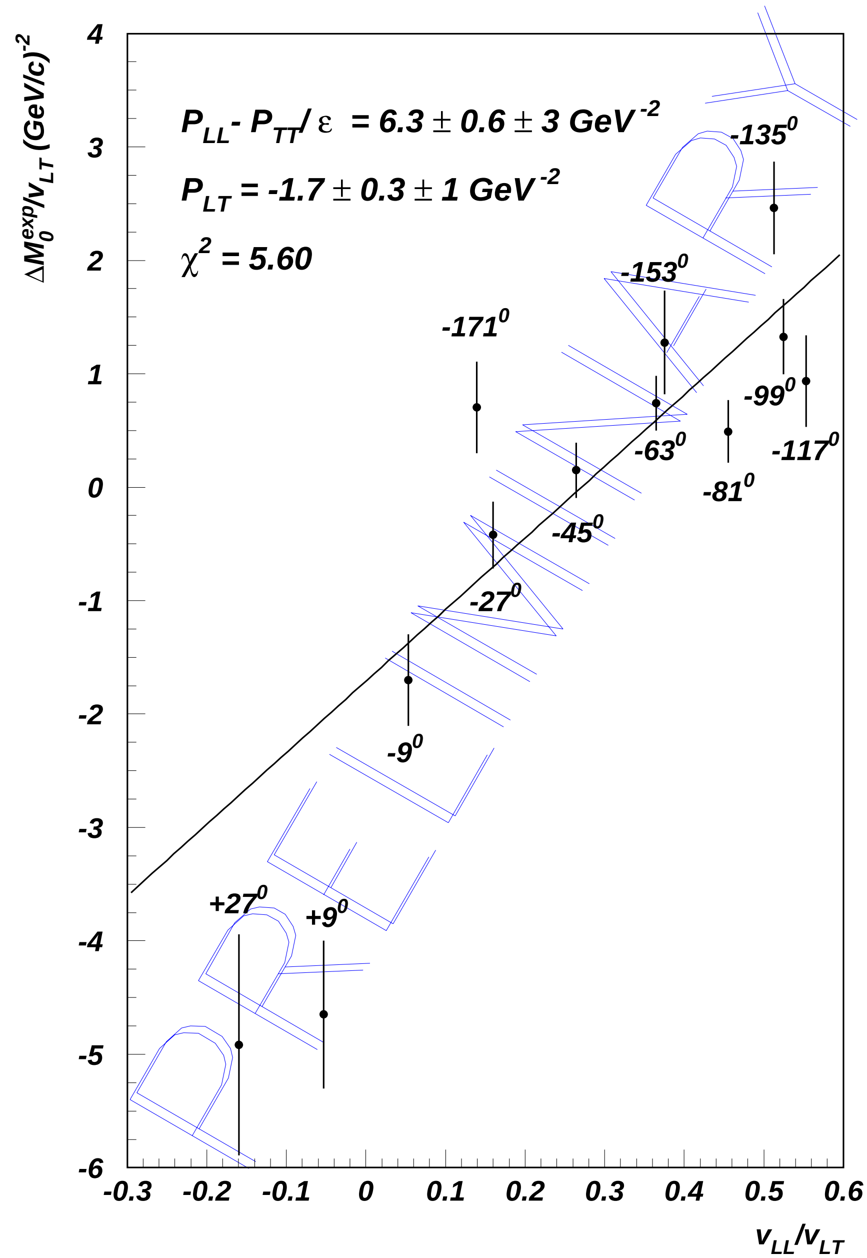

*Figure 8-2:* $(\mathcal{M}_0^{exp} - \mathcal{M}_0^{BH+Born})/v_{LT}(\varphi,\theta_{cm}^{\gamma^*\gamma})$ *(in the figure denoted as* $\Delta\mathcal{M}_0^{exp}/v_{LT}$*) as a function of* $v_{LL}(\varphi,\theta_{cm}^{\gamma^*\gamma})/v_{LT}(\varphi,\theta_{cm}^{\gamma^*\gamma})$ *(in the figure* $\mathsf{v}_{LL}/\mathsf{v}_{LT}$*). The solid line represents the linear fit to the data points with coefficients as indicated.*

error. For each data point, the value for $\theta_{cm}^{\gamma^*\gamma}$ is indicated on the figure. It is clear that the data points on this plot are not fully aligned, as such a more precise data-analysis will have to be performed. One also observes that the two points corresponding to $\theta_{cm}^{\gamma^*\gamma} = +27°$ and $\theta_{cm}^{\gamma^*\gamma} = +9°$ are rather far out. This is not surprising since in figure 7-9 there is an indication that these two points are too high. Consequently, a second linear fit has been made to the data points, omitting these two data points. The values that result from such a fit are :

$$P_{LL} - \frac{1}{\epsilon} P_{TT} = 4.7 \pm 0.7 \pm 3 \ (GeV)^{-2} \quad P_{LT} = -1.1 \pm 0.3 \pm 1 \ (GeV)^{-2} \quad \text{(8-4)}$$

They are within the error bars compatible with the results found when fitting all 12 data points.

After determining these indicative values for the two structure functions, one can calculate the photon electro-production cross section values that take into account these effects of the generalized polarizabilities and compare the experimental data to the theoretically calculated distributions. This has been done in figure 8-3. Here, the experimental photon electro-production cross section values are the same as in figure 7-9. The solid line, however, now represents the photon electro-production cross section, taking into account the polarizability effect due to the two structure functions as obtained in equation (8-3). The dotted line represents the BH+Born cross section. Again one sees that the two points $\theta_{cm}^{\gamma^*\gamma} = +27°$ and $\theta_{cm}^{\gamma^*\gamma} = +9°$ that are taken into account when making the linear fit in figure 8-2 and from which one already stated they are not “clean” yet, are not at all in agreement with the theoretically calculated cross section behaviour. In figure 8-4, the same is presented, but the polarizability effect that is taken into account here is the one obtained in equation (8-4), thus omitting the two data points at $\theta_{cm}^{\gamma^*\gamma} = +27°$ and $\theta_{cm}^{\gamma^*\gamma} = +9°$, respectively.

In figure 8-5, again the two structure functions are presented as a function of $Q^2$. The RCS and MAMI results are indicated, analogue to figures 1-13 and 2-6. Also the preliminary values that are obtained in this chapter are indicated on the figures. The solid line represents the HBChPT approximation. Remark that the value of $\epsilon$ is 0.62 for the MAMI result and the HBChPT prediction, and 0.951 for the TJNAF result.

An important remark that has to be made is that the values for the structure functions that are mentioned here, are only indicative values that give a preliminary estimation for the two structure functions. As has been shown, there still is a lot of work to be done before being able to have suffucient confidence in the obtained values for the structure functions.

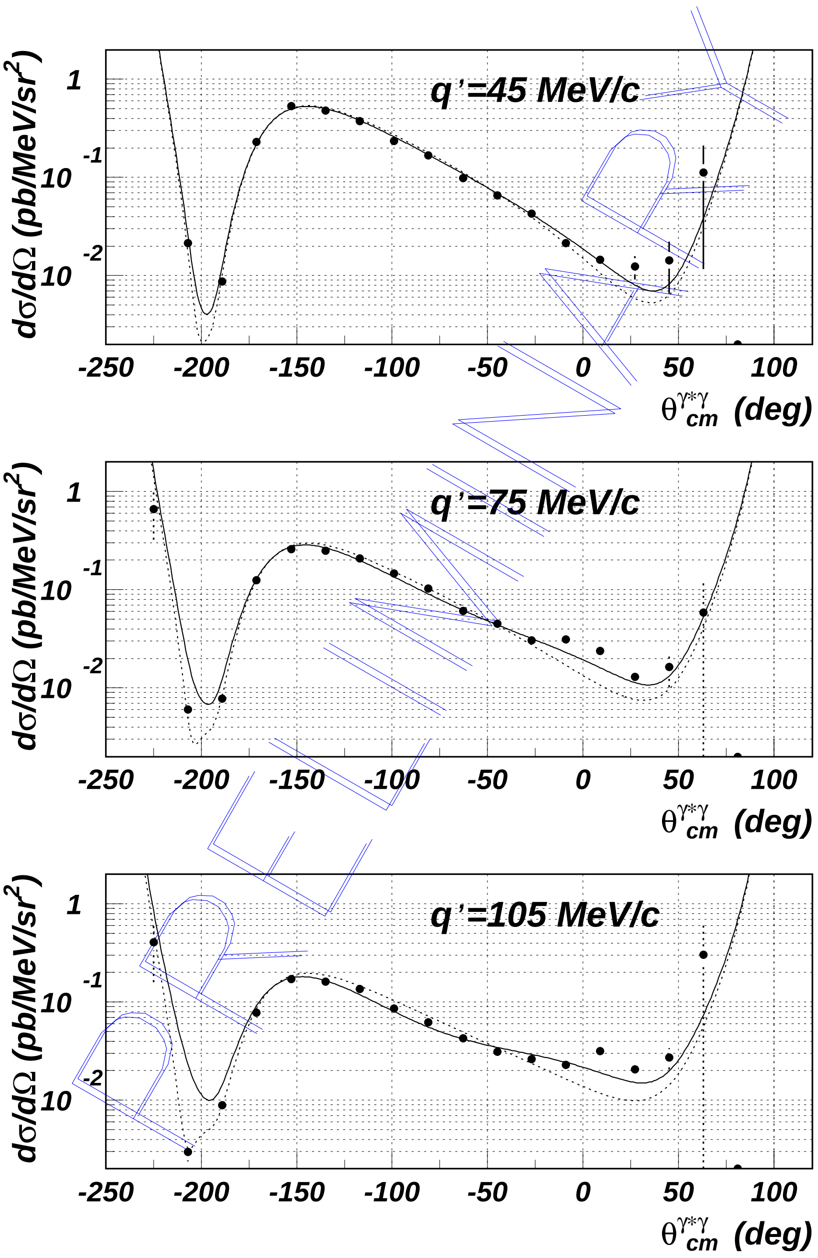

*Figure 8-3: Photon electro-production cross sections at* $Q^2$*=1.0(GeV/c)*$^2$ *as a function of* $\theta_{cm}^{\gamma^*\gamma}$*. The solid lines represent the cross section values containing a polarizability effect as defined in equation (8-3), the dotted line represents the BH+Born cross section. The considered range in* $\theta_{cm}'^{\gamma^*\gamma}$ *is* $[60°, 120°]$*.*

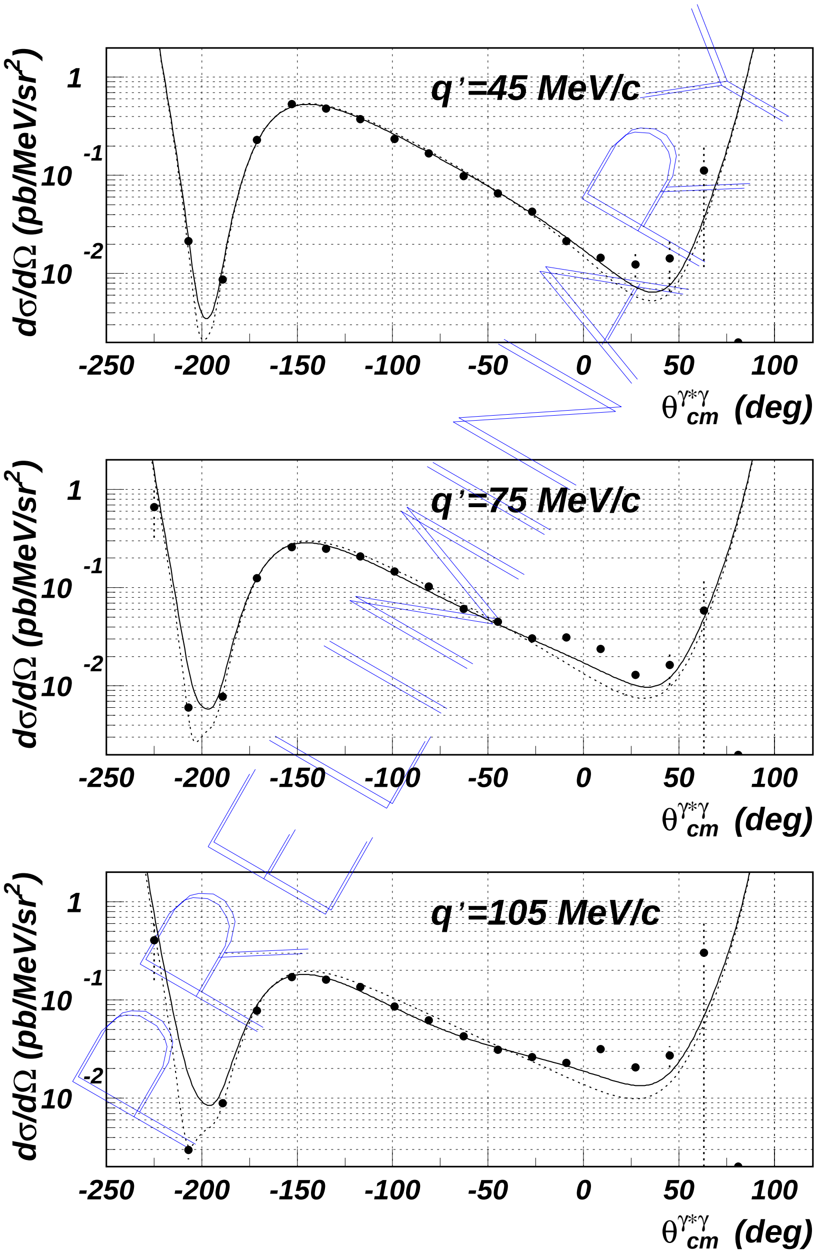

*Figure 8-4: Photon electro-production cross sections at* $Q^2$*=1.0(GeV/c)*$^2$ *as a function of* $\theta_{cm}^{\gamma^*\gamma}$*. The solid lines represent the cross section values containing a polarizability effect as defined in equation (8-4), the dotted line represents the BH+Born cross section. The considered range in* $\theta_{cm}'^{\gamma^*\gamma}$ *is* $[60°, 120°]$*.*

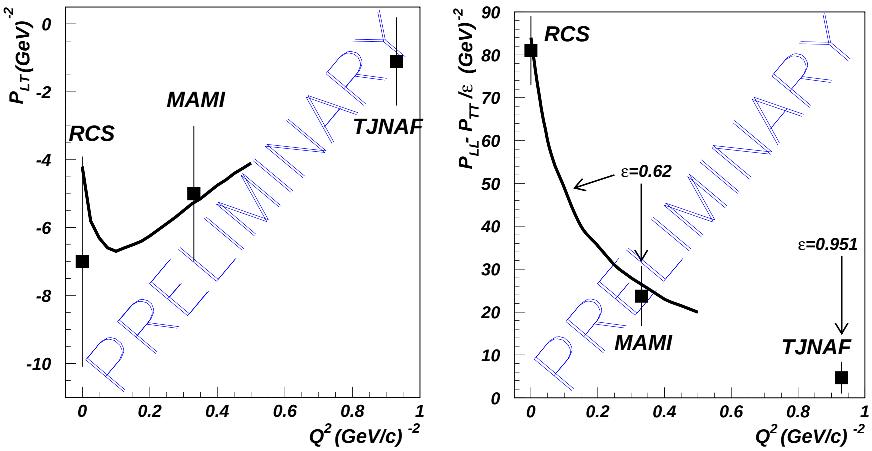

*Figure 8-5: Results for the two structure functions, obtained in RCS (see figure 1-13), VCS at MAMI (see figure 2-6) and VCS at TJNAF (see equation (8-4)). The solid line represents an approximation of the HBChPT predictions .*

## 8.3 Conclusion

In this chapter preliminary indicative values for the two structure functions $(\mathbf{P_{LL}}(\mathsf{q}_{cm}) - \frac{1}{\epsilon}\mathbf{P_{TT}}(\mathsf{q}_{cm}))$ and $\mathbf{P_{LT}}(\mathsf{q}_{cm})$ that are accessible in an unpolarised photon electro-production experiment have been obtained at $Q^2 = 1.0\ (GeV/c)^2$, $\mathsf{q}_{cm}^{mean}$=1084.1 MeV/c and $\epsilon^{mean}$=0.951 ($\tilde{Q}^2 = 0.93\ (GeV/c)^2$). The values that result from this analysis will become more precise as the analysis progresses in the future. In order to improve the results, the data has to become "cleaner". Once everything is under control (resolutions, offsets, ...) a new determination of the two structure functions can be made. These values can then be used to start the iteration procedure, which will yield more precise values for the two structure functions. Evaluating the change of the structure functions due to a first iteration, will indicate how well they are determined and if other iterations are needed.

# Summary and Outlook

Up to now, a fundamental problem of subatomic physics is the characterization of the internal structure of the nucleon. At short distance this structure can be described by point-like quarks and gluons, but at larger distance (of the order of the nucleon's size) the situation becomes vague. In the exploration aiming to bridge particle and nuclear physics, electromagnetic probes play an important role. Indeed, the electromagnetic interaction is well understood and it gives access to valuable information on the hadronic structure. For many years, experiments and studies have been performed in the framework of electron scattering, real Compton scattering and deep-inelastic scattering. These experiments have lead to the knowledge of the nucleon form factors, the nucleon electric and magnetic polarizability and structure functions. It is only recently, with the advent of the new generation of electron accelerators and high precision detectors, that a new electromagnetic probe has become accessible : Virtual Compton Scattering (VCS). Below the pion production threshold this fundamental exclusive reaction can be interpreted as electron scattering off a nucleon that is polarised by the presence of quasi-constant electric and magnetic fields. This process can be accessed experimentally through the photon electro-production reaction $e + p \to e' + p' + \gamma$ and reveals new insights in the nucleon internal structure in the form of 6 generalized polarizabilities. These generalized polarizabilities can be pictured as quantifying the effect of an electromagnetic perturbation on the nucleon components. They are an extension of the electric and magnetic polarizabilities obtained in real Compton scattering and they give information on the deformation of charge- and magnetisation distributions inside the nucleon, obtained in elastic scattering. As such, virtual Compton scattering generalizes the real Compton scattering process and is complementary to electron scattering on a free nucleon.

In the first part of this thesis, the physics framework of the VCS process below the pion production threshold has been outlined as well as the formalism to extract information on the generalized polarizabilities. This has been done with two VCS experiments in mind : the VCS experiment at MAMI, which was the first experiment to measure photon electro-production reaction cross sections below the pion production threshold at $\tilde{Q}^2$=0.33(GeV/c)$^2$, and the VCS experiment at

TJNAF of which one of the goals was to measure photon electro-production reaction cross sections below the pion production threshold at Q$^2$=1.0(GeV/c)$^2$.

The second chapter of this thesis gives a short overview of the VCS experiment at MAMI. This measurement, which has been performed in 1995-1997, was the first experiment dedicated to the extraction of information on the generalized polarizabilities at $\tilde{Q}^2$=0.33(GeV/c)$^2$. It showed that VCS experiments are feasible, but are not that easy since high accuracy on the cross section values is needed in order to identify a polarizability effect. Nevertheless, two structure functions have been determined at $\tilde{Q}^2 = 0.33\ (GeV/c)^2$ : $(\mathbf{P_{LL}}(\mathsf{q}_{cm}) - \frac{1}{\epsilon}\mathbf{P_{TT}}(\mathsf{q}_{cm})) = 23.7 \pm 2.2 \pm 0.6 \pm 4.3\ GeV^{-2}$ and $\mathbf{P_{LT}}(\mathsf{q}_{cm}) = -5.0 \pm 0.8 \pm 1.1 \pm 1.4\ GeV^{-2}$. These two structure functions are linear combinations of 5 of the 6 generalized polarizabilities. The results are compatible with heavy-baryon chiral perturbation predictions.

The main effort of the present work was focused on the analysis of the VCS experiment performed at TJNAF. The experimental setup used for this experiment is described in chapter 3. Elastic scattering data and VCS data at Q$^2$=1.0(GeV/c)$^2$ have been analysed in chapter 5 and differential cross sections have been obtained for each process. In order to obtain precise values for these cross sections, an extensive Monte Carlo simulation was used. This simulation code, which is detailed in chapter 4, generates events according to the BH+Born (or elastic scattering) cross section behaviour, taking into account the experimental setup and resolution effects. The results of the analysis of the elastic scattering data are presented in chapter 6. These results show that the calibration and resolutions in the center of the acceptance of both spectrometers are reasonably well controlled. Near the edges, however, the situation is less favourable. This has an impact on the VCS cross sections, since the VCS kinematics cover the complete spectrometer acceptances. The analysis of the VCS data has lead to preliminary results for the photon electro-production reaction cross sections which are extensively presented in chapter 7. They are evaluated as a function of $\mathsf{q}'_{cm}$ and $\theta_{cm}^{\gamma^*\gamma}$, the outgoing photon momentum and the polar angle between incoming virtual and outgoing real photon, respectively, and at fixed $\mathsf{q}_{cm}$ and $\epsilon$.

In order to extract the two structure functions, it has been verified that at low $\mathsf{q}'_{cm}$, the photon electro-production cross section converges, within the error bars, to the BH+born cross section value. This is the first important step to be made when extracting information on the generalized polarizabilities from photon electro-production cross sections. Although it is clear that the data-analysis can be further improved in the future, a first attempt was made in chapter 8 to extract preliminary indicative values for the two structure functions at Q$^2$ = 1.0 (GeV/c)$^2$, $\mathsf{q}_{cm}$ = 1084.1 MeV/c and $\epsilon = 0.951$ ($\tilde{Q}^2\ =\ 0.93\ (GeV/c)^2$) : $(\mathbf{P_{LL}}(\mathsf{q}_{cm}) - \frac{1}{\epsilon}\mathbf{P_{TT}}(\mathsf{q}_{cm})) =$

$4.7 \pm 0.7 \pm 3\ GeV^{-2}$ and $\mathbf{P_{LT}}(\mathsf{q}_{cm}) = -1.1 \pm 0.3 \pm 1\ GeV^{-2}$. These are only indicative values that give a preliminary estimation for the two structure functions.

In the future, large efforts will have to be made in order to improve the quality of the data and the systematical accuracy on the obtained results. Once this goal is reached, one can extract again the values for the two structure functions with better precision and reliability. Moreover, the experiments that are presented in this thesis exploit only one possibility to explore the field of VCS and its related generalized polarizabilities. Double polarised experiments e.g. will yield more information on the generalized polarizabilities, the recently developed dispersion formalism opens the possibility to analyse the data above the pion production threshold in order to extract information on the nucleon structure, ... . As such, VCS promises to open a variety of ways that lead to bridging the subhadronic and nuclear world.

# Appendix A

# Spectrometer Setup Kinematics

The next tables give an overview of all kinematical settings that were used to take data for the VCS experiment E93-050. For all kinematical settings during the experiment, the beam energy was set to be 4.045 GeV. The kinematical settings can be divided into 5 parts :

- Electron and hadron arm optics and acceptance calibration at $Q^2$=1 (GeV/c)$^2$ (see table A-1).
- VCS data acquisition below pion production threshold (polarizability domain) at $Q^2$=1 (GeV/c)$^2$ (see table A-2).
- Electron and hadron arm optics and acceptance calibration at $Q^2$=1.9 (GeV/c)$^2$ (see table A-3).
- VCS data acquisition below pion production threshold (polarizability domain) at $Q^2$=1.9 (GeV/c)$^2$ (see table A-4).
- VCS data acquisition in the resonance region(see table A-5).

The first column gives the names of the kinematical settings, the second column indicates the target that is used. The next four columns resume the electron spectrometer characteristics : first the central momentum setting relative to the place of the elastic peak in the focal plane, next the momentum setting of the spectrometer followed by its nominal angle and finally the collimator that is used. The following three colums give the momentum setting, nominal angle and collimator for the hadron arm. For the calibration settings, the last column shows whether this kinematical setting serves to calibrate the spectrometer optics (matrix) or the spetrometer acceptance. The table summarizing the resonance data is slightly different, but self-explaining.

| | | electron spectrometer | | | | hadron spectrometer | | | goal |
|---|---|---|---|---|---|---|---|---|---|
| names | target | $\frac{\delta p}{p}$ | P | $\theta_E$ | colli | P | $\theta_H$ | colli | |
| ca_1_1 | H_15cm | +0 | 3.496 | 15.42 | sieve | 1.143 | -54.28 | 6 msr | E-matrix |
| ca_1_2 | H_15cm | +0 | 3.496 | 15.42 | 6 msr | 1.143 | -54.28 | 6 msr | E-accept |
| ca_1_3 | E_4cm | +0 | 3.496 | 15.42 | 6 msr | 1.143 | -54.28 | 6 msr | E-z_matrix |
| ca_1_4 | E_10cm | +0 | 3.496 | 15.42 | 6 msr | 1.143 | -54.28 | 6 msr | E-z_matrix |
| ca_1_5 | E_15cm | +0 | 3.496 | 15.42 | 6 msr | 1.143 | -54.28 | 6 msr | E-zz_matrix |
| ca_1_6 | $C^{12}$ | +0 | 3.496 | 15.42 | 6 msr | 1.143 | -54.28 | 6 msr | E-zz_matrix |
| ca_1_7 | H_15cm | -4 | 3.356 | 15.42 | sieve | 1.143 | -54.28 | 6 msr | E-zmatrix |
| ca_1_8 | H_15cm | -4 | 3.356 | 15.42 | 6 msr | 1.143 | -54.28 | 6 msr | E-zaccept |
| ca_1_9 | H_15cm | -2 | 3.426 | 15.42 | sieve | 1.143 | -54.28 | 6 msr | E-zmatrix |
| ca_1_10 | H_15cm | -2 | 3.426 | 15.42 | 6 msr | 1.143 | -54.28 | 6 msr | E-zaccept |
| ca_1_11 | H_15cm | +2 | 3.566 | 15.42 | sieve | 1.143 | -54.28 | 6 msr | E-zmatrix |
| ca_1_12 | H_15cm | +2 | 3.566 | 15.42 | 6 msr | 1.143 | -54.28 | 6 msr | E-zaccept |
| ca_1_13 | H_15cm | +4 | 3.636 | 15.42 | sieve | 1.143 | -54.28 | 6 msr | E-zmatrix |
| ca_1_14 | H_15cm | +4 | 3.636 | 15.42 | 6 msr | 1.143 | -54.28 | 6 msr | E-zaccept |
| ca_1_15 | H_15cm | +0 | 3.496 | 15.42 | 6 msr | 1.143 | -54.28 | sieve | H-matrix |
| ca_1_16 | H_15cm | +0 | 3.496 | 15.42 | 6 msr | 1.143 | -54.28 | 6 msr | H-accept |
| ca_1_17 | E_4cm | +0 | 3.496 | 15.42 | 6 msr | 1.143 | -54.28 | 6 msr | H-z_matrix |
| ca_1_18 | E_10cm | +0 | 3.496 | 15.42 | 6 msr | 1.143 | -54.28 | 6 msr | H-z_matrix |
| ca_1_19 | $C^{12}$ | +0 | 3.496 | 15.42 | 6 msr | 1.143 | -54.28 | 6 msr | H-z_matrix |
| ca_1_20 | H_15cm | +0 | 3.496 | 15.42 | 6 msr | 1.143 | -55.78 | sieve | H-matrix |
| ca_1_21 | H_15cm | +0 | 3.496 | 15.42 | 6 msr | 1.143 | -55.78 | 6 msr | H-accept |
| ca_1_22 | H_15cm | +0 | 3.496 | 15.42 | 6 msr | 1.143 | -55.08 | sieve | H-matrix |
| ca_1_23 | H_15cm | +0 | 3.496 | 15.42 | 6 msr | 1.143 | -55.08 | 6 msr | H-accept |
| ca_1_24 | H_15cm | +0 | 3.496 | 15.42 | 6 msr | 1.143 | -53.68 | sieve | H-matrix |
| ca_1_25 | H_15cm | +0 | 3.496 | 15.42 | 6 msr | 1.143 | -53.68 | 6 msr | H-accept |
| ca_1_26 | H_15cm | +0 | 3.496 | 15.42 | 6 msr | 1.143 | -52.78 | sieve | H-matrix |
| ca_1_27 | H_15cm | +0 | 3.496 | 15.42 | 6 msr | 1.143 | -52.78 | 6 msr | H-accept |

Table A-1: *Elastic Kinematics for calibration of electron and hadron spectrometer at* $Q^2$*=1(GeV/c)*$^2$.

|  |  | electron spectrometer |  |  |  | hadron spectrometer |  |  |
|---|---|---|---|---|---|---|---|---|
| names | target | $\frac{\delta p}{p}$ | P | $\theta_E$ | colli | P | $\theta_H$ | colli |
| da_1_1 | H_15cm | -1.8 | 3.433 | 15.42 | 6 msr | 0.932 | -53.0 | 6 msr |
| da_1_2 | H_15cm | -1.8 | 3.433 | 15.42 | 6 msr | 0.932 | -50.0 | 6 msr |
| da_1_3 | H_15cm | -1.8 | 3.433 | 15.42 | 6 msr | 0.932 | -47.0 | 6 msr |
| da_1_4 | H_15cm | -1.8 | 3.433 | 15.42 | 6 msr | 0.977 | -53.0 | 6 msr |
| da_1_5 | H_15cm | -1.8 | 3.433 | 15.42 | 6 msr | 0.977 | -50.5 | 6 msr |
| da_1_6 | H_15cm | -1.8 | 3.433 | 15.42 | 6 msr | 0.977 | -48.0 | 6 msr |
| da_1_7 | H_15cm | -1.8 | 3.433 | 15.42 | 6 msr | 0.977 | -45.0 | 6 msr |
| da_1_8 | H_15cm | -1.8 | 3.433 | 15.42 | 6 msr | 1.037 | -52.0 | 6 msr |
| da_1_9 | H_15cm | -1.8 | 3.433 | 15.42 | 6 msr | 1.037 | -49.5 | 6 msr |
| da_1_10 | H_15cm | -1.8 | 3.433 | 15.42 | 6 msr | 1.037 | -47.0 | 6 msr |
| da_1_11 | H_15cm | -1.8 | 3.433 | 15.42 | 6 msr | 1.037 | -44.5 | 6 msr |
| da_1_12 | H_15cm | -1.8 | 3.433 | 15.42 | 6 msr | 1.107 | -50.5 | 6 msr |
| da_1_13 | H_15cm | -1.8 | 3.433 | 15.42 | 6 msr | 1.107 | -47.5 | 6 msr |
| da_1_14 | H_15cm | -1.8 | 3.433 | 15.42 | 6 msr | 1.107 | -44.5 | 6 msr |
| da_1_15 | H_15cm | -1.8 | 3.433 | 15.42 | 6 msr | 1.187 | -50.0 | 6 msr |
| da_1_16 | H_15cm | -1.8 | 3.433 | 15.42 | 6 msr | 1.187 | -48.5 | 6 msr |
| da_1_17 | H_15cm | -1.8 | 3.433 | 15.42 | 6 msr | 1.187 | -46.5 | 6 msr |

Table A-2: *VCS data acquisition below pion production threshold at* $Q^2$*=1(GeV/c)*$^2$.

| | | electron spectrometer | | | | hadron spectrometer | | | goal |
|---|---|---|---|---|---|---|---|---|---|
| names | target | $\frac{\delta p}{p}$ | P | $\theta_E$ | colli | P | $\theta_H$ | colli | |
| ca_2_1 | H_15cm | +0 | 3.006 | 23.01 | sieve | 1.730 | -42.78 | 6 msr | E-matrix |
| ca_2_2 | H_15cm | +0 | 3.006 | 23.01 | 6 msr | 1.730 | -42.78 | 6 msr | E-accept |
| ca_2_3 | E_4cm | +0 | 3.006 | 23.01 | 6 msr | 1.730 | -42.78 | 6 msr | E-z_matrix |
| ca_2_4 | E_10cm | +0 | 3.006 | 23.01 | 6 msr | 1.730 | -42.78 | 6 msr | E-z_matrix |
| ca_2_5 | E_15cm | +0 | 3.006 | 23.01 | 6 msr | 1.730 | -42.78 | 6 msr | E-z_matrix |
| ca_2_6 | $C^{12}$ | +0 | 3.006 | 23.01 | 6 msr | 1.730 | -42.78 | 6 msr | E-z_matrix |
| ca_2_7 | H_15cm | -4 | 2.886 | 23.01 | sieve | 1.730 | -42.78 | 6 msr | E-matrix |
| ca_2_8 | H_15cm | -4 | 2.886 | 23.01 | 6 msr | 1.730 | -42.78 | 6 msr | E-accept |
| ca_2_9 | H_15cm | -2 | 2.946 | 23.01 | sieve | 1.730 | -42.78 | 6 msr | E-matrix |
| ca_2_10 | H_15cm | -2 | 2.946 | 23.01 | 6 msr | 1.730 | -42.78 | 6 msr | E-accept |
| ca_2_11 | H_15cm | +2 | 2.066 | 23.01 | sieve | 1.730 | -42.78 | 6 msr | E-matrix |
| ca_2_12 | H_15cm | +2 | 3.066 | 23.01 | 6 msr | 1.730 | -42.78 | 6 msr | E-accept |
| ca_2_13 | H_15cm | +4 | 3.126 | 23.01 | sieve | 1.730 | -42.78 | 6 msr | E-matrix |
| ca_2_14 | H_15cm | +4 | 3.126 | 23.01 | 6 msr | 1.730 | -42.78 | 6 msr | E-accept |
| ca_2_15 | H_15cm | +0 | 3.006 | 23.01 | 6 msr | 1.730 | -42.78 | sieve | H-matrix |
| ca_2_16 | H_15cm | +0 | 3.006 | 23.01 | 6 msr | 1.730 | -42.78 | 6 msr | H-accept |
| ca_2_17 | E_4cm | +0 | 3.006 | 23.01 | 6 msr | 1.730 | -42.78 | 6 msr | H-z_matrix |
| ca_2_18 | E_10cm | +0 | 3.006 | 23.01 | 6 msr | 1.730 | -42.78 | 6 msr | H-z_matrix |
| ca_2_19 | $C^{12}$ | +0 | 3.006 | 23.01 | 6 msr | 1.730 | -42.78 | 6 msr | H-z_matrix |
| ca_2_20 | H_15cm | +0 | 3.006 | 23.01 | 6 msr | 1.730 | -43.28 | sieve | H-matrix |
| ca_2_21 | H_15cm | +0 | 3.006 | 23.01 | 6 msr | 1.730 | -43.28 | 6 msr | H-accept |
| ca_2_22 | H_15cm | +0 | 3.006 | 23.01 | 6 msr | 1.730 | -42.18 | sieve | H-matrix |
| ca_2_23 | H_15cm | +0 | 3.006 | 23.01 | 6 msr | 1.730 | -42.18 | 6 msr | H-accept |
| ca_2_24 | H_15cm | +0 | 3.006 | 23.01 | 6 msr | 1.730 | -43.98 | sieve | H-matrix |
| ca_2_25 | H_15cm | +0 | 3.006 | 23.01 | 6 msr | 1.730 | -43.98 | 6 msr | H-accept |
| ca_2_26 | H_15cm | +0 | 3.006 | 23.01 | 6 msr | 1.730 | -41.58 | sieve | H-matrix |
| ca_2_27 | H_15cm | +0 | 3.006 | 23.01 | 6 msr | 1.730 | -41.58 | 6 msr | H-accept |

Table A-3: *Elastic Kinematics for calibration of electron and hadron spectrometer at* $Q^2$*=1.9(GeV/c)*$^2$.

|  |  | electron spectrometer |  |  |  | hadron spectrometer |  |  |
|---|---|---|---|---|---|---|---|---|
| names | target | $\frac{\delta p}{p}$ | P | $\theta_E$ | colli | P | $\theta_H$ | colli |
| da_2_1 | H_15cm | -1.8 | 2.950 | 23.01 | 6 msr | 1.427 | -42.0 | 6 msr |
| da_2_2 | H_15cm | -1.8 | 2.950 | 23.01 | 6 msr | 1.427 | -40.0 | 6 msr |
| da_2_3 | H_15cm | -1.8 | 2.950 | 23.01 | 6 msr | 1.427 | -38.0 | 6 msr |
| da_2_4 | H_15cm | -1.8 | 2.950 | 23.01 | 6 msr | 1.518 | -42.5 | 6 msr |
| da_2_5 | H_15cm | -1.8 | 2.950 | 23.01 | 6 msr | 1.518 | -39.5 | 6 msr |
| da_2_6 | H_15cm | -1.8 | 2.950 | 23.01 | 6 msr | 1.518 | -37.5 | 6 msr |
| da_2_7 | H_15cm | -1.8 | 2.950 | 23.01 | 6 msr | 1.598 | -41.1 | 6 msr |
| da_2_8 | H_15cm | -1.8 | 2.950 | 23.01 | 6 msr | 1.598 | -39.3 | 6 msr |
| da_2_9 | H_15cm | -1.8 | 2.950 | 23.01 | 6 msr | 1.598 | -37.1 | 6 msr |
| da_2_10 | H_15cm | -1.8 | 2.950 | 23.01 | 6 msr | 1.688 | -40.0 | 6 msr |
| da_2_11 | H_15cm | -1.8 | 2.950 | 23.01 | 6 msr | 1.688 | -39.0 | 6 msr |
| da_2_12 | H_15cm | -1.8 | 2.950 | 23.01 | 6 msr | 1.688 | -37.5 | 6 msr |
| da_2_13 | H_15cm | -1.8 | 2.950 | 23.01 | 6 msr | 1.768 | -38.5 | 6 msr |
| da_2_14 | H_15cm | -1.8 | 2.950 | 23.01 | 6 msr | 1.768 | -38.0 | 6 msr |

Table A-4: *VCS data acquisition below pion production threshold at* $Q^2$*=1.9(GeV/c)*$^2$.

| | | electron spectrometer | | | | hadron spectrometer | | |
|---|---|---|---|---|---|---|---|---|
| names | target | s(GeV) | P | $\theta_E$ | colli | P | $\theta_H$ | colli |
| res_s_1.30 | H_15cm | 1.30 | 3.282 | 15.77 | 6 msr | 1.323 | -45.41 | 6 msr |
| res_s_1.50 | H_15cm | 1.50 | 3.176 | 16.04 | 6 msr | 1.418 | -41.67 | 6 msr |
| res_s_1.75 | H_15cm | 1.75 | 3.043 | 16.39 | 6 msr | 1.539 | -37.49 | 6 msr |
| res_s_2.00 | H_15cm | 2.00 | 2.909 | 16.76 | 6 msr | 1.662 | -33.82 | 6 msr |
| res_s_2.25 | H_15cm | 2.25 | 2.776 | 17.16 | 6 msr | 1.787 | -30.60 | 6 msr |
| res_s_2.50 | H_15cm | 2.50 | 2.642 | 17.59 | 6 msr | 1.914 | -27.75 | 6 msr |
| res_s_2.80 | H_15cm | 2.80 | 2.482 | 18.15 | 6 msr | 2.067 | -24.75 | 6 msr |
| res_s_3.20 | H_15cm | 3.20 | 2.269 | 18.99 | 6 msr | 2.274 | -21.34 | 6 msr |
| res_s_3.60 | H_15cm | 3.60 | 2.056 | 19.96 | 6 msr | 2.482 | -18.46 | 6 msr |
| res_s_4.00 | H_15cm | 4.00 | 1.843 | 21.09 | 6 msr | 2.691 | -15.99 | 6 msr |
| names | target | $Q^2$((GeV/c)$^2$) | P | $\theta_E$ | colli | P | $\theta_H$ | colli |
| res_q_.60 | H_15cm | .60 | 2.931 | 12.91 | 6 msr | 1.567 | -29.01 | 6 msr |
| res_q_1.0 | H_15cm | 1.0 | 2.718 | 17.34 | 6 msr | 1.843 | -29.30 | 6 msr |
| res_q_1.5 | H_15cm | 1.5 | 2.451 | 22.42 | 6 msr | 2.166 | -27.83 | 6 msr |
| res_q_2.0 | H_15cm | 2.0 | 2.185 | 27.51 | 6 msr | 2.473 | -25.68 | 6 msr |
| res_q_2.5 | H_15cm | 2.5 | 1.919 | 32.96 | 6 msr | 2.772 | -23.28 | 6 msr |
| res_q_3.0 | H_15cm | 3.0 | 1.652 | 39.13 | 6 msr | 3.064 | -22.74 | 6 msr |
| res_q_3.2 | H_15cm | 3.2 | 1.508 | 42.65 | 6 msr | 3.180 | -19.48 | 6 msr |

Table A-5: *VCS data : excitation curve at* $Q^2$*=1 (GeV/c)*$^2$, $\theta_{cm}^{\gamma^*\gamma} = 180°$ *and VCS data :* $Q^2$ *dependence at at s=2.36 GeV*, $\theta_{cm}^{\gamma^*\gamma} = 180°$.

# Appendix B

# Coordinate Systems

A short review of the coordinate systems used in this thesis is given here. For more detailed information, see reference [71]. All the systems presented here are Cartesian and the angular coordinates refer to the tangent of the angle.

## Hall A Laboratory Coordinate System (HLCS)

The origin of the HLCS is defined by the intersection of the non-rastered electron beam and the axis of rotation of the solid target system. This point is supposed to be the center of the Hall A. The positive z direction is the forward electron beam direction, the y direction is pointing upwards as defined by gravity. Angles are defined with respect to this origin and a ray pointing along the positive z-axis. The angle $\theta$ is 0 along the z axis and covers a range from 0° to 180° in the x-z plane. $\phi$ is the out-of-plane angle between a vector and its projection on the x-z plane. In figure B-1 this coordinate system is presented.

## Spectrometer Reconstructed Coordinate System/Target Coordinate System

The z axis of the Target Coordinate System is defined as the line perpendicular to the sieve slit surface and going through the center of the central sieve-slit hole. The positive z direction points away from the target. The x axis of this coordinate system is parallel to the sieve slit surface and points down as defined by gravity. The origin of the target coordinate system is defined to be the point on the z axis at a fixed distance from the sieve slit surface. This distance is 1183 mm for the electron spectrometer and 1174 mm for the hadron spectrometer. Under ideal circumstances the center of this target coordinate system coincides with the center of the Hall A and the center of rotation of the two spectrometers. The x-z plane should be parallel

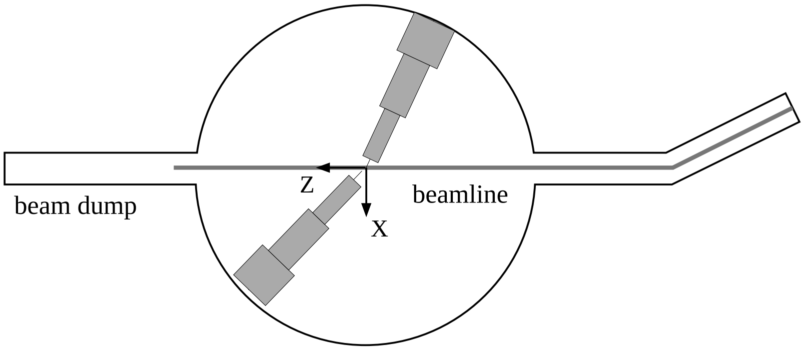

*Figure B-1: Hall A Laboratory Coordinate System (HLCS).*

with the y axis of the HLCS. The angle $\theta_{tg}$ is the out-of-plane angle defined as $\frac{dx_{tg}}{dz}$, $\phi_{tg}$ the in-plane angle defined as $\frac{dy_{tg}}{dz}$. In figure B-2 this coordinate system is shown. $\Theta_0$ is the nominal angle of the spectrometer. Each one of the two spectrometers has its own target coordinate system.

## Spectrometer Detector Coordinate System (SDCS)

The origin of the SDCS is defined by the intersection of wire 184 in the first wire plane (U1) and the perpendicular projection of wire 184 in the second wire plane (V1) onto the first wire plane. The z axis is perpendicular to the wire plane and pointing upwards. The x axis is defined as the projection on the first wire plane of the vector difference between the spectrometer central ray and a ray for which the momentum has been increased by an infinitesimal amount. Its direction is fixed by demanding an increase in momentum. Figures B-3 and B-4 give a clear view of this coordinate system.

## Transport Coordinate System (TCS)

The TCS is configured by rotating the SDCS by 45° clockwise around its y axis. In ideal circumstances the z axis of the TCS coincides with the spectrometer central ray. A side view of the TCS is presented in figure B-5.

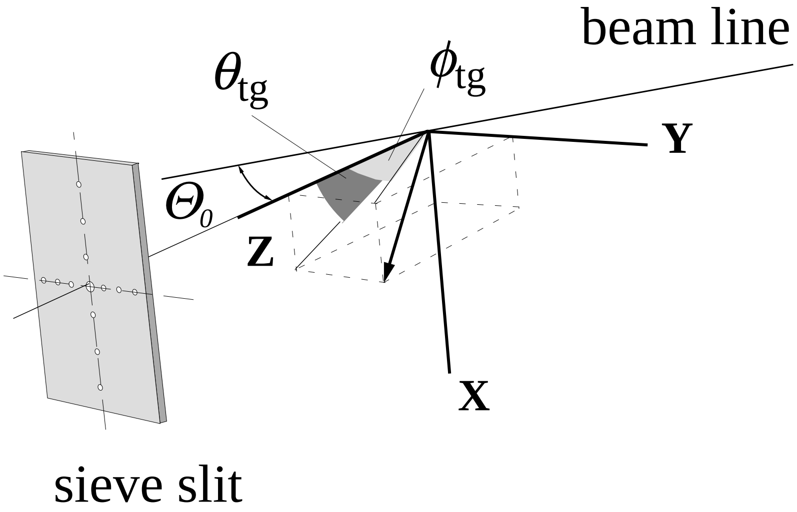

Figure B-2: Target Coordinate System.

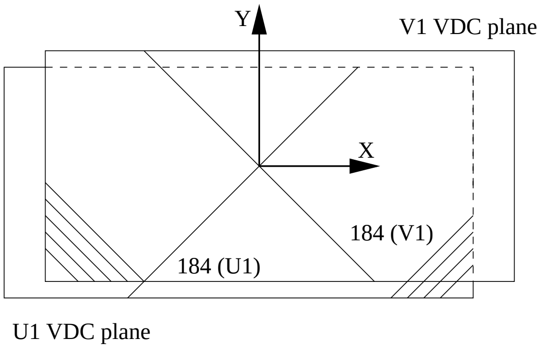

Figure B-3: Spectrometer Detector Coordinate System (top view).

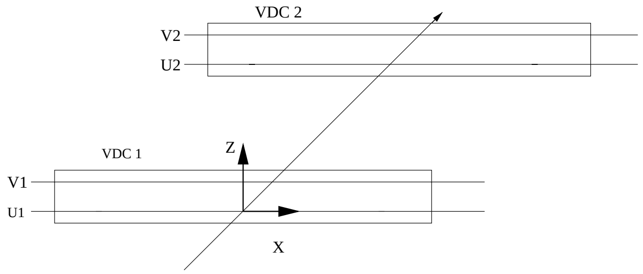

*Figure B-4: Spectrometer Detector Coordinate System (side view).*

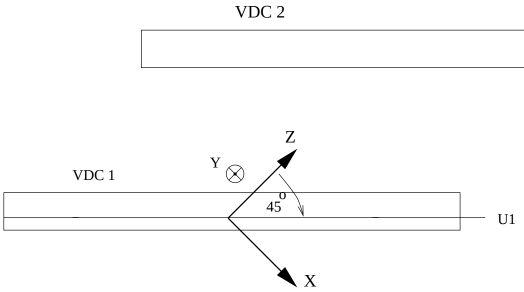

*Figure B-5: Transport Coordinate System (top view).*

# Spectrometer Focal Plane Coordinate System (SFPCS)

The SFPCS is a rotated coordinate system. It has the same origin as the SDCS, and the x-z planes of the two systems coincide. However, the SFPCS z-axis (and therefore also its x-axis) is defined as the projection of the local central ray on the x-z plane. This implies that the z axis rotates as a function of the particles relative momentum $\frac{\Delta p}{p}$. In figure B-6, this coordinate system is shown.

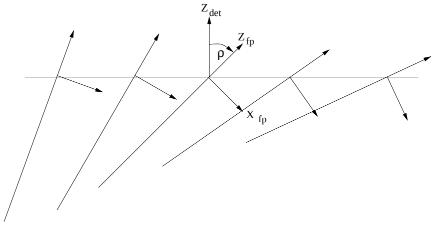

*Figure B-6: Spectrometer Focal Plane Coordinate System as a function of the focal plane position.*

# References

[1] B. Povh, K. Rith, C. Scholz and F. Zetsche, Particles and Nuclei, Springer-Verlag Berlin Heidelberg (1999)

[2] P. E. Bosted, Phys. Rev. C 51, 409 (1995)

[3] G. Höhler, et al., Nucl. Phys. B114, 505 (1976)

[4] J. Roche, Thèse d'Université, Blaise Pascal, DAPNIA/SPhN-98-06T (1998)

[5] M. K. Jones, et al., Phys. Rev. Lett. 84, 1398 (2000)

[6] Lord Rayleigh, Phil. Mag. 47, 375 (1899)

[7] M. Gell-Mann et al., Phys. Rev. 96, 1433 (1954); F. E. Low, Phys. Rev. 96, 1428 (1954)

[8] A. L'vov, Int. J. Mod. Phys. A8, 5267 (1993)

[9] D. Drechsel, et al., proceedings of the workshop 'Chiral Dynamics : Theory and Experiment', Mainz (1997); D. Drechsel, et al., MKPH-T-99-9 or hep-ph/9904290

[10] B. B. Govorkov, et al., Sov. Phys. Doklady 1, 735 (1957)

[11] V. I. Gol'danski, et al., Sov. Phys. JETP 11, 1223 (1960)

[12] B. E. MacGibbon et al., Phys. Rev. C52, 2097 (1995)

[13] P. S. Baranov, et al., Sov. J. Nucl. Phys. 21, 355 (1975)

[14] F. J. Federspiel, et al., Phys. Rev. Lett. 67, 1511 (1991)

[15] A. Zieger, et al., Phys. Lett. B 278, 34 (1992)

[16] E. Hallin, et al., Phys. Rev. C 48, 1497 (1993)

[17] Olmos de Léon V., Ph.D. thesis, University Mainz (2000)

[18] A. M. Baldin, Nucl. Phys. 18, 318 (1960); L. I. Lapidus, Zh. Eksp. Teor. Fiz. 43, 1358 (1962) [Sov. Phys. JETP 16, 964 (1963)]

[19] M. Damashek and F.J. Gilman, Phys. Rev. D 1, 1319 (1970)

[20] D. Babusci, G. Giordano and G. Matone, Phys. Rev. C 57, 291 (1998)

[21] P.A.M. Guichon and Marc Vanderhaeghen, Virtual Compton Scattering off the nucleon, Progress in Particle and Nuclear Physics, Vol. 41, 125 (1998)

[22] F.E. Low, Phys. Rev. 110, 974 (1958)

[23] D. Lhuillier, Thèse d'Université, Caen, DAPNIA/SPhN-97-01T (1997)

[24] P.A.M. Guichon, et al., Nucl. Phys. A591, 606 (1995)

[25] D. Marchand, Thèse d'Université, Blaise Pascal, DAPNIA/SPhN-98-04T (1998)

[26] A.J.F. Siegert, Phys. Rev. 52, 787 (1937)

[27] D. Drechsel, et al.,Phys. Rev. C 55, 424 (1997)

[28] D. Drechsel, et al.,Phys. Rev. C 57, 941 (1998)

[29] M. Vanderhaeghen, Phys. Lett. B 402 243 (1997)

[30] H. Schmieden, Eur. Phys. J. A 1, 427 (1998)

[31] G.Q. Liu et al., Aust. J. Phys. 49, 905 (1996)

[32] B. Pasquini, S. Scherer and D. Drechsel, to appear in Phys. Rev. C63

[33] M. Vanderhaeghen, Phys. Lett. B 368, 13 (1996)

[34] A. Metz et al., Z. Phys. A 356, 351 (1996); 359, 165 (1997)

[35] T.R. Hemmert et al., Phys. Rev. D 55, 2630 (1997); Phys. Rev. Lett. 79, 22 (1997); nucl-th/9910036

[36] T.R. Hemmert et al., Phys. Rev. D 55, 5598 (1997)

[37] V. Bernard, et al., Phys. Lett. B 319, 269 (1993)

[38] B. Pasquini et al., Phys. Rev. C (in print) (2000)

[39] M. Vanderhaeghen et al., World Schientific (submitted)(2000)

[40] D. Drechsel et al., Nucl. Phys. A 645, 145 (1999)

[41] X. Ji et al., Phys. Rev. D 61, 074003 (2000)

[42] K. B. Vijaya Kumar et al., Phys. Lett. B 479, 167 (2000)

[43] G.C. Gellas et al., Phys. Rev. Lett. 85, 14 (2000)

[44] J. Roche, et al., Phys. Rev. Lett., Vol 85, 708 (2000)

[45] J. Friedrich, Ph. D. University Mainz (2000)

[46] M. Vanderhaeghen, et al., Phys. Rev. D 62, 014013 (2000)

[47] N. D'Hose, private communication (article in preparation)

[48] Hemmert T.R., B.R. Holstein, G. Knöchlein, D. Drechsel, Phys. Rev. D 62, 014013 (2000)

[49] World Wide Web page of TJNAF Hall A, http://hallaweb.jlab.org (2000)

[50] A. Deur, La cible cryogenique du hall A du Thomas Jefferson National Accelerator Facility, Universite Blaise Pascal internal report 1997 (unpublished)

[51] C. Hyde-Wright, L. Todor, G. Laveissiere, Beam Position Studies for E93-050, E93-050 internal report 1999 (unpublished)

[52] B. D. Diederich et al., Charge Determination in Hall A at Jefferson Lab, Jlab internal report 1998 (unpublished)

[53] R. Suleiman, Hall A Cryogenic and Dummy Targets Information, Jlab internal report TN-98-007,1998 (unpublished)

[54] K. McCormick, Cryotarget Density Dependence on Beam Current, Jlab internal report 1999 (unpublished)

[55] S. Jaminion, Thèse d'Université, Blaise Pascal, in print

[56] J. Alcorn, J. LeRose, S. Nanada, E. Offerman, The Hall A Sextupole Crisis

[57] S. Jaminion, H. Fonvieille, technical note 'HRS Optics Optimization with extended targets' (2000)

[58] S. Jaminion, H. Fonvieille, technical note 'A study of optic Databases resolution' (2000)

[59] L. Todor, PhD thesis, 'Virtual Compton Scattering in Resonance Region', Old Dominion University, in print

[60] World Wide Web page of TJNAF Hall A Spectrometers, http://hallaweb.jlab.org/equipment/high_resol.html (2000)

[61] CEBAF Conceptual Design Report - Basic experimental equipment April 13, 1990

[62] K. Fissum et al., VDC Manual V2.1,MIT-LNS internal report 1997 (unpublished)

[63] L. Van Hoorebeke et al., in preparation

[64] L. Van Hoorebeke, internal notes 'A Manual for the use of the VCS Simulation Package VCSSIM, RESOLUTION and ANALYSIS' (1999)

[65] L. Van Hoorebeke, internal notes 'Electron Energy Loss Distributions for Real Radiation Effects used in VCSSIM', 'Some Considerations on the Implementation of Real Radiation Effects in VCSSIM' (1998)

[66] Review of Particle Physics C Vol 3, 178 (1998)

[67] L. Van Hoorebeke, internal notes 'Determination of the Integrated Luminosity in VCSSIM' (2000)

[68] N. Liyanage, internal note 'Optics Commissioning of the Hall A High Resolution Spectrometers' (1998)

[69] L. Van Hoorebeke, resolution code of Monte Carlo simulation for VCS at TJNAF (2000)

[70] L. Van Hoorebeke, private communications

[71] E. Offerman et al., ESPACE manual version 2.7.0 (1999)

[72] G. Laveissiere, internal note 'Asynchronization Problems of the BPM/Raster ADC for E93-050' (1999)

[73] J. Gomez, private communications

[74] S. Jaminion and H. Fonvieille, internal report, 'Ytarget optimisation for E93-050 experiment. Part I : $Q^2$=1(GeV/c)$^2$.'PCCF-RI-9816

[75] R. Michaels, internal note 'Electronic Dead Time Measurements' (2000)

[76] M. Jones, internal note 'Report on Electronic Dead Time' (2000)

[77] M. Liang, internal note 'DAQ Dead-time study for E93-050' (1999)

[78] R. Disalvo et al., internal note 'Scintillators efficiency' (2000)

[79] P.Y. Bertin, et al., internal note 'Minimization Method fro Jlab E93050-VCS experiment' (1999)

[80] C. Jutier, Old Dominion University, private communications.

[81] H. Fonvieille, internal note 'Practical use of radiative corrections to measured cross sections $d^5\sigma(ep \to ep\gamma)$'(2000)

[82] M. Vanderhaeghen, et al., 'QED radiative corrections to virtual Compton scattering', Phys. Rev. C 62, 025501 (2000)

[83] H. Fonvieille, et al., internal note 'Summary of Meeting on VCSSIM' (1999)

# Samenvatting

Een fundamenteel probleem in de hedendaagse subatomaire fysica is de karakterisatie van de interne structuur van het nucleon. Op korte afstandsschaal kan de nucleonstructuur beschreven worden door het samenspel van quarks en gluonen, maar op grotere schaal (van de grootte van de afmetingen van het nucleon) worden de zaken minder duidelijk. Er bestaan verschillende theoretische modellen die deze structuur van het nucleon beschrijven, doch er zijn experimentele gegevens nodig om veronderstellingen die gemaakt worden te staven en om waarden te bekomen voor parameters die in deze modellen gebruikt worden. In die zoektocht naar de brug tussen deeltjes- en kernfysica speelt de electromagnetische probe een belangrijke rol. Inderdaad, de electromagnetische interactie is goed gekend en ze verschaft waardevolle informatie over de nucleonstructuur. Verschillende decennia lang zijn experimenten en studies verricht via elastische electronverstrooiing, reële comptonverstrooiing en diep-inelastische verstrooiing. Deze inspanningen hebben geleid tot de kennis van de electrische ($\bar{\alpha}_E$) en magnetische ($\bar{\beta}_E$) polarizeerbaarheden, de nucleon vormfactoren en structuurfuncties. De laatste jaren echter, met de komst van de nieuwe generatie electronenversnellers en detectoren, werd een nieuwe probe beschikbaar : de Virtuele Compton Verstrooiing (VCS) aan het nucleon. Dit proces verwijst naar de interactie waarbij een virtueel foton, met negatief vier-momentum in het kwadraat $Q^2$, geabsorbeerd wordt door een nucleon dat een reëel foton uitstuurt om weer naar zijn grondtoestand te keren. Beneden de drempel van de pionenproductie kan deze interactie voorgesteld worden als electronverstrooiing aan een nucleon dat zich in een quasi-constant electromagnetisch veld bevindt van het uitgaande reële foton. Dit proces kan experimenteel bestudeerd worden via de foton electroproductie reactie ($e + p \rightarrow e' + p' + \gamma$) en geeft nieuwe informatie over de interne nucleonstructuur in de vorm van 6 veralgemeende polarizeerbaarheden. Deze veralgemeende polarizeerbaarheden kunnen gezien worden als grootheden die het effect van een electromagnetische perturbatie op de nucleon componenten kwantificeren. Ze zijn een veralgemening van de electrische en magnetische polarizeerbaarheden uit reële comptonverstrooiing ($Q^2$=0 (GeV/c$)^2$) en ze beschrijven hoe de ladings- en stroomdistributies in het nucleon, bekomen uit elastische electronverstrooiing, zich gedragen onder de invloed van een uitwendige electromagnetische verstoring. In die zin is VCS een veralgemening van reële comptonverstrooiing en complementair aan electronverstrooiing aan een vrij nucleon. Tot op heden hebben 2 VCS experimenten plaatsgevonden die tot doel hebben informatie te bekomen over de veralgemeende polarizeerbaarheden bij verschillende $Q^2$ : het VCS experiment aan MAMI (1995-1997) bij $\tilde{Q}^2$=0.33(GeV/c)$^2$ en het VCS experiment aan TJNAF (1998) bij $Q^2$=1.0(GeV/c)$^2$ en $Q^2$=1.9(GeV/c)$^2$. Een derde VCS experiment bij $Q^2$=0.05 (GeV/c)$^2$ is gepland aan BATES. De experimentele studie van de evolutie van de veralgemeende polarizeerbaarheden in functie van $Q^2$, die de ruimtelijke resolutie van de electromagnetische probe bepaalt, zal toelaten om de theoretische modellen te testen en te beoordelen. In het eerste hoofdstuk van dit doctoraatswerk wordt het fysische kader van VCS en de veralgemeende polarizeerbaarheden uitgewerkt. Ook wordt uitgelegd hoe het meten van (ongepolariseerde) foton electroproductie reacties leidt tot informatie over (combinaties van) veralgemeende polarizeerbaarheden.

Het tweede hoofdstuk geeft een samenvatting van de analyse en de resultaten van het experiment dat als eerste het VCS proces beneden de pionendrempel bestudeerd heeft met als doel het verwerven van informatie over de veralgemeende polarizeerbaarheden. Dit was de meting uitgevoerd aan het Mainzer Microtron (MAMI) in Duitsland in 1995-1997. Het heeft aangetoond dat VCS experimenten mogelijk zijn, maar niet zo eenvoudig aangezien een grote nauwkeurigheid vereist is voor de bekomen werkzame doorsneden van de foton electroproductie reactie. Inderdaad, het effect van de veralgemeende polarizeerbaarheden manifesteert zich in de werkzame doorsnede als een kleine afwijking (±10%) van de volledig gekende BH+Born werkzame doorsnede. Deze theoretische werkzame doorsnede is gebaseerd op de globale eigenschappen van het proton (lading, massa, anomaal magnetisch moment, vormfactoren). Desalniettemin is men erin geslaagd de waarden van 2 structuurfuncties, die lineaire combinaties zijn van 5 van de 6 veralgemeende polarizeerbaarheden, te bepalen bij $\tilde{Q}^2 = 0.33\ (GeV/c)^2$ : $(\mathbf{P_{LL}}(\mathsf{q}_{cm}) - \frac{1}{\epsilon}\mathbf{P_{TT}}(\mathsf{q}_{cm})) = 23.7 \pm 2.2 \pm 0.6 \pm 4.3\ GeV^{-2}$ en $\mathbf{P_{LT}}(\mathsf{q}_{cm}) = -5.0 \pm 0.8 \pm 1.1 \pm 1.4\ GeV^{-2}$. Deze waarden zijn in overeenstemming met voorspellingen van de heavy-baryon perturbation theorie.

In 1998 vond het tweede VCS experiment plaats aan de Thomas Jefferson National Accelerator Facility (TJNAF) in de Verenigde Staten. Hierin werden foton electroproductie reacties gemeten bij $Q^2 = 1.0(GeV/c)^2$, $Q^2 = 1.9(GeV/c)^2$ en in het resonantie gebied. Het huidig doctoraatswerk richt zich vooral op de analyse van de data genomen bij $Q^2 = 1.0(GeV/c)^2$. De experimentele opstelling die gebruikt is voor dit experiment wordt beschreven in het derde hoofdstuk. Een continue electronenbundel met een energie van 4045 MeV interageerde met een 15 cm lange vloeibare waterstof target. Het verstrooide electron en terugstootproton werden in coincidentie gedetecteerd in de 2 hoge resolutie spectrometers van Hall A. Na reconstructie van momentum- en vertexinformatie van het verstrooide electron en terugstootproton, werd het vier-momentum van het ontbrekende (niet gedetecteerde) deeltje gereconstrueerd. Dit vier-momentum geeft de mogelijkheid om het ontbrekende deeltje te identificeren : VCS interacties eisen dat de ontbrekende massa de foton massa, $m_\gamma = 0\ MeV/c^2$, is, pionenproductie interacties daarentegen zijn gekenmerkt door een ontbrekende massa van $m_{\pi^0} \approx 135\ MeV/c^2$. De fase-ruimte die toegankelijk was tijdens dit experiment liet geen detectie toe van andere reacties. Dankzij de goede energieresolutie van de TJNAF faciliteit was het mogelijk om foton- en pionproductie te onderscheiden door reconstructie van de ontbrekende massa.

Het vierde hoofdstuk beschrijft de Monte Carlo simulatie die gebruikt wordt voor het berekenen van de "ruimtehoeken" die nodig zijn voor het bepalen van experimentele werkzame doorsneden. Deze simulatie genereert evenementen volgens een BH+Born (of elastische) werkzame doorsnede gedrag. De experimentele opstelling en resoluties, stralingseffecten en energieverliezen worden in rekening gebracht. Deze simulatie biedt, naast het genereren van ruimtehoeken, een waaier aan mogelijkheden die bijgedragen hebben tot de analyse van het experiment. Het is een onmisbare hulp in de zoektocht naar volledige kennis van de experimentele opstelling en fysische processen die zich afspelen.

In het vijfde hoofdstuk wordt de analyse van de data bij $Q^2 = 1.0\ (GeV/c)^2$ uitvoerig beschreven. De oorspronkelijke data, verzameld tijdens de metingen, worden stap voor stap bewerkt en geanalyseerd om uiteindelijk tot differentiële werkzame doorsneden te komen. De analyse van de elastische verstrooiingsdata, gepresenteerd in het zesde hoofdstuk, leert dat in het centrum van de acceptantie van beide spectrometers de calibratie en resoluties redelijk goed gekend zijn. De randen van de acceptantie echter, zijn minder onder controle. Dit heeft invloed op de analyse van de VCS data, aangezien deze de volledige spectrometer acceptanties bestrijken. De analyse van de VCS data heeft geleid tot voorlopige werkzame doorsneden voor de foton electroproductie reactie. Deze worden uitvoerig voorgesteld in het zevende hoofdstuk. De werkzame doorsneden worden geëvalueerd in functie van $\mathsf{q}'_{cm}$ en $\theta_{cm}^{\gamma^*\gamma}$, het momentum van het uitgaande foton en de polaire hoek tussen het inkomende virtuele en uitgaande reële foton, respectievelijk, bij vaste waarden van $\mathsf{q}_{cm}$ (momentum van het virtuele foton) en $\epsilon$ (de polarizatiegraad van het virtuele foton).

Om uiteindelijk de 2 structuurfuncties te bepalen hebben we eerst geverifiëerd dat de foton electroproductie werkzame doorsnede, bij lage $\mathsf{q}'_{cm}$, wel degelijk convergeert, binnen de foutenvlaggen, naar de BH+Born werkzame doorsnede. Dit is immers de eerste, noodzakelijke stap die moet genomen worden bij het extraheren van informatie over de veralgemeende polarizeerbaarheden. Alhoewel het duidelijk is dat de analyse van de data in de toekomst nog zal moeten verbeteren, is in hoofdstuk 8 een eerste poging ondernomen om voorlopige, indicatieve waarden voor de 2 structuurfuncties te bepalen bij $\mathrm{Q}^2 = 1.0\ (\mathrm{GeV/c})^2$, $\mathsf{q}_{cm} = 1084.1$ MeV/c en $\epsilon = 0.951$ ($\tilde{Q}^2 = 0.93\ (GeV/c)^2$) : $(\mathbf{P_{LL}}(\mathsf{q}_{cm}) - \frac{1}{\epsilon}\mathbf{P_{TT}}(\mathsf{q}_{cm})) = 4.7 \pm 0.7 \pm 3\ GeV^{-2}$ en $\mathbf{P_{LT}}(\mathsf{q}_{cm}) = -1.1 \pm 0.3 \pm 1\ GeV^{-2}$. Dit zijn enkel indicatieve waarden die een eerste schatting geven voor de 2 structuurfuncties.

In de toekomst zullen nog grote inspanningen moeten geleverd worden om de kwaliteit van de data en de systematische onzekerheid op de bekomen resultaten te verbeteren. Eenmaal dit doel bereikt, kan men nauwkeuriger waarden voor de 2 structuurfuncties bepalen. Bovendien vertegenwoordigen de 2 experimenten die aan bod komen in dit doctoraatswerk slechts een van de mogelijkheden die er zijn om het veld van VCS en de veralgemeende polarizeerbaarheden te verkennen. Dubbel gepolariseerde experimenten bijvoorbeeld kunnen nog meer informatie verschaffen over de veralgemeende polarizeerbaarheden, het recent ontwikkelde dispersie-formalisme opent de mogelijkheid om data boven de drempel van pionenproductie te gebruiken om informatie over de nucleonstructuur te verzamelen, ... . Het is dus duidelijk dat VCS belooft een verscheidenheid aan wegen te openen die zullen helpen bij het opklaren van de schemerzone tussen de subhadronische en nucleaire wereld.

# Dankwoord

Met plezier schrijf ik tot slot nog een klein dankwoordje aan iedereen die rechtstreeks of onrechtstreeks een rol gespeeld heeft bij het tot stand komen van dit doctoraatswerk :

Niet in het minst mijn promotor, Robert Van de Vyver die er, samen met de andere leden van de onderzoeksgroep, voor zorgde dat het aangenaam vertoeven was op het INW, zelfs op momenten dat Virtual Compton Scattering meer weg had van Very Catastrophic Scattering ... . Luc, die mij van de eerste tot de laatste dag met raad en daad heeft bijgestaan in de wereld van virtuele en alle mogelijke andere deeltjes. Dirk, Heidi, Bob, Michael, Katty en Brecht voor de aangename en ontspannen werksfeer.

C'est avec plaisir que j'adresse un mot de remerciement a tous mes collègues de Clermont-Ferrand : Pierre, Hélène, Géraud, Stéphanie et Rachele. Pas seulement pour leur aide et les nombreuses contributions dans l'analyse des données, mais aussi pour l'acceuil chaleureux pendant tous mes petits voyages en Auvergne.

A Domi, je voudrais dire "on y est arrivé, grâce aux margaritas et malgré le lead-glass !! Merci pour ton aide et les nuits folles aux Etats-Unis !"

I also want to thank Nicole, Sophie, Charles, Luminita, Christoph and all the other members of the VCS-collaboration for their valuable inputs that were necessary for the progress during my PhD-work.

Uiteraard was er meer nodig dan een groep mensen die vol enthousiasme het VCS-avontuur in wilden duiken. Daarom wil ik ook de universiteit van Gent danken die mij de mogelijkheid geboden heeft deel te nemen aan deze toch wel onvergetelijke onderneming.

Tot slot mogen zeker mijn ouders, mijn zus, Piet, familie en vrienden niet ontbreken in dit dankwoordje. Zij hebben mij gedurende mijn onderzoekswerk immers gesteund en gezorgd voor al die niet-virtuele-compton verstrooiing.